Out of Equilibrium Dynamics in Magnetic and Superconducting Nanostructures

Antonio Lara Cala

A thesis submitted in partial fulfillment of the requirements for the degree of Doctor of Philosophy

Departamento de Física de la Materia Condensada
Universidad Autónoma de Madrid

Thesis directed by Farkhad Aliev Kazanski

2017

Contents

Part I

Introduction

Acknowledgements

Una gran cantidad de personas han contribuido con su ayuda al desarrollo de esta tesis. Me gustaría en primer lugar agradecer a mi director de tesis, Farkhad Aliev, haber depositado su confianza en mi para realizar esta tesis en el grupo Magnetrans de la UAM. Sin sus consejos y supervisión durante estos últimos años este trabajo no habría sido posible. No solamente su disponibilidad y la continua discusión de ideas han servido para profundizar en los aspectos más técnicos, sino que también ha facilitado enormemente el contacto con otras instituciones e investigadores que, directa o indirectamente, han contribuido decisivamente al desarrollo de este trabajo. Además, en el día a día he aprendido de él la manera de enfrentarme a las dificultades que surgen frecuentemente en la investigación de una forma más independiente.

A continuación me gustaría destacar la también esencial labor de los otros miembros del grupo Magnetrans. En primer lugar, Ahmad Awad, quien me precedió en el laboratorio, y me enseñó todo sobre el funcinamiento del mismo. David Herranz, que siempre estuvo disponible para cualquier cosa que necesitase. Juan Sierra y Vladimir Pryadun, por poner a punto el sistema de medidas de alta frecuencia, una década antes de que yo lo haya utilizado, y que siempre ha funcionado tan bien. Arkadi Levanyuk y Raúl Villar, de quienes, pese a no haber compartido con ellos tanto tiempo como me hubiera gustado, he aprendido tanto. Juan Pedro Cascales, con quien he compartido gran parte de mi tiempo en el laboratorio, y con quien el laboratorio siempre ha sido mucho más que un lugar de trabajo. Isidoro Martínez, que siempre ha estado ahí para hacer que las cosas fueran más fáciles. Dennis Dieleman, quien en tan poco tiempo aportó tanto al laboratorio y me enseñó tanto sobre simulaciones. Pablo Andrés, pese a su breve paso por el laboratorio, nos ayudó enormemente a todos a implantar las simulaciones GPU. Por último, Javier Robledo, que me ayudó con algunos de los resultados de esta tesis.

Esta tesis no habría sido posible sin la continua ayuda de los diferentes técnicos de la UAM, sin duda los mayores expertos en sus respectivos campos: Javier Díaz, por su silenciosa pero imprescindible labor para conseguir helio líquido cuando le avisábamos con tiempo, o de improviso. Santiago y José María, por su dedicación y de dejar a un lado todos sus encargos para hacer las piezas más inverosímiles en un tiempo mínimo, así como agilizar la interacción con el SEGAINVEX. José Luis, por toda su ayuda con la electrónica, y reparación de equipos. Andrés Buenía, por su ayuda cada vez que algún equipo de vacío no funcionó.

Otras personas del Departamento que han resultado imprescindibles han sido Elsa, Luisa y Ángeles, por su ayuda con todas las tareas administrativas, Stefan, por su ayuda con la informática, y Macarena, quien siempre ha mantenido el orden y la limpieza en el laboratorio.

Otros compañeros de tesis han sido un apoyo importante. En ningún orden concreto, Antón, Carlos Sánchez, Carlos González, Edwin, Blanca, Ana, Willie y Pepe.

La colaboración con investigadores de otros centros ha sido decisiva en algunas partes de la tesis. En concreto, sin las muestras crecidas por Vitali Metlushko (U. Illinois), Alejandro Silhanek (KU Leuven), José Luis Prieto (UPM), Oleksandr Dobrovolskiy (U. Frankfurt) y Konstantin Ilin (IMS Karlsruhe) esta tesis no sería posible.

Las medidas de los investigadores del ICMM-CSIC de MFM (con la ayuda de Agustina Asenjo y Óscar Iglesias), y de imanación con SQUID (Mar García-Hernández) han sido muy útiles para confirmar algunos resultados.

La discusión con Konstantin Guslienko y Yuri Galperin nos ha servido para aclarar muchas interpretaciones teóricas.

Agradezco también a José María de Teresa su predisposición a acogerme en su grupo durante una estancia breve con el programa Nanolito, y a Jassiek Michalik, por todo lo que me enseñó sobre litografía.

También quiero mencionar al programa COST por su ayuda para participar en el congreso Vortex en 2015 y al programa Erasmus por su ayuda para participar en la Escuela de Verano sobre magnetismo en Nijmegen en 2015.

Es inevitable agradecer a la Universidad Autónoma de Madrid su ayuda mediante las becas de Ayuda para Inicio de Estudios de Posgrado, y posteriormente la beca FPI-UAM, con la que he podido realizar esta tesis.

To finish, I would like to thank in English, in the hope that he will read it, Dr. Pavel Kabos for all his help and dedication before, during and after my stay at NIST in 2016. He helped in inimaginable ways to make this an unforgettable experience, from the scientific and personal point of view. Also, other people's help was critical at some points to keep things moving forward: Stephen Russek, with his resourcefulness every time we hit a dead end, Sam Beweger with all his patience and knowledge showing me about the SMM system, and Joel Weber for his technical help and skill in the clean room, and for presenting the results of this stay in the MMM conference. Also NIST secretaries Anna Coleman and Mary Gorman helped greatly in all the bureaucratic process.

Resumen

Historicamente, la respuesta magnética a altas frecuencias (permeabilidad magnética a frecuencias de microondas) se ha estudiado en primer lugar en sistemas cercanos al equilibrio. Los esfuerzos más recientes hacia la miniaturización han resultado en dispositivos que frecuentemente se encuentran en condiciones fuera del equilibrio (estados metaestables). Algunos ejemplos son los sistemas superconductores con vórtices anclados, sistemas con vórtices en estado crítico (estado Bean) sistemas magnétios con estados magnéticos complejos en los que participan paredes de dominios.

Esta tesis estudia la respuesta a altas frecuencias de sistemas magnéticos y superconductores en condiciones fuera de equilibrio. Como continuación del trabajo iniciado por el Dr. A. A. Awad, se comienza explorando formas de estabilizar estados metaestables (estados de doble vórtice) en elementos magnéticos cilíndricos de tamaño micrométrico donde aparecen paredes de dominio. En estos sistemas se observó cómo las ondas de espín puede propagarse sólo a través de paredes de dominio (los conocidos como "magnones de Winter"), y no en las demás zonas de los elementos magnéticos. Este sistema tiene interesantes propiedades, ya que permite dirigir ondas de espín a lo largo de caminos bien definidos y estrechos, sin que se extiendan a toda la geometría del sistema, como habitualmente ocurre. Las paredes de dominio presentes en el estado de doble vórtice son metaestables, e incluso si se pueden estabilizar durante algunas horas en muestras reales gracias a los defectos y el amortiguamiento magnético, finalmente acaban por moverse y el estado metaestable de doble vórtice decae al estado fundamental de vórtice individual.

El capítulo 3 explora una forma de fijar vórtices y paredes de dominio, para estabilizar estos estados metaestables, mediante la creación de nano agujeros en los elementos magnéticos, capaces de fijar estructuras magnéticas.

Después, en el capítulo 4, consideramos la posibilidad de la propagación de ondas de espín a través de paredes de dominio dentro de elementos magnéticos, solo que esta vez en estados que no decaen con el tiempo. Los sistemas elegidos son elementos micrométricos con forma triangular, donde las paredes de dominio tienen una estructura magnética más estable. En primer lugar, hay paredes de dominio en el estado fundamental de vórtice. Además, al aplicar un campo magnético aparecen unas nuevas regiones cerca de los bordes donde se acumula un exceso de energía de canje (similar a una pared de dominio, solo que en este caso se encuentra en el borde del triangulo, y discurre paralela a él), y de nuevo las ondas de espín se propagan con mayor amplitud por estas regiones que por las demás, en el interior del triángulo.

Los sistemas superconductores también pueden exhibir un comportamiento no trivial fuera del equilibrio, en este caso cerca de la transición superconductora, donde el fenómeno de estimulación por microondas cobra importancia. En el capítulo 6 estudiamos el efecto que tienen los vórtices en movimiento cerca de la temperatura crítica, en el régimen de estimulación, cuyos efectos hemos aprovechado para estudiar la disipación de vórtices. También, para comprender los resultados experimentales, hemos desarrollado un programa

para realizar simulaciones numéricas que resuelve la ecuación de Ginzburg Landau dependiente del tiempo. Este programa se explica en detalle en el capítulo 5.

Por último, el último fenómeno fuera de equilibrio que hemos estudiado en este trabajo está relacionado con las avalanchas de flujo magnético en superconductores, de nuevo cerca a la transición superconductora. Hemos observado cómo el efecto de estimulación de superconductividad contribuye a reforzar las barreras de potencial que el flujo magnético debe superar para entrar en el interior de la muestra superconductora.

Abstract

Historically, high frequency magnetic response (microwave magnetic permeability) has been first studied in macroscopic systems close to equilibrium. The more recent efforts towards miniaturization of devices have resulted in systems which are often found in conditions out of equilibrium (metastable) states. Examples of this are superconducting systems with pinned vortices, the formation of a pinned vortex Bean's critical state or magnetic structures in some complex magnetic states involving domain walls.

This thesis studies the high frequency response of magnetic and superconducting systems in out of equilibrium conditions. As a continuation of the work by Dr. A. A. Awad, this thesis starts by exploring ways of stabilizing metastable states (double vortex states) in magnetic micron sized dots with domain walls present. In such systems it was observed how spin waves can propagate only through the domain walls (the so called "Winter's magnons", and not anywhere else in the dot. This has interesting properties, since it allows to direct spin waves along specific and narrow paths, without them "spilling" everywhere, as usually tends to happen. The domain walls present in the double vortex state are metastable, and even if they can be stabilized for some hours in real samples, thanks to pinning and defects, they eventually move, and the metastable double vortex system decays into the ground state single vortex state.

Chapter 3 explores a way to pin vortices and domain walls, to stabilize such states, by drilling holes in the magnetic dots, capable to trap them.

Next, in chapter 4, we explore the possiblity of propagaing spin waves through domain walls in dots again, only that this time in non decaying systems. The system of choice is triangular magnetic dots, where domain walls have a more stable structure. First, there are domain walls in the ground state (vortex state). Second, under an applied field, new regions near the dot edges accumulate an excess of exchange energy (similar to a domain wall, only that it lays next to the dot border), and again, waves propagate especially well in those regions, compared to the inside of the dot. This case is another example of perturbations out of equilibrium, since these regions can only be maintained under the external action of a bias magnetic field.

Superconducting systems can also exhibit non trivial behaviors out of equilibrium, in this case close to the superconducting transtion, where stimulation of superconductivity by microwaves is a noticeable phenomenon. In chapter 6 we explore the effect of moving vortices close to the critical temperature, in this stimulated regime, whose effects we have used as a tool to study the dissipation of vortices. Also, to understand the experimental results, we have developed a simulation software to solve the Time Dependent Ginzburg Landau equation. This program is explained in detail in chapter 5.

Finally, the last out of equilibrium phenomenon studied in this work is magnetic flux

avalanches, again close to the superconducting transition. We have studied how the effect of stimulation of superconductivity takes place to strenghthen the potential barriers that must be overcome for avalanches to enter the sample.

Abbreviations and symbols

Abbr. or symbol	Definition
AFM	Atomic force microscope
B state	Buckle state (triangular dots)
Co	Cobalt
ξ	Coherence length (superconductors)
DMV	Double magnetic vortex
DV	Double vortex
DW	Domain wall
E-SWs	Edge spin waves
E-DWs	Edge domain walls
Fe	Iron
FFT	Fast Fourier Transform
κ	Ginzburg-Landau parameter (superconductors)
λ	London penetration depth (superconductors)
MFM	Magnetic force microscope
MSSC	Microwave stimulated superconductivity
mw	Microwaves
Ni	Nickel
Py	Permalloy
Ψ	Superconducting order parameter
SMM	Scanning microwave microscopy
SV	Single vortex
SW	Spin wave
SC	Superconductor
SQUID	Superconducting quantum interference device
TDGL	Time dependent Ginzburg-Landau
VNA	Vector network analyzer

1. Physical introduction

The goal of this chapter is to provide a description of the physical phenomena that will be discussed in later chapters, thorough enough so that our results can be understood, but not diving into too many details. In some cases, to avoid unnecessary complications, some demonstrations will be placed in the appendices for further information.

1.1 Static magnetism

First, a general introduction to static magnetism is provided, to describe some essential concepts that will be referred throughout the following chapters.

General magnetism

Magnetism in materials was already known in ancient Greece, where magnetite (Fe_3O_4), capable of magnetizing iron, was found in the city of Magnesia, after which magnets are named. However, it was only after a long time, in the early XIX century that magnetism started to be understood. In 1820 Oersted observed a magnetic field generated by an electric current, linking electricity and magnetism. Since then, magnetism quickly became an active field of research, and a number of discoveries were made by the most important physicists of the time (Faraday, Gauss, Ampère, Maxwell...). The discoveries on which our current understanding of magnetism is based date from the early XX century. For example, in 1895 Pierre Curie showed the existance of the Curie temperature, and Pierre-Ernest Weiss in 1906 proposed the existence of magnetic domains. Later, more detailed descriptions of the magnetization of the domain walls separating domains were provided by Landau, Bloch and Néel. Nowadays magnetism is a well known phenomenon which, however, keeps producing interesting and applicable resutls, and will probably do for many more years. This is so because of the different types of magnetism that exist, and how they combine with each other, and with other apparently non-magnetic phenomena to produce new effects (all the different magnetoresistive effects, spin waves, anisotropic effects, etc), not to mention all the measurement techniques used and develop for the study of magnetic properties (MFM, microwave measurements, Lorentz microscopy, dichroism, SQUID, etc).

Magnetism is present in matter in a number of forms, depending on its physical origin. Some of the most relevant are diamagnetism, paramagnetism, ferromagnetism and antiferromagnetism.

One could also consider, to a certain extent, superconductivity as a magnetic phenomenon, but its origin and implications are very different from the previous, and superconductors include also other non magnetic properties such as zero electrical resistance that cannot be found in any other type of magnet. For this reason, superconductors will be described in a different section.

Before going into more details, some basic definitions that will be used throughout the text are presented. Objects having an electric charge (q) and an angular momentum ($\vec{J}$) possess a magnetic moment $\vec{m}$ which interacts with magnetic fields $\vec{H}$. Magnetization ($\vec{M}$) is defined as the "density of magnetic moments per unit volume ΔV", in the limit: $\vec{M} = \lim_{\Delta V \to 0} \frac{\Delta \vec{m}}{\Delta V}$. We will use the term "magnetic field" to refer to the quantity $\vec{H}$, and "magnetic flux density", or "magnetic induction" to refer to $\vec{B}$. In vacuum they are parallel, and proportional by a factor which depends on the units system. Inside magnetic materials both fields are related by the magnetization: $\vec{B} = \mu_0(\vec{H} + \vec{M})$. $\vec{B}$ represents the total field, and $\vec{H}$ removes the effect of magnetizations, so only considers fields not generated by the induced magnetization in samples. μ_0 is the permeability of vacuum, with a value of $\mu_0 = 4\pi \cdot 10^{-7}\mathrm{NA}^{-2}$ in the International System of units. It is common to define the magnetic permeability of a material by its permeability relative to the vacuum: $\mu = \mu_0\mu_r$. Magnetic permeability represents how well a material allows the existance of magnetic fields inside it. Another useful quantity is magnetic susceptibility, χ, defined as: $\vec{M} = \chi\vec{H}$, so that $\mu_r = 1 + \chi$.

After the discovery by Oersted it was soon clear that moving electric charges generate magnetic fields. The magnetic field created by a differential element of electric current was described by Jean-Baptiste Biot and Félix Savart in 1820 as:

$$d\vec{B} = \frac{\mu_0}{4\pi} \frac{I d\vec{l} \times \vec{r}}{|\vec{r}|^3} \tag{1.1}$$

Where I is the magnitude of the current, $d\vec{l}$ is its differential direction, and $\vec{r}$ the vector connecting the current element and the point where the magnetic induction is measured. In the classical picture, magnetic moments themselves are nothing but tiny current loops that interact with magnetic fields just like any other current. Any charged rotating object can be understood as circulating currents, and the magnetic moment depends on the angular momentum through the gyromagnetic ratio: $\gamma = \frac{|\vec{m}|}{|\vec{J}|}$. Quantum theory later exposed the correct way to know the magnetic moment of an atom, by relating it to its total quantum angular momentum (spin + orbital).

Ferromagnetism

In this thesis we will only consider the case of ferromagnetism, the only type of magnetism that we have studied at room temperature. The most famous examples of ferromagnets are iron (Fe), cobalt (Co) and nickel (Ni). In these transition metals the unpaired electrons of the $3d$ shell are responsible for magnetism (figure 1.1). The dashed blue line is the $n = 3$ shell, where unpaired $3d$ electrons (black and white dots with arrows) are located. The rest of the $3d$ electrons (black and white dots with no arrows) are paired and do not contribute to ferromagnetism. The other 8 electrons in each $n = 3$ shell (gray dots) are the $3s$ and $3p$ electrons, all paired up and not contributing to magnetism either.

Once a material has a distribution of magnetic moments (actually, regardless of their origin), we can consider the effects resulting of their mutual interactions. The ground state of a ferromagnet (this is, the orientations of the magnetic moments) is, then, a result of the minimization of the sum of all the energy terms present. Next, a description of them is provided:

Exchange energy: The first attempt to explain ferromagnetism was proposed by Weiss in 1907. He suggested that each magnetic moment interacts with a mean field (or "molecular field") created by the rest of moments. Although this model is capable of predicting some behavior of ferromagnets, like the temperature dependence of the magnetization, the physical origin of this field was not clear. Later, the effect that actually

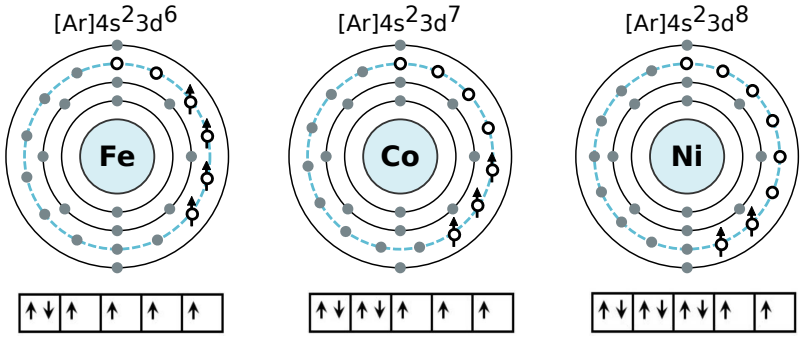

Figure 1.1: *Filling of electronic orbitals in Fe, Co and Ni.*

takes place, now called exchange interaction, was identified as a consecuence of Pauli's Exclusion Principle and is a short range interaction between atomic magnetic moments. We can consider the orbitals of the unpaired electrons of two neighbor atoms. Since electrons are fermions, they cannot occupy the same quantum state. Then, if they get close to each other, they would need to have their spins alligned antiparallel. Therefore, having their spins parallel ensures that they will keep apart from each other. In this case, the electrostatic energy due to their interaction will decrease. Due to this, having parallel spins, the energy is lower on average. The same arguent can be extended to a larger set of electrons, for example corresponding to the unpaired electrons of the atoms in a ferromagnet. However, it is important to note that this interaction is important only in short distances, in contrast to the dipolar interaction. The exchange length, which in the International System is $\sqrt{\frac{2A}{\mu_0 M_s^2}}$, gives an idea of what this distance is. Tipically the exchange interaction is modeled via the Heisenberg hamiltonian between neighboring spins:

$$E_{exch} = -J\vec{S}_1 \cdot \vec{S}_2 \tag{1.2}$$

J is a constant, positive in ferromagnets, and negative in antiferromagnets. As will be explained, micromagnetic simulations also use this model of exchange interaction.

Dipolar energy (shape anisotropy): The long range magnetic interaction is described by the Biot-Savart law. This law can be used to calculate the magnetic field created by a current. Modelling a magnetic dipole as the limit of a circular current very small in radius, with a magnetic moment $\vec{m}$, the magnetic field it generates is:

$$\vec{B}(\vec{r}) = \frac{\mu_0}{4\pi}\left(\frac{\vec{r}(\vec{m}\cdot\vec{r})}{|\vec{r}|^5} - \frac{\vec{m}}{|\vec{r}|^3}\right) \tag{1.3}$$

It is an anisotropic, long range interaction that, unlike the exchange interaction, tends to align magnetic moments in different relative orientations depending on their relative position. One would need to sum such contribution of every magnetic moment in a magnet to calculate the stray field that it generates in space.

The dipolar interaction is the main interaction between separate magnets, that brings them together or repels them. Inside a magnetic material the magnetic moments also create a magnetic field, usually referred to as demagnetizing field. This is the field that goes from the induced north poles to the induced south poles inside the magnet (figure 1.2 c). This internal dipolar field is the source of the so called shape anisotropy. In order to reduce the magnetic poles at the surface, and therefore the field outside the sample, the

demagnetizing field tends to align magnetization parallel to the sample edges, and is also responsible for forming magnetic domains.

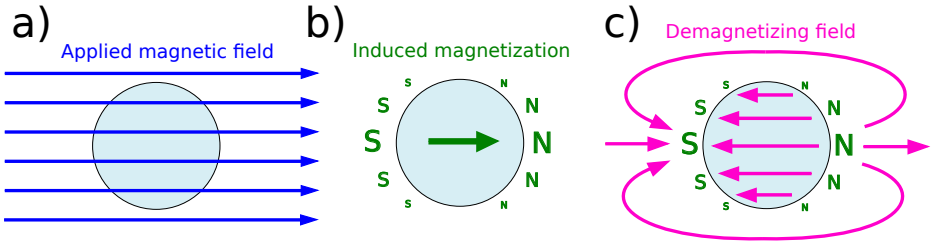

Figure 1.2: *a) Applied magnetic field on a magnetic sample. b) Induced magnetization. Induced north (N) and south (S) poles at the sample edges. c) Demagnetizing field created by the induced poles.*

The magnetic field applied on a magnet needs therefore to be corrected with the demagnetizing field if we want to compute the total field.

$$\vec{H} = \vec{H}_a - \vec{H}_d \tag{1.4}$$

In complex systems, with large numbers of magnetic moments, instead of dealing individually with each moment, it is more convenient to use the so called demagnetizing factors, which relate the demagnetizing field to the magnet geometry:

$$\vec{H}_d = N_d \vec{M} \tag{1.5}$$

The demagnetizing factors have analytic expressions for simple geometries, but must be computed numerically for complex cases. The simulation softwares used in this thesis do this automatically (and it is one of the most computationally demanding tasks). The idea is to calculate the so called demagnetizing tensor for every pair of cells in the simulation. Without going into too many details, for every pair of cells there is a tensor:

$$N = \begin{pmatrix} N_{xx} & N_{xy} & N_{xz} \\ N_{xy} & N_{yy} & N_{yz} \\ N_{xz} & N_{yz} & N_{zz} \end{pmatrix}$$

where each component represents the dipolar magnetostaic coupling between the two cells i and j[1]:

$$N_{ij} = -\frac{1}{4\pi V} \int_V \mathrm{d}V \int_{V'} \vec{\nabla}'_i \vec{\nabla}'_j \left(\frac{1}{|\vec{r} - \vec{r}'|} \right) \mathrm{d}V'$$

Therefore, for each cell, there are N different demagnetization tensors (being N the number of cells), and for that reason, the amount of tensors to be calculated grows as the square of the number of cells. The tensors N_{ij} are independent on time (as long as the shape of the magnetic object remains unchanged throughout the simulation), therefore they only need to be calculated once.

Magnetocrystalline anisotropy: Magnetic materials can exhibit magnetocrystalline anisotropy when it takes more energy to magnetize them in some directions than in others. This effect is due to the spin orbit interaction between the electrons magnetic moment and the crystal lattice. The anisotropy occurs when one direction is energetically favorable over the others, making mangetization align parallel to that direction spontaneously. The samples considered in this thesis do not have this kind of anisotropy.

Zeeman energy: This term describes the interaction of magnetic moments with an applied magnetic field. It is of the well known form:

$$E_z = -\mu_0 \int_V \vec{M} \cdot \vec{H}_a \mathrm{d}V$$

For a magnetic volume V with a magnetization distribution given by $\vec{M}$. Really, the origin of the Zeeman energy and the dipolar interaction are the same, but in the case of dipolar interaction we are making explicit the expression of the magnetic field generated by a magnetic moment.

Every ferromagnet has a characteristic Curie Temperature T_C (not to be confused with the critical temperature of superconductors, T_c), above which spontaneous magnetization is destroyed by thermal fluctuations. Above T_C the ferromagnet behaves as a paramagnet, which can still be magnetized by an applied magnetic field. Its magnetic susceptibility in this paramagnetic regime follows the law: $\chi \sim \frac{1}{(T-T_C)^\gamma}$, with γ a critical exponent that depends on the material[2]. Typical Curie temperatures of usual ferromagnets are several hundred degrees above room temperature, so we will not need to worry about this issue unless an external heat source is acting on the magnet.

Magnetic domains

Magnetic domains appear in many magnetic systems in the ground state as a way of reducing the magnetostatic energy of the stray field (field generated by the magnetized sample). If the magnetization distribution is "fragmented" into many small domains, with uniform magnetization in each domain, pointing in random directions, the total stray field will be reduced, making the magnetic sample be in a more stable state. Since the exchange energy, which aligns the magnetic moments parallel only acts in a short range, nothing prevents the domain structure. Inside each domain the exchange interaction forces the moments in the same direction. Between domain there are domain walls, with an extra cost of exchange energy, lower than the gain of energy that is achieved by not creating a large stray field if the sample was magnetized uniformly.

Domain walls

Domain walls (DW) are the regions that separate magnetic domains. They are then a region of smooth transition where magnetization rotates and matches the direction of each domain at the ends of the wall. Two main types of domain walls exist, Bloch walls, and Néel walls, figure 1.3. In Bloch domain walls, magnetization rotates out of the plane to match the directions of neighboring domains. This type of walls is more typical in bulk systems.

In Néel walls magnetization rotates in the plane formed by the directions of the neighboring domains. This type of wall is more common in thin systems, like thin films or dots, and is the one we find in later chapters in this thesis. If a DW is trapped in a non-magnetic defect, part of the exchange energy associated to the wall is lost, being the DW more stable when pinned, as shown in chapter 3.

Magnetic structures in confined systems

In this thesis we have worked on magnetic samples consisting of litographically defined dots of lateral sizes between 1 and 2 μm, and thicknesses between 30 and 100 nm. In this range of sizes, most of the time (depending also on the dot shape, and magnetic field history) the ground state at zero field is the so called "vortex state". Calculations have

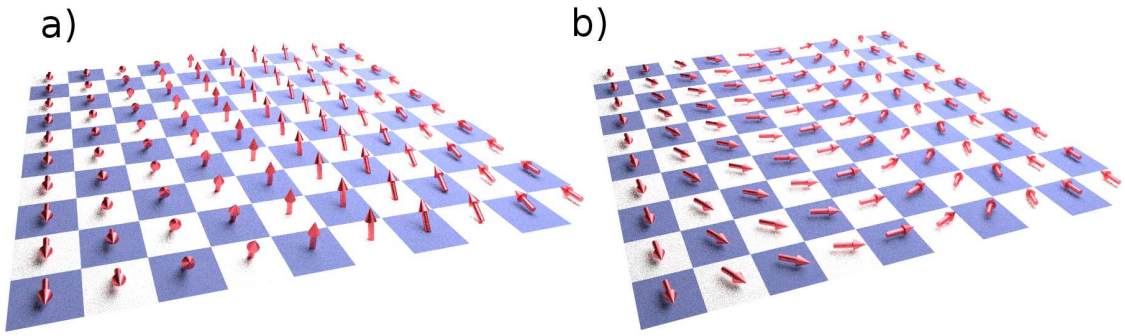

Figure 1.3: *a) Bloch wall. b) Néel wall*

allowed to create phase diagrams[3] to predict the magnetic ground state of a dot depending on the aspect ratio of its thickness and lateral size, figure 1.4.

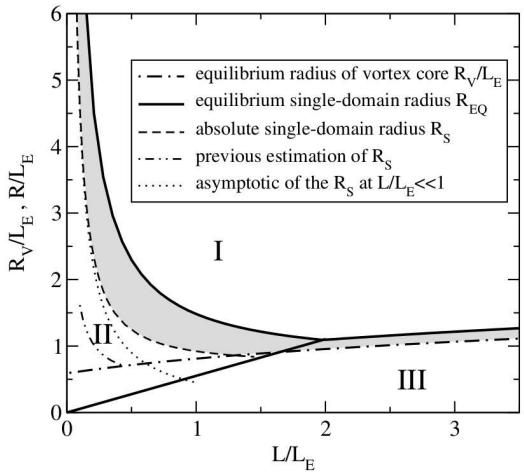

Figure 1.4: *Magnetic phase diagram in cylindrical dots[3]. I: Vortex state, II: In plane saturation, III: perpendicular to the plane saturation.*

These diagrams are valid for relatively small dots. When dots substantially larger than the exchange length are considered, magnetization is fragmented in domains, and the diagrams no longer apply. At higher fields the vortex state can be annihilated, leaving us with a dot saturated in the direction of the applied field. Saturation does not imply, however, that all the spins are parallel. To minimize the stray field outside the sample, magnetization near the sample edges tends to allign parallel to them. On the other hand, far from the edges this effect is weaker, and magnetization is less pinned. This is a consecuence of shape anisotropy and is responsible, for example, of constraining magnetization parallel to the plain in thin planar samples.

Vortex state

The vortex state is an arrangement of the magnetization that consists of in-plane magnetization curling around a certain point, called vortex core. In this core, magnetization points out of the plane.

Figure 1.5 shows a simulated vortex in a circular Permalloy dot. Magnetic vortices can appear in small samples, like magnetic dots of the appropriate dimensions (in which case the whole dot is in the vortex state), or in larger samples where there can be several

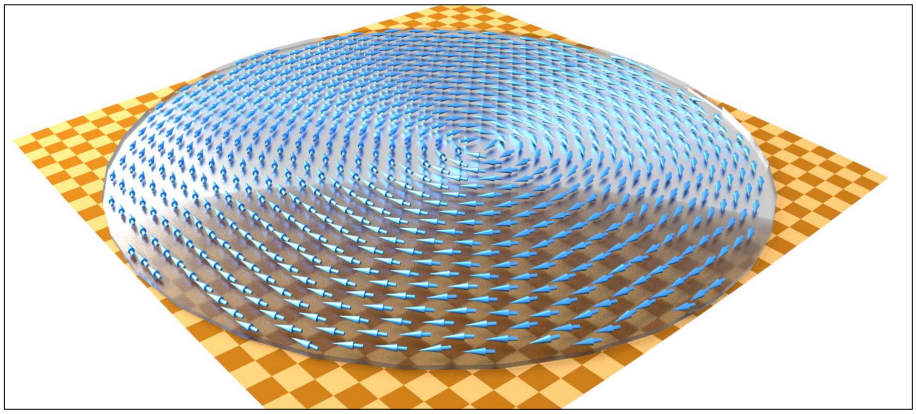

Figure 1.5: *Simulation of a single vortex state in a circular Py dot, 1µm diameter, 50nm thick.*

vortices connected by domain walls at the same time.

Shinjo et al.[4] observed directly for the first time magnetic vortices with MFM (figure 1.6) in 50 nm thick Py dots with diameters ranging from 0.3 to 1 μm.

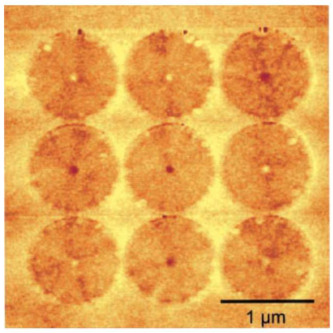

Figure 1.6: *First vortex core MFM images in permalloy dots[4].*

Magnetization reversal in the vortex state

Vortices move under an applied field. Given their curling features, there will always be part of the in plane magnetization pointing in the direction of an external in plane field. This direction of the magnetization will be reinforced by the magnetic field, which will tend to align parallel to it the magnetic moments in the rest of the sample. As a result, the vortex core will be "pushed" in perpendicular direction to the applied field, as the in plane magnetization parallel to it grows larger. Eventually, under a sufficiently large external field, the vortex will be expelled from the sample (at the so called "annihilation field"), leaving the sample saturated in the field direction. The sample can increase its magnetization further under still higher fields, since it tends to align parallel to the edges. When the field is reduced again, the vortex may appear (if the sample is under a critical thickness, the initial vortex will not be recovered, details in chapter 4). The field at which this happens is called "nucleation field", and is lower in value than the annihilation field. As a result of the annihilation nucleation process, the typical hysteresis loops of magnetic dots in the vortex state look like the one shown in figure 1.7.

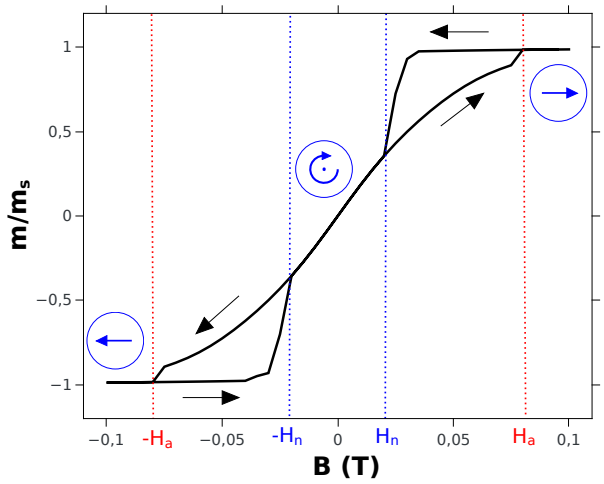

Figure 1.7: *Simulation of a hysteresis loop for a 50 nm thick, 1 μm diameter, Py dot. H_a is the annihilation field, and H_n the nucleation field. The blue sketches show the magnetic state, vortex (center) or saturated (sides).*

Metastable magnetic states

Starting from a saturated state, and given the appropriate sample dimensions, metastable states can appear before reaching the vortex state. To have these metastable states, it is necessary to have a sample of an aspect ratio such that there is a vortex state, but close to the in plane saturation region in the phase diagram (for example, somewhere in the highlighted region in the phase diagram in figure 1.4). It was observed in[5] and confirmed[6] that, under certain conditions, Permalloy (Py) dots underwent a metastable state called "double magnetic vortex" (DMV), figure 1.8, before reaching the ground single vortex state.

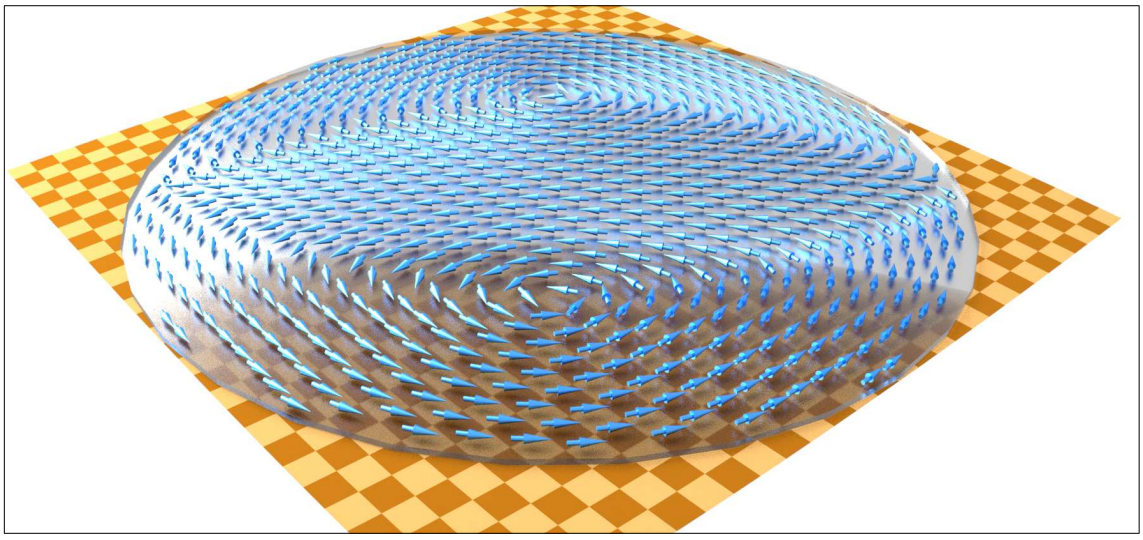

Figure 1.8: *Simulation of a double vortex state in a circular dot.*

These metastable states are not the ground state, and can last up to some hours in a real sample with pinning, but they decay into the vortex state sooner or later. An interesting feature of these metastable multivortex states is that there are domain walls connecting the vortices with edge antivortices in the edges. Figure 1.8 shows a simulation of a circular Py dot, 1 μm in diameter.

Samples capable of showing metastable states present very different hysteresis loops

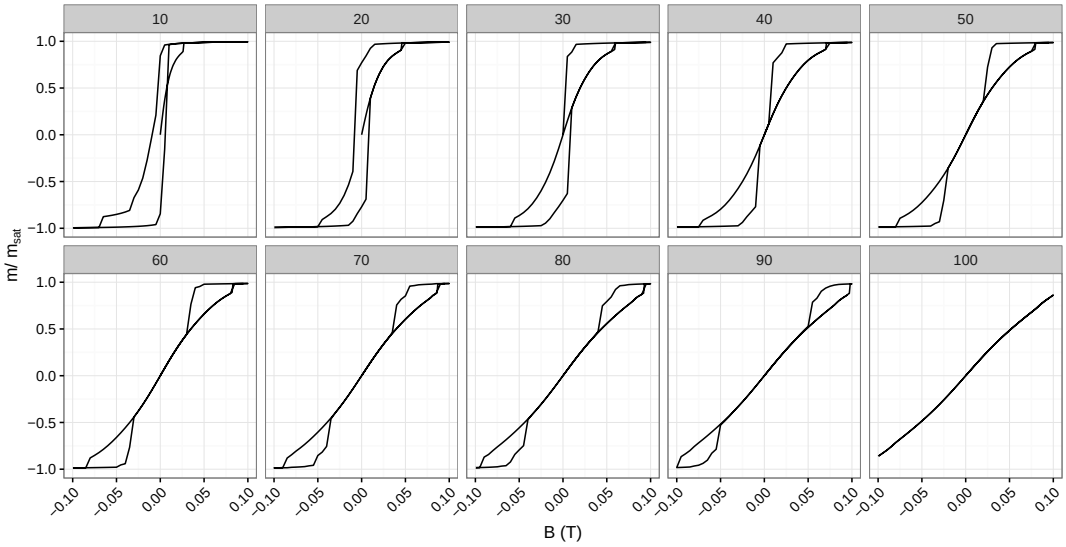

Figure 1.9: *Simulated hysteresis for a cylindrical dot. Thickness is specified, in nm, on top of each panel.*

from those which do not. The main difference is that the vortex state produce very low coercive fields, given its high symmetry around the vortex core, while metastable states have nonzero magnetization. When the metastable state is robust (for samples so thin that their ground state is saturated in one direction) one needs to apply negative fields to destroy it, and recover the single vortex state. Then, samples with metastable states tend to present wide hysteresis loops, with nonzero remanence, in contrast to samples with a strong vortex. In figure 1.9 we compare simulated hysteresis loops for a permalloy dot, 1 μm in diameter, and thicknesses ranging from 10 to 100 nm. Thinner dots show wider loops since reversal takes place via metastable states.

Polygonal dots

Arguably, the most studied dots are cylindrical, and thin in the z direction. They are commonly referred to as "circular" dots (since they are so thin, their behavior in the z direction, perpendicular to the plane, is uniform throughout the sample). In these samples is where the vortex state is the most evident, and homogeneous. The high symmetry of these samples allows them to be insensitive to the applied in plane magnetic field direction, only to its magnitude.

But the magnetic vortex state is not unique of circular dots. Any kind of confined magnetic sample of the appropriate dimensions can present vortices. Therefore, it makes sense to try to look for them in other geometries. The simplest one is triangular. Indeed, the vortex state has been found in triangular dots[7,8]. The next step would be to go to square shapes. Again, the vortex state has been found there[9,10]. The same behavior as in circular samples is observed. At high enough fields the vortex is annihilated (H_a, annihilation field), and lowering the field again, it is nucleated (H_n, nucleation field). What is different from the circular samples is that in the vortex state there are clearly defined magnetic domains, that curl around the vortex core in a not smooth way, as happens in the circular case. These domains are separated by domain walls (DWs). Observing the magnetization distribution (figure 1.10 and 4.2 of chapter 4) it is easy to see that these domain walls always connect the vortex core to the sample corners, at least in the case of not very complicated geometries and a single vortex. These domain walls can have an

interest in themselves, as we will explain later. The circular case can be regarded as a polygonal shape with infinite corners, therefore the corresponding infinite domain walls would smoothly blend and thus are not observed, only a smooth curvature around the vortex core. Indeed, as shown in figure 1.10, the vortex state of polygonal samples with an increasing number of sides look increasingly similar to circular samples.

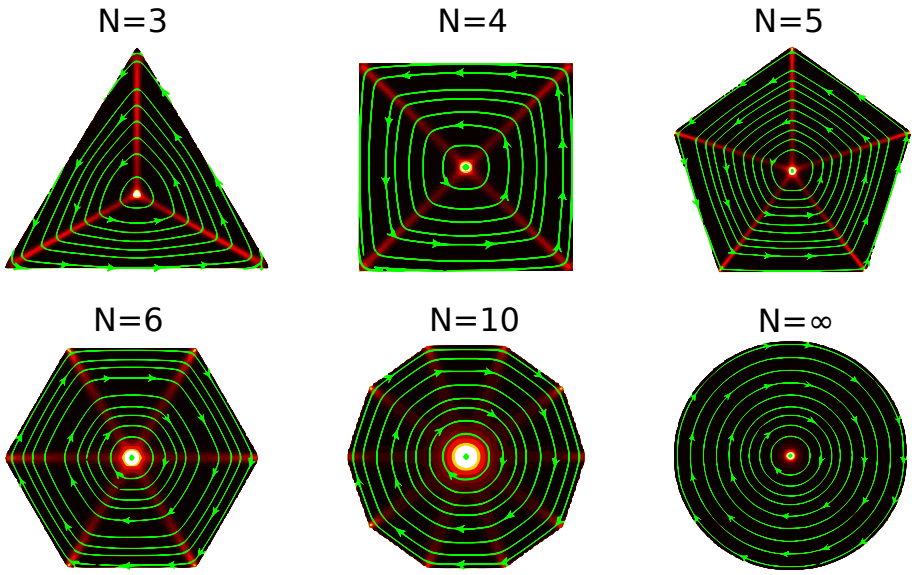

Figure 1.10: *Simulation of polygonal permalloy dots (all are enclosed in a square box of* 1×1 μ*m and 50 nm thick, in the vortex state at zero field. The color scale represents the exchange energy density, maximum at domain walls or vortices. The green streamlines with arrows represent the magnetization direction. N is the number of sides of each polygon.*

In this thesis we have focused in the case of triangular samples, where the domain walls in the vortex state are the most separated from one another and therefore can be studied more clearly. Also, it makes sense to start with the triangular shape first, since it is (in principle) the simplest case.

Triangular dots (as also happens in any other non-square polygonal shape) have the feature that no matter how one applies the external magnetic field, it will never be either parallel or perpendicular to all of the sample sides at the same time.

Previous studies in triangular dots[11] demonstrated that there are three possible magnetic states:

- Vortex state: As explained above, a vortex state, with three DWs connecting the vortex core and the triangle corners. In figure 1.10, a simulation of the vortex state is shown, where arrows represent the magnetization direction, and the color scale represents the exchange energy density. This is higher at the vortex core and the DWs, where magnetization turns locally a larger angle.
- B state (or "buckle" state): This state appears when the external field is applied parallel to one of the sides and is strong enough to destroy the vortex state. As explained above, magnetization near the edges will try to align parallel to them (to minimize stray field), while it is more able to rotate far from them, and orient in the external field direction. Therefore, in the B state magnetization is aligned with the side parallel to the external field, and the area nearby. On the other hand, close to the sides inclined with respect to the external field, it is parallel to those sides, not to the external field. In between these regions, there is a gradual turning of the

magnetization, to link these two areas. It could be considered a domain wall, but one domain would then be "outside" of the dot, alligned parallel to the inclined sides. In any case, there is an excess of exchange energy in this area, as shown in the color scale of figure 1.11.

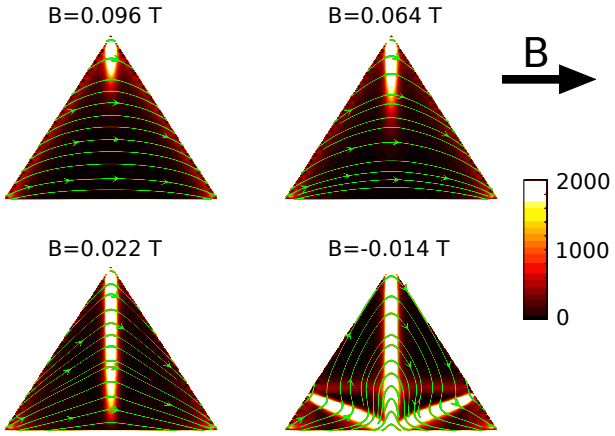

Figure 1.11: *Simulation of the B state at different fields for a 1µm, 30 nm thick, triangular dot. Positive fields are directed from left to right. Green lines and arrows represent the magnetization direction. The color scale represents exchange energy density, in J/m^3.*

- Y state: If the field is applied perpendicular to one of the triangle sides and is strong enough the destroy the vortex state, we get the the Y state. In this state something similar to the B state happens, but now none of the sides are parallel to the field. Near the two inclined sides there will be a rotation of magnetization, as we get close to the center. However, the strongest rotation takes place at the side perpendicular to the direction of the applied field. This is where the excess of exchange energy will be. But contrary to the B state, there is a "magnetic defect" at the center of this area, in the form of a half anti vortex (HAV). It appears due to the symmetry in the direction of the field. An antivortex looks like the gradient of a saddle point function. An example of Y state is shown in figure 1.12.

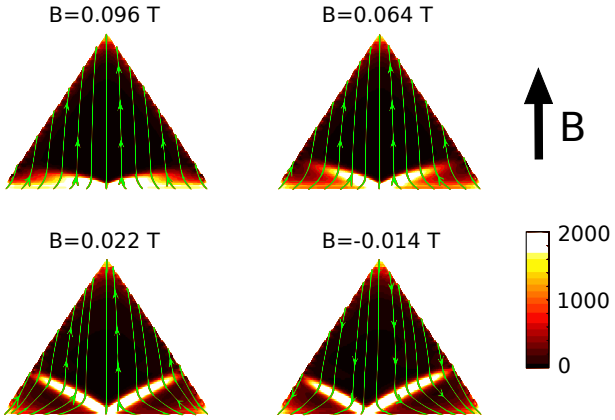

Figure 1.12: *Y state at different fields for a 1µm, 30 nm thick, triangular dot. Positive fields are directed from bottom to top. Green lines and arrows represent the magnetization direction. The color scale represents exchange energy density, in J/m^3.*

- Arbitrary field direction: When there is an applied magnetic field, high enough to saturate the sample, but in an arbitrary direction, the resulting magnetic state will be in between the B and Y states.

Anisotropic magnetoresistance

The anisotropic magnetoresistive effect (AMR) was the first direct relation ever observed between magnetic field and electrical resistance, by Lord Kelvin in 1851. AMR occurs when a magnetic field reorients the magnetic moments localized in the atomic lattice inside a magnetic material, and therefore the scattering section of the atoms relative to the conduction electrons in a specific direction changes. A detailed treatment of this phenomenon requires taking into acount the spatial distribution of the electronic orbitals participating in the magnetism of the material. In practice, always an applied magnetic field both parallel or antiparallel to the direction of the current will give a higher AMR, whereas the minimum value is achieved when both vectors are perpendicular (figure 1.13).

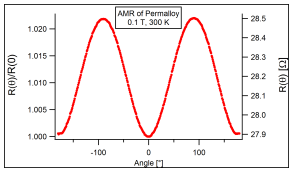

Figure 1.13: *AMR vs angle of $\vec{H}$ and $\vec{J}$ of a Py film[12].*

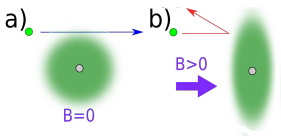

Figure 1.14: *Classical interpretation of AMR.*

More intuitively, in a classical picture, one can think of the electrons in an atomic orbital as distributed in spherical shells. When a magnetic field is applied, these spherical shells become elipsoidal, flatter in the plane perpendicular to the field. Thus, the scattering cross section for conduction electrons is larger in the direction of the field (figure 1.14). AMR measurements can easily be done by taking I-V curves of a sample under a magnetic field. Tipically 4-probe connections are made, to isolate the sample from the cables, but we have been able to detect the AMR signal of a single magnetic micron-sized dot with a 2-probe configuration, as explained in chapter 3.

1.2 Dynamic magnetization

Next, some basic concepts concerning spin waves and magnetization dynamics are presented.

Landau-Lifshitz-Gilbert equation

Although a quantum description of spin dynamics would be more complete and accurate (such model describes the resonance frequency as that which coincides with the difference in energy between two levels, that gives raise to transitions between them, periodic in time[13]), magnetization dynamics in practical systems can be conveniently described by the fenomenological Landau-Lifshitz-Gilbert (LLG) equation. This equation describes magnetization precession about the equilibrium position (parallel to the local direction of the effective field $\vec{H}_{eff}$ inside the material) as a result of a torque, in the International System of Units[14]:

$$\frac{d\vec{M}}{dt} = -\mu_0\gamma(\vec{M}\times\vec{H})$$

Additionally, a damping term is included to account for the losses of energy that magnetization produces when it rotates. The LLG equation then becomes:

$$\frac{d\vec{M}}{dt} = -\mu_0\gamma(\vec{M}\times\vec{H}) + \frac{\alpha}{M_S}\left(\vec{M}\times\frac{d\vec{M}}{dt}\right) \tag{1.6}$$

The LLG equation is a first order differential equation that describes the precession of magnetic moments in the presence of magnetic fields as a function of time.

Here, γ is the electron gyromagnetic ratio, of value $\gamma = \frac{e \cdot g_e}{2m_e}$, with $g_e = 2.00231...$, μ_0 is the magnetic permeability of vacuum, $\vec{M}$ is the magnetization and $\vec{H}_{eff}$ the effective field. M_S is the saturation magnetization

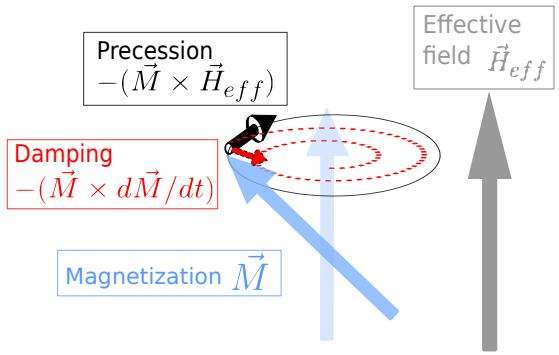

Figure 1.15: *Precession of magnetic moments around the direction of an effective magnetic field (gray arrow). Damping makes magnetization oscillations decay to this direction (blue arrow).*

If the magnetic moment is subject to the influence of other magnetic moments (this is, if we consider a magnetic moment inside a magnetic material, not an isolated magnetic moment in vacuum) it is necessary to consider the effective field, not just the applied field. These two can differ substantially in some cases, due to terms such as shape or crystalline anisotropy, as well as the exchange field, which are not present in the vacumm.

The first term on the left hand side describes the torque exerted by the magnetic field on the magnetic moment. The second term describes the damping. From the vector products one can easily see that the torque is actually directed perpendicular to the plane formed by the $\vec{M}$ and $\vec{H}_{eff}$ vectors, while the damping tends to align both vectors parallel, as shown in figure 1.15. Damping is present in any magnetic sample and its origin is in the interaction of electrons and phonons or magnons. Defects can enhance damping, and external sources of energy can decrease it, as in the case of spin transfer torque[15]

In practice this equation is typically solved numerically for different cases. For example, in systems where it is expected a coherence of phase (i. e. all magnetic moments precess in phase), it is enough to solve the LLG equation once with the appropriate parameters for the specific case. This are the so called macrospin simulations, for example useful in describing spin valve systems. For more complicated systems, the equation is implemented in a finite differences, or finite elements scheme, and solved as a function of position for systems that can have arbitrary shapes, fields, material parameters, etc. We will use this approach during this thesis thanks to the OOMMF[16] software, and during the latest stages of the thesis, also the MuMax3[17] software. Both programs are described later in this introduction.

Spin waves

Due to the different magnetic interactions between magnetic moments inside a magnet, when a magnetic moment rotates, the neighboring moments will rotate too, as a response to the changes in the effective field. In this way, energy can propagate inside the magnet as spin waves, that perturb the magnetic moments out of their equilibrium positions. There are different types of spin waves, characterized by different disperssion relations (figure 1.16), depending on the relative orientation of the magnetization and the wavevector (typically designated by $\vec{q}$ or $\vec{k}$), which indicates the wave direction of propagation.

Ferromagnetic Resonance

Ferromagnetic resonance (FMR) is a spectroscopic technique that allows to study the spin wave spectrum of magnetic structures. A large portion of the work of this thesis makes use of this technique to study the spin wave spectrum of confined magnetic nanostructures.

The FMR technique is named after the FMR phenomenon, observed in 1911 by V. K. Arkad'yev, who observed a strong absorption of UHF waves by ferromagnets. In 1935 L. Landau and E. Lifshitz predicted the FMR effect at the Larmor precession frequency. In 1946 the effect was verified by J. Griffiths and E. Zavoiskij. If a ferromagnet, described by a vector field $\vec{M}$ is irradiated with an electromagnetic field, the magnetic component of the field will exert a torque, as perviously described for the LLG equation, of the form:

$$\tau = -\frac{d\vec{M}}{dt} = \gamma\vec{M}\times\vec{B} = \mu_0\gamma\vec{M}\times\vec{H}$$

We will consider the general case of an ellipsoid. The static magnetic field is applied in z, and the high frequency field in x. Therefore the projection of $\vec{m}$ in z will be constant, since the magnetization vector will just precess around z. This facilitates the election of the demagnetizing factors. For a general ellipsoid we have $H_x^i = H_x - N_xM_x$; $H_y^i = -N_yM_y$;$H_z^i = H_z - N_zM_z$ Substituting in the torque equation: $\frac{dM_x}{dt} = \mu_0\gamma[H_z+(N_y-N_z)M_z]M_y$; $\frac{dM_y}{dt} = \mu_0\gamma[M_zH_x - (N_x-N_z)M_xM_z - M_xH_z]$; $\frac{dM_z}{dt} \simeq 0$;

Assuming oscillating solutions $e^{i\omega t}$, the susceptibility in the x direction becomes:$\chi_x = \frac{M_x}{H_x} = \frac{\chi_0}{1-(\omega/\omega_0)^2}$, where $\chi_0 = \frac{M_z}{H_z+(N_x-N_z)M_z}$. The resonance frequency is

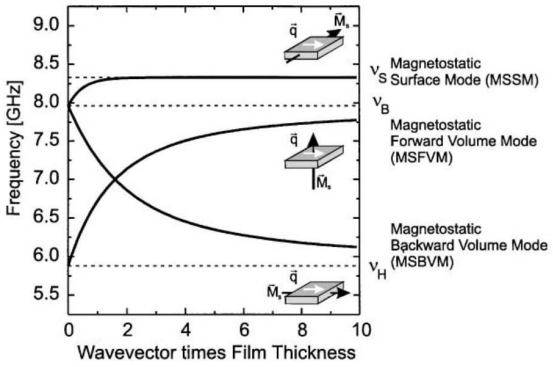

Figure 1.16: *Dispersion relation of the different types of spin waves*[18].

$$\omega_0 = \mu_0\gamma_0\sqrt{(H_z+[N_y-N_z]M_z)(H_z+[N_x-N_z]M_z)}$$

For the specific case of an infinte thin film (in the XZ plane, more relevant to us, the demagnetizing factors are: $N_x = N_z = 0$; $N_y = 1$ in the International System. The resonance frequency becomes:

$$\omega_0 = \gamma\sqrt{(\mu_0(H_z+M_z))(\mu_0H_z)} = \gamma\sqrt{(B_z+\mu_0M_z)B_z}$$

Including anisotropy, the demag factors are modified, and their effect on the new effective fields (different from the previous fields) is: $H_x^e = -N_x^eM_x$; $H_y^e = -N_y^eM_y$.

After some simplifications we arrive at:

$$\boxed{\omega_0 = \gamma\sqrt{(B_z+\mu_0M_z+B_k)(B_z+B_k)}} \tag{1.7}$$

Figure 1.17 shows experimental FMR measurements done taken with our VNA setup, and a fitting of Kittel's equation.

Spin waves in confined structures

Ferromagnetic resonance is the lowest frequency mode, since it has infinite wavelength. It is the only mode one finds in infinite films (apart from vertical modes), but it can also exist in confined structures. It happens when they are in a saturated state (due to an external field, or some anisotropy in the sample). Then, all the magnetic moments will precess in phase, as in FMR in infinite films. But there will be other modes at higher

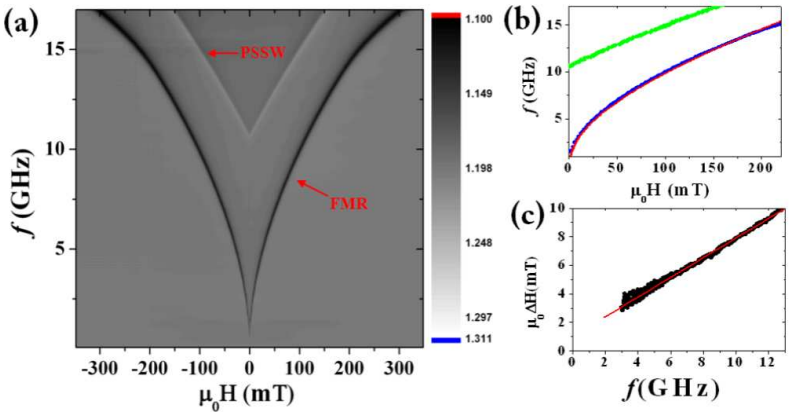

Figure 1.17: *a) FMR spectrum of a 36 nm Py film. b) resonance frequency extracted peaks as function of the applied field. Red: FMR. Green: Perpendicular standing spin wave mode (PSSW). c) Measured linewidth as function of field, the red line is the linear fit.*

frequencies, depending on the geometry. If standing wave-like modes can develop due to enclosing spin waves, there will be a set of resonant modes, each with more oscillation nodes the higher the frequency. Also, if the sample is not saturated, for example in the vortex state, other types of modes can appear, mainly radial and azimuthal.

Radial modes

Radial modes in the vortex state imply that there is symmetry in the azimuthal direction, around the vortex core. They are typically found in circular dots thinner and of larger diameter than those considered in this thesis, therefore not much further attention will be paid to these modes. Figure 1.18 shows simulations and MOKE measurements (left and right of each column, respectively), both for amplitude and phase (left and right columns, respectively) of the time evolution of the Fourier transform of the time signal. From top to bottom they present an increasing number of nodes in the radial direction, at 2.8, 3.9 and 4.5 GHz, with no nodes in the azimuthal direction.

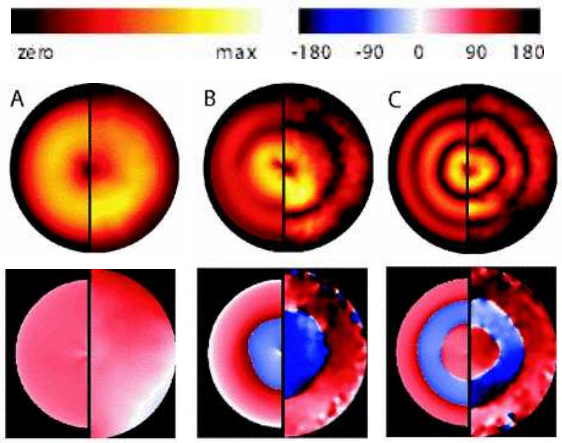

Figure 1.18: *Radial modes in circular dots[19] (adapted figure). Each half picture to the left side is a simulation, and to the right side, a measurement.*

Azimuthal modes

Azimuthal modes on the other hand do present a dependence on the azimuthal angle around the vortex core. These modes are more common for the dot sizes that we consider.

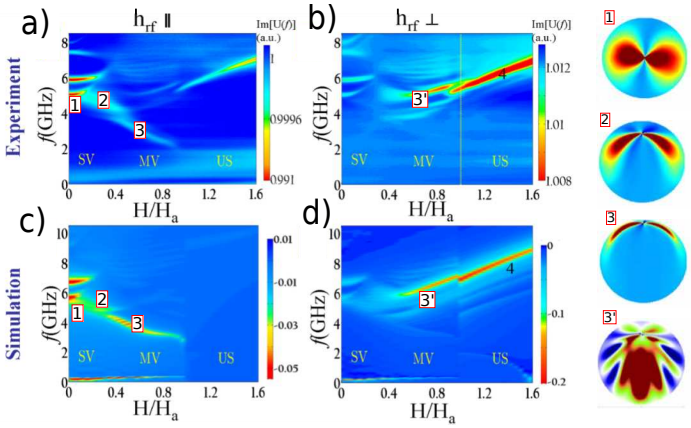

Figure 1.19: *a) and c) Measured and simulated spin wave spectrum of a circular dot array with $\vec{H}$ and $\vec{h}_{rf}$ parallel. b) and d), the same, for $\vec{H}$ and $\vec{h}_{rf}$ perpendicular. The right column shows simulated amplitude profile of the tagged eigenmodes in a), b), c) and d)[20] (adapted figure).*

Figure 1.19 shows the FMR spectra of an array of permalloy circular dots, as a function of field and frequency. Eigenmodes appear as drops in the transmission of microwave power, meaning that power is being absorbed and dissipated at those frequencies and fields by the dots. Simulations c and d reproduce very well the modes field dependence of the actual measurements a and b, of parallel and perpendicular orientations of the bias field and the high frequency magnetic component of the field generated at the waveguide.

Winter's magnons

Spin waves can be confined in domain walls. As Winter noted[21], a ferromagnet with domain walls can have spin waves outside the domain wall, and also confined within them. We have carried out extensive experiments and simulations on this fact in the case of ferromagnetic dots.

The first time this was observed in Py dots[6] the domain walls were those corresponding to the double vortex state, described previously in section 1.1. Measurements showed that for thinner dots, the single vortex state is weaker, and below some critical thickness (25 nm for 1 μm diameter Py dots), a double vortex state can show up during the reversal process. This state gives raise to a new set of eigenmodes, detected with a VNA-FMR setup. Figure 1.20 shows two different FMR spectra, for 50 nm and for 20 nm thick dots, along with their respective hysteresis curves, which for the case of 20 nm no longer looks like that of typical single vortex systems (in particular, it doesn't show zero remanence).

As predicted by Winter, spin waves can exist both inside and outside of the domain walls. At lower frequencies, they are specially visible inside the walls, and as the frequency is increased, they start to spread out as well (figure 1.21). This type of spin waves opens a new perspective for spin waves applications since, in principle, these spin waves could be directed along certain paths inside a magnetic structure, and not others. This interest has motivated part of the research done in this thesis, both studying this type of quasi 1D spin waves in different structures, as well as finding ways to pin domain walls, so that these paths that spin waves can follow are well set and defined based on the target application.

In particular, the domain walls that are present in the double vortex state in circular

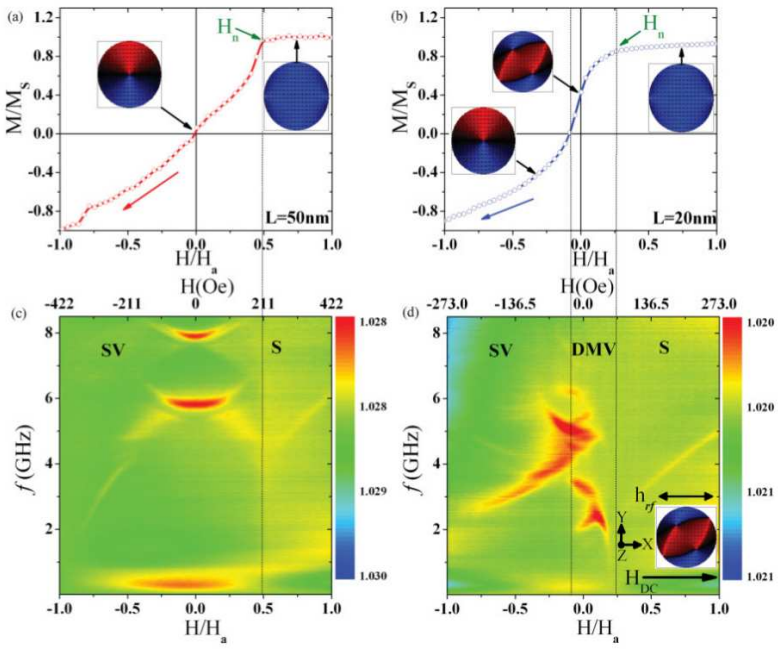

Figure 1.20: *a) and b) M vs H measurements of 50 nm and 20 nm Py circular dots (1 μm diameter). c) and d) Spin wave spectrum as a function of field for both arrays of dots*[22].

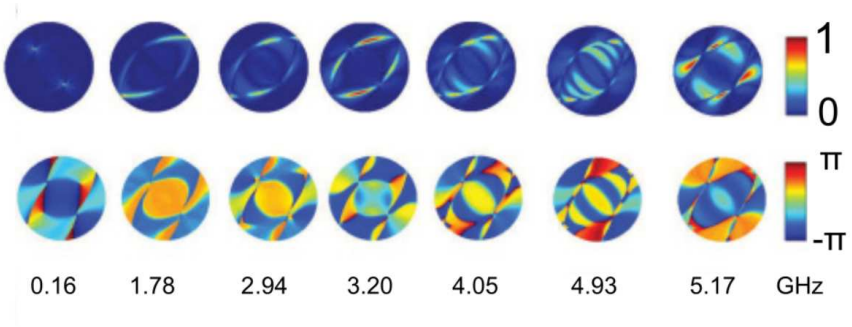

Figure 1.21: *Spin wave modes at different eigenfrequencies inside domain walls in the double vortex state in circular Py dots*[6] *(adapted figure).*

dots are not very stable (depending on factors like defects, they can last up to some hours or even days on real structures, but eventually will decay). To face the challenge of finding other strategies to create paths that Winter-like spin waves can follow, we have adopted two approachas. First, using dots with their walls inclined with respect to the external field. As described in section 1.1, domain wall-like structures appear in such case at the dot edge. In this case, spin waves can be confined to narrow regions next to the edge. A second strategy is pinning domain walls with artificial defects. In this case, one could find ways to establish a path that spin waves would follow, by trapping it in defects and driving the sample through a histeretic cycle.

1.3 Superconductivity

To conclude this chapter, some superconductivity concepts are provided, that will be necessary for chapter 6.

General superconductivity

Superconductivity (SC) was discovered in 1911 by H. K. Onnes, and up to the present day it is a topic under exhaustive research. Intense efforts have been made ever since to try to understand the underlying mechanism behind this phenomenon, both experimentally and theoretically. As a result, several Nobel prizes have been awarded to research related to superconductivity, such as those to K. Onnes (1913). J. Bardeen, L. Cooper and J. Schrieffer (1972), I. Giaever and B. Josephson in (1973), G. Bednorz and A. Müller in (1987) and A. Abrikosov, V. Ginzburg and A. Leggett (2003).

The first manifestation of superconductivity was the loss of electrical resistance in Hg when cooled at very low temperatures (figure 1.22). Indeed, superconducting materials undergo a phase transition from normal conduction to the superconducting state when they are cooled below the critical temperature (T_c).

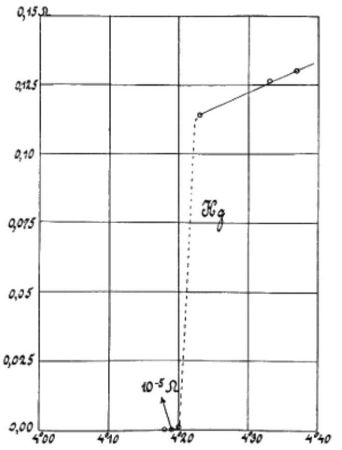

Figure 1.22: *First notice of superconductivity, in Hg.*

Type I superconductivity

Later other properties were discovered. Besides the zero resistance, the other most important feature of superconductors is the Meissner effect, by which superconductors expell any magnetic flux that might be inside of them. This happens thanks to lossless "supercurrents" that screen the superconductor. These currents flow mainly in the surface of the superconductor, and quickly decay inside of it. Then, superconductors behave as perfect diamagnets. If the applied field, however, is strong enough, superconductivity will be lost, as shown in figure 1.24 a. Superconductors, however are not perfect conductors, since a perfect conductor can have a magnetic field inside if before the phase transition the field was already there.

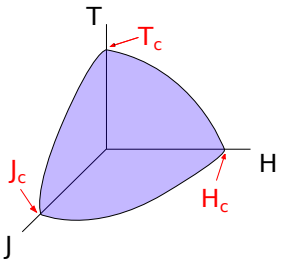

Figure 1.23: *Phase diagram of a type I superconductor. The surface encloses the SC phase.*

Both a high temperature and magnetic field contribute to the destruction of the superconducting state. It is customary to describe this with a temperature dependent critical magnetic field $H_c(T)$. Figure 1.23 shows a typical phase diagram for such a superconductor. In this figure, also a critical current dependence is explicitely shown. The critical current, J_c is the maximum current that a superconductor can carry before it destroys superconductivity, and is closely related with the critical field, since the current generates stray fields itself.

Type II superconductivity

There exist, however the so called Type II superconductors (which include some elemental superconductors, such as niobium, vanadium and technetium, some alloys, and high temperature superconductors like BSCCO and YBCO), in which magnetic fields above the "lower critical field" H_{c1} can penetrate gradually inside the superconductor, figure

1.24 b. Magnetic field enters in this case as quantized magnetic flux units, of flux value $\phi_0 \simeq 2.0678 \times 10^{-15}$ Wb, called superconducting vortices. When a second critical field is reached, H_{c2}, typically of much larger value than H_{c1}, superconductivity is finally lost, reaching again the normal state.

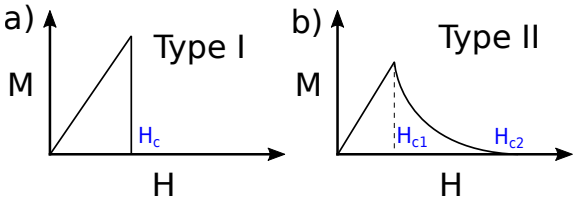

Figure 1.24: *Magnetization curves of type I and type II superconductors.*

Critical state model

Type II superconductors in the presence of a strong enough magnetic field will start to lose their superconductivity and field penetration will occur from the outermost parts of the sample towards the center. This relates to the hysteretic behavior of the so called "hard" superconductors, characterized by very low H_{c1} and very high H_{c2}. This is described by the critical state Bean's model[23].

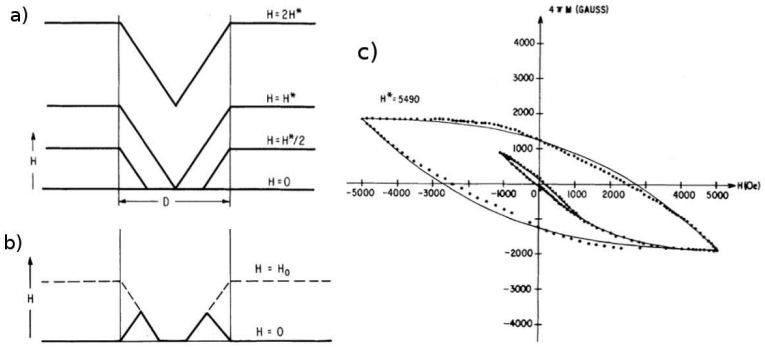

Figure 1.25: *a) Entrance of field in a superconducting cylinder by increasing the applied field. b) Decrease of the applied field to the final state in a). c) Hysteresis curve. Dots are measurements, the line is a Bean's model calculation[23] (adapted figure).*

By the time this model was proposed, the idea of superconducting vortices had been put forward by Abrikosov, but no direct experimental evidence existed yet, only indirect, for example, from hysteresis loops. Vortices need to overcome an energy barrier (Bean Livingston barrier). The main assumption of Bean's model is that any local voltage inside the superconductor will generate a local current of value equal to the critical current. Such critical current separates vortices from the region which still remains flux free (farther into the bulk). As the applied field increases, vortices penetrate more inside the sample. If the applied field is decreased, a current in the opposite direction of the existing one will start to be induced in the surface, growing in strength. But the applied field will need to go to negative values to reverse the magnetization. This is the origin of the histeretic behavior of type II superconductors.

Type III superconductivity

Type III superconductivity refers to the fact that under high fields parallel to the surface of a superconducting film superconductivity is first lost in the bulk, and remains stronger at the sample surface. The critical field for annihilating this surface superconductivity has been found[24] to be $2.39\kappa H_c$, with κ the Ginzburg-Landau parameter, and H_c the bulk critical field. High enough fields can make a superconducting sample present only surface superconductivity. These Type III superconductors can be used to create superconducting / normal / superconducting (SNS) junctions in a uniform film under an in-plane magnetic field.

BCS theory

Developed in 1957 by Bardeen, Cooper and Schriefer[25] (awarded with the 1972 Nobel Prize in Physics for this theory) this theory gave the first microscopic description of the interaction between electrons in a superconductor. By solving a variational problem for the electrons at the Fermi energy (therefore, the electrons that contribute to elecetrical conduction) they found that it is energetically favorable that electrons bind up into pairs, called "Cooper pairs". The interaction that keeps these pairs together is phonon mediated. A classical picture helps to understand the process: an electron that moves across a positive ion lattice will attract the positive iones towards it. The ions, that respond in longer timescales, will be desplaced, momentarily creating an excess of positive charge that will tend to attract a second electron to where the first one was a moment ago. Fig 1.26 shows a depiction of this process.

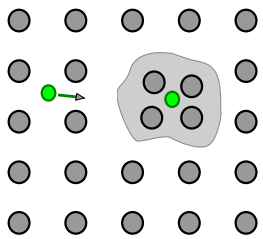

Figure 1.26: *Phonon mediated attraction of two electrons forming a Cooper pair. Gray dots are lattice ions. Green dots are electrons. The gray shaded area has an excess of positive electric charge.*

In the most basic case the electrons that form a Cooper pair will have opposite spins and wavevectors. More complex configurations, such as d-wave superconductivity exist, but fall beyond the scope of this thesis. Electrons paired into Cooper pairs are the responsible ones for the properties of a superconductor. Cooper pairs are bosons, and they are at the Fermi energy. As such, they all can occupy the same quantum state. In practical systems they form a "macroscopic condensate", in which a single wavefunction can describe all the superconducting electrons of a macroscopic sample. This is the reason for the zero electrical resistance: electrical resistance is the macroscopic manifestation of scattering of electrons with ions. When a large portion of the electrons of the material can be described with a single wavefunction, a single scattering process of one electron is not enough to disturb the whole macroscopic wavefunction, therefore scattering processes do not have a noticeable effect[26].

The BCS theory also establishes a relationship between the uncertainty in the condensate phase and the number of particles, similar to the Heisenberg's uncertainty relation. A gap in the density of states of the normal electrons (sometimes called spectrum of excitations) opens around the Fermi energy, with a width 2Δ, meaning that in the superconducting state no normal electrons can occupy those energies, and Cooper pairs condense at the Fermi energy. The gap shrinks as $T \to T_c$ (figure 1.29).

Ginzburg Landau theory

One of the main theories that explains superconductivity is that of V. Ginzburg and L. Landau, proposed in 1950. It does not derive superconductivity from microscopic

interactions, as the BCS theory does, but it is rather a macroscopic theory based on the theory by Landau for general phase transitions[27]. A macroscopic wave function $\Psi = re^{i\theta}$ describes the superconducting condensate. It is a complex scalar field, whose amplitude is related to the density of superconducting electrons (Cooper pairs) as $n_s = |\Psi(\vec{r})|^2$. On the other hand, the phase is related to the supercurrents inside the superconductor. The wavefunction is assumed to vary very little inside the so called coherence length (ξ).

The amplitude is $|\Psi| = 0$ in normal regions, and $|\Psi| = 1$ in perfectly superconducting regions. The amplitude also represents the superconducting gap from the BCS theory. Where $|\Psi| = 0$ the gap has been closed, and no Cooper pairs are found.

The Ginzburg-Landau (GL) theory uses a variational method to minimize the free energy of the superconductor, and from this minimization the two GL equations result.

The Helmholtz free energy of a superconductor is:

$$F_s = F_n + \int_V \left\{ \alpha|\Psi|^2 + \frac{\beta}{2}|\Psi|^4 + \frac{1}{2m}\left|\left(-i\hbar\vec{\nabla} - \frac{e}{c}\vec{A}\right)\Psi\right|^2 + \frac{1}{8\pi}|\vec{B}|^2 \right\} dV$$

Where F_n is the normal metal component. It is more convenient for this case (since we can control the applied field) to work with the Gibbs free energy is given by $G = F - (\vec{H}\cdot\vec{B})/4\pi$. The first GL equation is obtained by minimizing the free energy with respect to Ψ^*, and the second by minimizing the free energy with respect to $\vec{A}$. The minimization of the free energy with respect to an arbitrary parameter x is done in the following way:

$$G_s(x+\delta x) - G_s(x) = 0$$

After performing these minimizations (details in Appendix B, section 8), the GL equations are found to be:

$$\alpha\Psi + \beta|\Psi|^2\Psi + \frac{\hbar^2}{2m}\left(-i\vec{\nabla} - \frac{e}{\hbar c}\vec{A}\right)^2\Psi = 0 \tag{1.8}$$

$$\frac{i\hbar e}{2m}(\Psi\vec{\nabla}\Psi^* - \Psi^*\vec{\nabla}\Psi) - \frac{e^2}{cm}\vec{A}|\Psi|^2 = \frac{c}{4\pi}(\vec{\nabla}\times\vec{B} - \vec{\nabla}\times\vec{H}) \tag{1.9}$$

In the absence of external currents, $\vec{\nabla}\times\vec{H} = 0$ and the supercurrent reduces to $\frac{c}{4\pi}(\vec{\nabla}\times\vec{B})$.

Ginzburg Landau theory is a particularization of a theory for phase transitions. Therefore, it works best near the phase transition of a superconductor. However, in practice it has been used with high success far from the transition[28].

Gor'kov showed in 1959 that GL theory is a limit of the BCS theory for spatially inhomogeneous regimes[29]. The GL theory has proved to be a very useful description of superconductors in the sense that it does not require precise knowledge of the microscopic mechanisms of superconductors in order to extract macroscopic quantities.

Gor'kov and Eliashberg also developed a time dependent version of the GL theory. A numerical implementation of it is part of the work of this thesis, and the whole topic is discussed in chapter 5 with more detail.

Superconducting vortices

Superconducting vortices were predicted by Abrikosov in 1957. Type I superconductors have $\kappa = \frac{\lambda(T)}{\xi(T)} < \frac{1}{\sqrt{2}}$, while type II have $\kappa > \frac{1}{\sqrt{2}}$. Type I have positive surface energy, and the formation of discrete vortices is unstable, which makes them merge in large uniform

normal metal regions when a field is applied, while in type II, vortices remain separated, thus being observable.

As explained above, superconducting vortices are the means by which magnetic field can enter inside a Type II superconductor. Vortices are not "discrete objects" with a sharp edge, but instead $|\psi|$ gradually decays until it reaches zero at the center of the vortex core. This means that closer to the center of the vortex core normal electrons are in higher concentrations than Cooper pairs. Just by paying attention to the electron concentration, one can regard them as "columns" of normal electrons, inside of which a magnetic field is not zero.

Vortices have an energy per unit length $\varepsilon = \frac{\phi_0^2}{4\pi\mu_0\lambda^2} K_0\left(\frac{\xi}{\lambda}\right)$, with K_0 the lowest order modified Bessel function.

It is common to study them in thin films where a magnetic field is applied perpendicular to the film plane, so that vortices are also perpendicular to the film plane. According to Bean's model, and confirmed by solving the TDGL equation, vortices enter the sample from the edges, towards the center. Only at high vortex concentrations can one see the Abrikosov lattice (the arrangement of high concentrations of vortices, typically in a triangular lattice, as in figure 1.27).

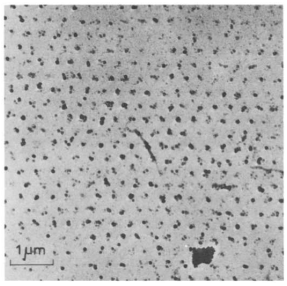

Figure 1.27: *First observation of a SC vortex lattice*[30].

When the vortex concentration is too high, their outer parts start to overlap, and it can be difficult to distinguish different vortices by looking at $|\psi|$. One can, however, keep track of them reasonably well by looking at the phase of ψ. While on $|\psi|$ a vortex is identified as a local minimum, if we look at the phase, the presence of a vortex is seen as a 2π local rotation around the vortex core (figure 1.28).

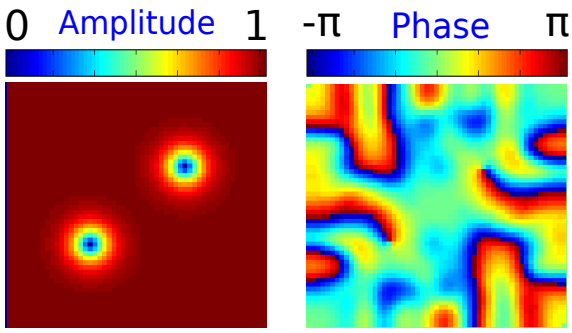

Figure 1.28: *Simulation of the order parameter Ψ (amplitude and phase) in a superconducting sample with two vortices. The only 2π rotation of the phase occurs at the vortices.*

The perpendicular to the plane field is not the only case that can be studied (although, experimentally, it can be the easiest). Some studies consider the case of vortices that tilt under an inclined field[31]. Indeed, vortices can be directed in any direction, trying to follow the external field (this is a result of the boundary conditions). For example, in figure 5.5 of chapter 5 tilted vortices are shown in a superconducting cube under an inclined field.

If the film is thick enough, one can even have vortices parallel to the film plane[32]. Since the Ginzburg Landau equations do not have a second time derivative term, objects described by these equations do not have inertia. This also applies to vortices, which then only move as long as a force is exerted on them.

Dissipation in superconductors

Dissipation of energy in superconductors is not so trivial as one may think from the drop of resistance when crossing the phase transition. In superconductors normal and superconducting electrons coexist. Closer to the critical teperature or the critical field, superconductivity is weaker and the number of Cooper pairs is low compared to the number of unpaired electrons. At nonzero frequencies, the same electric fields which cause the supercurrents to change, also interact with normal electrons, whose scattering from ions and impurities create resistance, according to Ohm's law. Each kind of electron, normal and superconducting have different properties, and are described as two parallel conduction "channels". For an arbitrary nonzero frequency well below that corresponding to the superconducting gap, the conductivity of the superconductor, from Drude's model, can be approximated by[29]:

$$\sigma(\omega) = \sigma_1(\omega) - i\sigma_2(\omega) = \frac{n_n e^2 \tau_n}{m} - i\frac{n_s e^2}{m\omega}$$

where n_s and n_n are the densities of superconducting and normal electrons, ω is the frequency, τ_n is the relaxation time of normal electrons (time between collisions with ions, which in the case of superconducting electrons is taken as infinte in this approximation). In analogy to an RL circuit, the normal electrons conduction channel can be associated to a purely resistive channel, in parallel with an inductive channel, that of superconducting electrons.

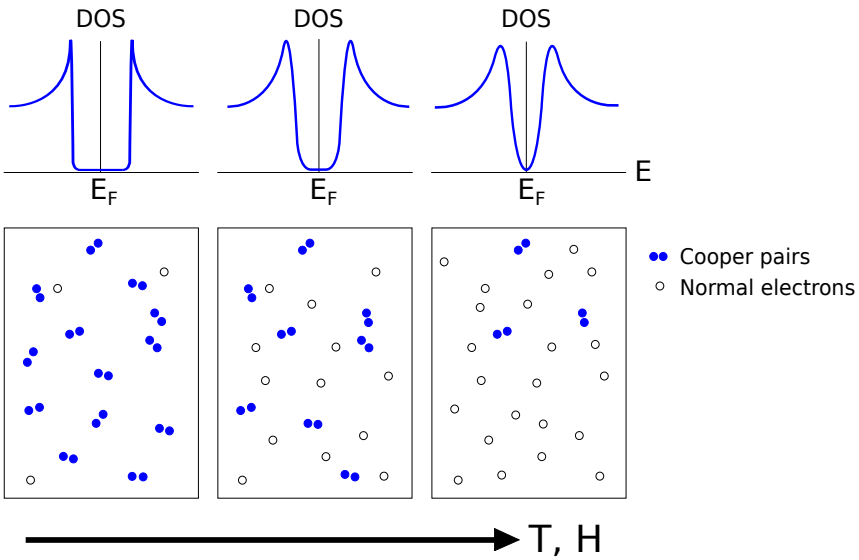

Figure 1.29: *Sketch of the two fluid model, with normal electrons (white) and Cooper pairs (blue) coexisting, for different temperatures, with a sharper o smoother gap.*

Not only do superconductors dissipate energy through these mechanisms. Another source of losses, more manageable with methods such as artificial pinning, is the dissipation created by moving vortices in type II superconductors. This is an important point since one of the most useful applications of superconductors today is carrying large currents with small losses. For this, type II superconductors are used, but the large stray fields that such large currents generate in systems like electromagnets (coils made of superconducting wire) introduce magnetic flux (and vortices) in the magnets themselves. These vortices then interact with the current the wires carry and experience a force given by the interaction of

the current with the magnetic flux quantum carried by the vortex (another way to look at it is that the currents interact with the supercurrents surrounding the vortex core). This interaction, given by the force $\vec{f} = \vec{J} \times \phi_0/c$, pushes vortices transversally to the current flow. When they move, they induce electric fields that produce Joule heating. This heating could potentially lead to the creation of zones in the normal state, which would heat up even more, and eventually all the superconducting state would be lost.

There are different regimes of motion of vortices, depending on how much they are pinned by defects:

- **Pinned vortices:** If vortices are sufficiently trapped they don't move enough to create noticeable dissipation, and the superconductor behaves, concerning dissipation, as type I.
- **Vortex creep:** This regime occurs when pinning is not so strong as to keep vortices from moving under the influence of an electric current. A thermal activation is present and enough to overcome pinning, but the pinning is still strong enough so that vortices do not flow freely, but rather, hoping between different pinning sites. The Anderson-Kim model assumes that vortices jump from site to site in "bundles", due to their mutual interaction[33]. In this case there is a jump rate given by $R = \omega_0 e^{-F_0/kT}$, being F_0 the activation energy for the jumps, and ω_0 a vibration frequency of the bundle, somewhere between 10^5 and 10^{11} Hz. The velocity of the jumps is a consequence of a "tilting" of the pinning potential landscape in one direction. It has been verified experimentally and predicted by this model that in the case of flux creep, there is a logarithmic time dependence. This means that, for example, the trapped field in a superconductor decays the same from second 1 to 10 than from second 10 to second 100. Gittleman and Rosenblum[34] showed in resistive measurements in different type II superconductors irradiated with microwaves in a range of frequencies, how there are two resistive regimes, depending on the frequency driving the vortex lattice (figure 1.30). At frequencies higher than a threshold frequency, resistivity increases, once the vortex lattice is released from their pinning sites. This threshold frequency was observed to be around 10^7 Hz, meaning that for our microwave measurements, typically above 1 GHz, we will be dealing with a flux flow regime and pinning of vortices by defects can be neglected (unlike pinning by artificial pinning centers, as we shall see later). More complicated models consider other types of situations and potentials[32,35]

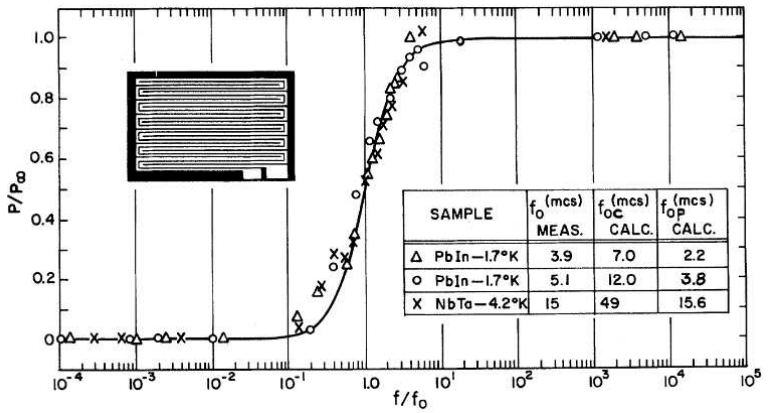

Figure 1.30: *Power absorption in the mixed state for subcritical currents as a function of frequency for different materials*[34].

- **Flux flow:** A moving vortex lattice, even if it is not pinned by defects, still experiences drag by a viscous force related to relaxation processes of quasiparticles. Unlike vortices in liquids, it has been observed that superconducting vortices are hardly dragged by the

currents, but flow almost completely perpendicular to them. As a result they have a low value of the so called Hall coefficient (α_H). Also, in the case that there are defects present, there is always a restoring force characterized by the Labusch constant ($\alpha_L = \partial^2 U/\partial r^2)|_{r=0}$. These different contributions to flux flow are considered in the equation of motion:

$$\eta\vec{v} + \alpha_H \vec{n} \times \vec{v} + \vec{\nabla} U = \phi_0(\vec{n} \times \vec{J}) + F_{thermal}$$

Here, $\vec{v}$ is the vortex velocity, η the viscous drag coefficient, $\vec{J}$ the electric current, ϕ_0 the quantum of magnetic flux, and $F_{thermal}$ a force representing the thermal fluctuations. This type of equation is typically solved in molecular dynamics simulations for superconducting vortices. In our case we will be dealing with vortices that transition from the flux flow regime to a trapped regime by a periodic pinning array, giving raise to matching conditions, as explained next.

Other terminology, more common perhaps in the context of high T_c superconductors, but applicable to vortices in general is the vortex glass vs vortex liquid phase. The vortex glass is the set of external parameters at which vortices remain pinned. When the "irreversibility line" is crossed, the vortex glass phase "melts", producing the vortex liquid phase. Again, these two phases are delimited by $H_{c1}(T)$ and $H_{c2}(T)$, where vortices exist.

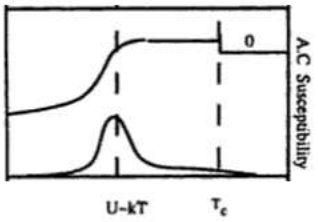

Figure 1.31: *Irreversibility line (labelled U-kT) from ac susceptibility[36] (adapted figure).*

The irreversibility line can be identified in *ac* susceptibility measurements like ours by the peak (figure 1.31) that appears in the imaginary part (more on this in chapter 6). This means that for temperatures higher than that which creates the peak in the imaginary part of χ vortices will be mobile, whereas below they will not. This does not mean that they will not interact at all with radiation, as will be discussed in more detail, when it comes to nonlinear phenomena, such as vortex core oscillations, or depinning of flux avalanches.

Superconductors with a periodic pinning array

Vortex motion is normally considered as a drawback for applications of superconductors, since it dissipates energy and can, in some cases, contribute to the loss of superconductivity.

Therefore, a big effort has been made to understand, predict and control vortex motion in different circumstances. This includes how vortices interact with defects and get trapped by them so that, even if they are present, they will not move and dissipate energy. These defects can be engineered in many different forms. For example, as atoms of a different element substituting some of the superconducting atoms, as linear defects, as intercalated planes[38], or (as we have studied) as arrays of pinning centers placed outside of the superconducting film. In our case, as it is typically done[39–43], we have worked with thin superconducting films deposited on top of a periodic array of magnetic dots. This creates a periodic potential, thanks to the combined effect of the geometric modulation of the film when deposited over the dots, and a magnetic one, due to the magnetic state of the dots. As will be explained later, the geometric

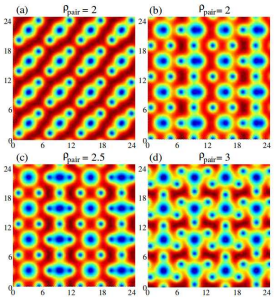

Figure 1.32: *Vortices in a pinning potential for different magnetic pinning centers strengths[37].*

contribution seems to be much more important than the magnetic one. The interesting thing about using a periodic array of pinning centers is that it gives important information about the number of vortices present in the sample.

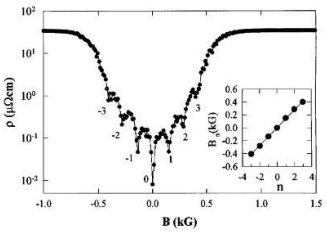

Figure 1.33: *Resistivity of a Nb film with an array of Ni dots vs field*[44].

This is so because when vortices fall into a potential well (in this case the magnetic dots), their movement is restricted compared to the case when they are out of such wells. Different kinds of magnets also distribute vortices around them in different ways (figure 1.32).

Then, a vortex trapped by a pinning center dissipates less energy under the same external excitation. A periodic pinning array has the property that when the number of superconducting vortices is a multiple of the number of pinning centers, they arrange themselves inside the pinning array in very stable configurations, being then the overall dissipation much lower. This has been clearly observed in many I-V curves measured in superconducting films with an array of dots over them (figure 1.33) in a perpendicular field, where abrupt drops in the sample resistance are observed at periodic fields. These specific fields are called "matching fields", or "matching conditions". Direct observation in spatial images[41] confirm this fact, not just resistive measurements.

Flux avalanches

So far, we have considered the usual cases, where magnetic field enters smoothly inside the superconducting sample as the external field increases. Moving vortices dissipate energy, which locally heats the superconductor in the areas through which the vortex has just moved. As we will see, the heat generated in the trajectory weakens superconductivity, even if the vortex is not there anymore.

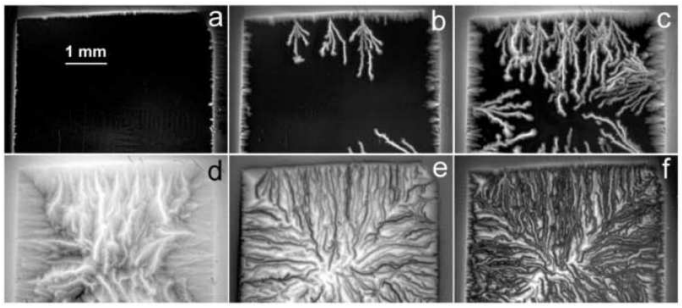

Figure 1.34: *MO images of flux penetration at 5 K. a)-d) Images at applied fields of 3.4, 8.5, 17, 60 mT, respectively. e), f) Images at 21 and 0 mT during field reduction*[45].

That weaken superconductivity energetically favors the presence of other vortices. If the heat diffusion is not fast enough, the trace left by a vortex can be used by other vortices, with the result that a "stream" of vortices follow this same path. In the critical state, such a disruption of the superconducting region can produce "flux avalanches", where many vortices enter the sample suddenly, following the same path.

Avalanches are typically found at temperatures much lower than T_c, but their morphology depends on temperature as well (sharper and longer branches, or shorter and more numerous). Figure 1.34 shows Kerr microscopy images of avalanches frozen inside the sample. The branches are magnetic field trapped inside the sample, not as individual vortices, but as the result of many vortices moving collectively assisted by a self feeding thermal mechanism. To a certain degree, one can influence the form of these branches, and force them along specific directions[47]. Avalanches produce undesired effects for applications, especially related to sudden losses of superconductivity or instabilities. Therefore a substantial effort is being made in finding ways to limit their presence or, at least, reduce their effects. The heating that microwaves produce on metals, due to eddy currents, can facilitate the appearance of avalanches in superconductors. This was shown in experiments with superconducting microwave resonators[46,48]. Figure 1.35 a shows a magnetic image of the microwave resonator. The red lines point to the superconducting resonator structure, and the green line to the gap. Figure 1.35 b shows a resonance curve of the resonator for different powers, at frequencies around the resonance frequency. The abrupt jumps represent flux avalanches, as a function of the input power (inset 3D figure) and how these avalanches are triggered at different frequencies.

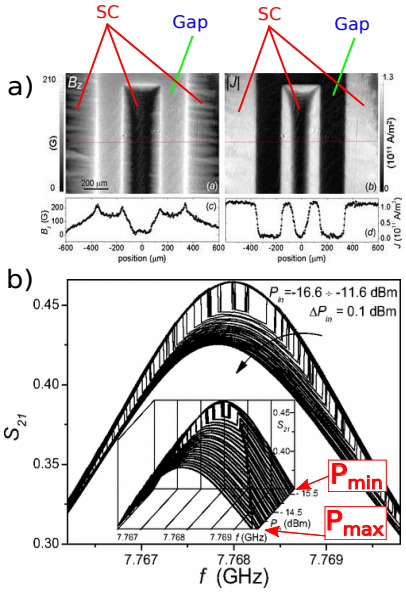

Figure 1.35: *a) Microwave resonator with avalanches. b) Triggering of avalanches with microwaves[46]. (adapted figure)*

Microwave Stimulated superconductivity

Between 1964 and 1966, it was found in different devices that superconductivity can be enhanced (instead of destroyed, as one would normally expect) in the presence of microwave radiation[49,50]. Some years later, Eliashberg[51] shed some light over the phenomenon that was taking place. This counter intuitive, out of equilibrium effect involves a redistribution of the normal electrons in the superconductor by the microwaves. Looking at the energy spectrum, at temperatures close to T_c, the superconducting gap starts to shrink, being populated by an increasing number of normal electrons. When the gap finally closes, superconductivity is completely destroyed. Subgap radiation (this is, with photon energies lower than the gap, therefore unable to split Cooper pairs) can interact with normal electrons, and excite them to higher energies. This means that radiation can widen the superconducting gap by pushing normal electrons, which started to populate it, to higher energies. The electrons excited to higher energies by microwaves will be more unstable, and they will recombine faster into Cooper pairs. Therefore, the dynamic equilibrium between normal and superconducting electrons can be biased towards the superconducting side with microwaves. These effects are sketched in figure 1.36. Further

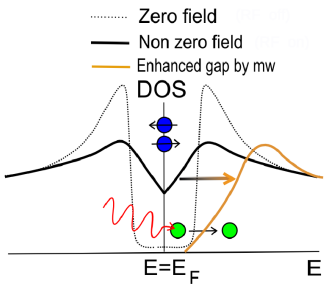

Figure 1.36: *Processes of the MSSC effect. Radiation excites normal electrons (green dots) away from the gap. The gap is effectively "opened". Higher energy electrons recombine faster into Cooper pairs.*

studies[52–55] confirmed the stimulation of type I superconductors.

2. Experimental techniques

In this chapter we describe the different experimental setups that have been involved in the work of this thesis, as well as the computational methods and programs used. At the end of the chapter, sample growth procedures will also be described. The main focus is on the vector network analyzer (VNA) setup, both at room temperature and at low temperatures (with a helium cryostat). We have used this setup for all the ferromagnetic resonance measurements, as well as high frequency measurements of microwave permeability on superconductors. In short, this is a spectroscopic technique in which the VNA generates a signal of variable frequency which is radiated to the sample we study. An electromagnet fixes the magnetic state and from the absorptions of energy (also detected with the VNA) we get information about the sample as a function of frequency.

2.1 Evolution of network analyzers

In contrast to other methods which require multiple instruments (high frequency circuits, amplifiers, etc), the usage of a VNA-based high frequency setup, although more expensive, is quite straightforward to use and very powerful. The VNA takes care of both the excitation signal and the measurement of the sample response. In the next subsections each of the main components will be described in more detail.

Before actual network analyzers, during the 1940s and 1950s, high frequency systems made use of devices such as klystrons and magnetrons, and measurements as a function of frequency had to be done manually point by point[56]. In the 60s, semiconductor technology started to get popular, and the previous devices started to be substituted by diode based systems. So far, only amplitude was taken into consideration (Scalar Network Analyzers). The first VNA, capable of measuring amplitude and phase (thus the V in VNA, "vector"), only reached 110 MHz. In 1967, HP developed a model that went up to 12 GHz. Also, at this time, S-parameters (sections 2.2 and 7 of appendix A) started to become the standard quantity that network analyzers worked with. By 1970, VNAs started to interact with computers to increase their capabilities, and in 1976 the first unit with a built-in microprocessor was developed. With the advent of cell phones in the 1980s, VNAs increased their range of applicability, and also became a common tool in avionics and radar technologies. At the same time, the first tools for simulating the response of high frequency systems helped develop devices faster and with better results. In the 1990s, wireless technologies quickly spread, and the demand for network analyzers increased rapidly. At this point they stopped being just research tools, and their commercialization and popularization became a reality. Since 2000, VNAs are widely used for a wide range of applications and the main effort by manufacturers is to push their limits in frequency range, error correction, etc, as well as add-ons that expand the number of ports, the types of systems that can be measured (like liquids, magnetic systems, etc), adapting the initial

concept of network analyzers to a much more demanding set of systems than they were originally created for, i.e. wireless communications.

2.2 The high frequency measurement setup

In order to probe the dynamic magnetic properties of the different samples studied in this thesis a basic VNA-based high frequency setup has been used, with the corresponding modifications when necesary. In this setup, the VNA is connected with high frequency coaxial cables to a coplanar waveguide (CPW).

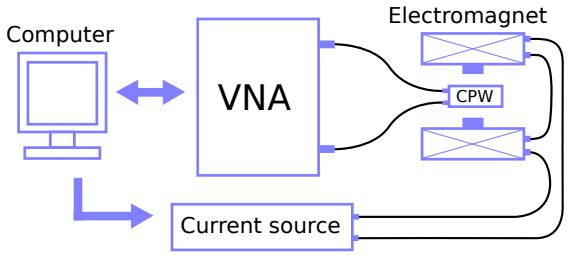

Figure 2.1: *Room temperature VNA-FMR setup.*

In this waveguide the high frequency signal generated by the VNA creates inhomogenous electric and magnetic fields. The field lines are confined in a small region of space above and below the metallic conductors of the waveguide. Placing a sample directly on top of the waveguide (even if some thin insulating layer is deposited over the magnetic sample, in order to protect it from mechanical damage) ensures that the electromagnetic fields radiated by the CPW will interact with the sample. The waveguide is placed inside an electromagnet, which allows to apply a static magnetic field in addition to the microwave field generated by the waveguide. For the case of the room temperature setup the electromagnet consists of a pair of Helmholtz coils, connected to each other and to a current source, with the CPW in between them. Two extensible ferrite cylinders can confine more the field lines (and reach higher fields for the same driving current) by bringing them closer together, with the spatial limitation of the sample holder or waveguide that is used. Figure 2.1 summarizes the basic elements of this setup and their connections.

Vector Network Analyzer

A simple way to describe a Network Analyzer is to consider it a black box (for a summary of the internals of network analyzers, see appendix A), with at least two ports. Each of these ports is capable of emitting and receiving high frequency waves. The parameters that are typically provided by a Network Analyzer are the so-called Scattering Parameters, usually grouped together in the Scattering Matrix. These parameters relate the voltage waves received on one port with the emitted ones by other ports.

In the absence of a signal emitted in one of the ports (as is normally the case) the definition of the S parameters for a two-port network simplifies, as:

$$S_{11} = \left.\frac{V_{1,r}}{V_{1,s}}\right|_{V_{2,s}=0} ; S_{21} = \left.\frac{V_{2,r}}{V_{1,s}}\right|_{V_{2,s}=0} ; S_{12} = \left.\frac{V_{1,r}}{V_{2,s}}\right|_{V_{1,s}=0} ; S_{22} = \left.\frac{V_{2,r}}{V_{2,s}}\right|_{V_{1,s}=0}$$

Here, for example, $V_{2,r}$ means voltage signal received in port 2, and $V_{1,s}$ means voltage signal sent from port 1.

Another advantage of Network Analyzers compared to other high frequency measurement systems is that they operate at different frequencies, which span a range that depends on each specific device. Modern analyzers typically cover from hundreds of MHz up to tens of GHz. More complex ones go beyond these limits. The normal way of operation is then fixing the signal amplitude and sweeping its frequency, in order to obtain the

frequency reponse. Another mode of operation does the opposite. For a fixed frequency, the amplitude of the signal is swept in a certain range of values. This is usually referred to as "power sweep".

Traditionally there were only the so-called "Scalar" Network Analyzers, capable of measuring only the amplitude of the scattering parameters. Most of the current Network Analyzers are "Vectorial": they can also measure the phase of the scattering parameters (this is, how much delay has a signal suffered since it was emitted by one port of the analyzer until it reached another port, or the same one in the case of reflection measurements). The phase information is necessary to, for example, distinguish the respective values of real and imaginary parts of the scattering parameters. Therefore the S parameters are complex numbers, whose amplitude and phase a VNA can measure.

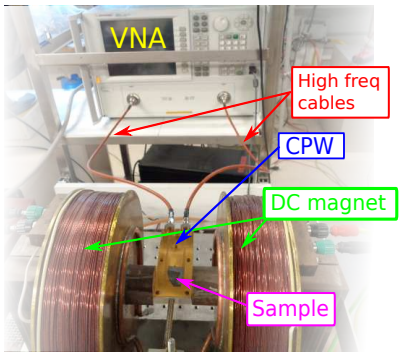

Figure 2.2: *Photograph of the high frequency measurement setup at room temperature.*

When working with circuits at high frequencies one needs to be careful, regardless of if a Network Analyzer of any other system is used. This becomes evident if the wavelength associated to the frequency in use is shorter than the length of the electrical circuit (the cables are normally the circuit elements that contribute the most to the total circuit length). In this case, a short wavelength signal can easily be scattered by some circuit elements, such as connectors, bends in the cable, or any impedance mismatch. When this happens part of the emitted signal will be reflected back to the port, and one risks that not enough signal power will reach the sample. On the other hand, signals of a wavelength much larger than the size of these types of sources of scattering will propagate through the cables with no reflections. The limit case is that of a DC signal, which could be thought of as having an infinite wavelength. See appendix A for more details on this.

Coplanar Waveguide

There are multiple types of waveguides which serve different purposes. In general, a waveguide is a structure that allows waves (in this case electromagnetic) to propagate through it. Stripline-like waveguides are very popular in high frequency printed boards and circuits, not only because of their good performance, but specially because of their planar structure, which allows for configurations of reduced size out of the plane. Their planar nature (sometimes several layers, sometimes only one) make them very appropriate to be grown with lithographic techniques, which also allows for a high fabrication rate in most of the cases. Traditional striplines consist of two planar conductors, vertically separated by a dielectric layer. One of the conductors will be connected to a ground, or reference, while the other will be connected to the signal relative to the reference.

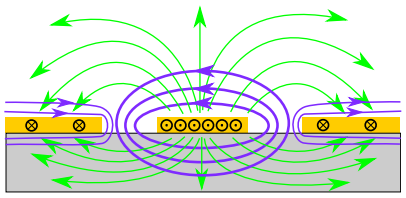

Figure 2.3: *Cross section of a CPW. Green and purple lines are electric and mangetic field.*

In this way, a current would flow between the conductors. Electric field lines are directed from the signal conductor to the ground, and magnetic field lines circulate around the current. Figure 2.4 shows a calculation of the in plane component of the magnetic field generated by a stripline as a function of distance[57]. These field lines then go through the

space above the stripline, towards the ground. A sample can be placed above the stripline so that these field lines incide on it.

A similar, but more convenient type of waveguide for this purpose is the coplanar waveguide. Its structure lies on a single plane, with the signal conductor in the middle and, generally, a ground on each side. In this case a larger amount of electromagnetic flux will be incident on the sample (see fig 2.3). One should note however that electric and magnetic fields generated by such waveguides are highly inhomogenous, and if the sample is large compared to the width of the central conductor, different parts of the sample will be affected by different field amplitudes and directions. In a CPW, current flowing through the central conductor is compensated by the same current flowing in the opposite direction throught the ground planes. However, in our case, since these planes are always much wider than the central conductor, the current density that they carry is much lower, and therefore the high frequency magnetic field generated by these grounds around them is much weaker than that of the central conductor, although it occupies a larger region. For this reason, we will neglect the field generated by the ground planes, but if we were interested in calculating it, we could use Karlqvist's equation[58].

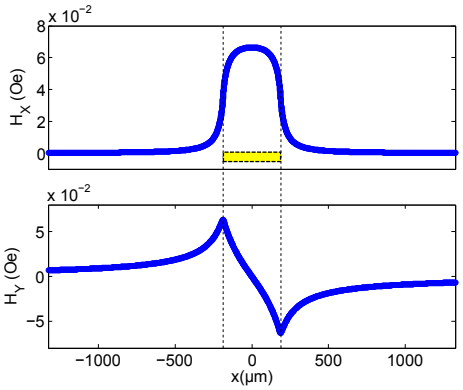

Figure 2.4: *Magnetic field generated by a stripline at a vertical distance of 20 nm (sample surface) and $P = 5$ dBm. The gray rectangle shows the dimensions of the central conductor of the CPW.*

The sample is placed onto the waveguide central conductor, to excite it with the microwave drive field ($\mathbf{h}_{\mathrm{rf}}$) up to about 0.1 Oe parallel to the plane. Figure 2.4 shows a calculation of the x and y components of the magnetic field generated near the central conductor, at a vertical distance of 20 nm for $P = 5$ dBm. The expressions found in[57] have been used for these calculations.

Designing a waveguide can be challenging for different reasons. The most important one is that it should have a characteristic impedance as close as that of the rest of the elements in the high frequency circuit as possible. Otherwise, reflections of energy will occur even before the signal is transmitted to the waveguide. There is always some freedom in choosing parameters such as the width of the central conductor and the gap between the central conductor and the grounds that one can tune, so that the capacitance and inductance of the waveguide change, and as a result the total impedance also changes. A rule of thumb that seems to work for the sizes of CPWs used in this thesis is using a gap that is 3/5 times the central conductor width. Care must be taken with small waveguides. In general, the narrower a conductor is, the higher its resistance. Therefore small waveguides will reach an unavoidable limit where one can never get down to the standard of 50 Ω, regardless of the waveguide shape. We have used different types of waveguides in this thesis: The first type existed already in our laboratory prior to this work. It is a U shaped waveguide which can be used in the room temperature setup and has two SMA (Sub Miniature A) connectors by Southwest Microwaves for high frequency cables. The CPW consists of commercial Roger laminates with a gold gladding on top. The central conductor has a uniform width of 375 μm and the gap between it and the ground conductors is 140 μm. The dielectric is a glass reinforced hydrocarbon/ceramic laminate with dielectric constant $\varepsilon_r = 3.66$. To isolate the grounds from fringe fields originated in the central strip a line of holes (via fence) is drilled at the edge of the ground plates,

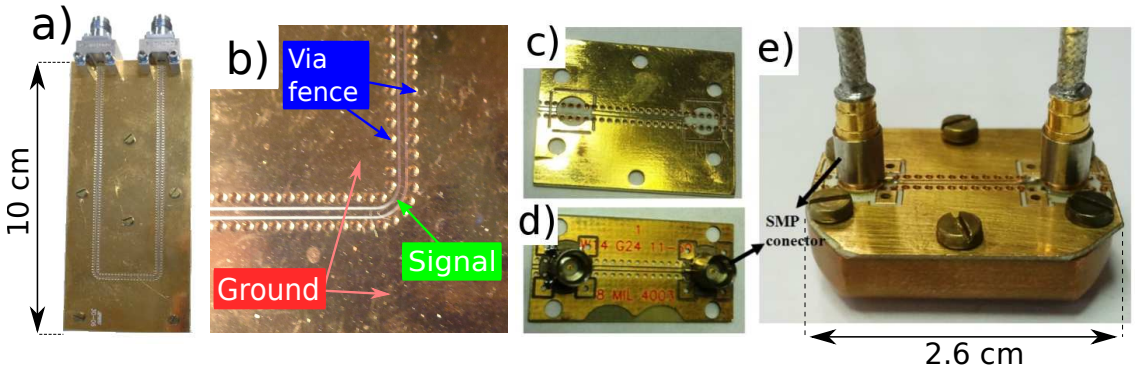

Figure 2.5: *a) Large CPW with SMA connectors for the room T setup. b) Detail of the grounds, via fence and signal conductor. c) Shorter CPW for the low T setup. d) Same as c), with soldered SMP connectors. e) Final configuration of the CPW as it goes inside the insert, fixed to a sample holder.*

separating them from the central line[59]. Figure 2.5 shows the different CPWs of this type.

The second type has the same parameters (central conductor width, gap, dielectic layers, etc) as the first type, but is straight and shorter. It is adapted to fit in the low temperature insert, inside the cryostat, thus its smaller size. The connectors in this case are of SMP type and are perpendicular to the plane. Different orientations with respect to the external field can be achieved by using high frequency cables with a straight connector, or one bent 90° and attaching the waveguide (with the sample mounted on top) to different holders to achieve different angles of orientation with respect to the external field.

This CPW is designed to have a characteristic impedance of 50 Ω up to 25 GHz. As mentioned earlier, these waveguides create inhomogeneous fields, and we are interested in knowing how much of this field concentrates right above the central conductor, where we place the sample. To account for the excitation on top of the central conductor, compared to far from it, in figure 2.6 we show a histogram of the distribution of intensities of the microwave field.

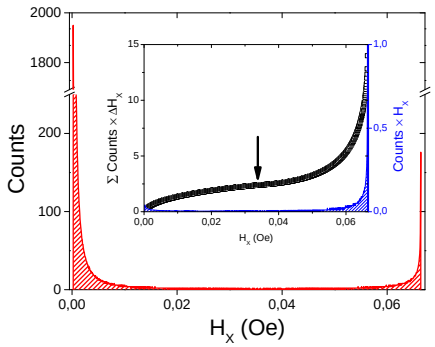

Figure 2.6: *Histogram of distribution of magnetic microwave field created by the CPW. The inset shows a weighted distribution of fields (blue area) and a cumulative distribution. The arrow marks the field at the edge of the central conductor.*

The largest value of the in plane field (corresponding to the middle of the central conductor) is found with a large frequency in the histogram, due to the almost parallel shape of the field close to this part of the waveguide. A large contribution can be seen in the histogram at low fields if long distances from the central conductor are considered in the calculations. With the appropriate weighting of each field with its frequency of appearance (inset), we find that at a field H_x=0.034 Oe (corresponding to the edge of the CPW), this weighted signal equals 17% of the maximum, which is achieved at the center of the CPW. Therefore, the region of the sample lying on top of the central conductor will be excited by an 83% of the total in plane field delivered by the waveguide. The rest of the excitation created by the central conductor lies beyond its boundaries. As mentioned above, the field generated by the grounds is neglected in these considerations, since the current density carried by

them is much lower, and the samples only cover these planes slightly, because they are placed covering almost only the central conductor.

The two previous waveguides have a relatively wide central stripline, which causes the current density to be lower and the high frequency field exciting the sample placed on top is weaker. A single magnetic dot like the ones we will be measuring is not at all enough to produce a visible signal in the VNA when at resonance. Then, samples typically consists of regular arrays of thousands, sometimes millions of dots. Smaller waveguides have also been used at room temperature to measure ferromagnetic dots. The idea behind using smaller waveguides is that they achieve higher high frequency current densities and, therefore, higher fields near the central stripline. Then, one would need a smaller amount of dots to still pick up a decent signal with the network analyzer. Also, these waveguides, grown by lithography, allow to study dots deposited directly in contact with the waveguide (deposited by lithograpy on the waveguide), instead of a separate sample which is placed on it. This brings the dots closer to the excitation source, since there are no air gaps, or protective resist layers as we have typically done with the larger samples used in the large waveguides. One of the smaller waveguides was made in collaboration with Prof. V. Metlushko, from the University of Illinois at Chicago. These waveguides are grown by optical lithography, on top of a 1×1 mm^2 array of triangular permalloy dots (more details on this sample in chapter 4). Using the small CPWs has drawbacks, too. First, one needs to be careful when designing them. Even with the help of high frequency design softwares, designing a small waveguide is always challenging, and often one needs to sacrifice the characteristic impedance, and have values higher than 50Ω. Finally, one needs to work with high frequency probes, less stable and more difficult to use than standard connectors such as SMA.

High frequency probes

High frequency signals are carried by special coaxial cables (next section) to reduce dissipations or reflections of the signal. To pass such signals to coplanar waveguides, adapters are used. For the aforementioned large coplanar waveguides, a SMA connector facilitates this. However, for connecting the coaxial cables to small waveguides, high frequency probes are used. Basically, they adapt an SMA cable to a ground - signal - ground probe which is placed with XYZ positioners in mechanical contact with the waveguides. Figure 2.7 shows how one of these probes would connect the VNA to a small waveguide. The probes we used are nonmagnetic GSG, K-type, by Picoprobe, with a 150 μm separation between the grounds and the central connector. They operate up to 40 GHz, way beyond the frequency range used in this thesis.

High Frequency Cables

Microwave signals are transported to the coplanar waveguides with special coplanar cables to transport high frequency signals. The cables have SMA connectors, and a torsion wrench is used, to tighten every connection with the same force. The cables are semi rigid, meaning that they don't collapse with gravity, but at the same time have a freedom of motion. In high frequency setups it is important to keep cables as straight as possible, since bents difficult the transport of high frequency signals, which can be reflected back to their source.

For our case, since we tipically compare frequency spectra as a function of applied magnetic field or temperature, every spectrum is normalized with respect to a reference spectrum (for example, the saturated state in a ferromagnet, or the normal state in a superconductor). In this case, high frequency calibration is not critical. However, in

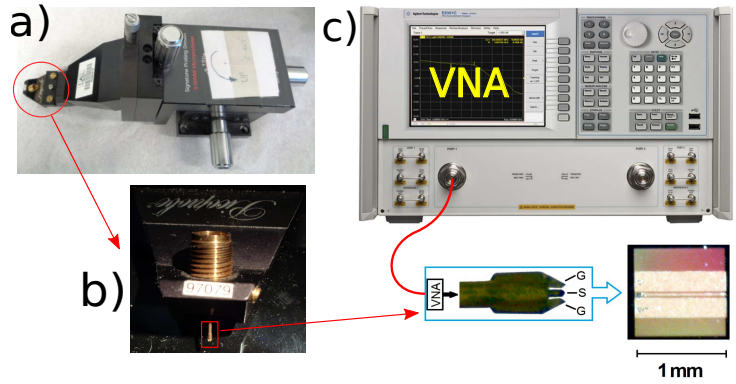

Figure 2.7: *a) High frequency probe mounted on an XYZ positioner. b) Detail of the probe. c) High frequency probe (detail of the tip), connecting a VNA to a small waveguide.*

measurements requiring a calibration, one needs to be careful with how different is the position of the high frequency cables during calibration and afterwards, when the cables are set for the experiment. If their position and shape is very different, the calibration can be spoiled.

The VNA emits a signal of some known power, but due to reflections inside the high frequency cables (two 0.6 m long cables to connect to the VNA, and two extra 1.5 m long cables in the insert to carry the signal inside the cryostat for the low temperature setup) and connectors, and their heating due to eddy currents, microwave power is not fully transmitted from one port of the VNA to the other. The value of the signal frequency (f) is related to the appearance of internal reflections, and a frequency sweep gives the information of how much power is transmitted at every frequency by means of the $S_{21}(f)$ parameter. The power of the signal at the CPW (P) is estimated as the average of the power emitted from port 1 and the power received at port 2, since the cables configuration connected to both ports is symmetric. We start from the definition of the transmission parameter in terms of voltages, when no signal comes out from port 2:

$$|S_{21}| = \left| \frac{V_{2,in}}{V_{1,out}} \right|$$

In this expression, $V_{2,in}$ refers to the voltage (amplitude and phase) of waves entering port 2, and $V_{1,out}$ to voltage of waves emitted from port 1. In terms of power, the expression for the amplitude is:

$$|S_{21}| = \sqrt{\frac{P_{2,in}}{P_{1,out}}}$$

Knowing $S_{21}(f)$, directly measured with the VNA, the power at port 2 is calculated as:

$$P_{2,in} = |S_{21}|^2 P_{1,out}$$

and the estimated power at the waveguide, P, is taken as the average:

$$P = \frac{P_{1,out} + P_{2,in}}{2} = P_{1,out} \frac{(1 + |S_{21}|^2)}{2}$$

It is to be noted that this P does not refer to the radiated electromagnetic energy incident on the sample, just to the power associated to the current that produces this radiation, as it propagates through the CPW. Again, this does not matter for our purposes, since **we**

are only interested in relative changes of susceptibility as a function of field or temperature, not its absolute value.
This correction helps to quantify the losses due to the relation between wavelength and length of the cables. Higher frequency signals suffer more reflections, and are not so well transmitted to the second port, which can be quantified via S_{21}. However, more factors can contribute to decrease the power that is delivered to the sample, such as not perfectly symmetric cables, that would decrease the accuracy of the previous average. Also, it is important to remember that working at low temperatures can result in important differences compared to room temperature, due to changes in the length of cables, etc. In our case, this is not a problem, since the range of variation of the temperature is small, always very close to T_c. Also, even if we could take into account all losses, the results presented in the main text are relative (throughout the range of powers considered, where transmission efficiency is invariant, since the frequency is fixed), and a correction of the absolute value of power will not affect the presence of the observed effects.

Measurement of the permeability parameter U

For the data analysis (i.e. calculation of the real and imaginary parts of U) the reflected signal is neglected (S_{11} coefficient of VNA), since its relative variation with respect to a reference trace is typtically more than 15 times lower in magnitude than the transmitted signal (S_{21} coefficient). Only when explicetly specified, specially in the case of measurements with high frequency probes, forcefully done in the reflection configuration, we use the S_{11} parameter. In this case, we replace in what follows S_{21} by S_{11}.

The permeability parameter was analyzed as the VNA transmission parameter (S_{21}) for every field, following the procedure in[60], to find the position and linewidth of the resonances:

$$\mu \propto U(f,P,H) = \frac{S_{21}(f,P,H)}{S_{21}(f,P,H_{\text{ref}})}$$

Here $S_{21}(f,P,H)$ and $S_{21}(f,P,H_{\text{ref}})$ are the (f) and (P) dependent forward transmission parameters at the applied field of interest H, and the reference field H_{ref} (the maximum applied field, higher than H_{c2}). For the case of superconductors, this expression is used when the temperature is kept constant and the field is changed. To remove unchanging resonances or reflections of the signal, due ta cables, connectors, etc, each trace is normalized by a similar trace taken at very high fields, corresponding to a saturated state with no resonances (or with resonances at frequencies out of the scale). An analogous analysis is used in the low temperature measurements, for field sweeps at constant temperature, or for the temperature sweeps at constant magnetic field, but normalizing at a reference temperature. It is necessary to achieve the normal state, either by increasing the temperature or the field, to have a clear signal corresponding to the superconducting response, when compared with the normal response, so well above T_c or H_{c2} conditions are necessary for a correct normalization. The quantity U is complex, and the imaginary part of $U = U' + iU''$ represents microwave losses, while the real part U' represents energy stored and exchanged between sample and circuit (CPW), in the case of superconductors, flux screening by the superconductor.
Once U is found, values of T_c and H_{c2} can be found when reaching high enough values of the temperature or field, so that the region in which the sample is in the normal state is clearly differentiated from the superconducting region.

Scanning Microwave Microscopy

In the last stages of this thesis, during a 3 month stay at the National Institute of Standards and Technology (NIST) labs in Boulder, CO, USA, an attempt to experimentally visualize edge spin waves was made, under the supervision of Dr. Pavel Kabos, using the technique known as Scanning Microwave Microscopy (SMM). No spatial distribution pictures of E-SW were achieved, but the principle of operation of this technique was put to the test, and some advances were made, being able to detect spin waves of an array of magnetic dots. This technique has been present for some years now, but its main area of application so far has been semiconductors being this, to the best of our knowledge, the first time that it has been applied to the case of spin waves. An active study of spin waves using this technique on samples fabricated by Dr. José Luis Prieto's group is in progress at the time of writing this thesis. More on this in chapter 4.

In brief, this technique combines the spatial resolution of an Atomic Forces Microscope (AFM) with the broadband highfrequency measurements of a network analyzer. Instead of the usual AFM tips, a special tip that extends a coaxial cable is used as a very narrow antenna. This antenna can be used to emit a high frequency signal, which would excite locally the material below it, or act as a receiver. Below the sample, there is another (larger) antenna. Both antennas connect to the two ports of a VNA, closing the high frequency circuit. Figure 2.8 shows a sketch of the system.

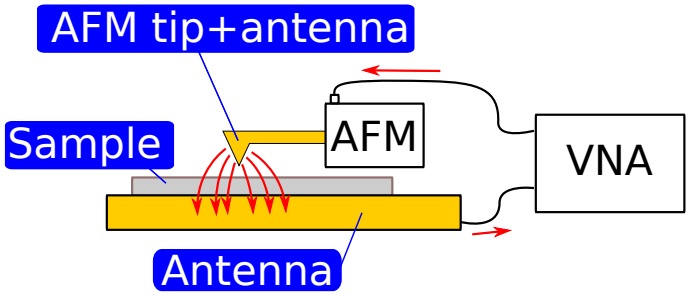

Figure 2.8: *Sketch of the Scanning Microwave Microscope.*

Since the main focus of this thesis is not AFM measurements, we will not go into details about the principles of AFMs here, we will just consider it a device capable of scanning, and take 2D maps of samples at resolutions as low as the nanoscale, thanks to piezoelectric positioners, capable of achieving very high spatial resolutions. The scanning is done with a special tip, placed on the piezo stage, that is flexible, and is bent due to the interactions with the surface being scanned. A laser is pointed toward the back side of the tip (facing away from the sample), and its reflection is directed to a photodetector that quantifies the deflection of the tip a every position in XY, which serves to reconstruct the topographical profile of the sample. At the same time, this device can send a microwave signal of a fixed frequency (due to restrictions in the commercial software that controls the whole measurement process), from the tip to the antenna under the sample, or viceversa. Doing this the microwave signal propagates through the sample, locally exciting spin waves. Another mode of operation is to fix the position in the XY plane, and sweep the magnetic field biasing the sample, to take spectroscopies as a function of field, which allows to detect FMR-like modes. More details are given about the measurements in chapter 4.

Cryogenic system

In order to study the high frequency electromagnetic properties of materials at low temperatures, a duplicate of the basic high frequency setup, placed inside a cryostat, has been used. This

cryostat is a SVT model by Janis, and it has a gas flow type of insert inside a high field superconducting electromagnet. It consists of a series of chambers, isolated from one another. The first (outermost) chamber is filled with liquid nitrogen at 77 K, to reduce thermal radiation to the inside chambers. Following the Stefan Boltzman law the radiated heat is reduced by a factor $\frac{300^4}{77^4} \simeq 230$.

A second chamber is filled with liquid ^{4}He, to cool down the sample. At the bottom of this chamber there is a *NbTi* superconducting magnet, by Cryomagnetics INC., capable of producing magnetic fields up to 9T in the vertical direction. For different field orientations with respect to the sample, the sample itself must be tilted with different sample holders.

Finally, the innermost chamber is where the sample holder is inserted. A capillar connects this chamber to the preceding one, which contains the liquid He. A needle valve that can be operated from the outside of the cryostat allows more or less helium to reach the sample holder, thus achieving a higher or lower cooling power. The cryostat is filled with liquid He at 4.2K. In order to achieve lower temeperatures than that, one needs to pump out helium. A rotary pump extracts helium gas from the chamber where the sample is located. Then, liquid helium from the next chamber is sucked in through the capillar. As it reaches the sample chamber, where there is a lower vapor pressure, due to the action of the rotary pump, it evaporates. As the gas expands and occupies a larger volume, it lowers its temperature. Thus the sample is cooled. To achieve a stable temperature, a temperature controller (model Lakeshore 340) is used. Two thermometers give the corresponding values of temperature to control the heating power in different parts of the system. In the insert chamber, the first thermometer (Cernox CX-1050-SD) serves for the coarse heating. Located in the sample holder there is a Carbon Ceramic CCS/A2 thermometer for fine adjustments of temperature. Both thermometers use the current value of temperature to calculate via a PID controller the power that needs to be applied to two resistors that heat up the evaporated helium. One is fixed inside the cryostat, for coarse control of the temperature, whereas the most precise one is a manganine wire coiled around the sample holder. It admits different ranges of power for achieving different ranges of temperatures. Figure 2.9 shows an actual photograph of the whole low temperature setup.

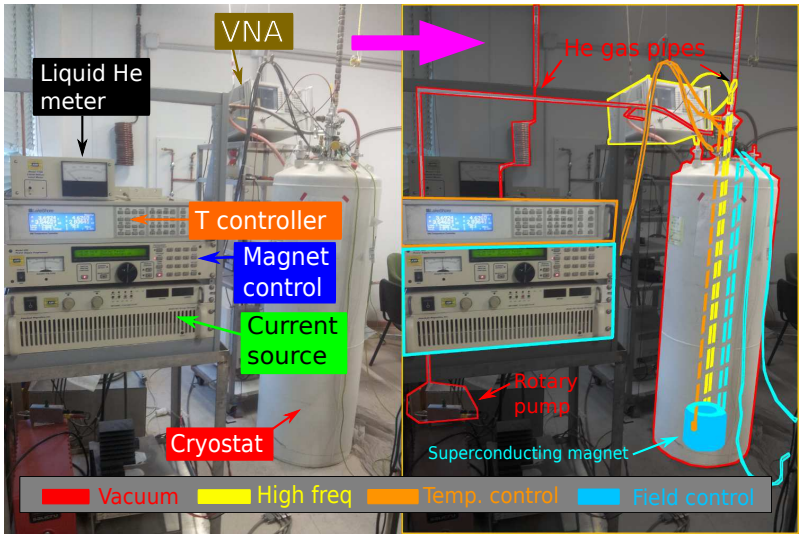

Figure 2.9: *Photograph of the cryostat system. The right picture highlights the different connections by color (legend at the bottom).*

All chambers are isolated from one another by vacuum chambers, in which one can

pump out any possible gases that could produce convective heat transfers. Also, for some modes of operation when we are interested in keeping a constant magnetic field inside the magnet (for instance, for temperature sweeps), a permanent current can be trapped inside the superconducting magnet using a "switch heater", a resistance that can interrupt the electric circuit connecting the cables from the current source to the magnet. This switch is of superconducting material, and an external current can be driven through it with the temperature controller. Doing so eliminates the superconductivity of this element. However, while no current goes through it, and it superconducts, it short circuits the two connections of the electromagnet and closes the circuit, confining the supercurrents in the magnet. From this moment, the external current source can be switched off. With all these measures, and depending on the type of usage that the cryostat has (specially if not very high fields are used) one can keep doing measurements during some 10 days without having to refill the cryostat with more liquid He, while measurements are taken uninterruptedly by a computer.

The sample holder is attached to the insert stick that holds all the connections and high frequency cables.

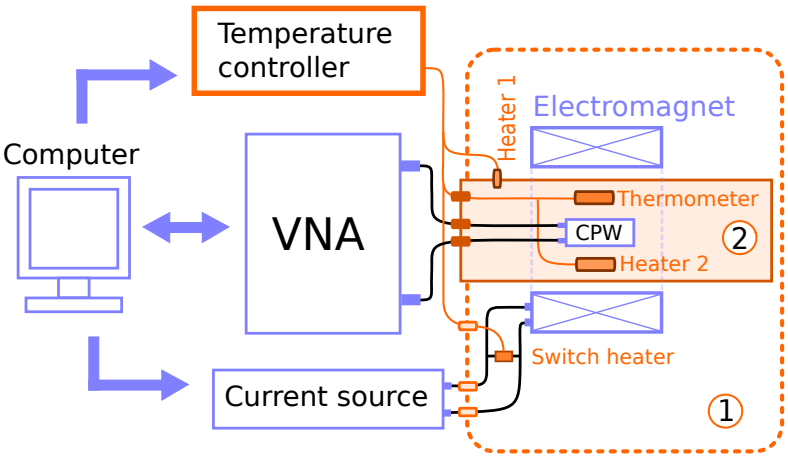

Figure 2.10: *Low temperature version of the VNA-FMR system. 1 represents the liquid helium chamber. 2 represents the insert chamber.*

Measurement procedure

The process of measurement and data analysis has been automated, so that one only needs to set the parameters of the measurement (values of magnetic field, microwave frequency or power ranges, temperature, etc), and a computer program will carry out the measurements non stop. In this way, time and helium consumption (in the case of low temperature measurements) is optimized. The computer is connected to the different devices (VNA, current sources, temperature controller, etc) via GPIB cables, and controls their actions with SCPI commands that are send in sequence with programs customized to meet each measurement requirement.

Fitting models

From the network analyzer raw data it's not obvious where the FMR resonant modes are, since its effect is small compared to that of the cables, waveguide, etc. Therefore, to get clear pictures of the resonance, the background signal must be removed. Two methods have been used throughout the thesis to achieve this:

- First, each trace taken by the network analyzer can be normalized (point-wise) by a reference trace (usually at a high field, such that the resonances are expelled from the frequency range of study, or in the normal state for the superconducting samples). Since

traces are "lists" of complex numbers, the amplitude "lists" are divided by the amplitude of the reference trace, and the phase of the reference trace is subtracted to the phase of each trace. This normally is enough to clearly see the modes, however, there are cases where the background fluctuates as well (drifts in temperatures, high frequency cables moved during the measurements, etc). A quick fix that was found to work well consists in subtracting the background of the frequency sweep data at every field individually. To do this, first we smooth the whole trace with enough neighbors in each point, knowing beforehand how wide the resonances are. By using a very "coarse" smoothing (with a lot of neighbor points to each point), we are left with a curve that reasonably well reproduces the shape of the background, but "overlooks" the resonances. Then, this smoothed background is subtracted to the raw data from which it was calculated, leaving a much flatter background and the resonant peaks more visible.

- Second, more difficult to interpret, but usually good to get rid of the background, and easier to do, is to take the differential plot of the whole spectrum as a function of frequency and field (or sometimes temperature in the case of superconductors). The main difficulty with differential plots is that they highlight only field dependent modes (or avalanch depinning powers, as done in chapter 6). Also, every resonance peak is transformed into two peaks when performing the derivative, one negative and one positive. This positive or negative value also depends on whether they go to higher or lower frequencies when changing the field, for a differential analysis on a given axis.

Measurement of magnetization curves with SQUID.

The hysteresis loops shown in this work have been measured with the help of Dr. M. García-Hernández at ICMM CSIC, in Madrid, Spain, with a commercial Quantum Design SQUID magnetometer. SQUIDs (Superconducting QUantum Interference Device) are currently the most sensitive magnetic field detectors. These systems base their field detection capabilities on Josephson Junctions.

2.3 Simulations

Micromagnetic simulations

Computer simulations of physical phenomena are becoming of critical importance in modern science. Not only do they have the potential to be much cheaper and accessible to use than some experimental setups, a big effort has been made during the last decades to optimize algorithms to provide faster and more precise methods of solving well known differential equations that accurately describe physical systems. In the case of our high frequency magnetic measurements in magnetic nanostructures we have made an extensive use of simulations to understand and explain the experimental results.

Magnetism at the nano and microscale are often described in the micromagnetic limit. This model, proposed by William Fuller Brown, Jr in 1963, assumes the magnetization of a sample to be a continuous vector field, forgetting then about the discrete nature of localized magnetic moments that give raise to the magnetic properties of materials. Once magnetization is described as a vector field that depends on the spacial coordinates, one can use computational methods such as finite differences or finite elements to solve the corresponding equations. As materials get more complex, or more focus is put on shorter timescales than we will consider here, micromagnetic simulations need to be replaced by atomistic simulations, or multiscale simulations.

The micromagnetic simulations described in this thesis have been performed with OOMMF[16] and MuMax3[17], both open source projects that solve the Landau Lifshitz

Gilbert equation by finite differences. The latter does that using GPU (graphics processing units) calculations, speeding up the simulations up to around x100, depending on the hardware. Thanks to a grant by nVIDIA's academic program, by the end of this thesis, such hardware could be put into use, expanding notoriously the previous computational capabilities of our group, concerning simulations. At the moment of writing this thesis, a second workstation with another GPU (nVIDIA Titan X) also donated through this academic program has just been set up, doubling our initial MuMax3 simulations availabilities.

One can input a set of parameters, including the size and shape of the sample, its magnetic damping, crystalline anisotropy, exchange stiffness, saturation magnetization, etc, as well as the initial magnetic state and the fields that are applied. After the calculations have finished a set of output files is produced, providing information about local magnetization, local magnetic field, etc.

The use that has been made throughout this thesis of these programs is the following[61]: First, one performs a hysteresis loop, typically applying the magnetic field in the plane of the sample. Once the dynamic oscillations of the magnetization have damped out under each field, a file containing the relaxed local magnetization is saved. The process is repeated for all the field values of interest. Then, each of these saved files is used as the starting point of a new simulation, in which the same static field is applied, in addition to a short magnetic field gaussian pulse. The oscillations of the studied magnetic modes have a period of about 0.1 ns, while the gaussian pulse is of 1 ps. For its amplitude we have used a value of 5 Oe.

The gaussian pulse takes the sample briefly out of equilibrium everywhere (as it is applied uniformly). After that, the magnetization will relax to its equilibrium position according to the LLG equation, in an oscillatory way. These oscillations will be small, if the pulse amplitude is not too high. The regions where the field pulse exerts a higher torque (close to 90° inclination with respect to the local magnetization) will oscillate the most. By keeping track of the time evolution of the local magnetization after each pulse, we can reconstruct the spectrum of excitations via Fourier Transform and the spatial distribution of amplitudes and phases for a specific eigenmodes frequency (which is identified as a peak in the excitation spectrum, see figure 2.11). With this information, one can recreate the time dependence of each eigenmode of magnetization separately from the other modes. Examples of this technique are exposed in chapter 4.

Alternatively, once identified the eigenmode frequencies, one can just apply an oscillating magnetic field of that frequency to excite only that mode as a function of time, and not just recreate the mode from the spectrum amplitude and phase data.

The obvious advantage of this method is that one only needs to apply a magnetic pulse once to obtain the dynamic response in the whole frequency spectrum (as high in frequency as allowed by the linewidth of the pulse, the shorter, the higher the frequencies available). In contrast, running individual simulations for a single frequency each time would be a very inefficient and time consuming approach in order to identify eigenmodes.

Example simulations

Figure 2.12 presents the excitation spectrum of a uniform Py film. One can clearly see the ferromagnetic resonance peak, and how it shifts to higher frequencies at higher applied fields. The spectrum is obtained after applying pulses to relaxed states, as described in the previous section. To simulate this type of FMR response in large thin films, it is useful to use periodic boundary conditions (PBC). One needs to be careful however, because if a high field is applied, or if one starts from a uniform magnetization in the same direction of the external field, due to symmetry, the moments will not have a preferred orientation to follow during the reversal process, and it will not occur. This does not happen in finite

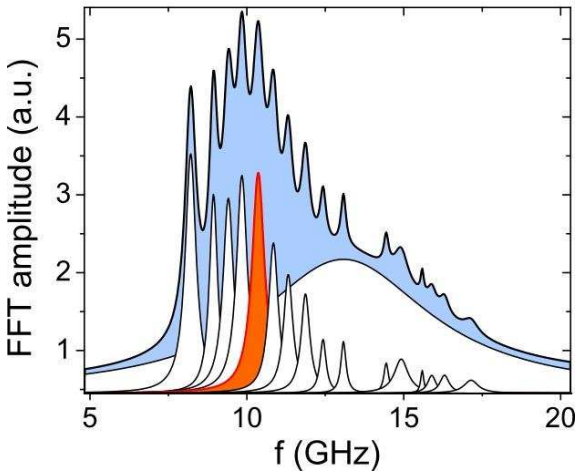

Figure 2.11: *Simulated eigenmodes of a 1 µm side triangle in the B state at 1000 Oe (details in chapter 4. The blue shaded curve is the whole spectrum (response to a 1 ps full width half maximum, 5 Oe amplitude, gaussian field pulse), and the individual peaks are obtained by a multi-peak fit with lorentzian curves. Only one frequency at a time of the whole spectrum (maximum of red curve) is selected for further applications.*

samples, due to edge effects, but it does in simulations with periodic boundary conditions. To solve it, **a slight inclination of the field is enough to break the symmetry**. Alternatively, one can start with a random initial state.

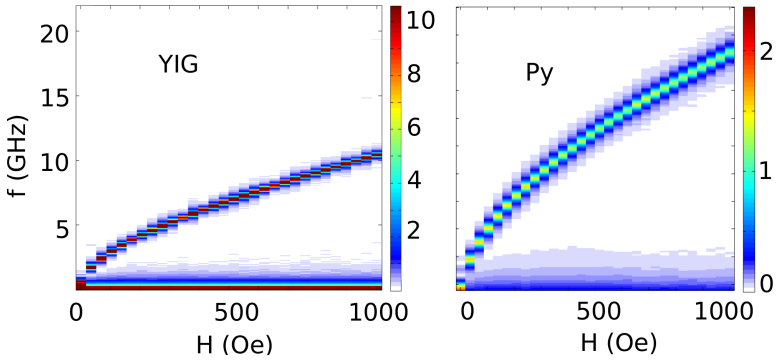

Figure 2.12: *Simulated spectrum of a YIG film and of a Py film. The color scale is FFT amplitude in a.u.*

Time dependent Ginzburg Landau simulations

Part of the work of this thesis has been dedicated to write a computer program to simulate the time dependent Ginzburg-Landau equation. This topic is dense and several details had to be addressed with care. Chapter 5 is dedicated to this simulation method, rather than sketching some properties here, to explain in more detail the challenges faced and the results obtained with these simulations.

2.4 Sample preparation

The samples studied during this thesis have been grown with different methods and in collaboration with Spanish and foreign research centers. Each chapter will describe in

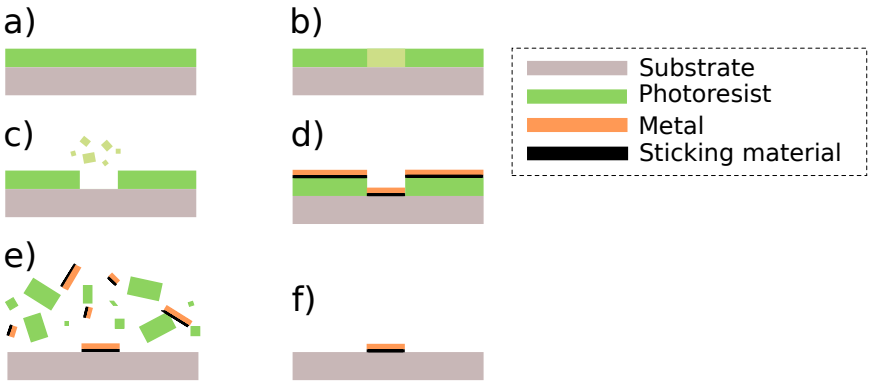

Figure 2.13: *Steps of the lithography-liftoff method. a) Photoresist layer deposited on substrate. b) Define patterns with lithography on photoresist. c) Remove lithographed areas of resist layer. d) Grow metal layer. e) Remove the remaining photoresist. f) The sample is ready after rinsing and drying.*

more detail the particularities of each sample, but now a summary of the different growth techniques is presented. The author has also obtained practical experience with some of these techniques during a 1 week stay at INA, Zaragoza, Spain, under the supervision of J. M. de Teresa, supported by a grant by the Nanolito Network.

Lithography and lift-off

Lithography (from Greek, $\lambda\iota\theta o\varsigma$, lithos, meaning - stone, and $\gamma\rho\alpha\varphi\varepsilon\iota\nu$, graphein - to write) in the context of micro and nanofabrication is a set of techniques with the same goal: modify the structure of a photoresistive layer deposited on a substrate by exposing it to some irradiation (light in the case of optical lithography, electrons in the case of electron beam litography), so that later the exposed area can be removed with a solvant (typically acetone), leaving the rest of the photoresist on the substrate. The whole structure is then placed inside a chamber where some material (in our case magnetic materials) is evaporated and cover the surface of the sample. The "holes" created during lithography allow the evaporated material to fall on top of the substrate, while the rest falls on the remaining photoresist. Finally, the photoresist with all the material coating it is removed from the substrate with a longer exposure to the solvant (figure 2.13). The lithographic process is done inside a clean room to avoid the deposition of dust particles, which would ruin the final result. The photoresistive material used in the samples studied is polymethyl methacrylate (PMMA), a positive photoresist (which means that the exposed areas are those that the solvants remove, i.e., the light or electron source marks the areas which will be removed).

Optical lithography

In optical lithography, or photolithography, the pattern is transferred to the photoresist layer with an optical mask, placed between the resist and the light source. The main advantage of this method is that once the mask has been created, it is fast to use, and the results are reproducible. The major drawback, at least for the application of this technique to nanofabrication, is the lateral resolution limited by the wavelength of light. The critical dimension (CD), representing the minimum size achievable is given by: $CD = k_1 \frac{\lambda}{NA}$ where k_1 is a constant that takes into account factors related to the lithography, λ is the wavelength of the light source and NA the numerical aperture of the lens (which represents the aperture angle of the cone of light projected form the lens).

Electron beam lithography

Electron beam (e-beam) lithography achieves a much higher resolution than optical lithography, and is the method with which all our samples involving dots are patterned. Typically, a scanning electron microscope is modified to incorporate the functionality of lithography. An electron beam is generated by thermionic emission, and then is focused with magnetic lenses on the substrate. This lenses deflect the beam, allowing to define patterns. The main drawback of this method is its slow speed, compared to the optical method. Also, some alignment steps have to be taken to make sure the patterns fall into place. For some tests during this work, in colaboration with the group of Dr. J. M. de Teresa (INA, Spain), we could experience how challenging it can be to create patterns fitting other existing patterns, so that they match and overlap as desired. Figure 2.14 shows a Scanning Electron Microscope (SEM) image of triangular dots grown by Dr. V. Metlushko with e-beam lithography.

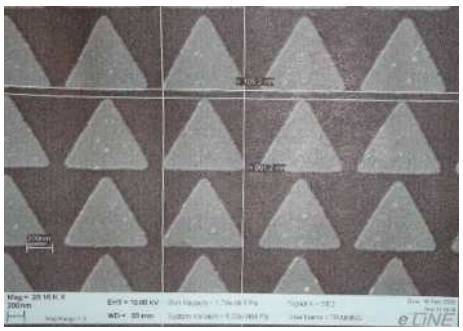

Figure 2.14: *SEM image of array of triangular 1μm dots. Sample and picture by V. Metlushko.*

Nanoimprint lithography

Nanoimprint lithography is a more advanced method which is capable of achieving a high resolution with a fast speed. In colaboration with Dr. V. Metlushko, form U. Illinois, Chicago, some of our samples have been grown with this method. It involves defining a pattern in a seal, which then is used for mechanically transfering that pattern (this is where the speedup occurs) to a substrate.

Sputtering

Once the pattern is transferred to the substrate, it is time to cover the sample with the target material. Then, after removing the resist unexposed to lithography, we will be left with the substrate and the patterned layer of deposited material on top. There are several ways to deposit the desired material on the substrate, but sputtering is the one our colaborators who grew the samples use. It involves exciting in some way a target of material, so that part of it is extracted, and falls on the sample substrate. Different sputtering methods involve different sources of excitation to extract material from the target. Some examples are electrons, ions or laser pulses. Several of our collaborators who have grown samples for us to measure use sputtering techniques (Dr. V. Metlushko, Dr. J. M. de Teresa's group, V. V. Moshchalkov's group).

Focused Ion Beam induced deposition

A growth method used for the cobalt dots described in chapter 3 involves deposition with focused ion beam, in collaboration with Dr. O. Dobrovolskiy. The sample substrate is located inside a chamber which is filled with gas molecules which contain the substance

that we want to deposit. Then, an ion beam (in our case Argon ions) patterns the shapes we desire to transfer to the substrate, by breaking the gas molecules deposited on the substrate surface into volatile and non-volatile components. The accumulation of non-volatile parts results in the deposition of the desired material with the correct shape onto the substrate. The main drawback of this method is that high purity is hardly achieved, since the non-volatile parts of the precursor gas that remain on the substrate contain other components, apart from the ones we wish (in our case, cobalt). But the high precision of the ion beam results in very well defined structures at the nanoscale. Also, ion milling can be used to further modify the shapes.

Part II

Results

3. Metastable states pinning

MAGNETIC dots in the single vortex state are firm candidates for new types of magnetic memories. Not only do their reduced size and tight packing in arrays constitute interesting alternatives to the currently used magnetic memories, but specially their capability of storing two bits of information per element, thanks to two intependent magnetic properties, polarity of the vortex core and chirality of the magnetization surrounding the dot. As pointed out in chapter 1, only dots of the appropriate dimensions can develop vortex states.

The double vortex state is a metastable state which can appear in magnetic dots of the appropriate aspect ratio (for 1 μm diameter, thickness lower than 25 nm). This state has some interesting properties, specifically for this thesis, the capability of confining and propagating spin waves through narrow domain walls. In the work presented in this chapter we pursue the goal of designing a new method to manipulate magnetic nanostructures to control in predictable ways the motion and trajectories of magnetic structures such as vortices or domain walls, pinning them at specific fields, and having them unpin at other fields. This can impact the way in which such dots can increase their potential applicability as novel magnetic memory cells, allowing for multi-level memories. Our goal is to explore this possibility as well, for some specific cases.

In this chapter we study magnetization reversal in circular Co disks with nanoholes through consecutive metastable states. In plane anisotropic magnetoresistance (AMR) and broadband susceptibility measurements accompanied by micromagnetic simulations reveal that cobalt disks with nanoholes show reproducible step-like changes in the AMR and magnetic permeability due to transitions between different intermediate states. Our findings are relevant for the development of multi-hole based spintronics and magnetic memory devices.

3.1 Introduction

Magnetization reversal in small magnetic elements is assisted by topological structures (TSs). A detailed theoretical analysis showed that the TSs usually found in simple magnetic elements can be decomposed into only two topologically different but simple objects: the vortex (V) and the half-antivortex (HAV)[62]. Controlling vortex, antivortex (AV), edge HAV and domain walls (DWs), which in turn can be decomposed into two HAVs with different or equal signs[63], becomes important for both fundamental and technological reasons[62,63]. Thus, recent studies revealed the importance of a controlled introduction of HAVs for effective domain wall displacement, manipulation[64] and dynamic response[65]. It has been found[66] that a DW moving in a finite strip at sufficiently high velocities is subject to the appearance of vortices besides the two half antivortices defining the original DW. Circularly and elliptically shaped ferromagnetic disks are basic elements of spin torque oscillators[67], magnonic devices[68] and magnetic memories[69,70]. Under certain

conditions these circular disks exhibit a single vortex (SV) ground state[69]. A similar state is also created in the free layer of a circular spin-valve structure by a strong spin torque caused by the adjacent perpendicularly magnetized layer[71]. It is expected that, vortex-based hybrid devices may represent a breakthrough for the implementation of spintronics in future telecommunication[72]. On the other hand, metastable vortex states emerging under the action of large spin-polarized currents have been predicted to damp spin torque oscillations[71].

Effectively controlling off equilibrium (metastable) states in magnetic disks and in particular stabilizing V and AV states[73] within the same device represent important emerging problems in nanomagnetism. Previously, the structuring of circular disks (mainly drilling holes or introducing notches) has been used for controlling the SV nucleation and propagation[74–81], thus modifying the azimuthal spin wave dynamics[82] or deterministically changing the sense of the vortex chirality[83]. For instance, suitable nanostructuring of permalloy (Py) disks introduces a bi-stable SV switching which was suggested as a basic mechanism for reprogrammable logic and data storage devices[84]. Micromagnetic simulations, however, indicate the important role played by HAVs for increasing the effectiveness of current induced V switching in spin-torque devices[64]. **Previous disks nanostructuring aimed at guiding SV trajectories only** (for example on guided magnetization reversal through a controlled sequence of ground states[65]). Different approaches are needed for an effective introduction of nontrivial TSs such as HAVs in circular magnetic disks.

In this chapter we study the **introduction of artificial pinning structures to guide magnetization reversal in circular disks through metastable magnetic configurations**, which are close to a double vortex state (DV) formed by two half antivortices and two vortices connected via DWs[6,85]. Figure 3.1 shows MFM images of a Co dot with a DV state at different applied fields. The DV state (proposed as a bit-cell for magnetic solid state data storage[86]), was previously stabilized by enhanced roughness in circular Py disks[6] and by the introduction of notches in elliptical Py disks[86]. Here we introduce hole-nanostructured circular magnetic disks (2000 nm diameter, 30 nm thickness, made of cobalt) as elements where HAVs can be stabilized for a broad range of magnetic fields. Using a set of two or three small nanoholes directed at 45° and 135° with respect to the external magnetic field we demonstrate a robust magnetization reversal through intermediate states with HAV and V states.

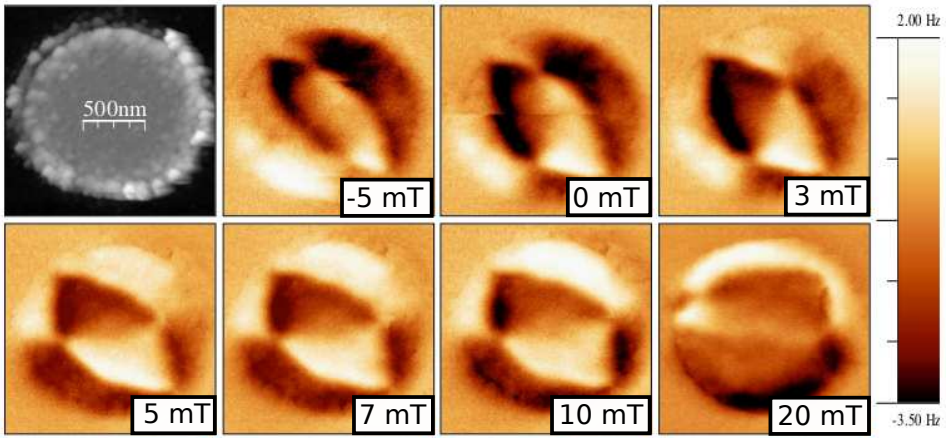

Figure 3.1: *MFM images of a 20 nm thick, 1 µm diameter, Co dot in the double vortex state. Magnetic field is applied in plane[87] (adapted figure).*

3.2 Sample preparation

The samples were prepared on top of silicon (Si) substrates covered with a 2 nm-thick silicon dioxide (SiO_2) layer. The substrate was pre-patterned with a layout of 300 nm thick gold contacts as shown in figure 3.2 a, grown by Dr. J. L. Prieto, UCM, Madrid. Next, the substrate was mounted into a high-resolution dual-beam scanning electron microscope (SEM, FEI Nova Nanolab 600). At the position where the Co disks were later on fabricated, the gold contacts were thinned by focused ion beam (FIB) milling to a remaining gold layer thickness of about 30 nm. This ensured good electrical contact between the electrodes and the Co dot. For the FIB milling process the beam parameters were 30 kV / 10 pA, the dwell time was 1 μs, and the pitch was 5 nm. Following the milling step, the Co disks were fabricated by focused electron beam induced deposition (FEBID) employing the precursor $Co_2(CO)_8$. Finally, the required number of cylindrical nanoholes of about 70 nm diameter was milled into the Co disks by FIB. SEM images of the samples thus fabricated are shown in figure 3.2 a. In the FEBID process the electron beam parameters were 5 kV / 1 nA and the process pressure was 1.2×10^{-5} mbar. Before the deposition, the chamber was evacuated down to 7×10^{-6} mbar. A visual inspection of the samples quality was done only several hours after the deposition processandin order to avoid autocatalytic dissociation of the residual Co on the substrate surface. The FEBID process was carried out by Dr. O. Dobrovolskiy and E. Begun at Goethe-Universitat Frankfurt am Main.

3.3 Measurements and simulations

IV measureent setup

Both anisotropic magnetoresistance (AMR) and dynamic susceptibility measurements were done by contacting the gold terminals to a high frequency probe (figure 3.2). For AMR measurements, a DC current was applied, and the voltage drop across the dot was measured with a nanovoltmeter. For dynamic susceptibility measurements, a vector network analyzer (VNA) was used for measuring the reflection parameter S_{11}, which is the ratio of the reflected and applied power. This parameter needs to be normalized to a reference value, to remove the influence of cables, gold contacts, etc. Here, we chose as a reference the value of S_{11} at the highest field applied. For further details on broadband measurements refer to chapter 2.

AMR simulations

To simulate the AMR curves, the angle $\theta(x,y)$ between the local current and the local magnetization in each simulation cell of a grid structure is needed, as changes in the resistance are proportional to $(\cos\theta)^2$. Static micromagnetic simulations have been done using OOMMF[16] to quantify the magnetization for different applied fields. The current distribution and the corresponding electric field were obtained by numerically solving the 2D Laplace's equation for the electric potential, figure 3.2 b. From the potential, the current direction is obtained via $\vec{E} = -\vec{\nabla}V$, under the reasonable assumption that currents always flow parallel to the electric field. The increase of the resistance was calculated by averaging the local increase of the resistance in each simulation cell. The parameters used in the micromagnetic simulations for Co are: 30 nm thickness, 2000 nm dot diameter and $5 \times 5 \times 30$ nm^3 cell size in the x, y and z directions correspondingly. The exchange stiffness is 1.4×10^{-11} J/m and the saturation magnetization $M_S = 1.4 \times 10^6$ A/m and the Gilbert damping constant $\alpha = 0.1$. The equilibrium criterion for changing the field is that every simulation cell precesses slower than 1° per ns[88]. The current is assumed to be parallel to the electric field and independent of the magnetic field.

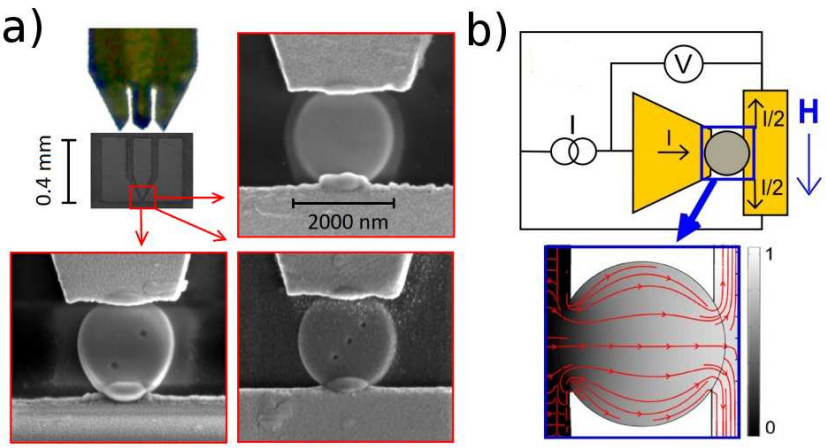

Figure 3.2: *a) Photograph of the probe that connects to the pads for AMR measurements. The arrows show SEM images of dots with different hole configurations. b) Sketch of the electrical connections to measure AMR, and a simulation via Laplace's equation of the current distribution (streamlines) and electric potental (color scale, a.u.).*

3.4 Results

Relaxation of saturated states

Figure 3.3 shows the simulated total energy of an initially saturated hole-free magnetic dot after reducing the saturating external magnetic field to zero, for different dampings. Before reaching the SV ground state, the dot undergoes a series of metastable states that appear as plateaus in the total energy for a few nanoseconds. In the long-time limit two possible states are observed: a metastable DV and the SV ground state, depending mainly on the value of the Gilbert damping constant α. In our hole nano-structuring we took into account previous studies which found[85] that the line connecting two vortices in the DV state is oriented at approximately 45° with respect to the direction of the saturating field before it was switched off, although larger disks (as in the present case) allow for more possibilities. Based on this, we focused on placing holes at 45° and 135° with respect to the direction of the applied field, with the idea of locating the holes at places where vortices are more likely to move, therefore facilitating their trapping.

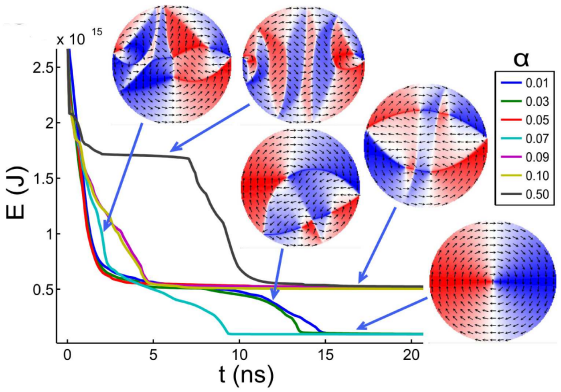

Figure 3.3: *Simulated relaxation of an initially saturated circular dot.*

Figure 3.3 shows that a number of metastable states with different internal TSs appear in the dot before it finally relaxes to the single SV state. Note that the winding number is conserved, so that antivortices (with value -1) appear alongside vortices (with value +1), to keep this quantity equal to +1, the value corresponding to the SV state. In the transition from states with multiple vortices to the SV state, both Vs and AVs can approach each

other and mutually annihilate inside the dot or at the edge. Previous works[74,75] dealt with trapping SV as it moves in the direction perpendicular to the applied field. However, DVs[85] do not usually move along this line, but rather rotate around the center of the dot in more complicated ways. Placing nanoholes off the direction perpendicular to the applied field therefore represents a good approach towards trapping both V and HAV states.

Measurements on a single dot

Figure 3.4 shows the AMR dependence on the applied magnetic field for a disk without holes. Only one clear transition is observed, corresponding to annihilation of a single vortex, occurring at low fields (below 100 Oe), compared to the transitions observed in disks with holes. This fact highlights the strong pinning that holes can exert on vortices or domain walls.

Figure 3.5 shows AMR data of Co disks with three different nanohole structures for which most reproducible results were obtained. The step-like changes suggest that intermediate states are involved with multiple V and HAV states. To verify this assumption, we have done micromagnetic simulations of the magnetic hysteresis of Co disks with nanoholes and complemented these results with AMR calculations shown in figure 3.5 a. Both the two and three nanohole structures show clear transitions between multiple intermediate TSs, as indicated by arrows. The corresponding magnetic states are shown in figure 3.6. Complementary broadband *ac* response measurements, also shown in figure 3.5 a by blue lines, further corroborate the presence of a number of intermediate well-defined magnetic states, correlating reasonably well with the signatures found in the dc measurements.

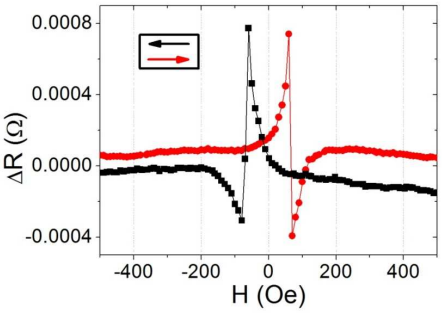

Figure 3.4: *AMR curves for a dot without holes*

In figure 3.5 a the *ac* response consists of an average of the normalized S_{11} parameter over the frequency range covered by the network analyzer (10 MHz to 9 GHz) as a function of the applied field. The data acquired by using both techniques point to the presence of the same intermediate states in the investigated samples. Micromagnetic simulations allow us to identify the intermediate states which develop in the disks with two or three centrally symmetric nanoholes, see figure 3.6. We have found that these states have multivortex character, containing both Vs and HAVs. They are therefore qualitatively different from those reported for disks with vortex core removal by a single central nanohole[82] or with nanoholes designed to capture only a SV[74].

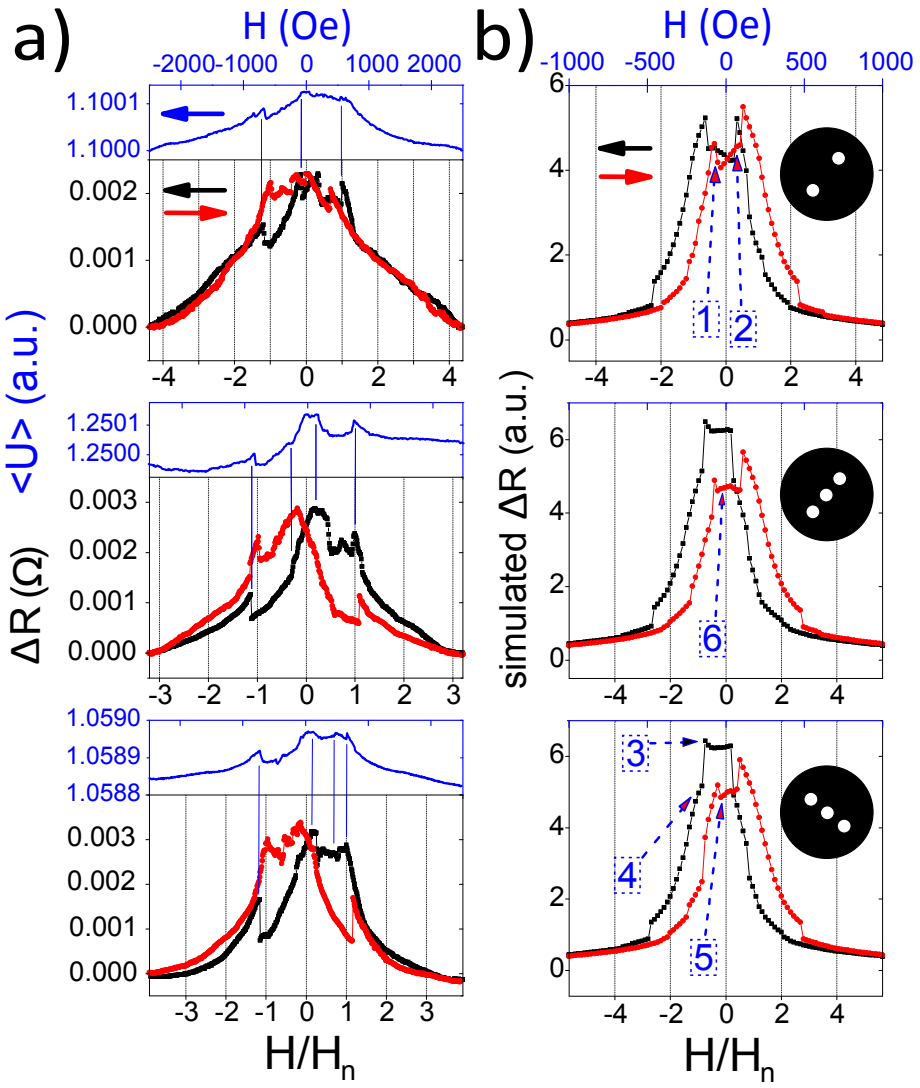

Figure 3.5: *a) Measurements and b) simulations of AMR. Each row corresponds to the hole placement shown in the right column.*

Comparison with simulations

A comparison of simulations and experimental results shows qualitatively similar jumps in magnetoresistance, occurring at quantitatively different values of applied field. We attribute these differences mainly to the far-from-perfect purity of Co that can be achieved with FIB induced deposition (about 90%)[89]. The unavoidable presence of molecules of the precursor gas inside the disk can represent an extra source of pinning for the magnetic topological structures, being higher fields necessary to release them than if the impurities were not present (as happens in simulations). Additionally, there is an uncertainty in choosing the parameters of the simulation, that could be relevant for studying both the ground and metastable states. This is shown in figure 3.3, that exposes the influence of damping on how fast the ground state is reached in simulations. The above discussed factors affecting the trapping of metastable states do not allow for a quantitative reproduction by simulation of the measured characteristic fields that release trapped metastable states. Our simulations, therefore, are mainly useful for identifying the processes involving the interaction of holes and magnetic topological defects, and

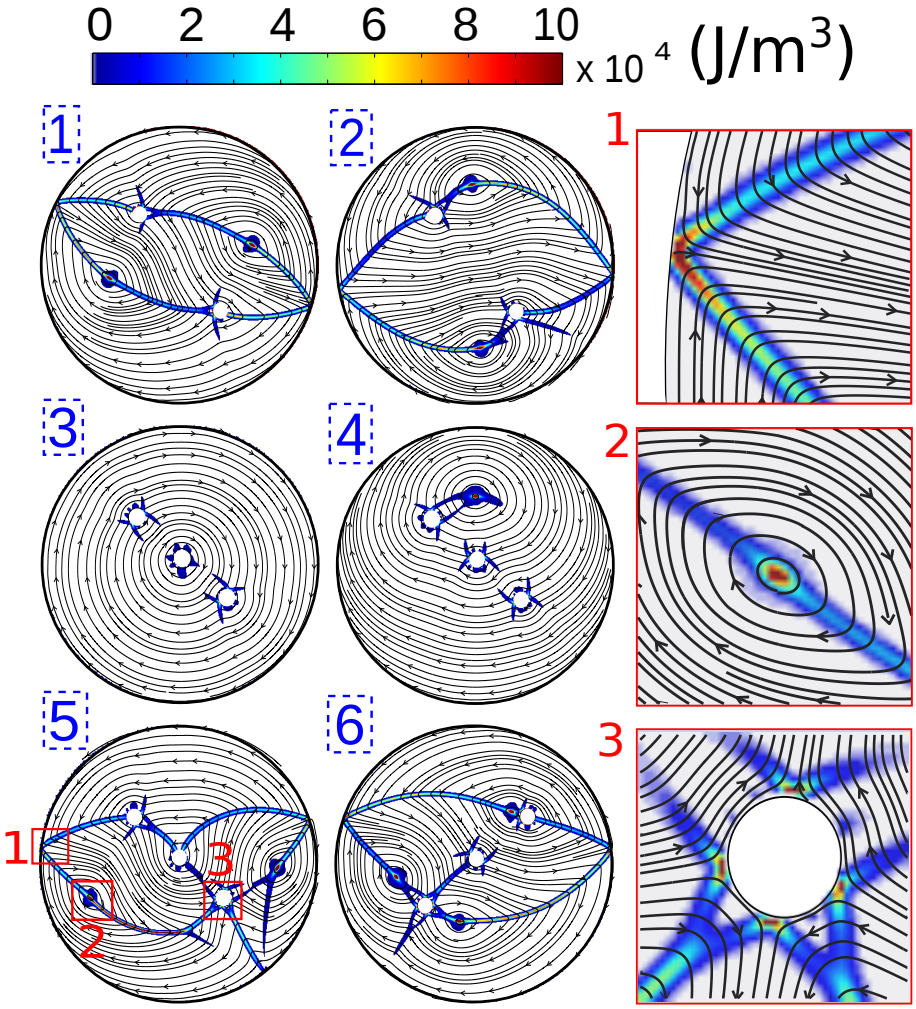

Figure 3.6: *Magnetic states of different dots. Streamlines with arrows represent the $\vec{M}$ direction. The color scale represents the exchange energy density (in J/m^3). The right column shows the zoomed areas marked in red in dot number 5.*

how this is reflected in AMR. The observed stabilization of multi-vortex intermediate / metastable states indicates that the nanohole arrangement leads to a reduction of energy of DV states via adequate pinning of both vortex cores and DWs by holes. Figure 3.6 shows representative magnetic configurations for which domain walls remain pinned to a nanohole even at the cost of increasing the domain wall energy by increasing its length. Varying the dot diameter allows for tuning the pinning force experienced by the topological structures, but can also result in different magnetic states during the reversal process. One reason for this is the distortion that nanoholes induce in the magnetization around them, which tends to align the magnetic moments parallel to the nanoholes' edges, just like it happens near any edge, in order to reduce the stray field outside the dot. Among different possible multivortex states, the DV state[6] composed of two half antivortices and two vortices connected via domain walls is the simplest one. Our dynamic simulations show that whenever an unstable domain wall meets a nanohole, it gets pinned due to the associated decrease in the exchange energy of the part corresponding to the nanohole diameter. Since domain walls occupy more space than a vortex core, they are more likely trapped by a nanohole than the vortex core itself. Therefore, due to the change of the

local magnetization orientation, the disks with intermediate multivortex states will exhibit abrupt changes of AMR as the field changes due to sudden DW depinning and less likely due to ortex pinning at nanoholes, as shown in figures 3.5 and 3.6.

Here we state as the main result of this work that the nanohole/field configuration used in our experiments provides a robust pathway towards introducing HAV states in circular disks. The reproducibility of the measurements is quite high; by measuring 20 curves we could check that the transitions are always present. The proposed method of controlling metastable states in circular magnetic disks is capable of providing a much richer variety of intermediate states than the one used to pin only a single vortex[74,75].

Since domain walls extend all over the dot if edge HAVs are present, several different more complex nanohole configurations are suggested. For example, with a 6-hole configuration forming a hexagon-type ring, our simulations and measurements show that a simpler AMR curve results, with smeared out transitions. The 6-hole configuration traps metastable multivortex states, but releases only a SV at sufficiently high fields, causing the AMR curves to look more similar to those of non-patterned disks, but with much higher remanence.

The multihole circular disks considered here could serve as basic elements for multistate memories, similarly to that suggested previously for elliptic dots with notches[86]. In order to take full advantage of the multilevel resistive states, one could incorporate dots with multivortex states as one of the electrodes in magnetic tunnel junctions (MTJs). Controllable DW displacement by perpendicular spin torque[90,91] could stimulate further development of these MTJs-based multilevel magnetic memories. Also, further studies could try not only to control the magnetic properties of devices by placing defects at different positions, but also to optimize the hole size for trapping magnetic structures. The hole should remain as small as possible and still possess an effective trapping capability, so that it weakly affects other device properties, in particular due to the unavoidable tendency of magnetization to align parallel to the hole edge.

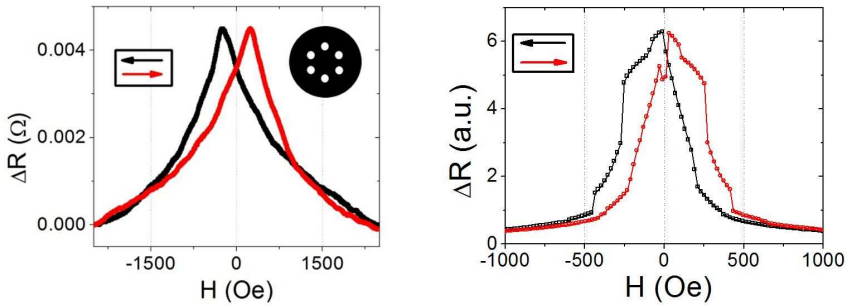

Figure 3.7: *Measurements (left) and AMR simulations (right) of a dot with 6 holes*

To conclude, we show the results obtained for the case of a dot with 6 holes distributed in a hexagonal ring shape (figure 3.7). This dot shows a smoother AMR curve than the disks with 2 or 3 holes in line, consisting in an increase of resistance followed by a sudden decrease at negative fields. Simulations show a similar type of response, but the maxima appear at lower values of field. This is probably due to the intrinsic defects in the cobalt deposited during the FIB induced deposition process that is not being taken into account in the simulations. In this case, simulations show how this hole structure is capable of trapping more easily a single vortex in one of the holes, that remains pinned until the sudden drop in magnetorresistance.

3.5 Summary and conclusions

In conclusion, we have found that magnetization reversal in circular cobalt disks with two or three centrally symmetric nanoholes takes place through intermediate multivortex states with edge half antivortices. These nanostructured disks are promising to create multilevel memories and patterned arrays with multilevel high frequency permeability characteristic features. Moreover, the proposed nanostructuring approach allows for gaining effective metastable states in small ferromagnetic elements, specially given the crucial role of half antivortex states in the optimization of spin torque induced magnetization reversal in vortex nano oscillators and possibly other spintronic devices. Similar nanostructuring strategies could be implemented for dots of different geometries (triangles, squares) and thicknesses with multivortex metastable states.

3.6 Perspectives

Artifitial and controlled pinning has proven to be a reliable method to stabilize out of equilibrium magnetic states. Thanks to ever increasingly complex and precise sample growth methods, creating such defects is something feasible, and does not represent a large bottleneck in time consumption in the overall growth process. We hope the results provided here, and in previous works, stimulate further research on this topic, to the point where very complex and unstable magnetic patterns can be stabilized, in order to take advantage of some of their special properties, which otherwise could not, given the tendency of the system to reach equilibrium. This could include developing new types of multi-level memories, structures to direct spin waves through specific paths, mainly in low magnetic damping materials, such as Py or Yttrium-Iron-Garnet (YIG), or to fix domain walls that move and could interfere with the desired behavior of magnetic systems of small dimensions.

4. Spin waves in magnetic dots

BROADBAND high frequency response of arrays of triangular Permalloy dots is the focus of this chapter. The dots have been studied under an in-plane magnetic field, applied parallel (buckle state) and perpendicular (Y state) to the triangles base, as well as in remanence, at low fields (vortex state). Micromagnetic simulations identify edge spin waves (E-SWs) as spin waves propagating along different sides of the triangles, depending on the applied field. Under a uniform high frequency field, quasi one-dimensional spin waves are emitted by the triangle vertex magnetic charges and gradually transform from propagating to standing due to interference with those emitted by other vertices. They are weakly affected by dipolar interdot interaction and variation of the aspect ratio. The applicability of such triangles as spin waves devices is explored further via simulations, by creating local excitations at eigenfrequencies. In this way, it is shown that E-SW can propagate long distances and change direction. Their presence also depends on the direction of the applied magnetic field. Different possible spin wave devices making use of E-SWs are proposed, including those which can operate at zero magnetic field, due to exchange bias.

4.1 Introduction

Transport of intrinsic angular momentum of electrons spin over long distances is one of the challenges of magnonics, spin calorics and spintronics.[92–96] Using spin orbit (SO) effects in SO-metal/magnetic insulator/SO-metal structures spin wave (SW) transmission over macroscopic distances has been recently achieved and explained.[97,98] As to metallic structures, the possibility of exciting and manipulating SW has been usually linked with the implementation of low damping materials such as Heusler compounds[99] or $Fe_{1-x}V_x$ alloys[100] and less attention has been paid to searching for new mechanisms for control over SW in magnetic materials already widely used, such as Permalloy. An effective alternative approach could be to explore the control over the SW dimensionality through their confinement to the inhomogeneous edge states that exist in perpendicular to the edge in plain bias field in non-elliptical magnetic elements.[99–101] However, the edge states in rectangular magnetic elements (to our best knowledge the only field configuration where edge states have been investigated so far) are interrupted by the topological magnetic charge.[102] As a consequence, the edge SWs (E-SWs) are suppressed near the element center[101] due to the above symmetry imposed interruption of the edge state.[102]

The possibility to excite and manipulate spin waves by magnetic fields or electric currents has opened perspectives for their implementation in communication and information processing and storage technologies[92,103–105]. Engineering of propagating and standing SWs in magnetic elements, as well as SW excitation and propagation in long strips or other two dimensional magnetic structures[92,102,105], has been a subject of recent intensive applied and fundamental research. Magnetic stripes with spin waves propagating in them

are currently basic elements of magnonic waveguides[92,105]. Very recent studies predict however the possibility of excitation and propagation of a different kind of SW modes, so called edge spin waves (E-SWs) in individual two dimensional magnetic structures[106,107] and extended magnonic crystals[108,109]. It has been suggested that E-SWs are capable of providing new functionalities to spintronic and magnonic devices. These features include an easy modulation of SW spectra by mechanical structuring of the boundaries of the waveguide[106], unidirectional SW propagation, easily channelization, twisting, splitting, and manipulation, in a magnetic field perpendicular to the plane[108,109]. Spin waves have recently been reported to propagate along the edges of long strips with inhomogeneous magnetization[110] when excited by a perpendicular extended antenna. However, these spin waves were found to **spread over the strip at high frequencies** transforming into two dimensional and losing therefore the edge character[110]. Observations of the E-SWs truly linked with the magnetically inhomogeneous edge states remain unclear.

Here we present experimental evidence of excitation and detection of quasi one-dimensional edge SWs emitted by the vertex magnetic charges of magnetic triangular dots. Previous interest in triangular magnetic dots[111–113] has recently been motivated by their **possible implementation as magnetic logic elements**[113] or versatile pinning centers for superconducting vortices[42]. These studies found that the influence of vertex topological magnetic charges diminishes with reduced lateral dimension[113] or with rounded corners[112]. As to the static magnetization distribution inside the dots, micromagnetic simulations and magnetic force microscopy[11,112,113] revealed three main topologically different magnetic states: V (with a vortex core in the triangle center), Y (with magnetic field applied perpendicular to one of the triangle sides) and B (with field parallel to one of the sides) states. Magnetization dynamics has been previously studied by Brillouin light scattering and simulations, in sub-360nm equilateral triangles[11,114] with strongly suppressed vertex magnetic charges. In such small triangles, magnetization tends to be uniform, without many possibilities to have inhomogeneous states as in the larger triangles which will be presented next.

Remarkably, the observed E-SWs are qualitatively distinct from SWs observed previously in quasi one dimensional (1D) magnonic crystals[115], 2D spin wave diffraction[116,117], SW interference patterns from point contact spin torque emitters[67,117–119] or edge waves in non uniform systems[120].

Our findings experimentally confirm a number of recent theoretical predictions[106–109] of the existence of a novel type quasi one dimensional SW propagating along the edges of ferromagnets, magnetic edge states in graphene and other magnetic structures with magnetic exchange energy stored near the device edges.

Gaining an effective control over SWs through their redirection[121–123], multiplexing[124] or data processing[125] is a very active research area nowadays. The global aim is the creation of SW based logic devices[126]. So far, the basic building blocks for SW transmission, redirection and control have consisted in straight or curved ferromagnetic strips[121,123,124]. Such elements transmit information via SW modes which have a restricted frequency range (typically below 9 GHz) and are essentially suppressed after turning (changing direction of propagation) up to 90 degrees or with increasing drive frequency[121,123,124]. This strongly limits the development of redirectional SW logic devices with broadband capabilities.

An effective incorporation of spin waves in data processing requires their transmission and direction control using more complicated structures than just straight micro waveguides - currently among basic elements of magnonic waveguides[127,128]. The capability of changing SW direction opens perspectives for the creation of novel logic elements based on SW interference[123].

4.2 Goals

The work presented in this chapter investigates experimentally and by micromagnetic simulations the broadband response of triangular dots of 1000 and 2000 nm side length and 30 and 100 nm thickness which, being much larger than studied before[11,114], have well defined edge and vortex states. With micromagnetic simulations we are able to identify the modes excited in all magnetic states as spin waves propagating through low magnetic field regions (domain walls in the vortex state, and "quasi" domain walls in the B and Y states, along the triangle edges).
Our measurement setup applies an almost homogeneous excitation to the dots located under the waveguide. Simulating this kind of excitation we will characterize the nature of these spin waves.
To end the chapter, we will present a generalization to non triangular dots of these results, showing that the relevant factor for edge spin waves is the angle between the applied magnetic field and the edges of the structure.

4.3 Sample preparation

Two sets of dots have been studied.

The first set consists of arrays of triangular Py dots fabricated by a combination of e-beam lithography and lift-off techniques on a Si(100) substrate, by Prof. V. Metlushko, at the Nanofabrication Facilies of the University of Illinois, Chicago. The dots in the array are 30 nm thick, have a 1000 nm side length and a 200nm vertical and horizontal spacing between neighbors (figure 4.1). The Py thickness of 30nm forces the B or Y states and suppresses the low field vortex state in a broad range of applied in-plane DC magnetic fields. Magnetic force microscopy (figure 4.2) and magnetization vs. field measurements (figure 4.3) confirm that the vortex state appears only in the virgin samples. Once it is saturated, depending on the field orientation either B or Y states are created in a robust way. Static simulations show that low field V ground state is present in 1000nm side equilateral triangular Py dots with thickness exceeding 50nm.

The array of dots is covered with a gold coplanar waveguide, grown by optical lithography, that generates a high frequency magnetic field (rf field). The CPW is 500 nm thick and consists of a central electrode 30 μm thick, separated of two ground conductors by a $20\mu m$ gap. Two kind of CPWs were designed, one straight, another with a 90° corner, to apply the DC field parallel or perpendicular to the rf field, which is always parallel to the triangles base. This let us study the B or the Y state with certainty.

The second set of dots, grown with by the group of J. L. Prieto, at ISOM, Universidad Politécnica de Madrid, consists of larger arrays of Py triangular dots, this time $2\mu m$ in side length, and of thicknesses of 30 and 100 nm. This last set were grown with the idea of comparing the stability of the vortex state at low fields as a function of the dot thickness.

4.4 Measurements and simulations

In the first set of samples, spin waves were excited with a coplanar waveguide (figure 4.1) which creates a nearly homogeneous in-plane excitation parallel to the triangles base situated above the central conductor (the field points out of plane specially in the gap region, due to the curling of field lines). An about 30 nm thick Si layer protects electrically Py dots from the CPW. The spin wave spectra have been studied at room temperature by broadband vector network analyzer based VNA-FMR technique. The measurements were made using a reflection configuration, that only requires measuring the S_{11} parameter, in

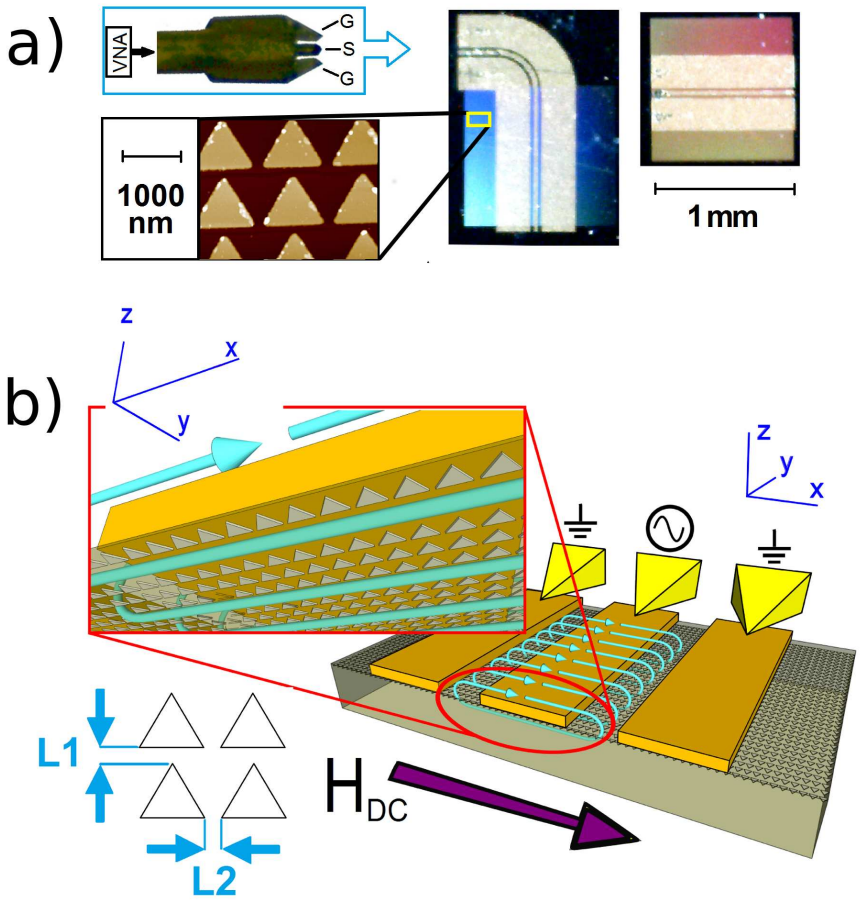

Figure 4.1: *a) High frequency probe and waveguides for the two field orientations. The blue and red/brown squares under the waveguides are the array of dots. AFM topography of some of the triangular dots. b) Depiction of the dots under the CPW, with both AC and DC field.*

which we fix H_{DC} and sweep S_{11} in frequency. This process is done iteratively for different values of H_{DC}.
To extract the dynamic magnetic response from the S_{11} parameter a differential analysis in H can be used, which allows to better observe field dependent eigenmodes and get rid of the constant phase ripple in the VNA measurements and the constant background signal due to cables and connectors. Alternatively, one can also normalize every S_{11} trace by a reference trace (at the highest applied field). This method does not remove the background signal (which degrades in time) as the differential method does but, as explained in section 2.2, the background can be removed artificially if one is careful and knows in advance the typical linewidth of the resonances.
The samples of the second set do not contain a waveguide deposited over the dots but instead consists of larger arrays of dots, to be placed over our large waveguide. In this case, transmission measurements (S_{21} parameter) are made.

Besides the broadband measurements, static and dynamics micromagnetic simulations have been made with OOMMF[16], and afterwards with MuMax3[17] (once we set up a workstation capable of GPU computing with the help of nVIDIA's academic program).

To investigate numerically the magnetization dynamics we use the field pulse - Fourier Transform method explained in chapter 2. The following set of parameters for Py have been used: exchange stiffness $A = 1.4 \times 10^{-11}$ J/m, saturation magnetization $4\pi M_s = 10.43 \times 10^3$ G, Gilbert damping $\alpha = 0.01$, and gyromagnetic ratio $\gamma/2\pi = 2.96$ MHz/Oe. The cell size used is 2.5 nm × 2.5 nm in plane, and 30 nm in vertical direction. To replicate the measurements, a bias field is applied homogeneously to the whole sample to reproduce the hysteresis loops, changing the value of the field step by step every 6 Oe, waiting until the system is relaxed (less than 0.1 degrees per nanosecond at every simulation cell). By tracking the time evolution of magnetization after a short field gaussian pulse for long enough (15 ns in this case), with Fourier Transform the amplitude and phase of the dynamic magnetization at each simulation cell can be obtained. With these amplitude and phase profiles, the time domain oscillation of isolated magnetization eigenmodes can be obtained. Dispersion relation of SWs (i.e. the dependence of frequency of excitations on their wave vector) can be obtained along specific directions using a two dimensional Fourier Transform to the cells comprising some path, during a certain amount of time.

4.5 Results

Charactrization of magnetic states

Magnetic force microscopy data, figure 4.2 b, indicates the formation of the B state at zero magnetic field after saturating the dots in the x direction, which is in qualitative agreement with static simulations.

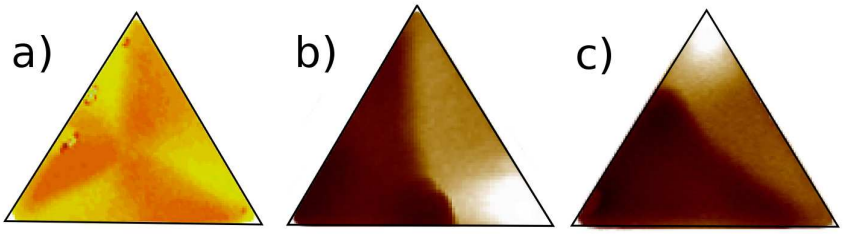

Figure 4.2: *MFM images of a triangular dot. a) Vortex state b) Remanent state after B state. c) Remanent state after Y state.*

Figures 4.2 a and c show MFM images of a vortex state (in a just-grown sample), without having ever applied magnetic field to it, and the remanent state after saturating perpendicular to the base (Y state). The latter is like the remanence of a B state, but rotated 120°. In each of these states edge domain walls (E-DWs) are formed in the close proximity to edges. The excess exchange energy in the B state has the unique topology of a nearly uniform 60 degree domain wall confined between the two vertex magnetic charges (figure 4.9, second row, third column).

Magnetization curves

The magnetization curves shown in Fig. 4.3, top row, were measured at fixed temperatures in magnetic field steps of 10 Oe using a SQUID magnetometer, in colaboration with Dr. Mar García from ICMM CSIC. The field is applied in both directions, parallel to the base (to induce a B state) or perpendicular to it (to induce a Y state).

It can be noted how the magnetization switching is more abrupt in the Y state (field perpendicular to the base). Also, the coercive field is lower in this case (62.5 Oe in the Y

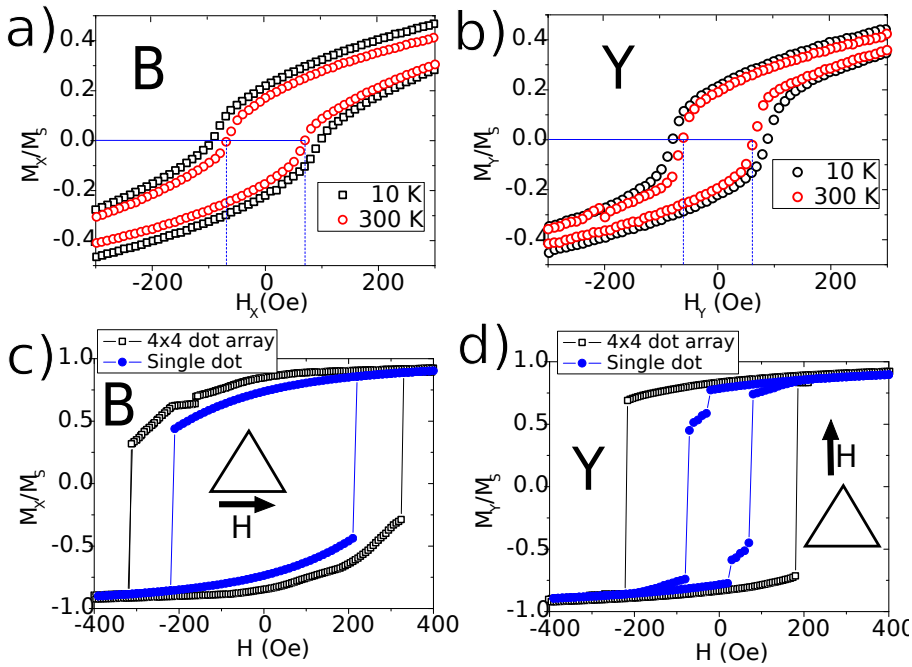

Figure 4.3: *a) and b) Measured hyteresis loops for Buckle and Y state. c) and d) Simulation of the corresponding loops.*

state, compared to 68.5 Oe in B state at $T = 300$ K; 83.5 Oe in the Y state compared to 97 Oe in the B state at $T = 10$ K). Our interpretation, suported by simulations, is that this is due to shape anisotropy, figures 4.3 c and d, since the inclined sides of the triangle favor more strongly the magnetization alignment perpendicular rather than parallel to the base. The measured, figures 4.3 a and b, and simulated, figures 4.3 c and d, hysteresis loops show some differences, mainly the "steps" present in the simulation, compared to the continuous change in measurements. It should be noted that the experimental measurements are performed on an array with hundreds of thousands of dots (possibly with small fluctuations in shape from one dot to another). Therefore a large averaging of the switching fields of different triangles provides the smooth shape of SQUID measurements. In contrast, in the simulations, due to limitations of time and computational capabilities, both a single dot and a 4x4 array of dots are simulated. Periodic boundary conditions could help to simulate the interdot interaction quicker, but one needs to be careful, since the real array is not infinite and some dots do not have a neighbor (and therefore, they can be expected to have a slightly different behaviour), but especially in the case of the Y state because, as will be shown later, neighbors affect each other much more than in the B state.

While in the measured array of dots there can be a distribution of switching fields, in the simulated array all dots switch at the same field. Also, in the measurements, the external field changes in a matter of seconds, much slower than the typical relaxation time of magnetization (ns), and changes in magnetization easily and smoothly follow changes in field. On the other hand, in simulations, the external field is changed in step-like instantaneous jumps. Each of these jumps excites dynamic magnetization precession in a broad frequency range that is damped out after some nanoseconds (this is the main cause of the large computational time). These jumps, at fields close to reversal can trigger it, as opposed to the measurement case where, at least, the large self inductance of the electromagnet guarantees that field changes are not instantaneous. Another source of some

discrepancy is that simulations do not consider the effect of temperature. As measurements show in figure 4.3 a and b there is a decrease of total magnetization at higher temperatures due to thermal excitation of spin precession. This effect is not included in simulations. In any case, it can be seen that in the Y state, at high fields both branches (reducing and increasing field) get closer, due to shape anisotropy. As will be discussed later, interdot coupling is more important in the Y state, and simulated hysteresis loops show this, being much more similar the hysteresis loops for a single dot and for a 4×4 array of dots in B state than in Y.

Static magnetic states

Next, the three possible magnetic states in micron size triangular dots are recalled:
Vortex state: The V state appears at low fields and in plane fields easily annihilate it. Three domain walls connect the vortex core to the vertices. In our 30 nm dots vortices exist only before saturating the sample, but dots thicker than around 50 nm can recover the vortex when lowering the field (section 4.5).
Buckle state: An in plane magnetic field parallel to one edge of a triangle orients magnetization parallel to it everywhere except the two other edges (where magnetization tries to follow the border). The transition region between close and far from these borders creates some exchange "channels" with an excess of exchange energy through which SWs can propagate. Previous works[11,114] have not identified these confined waves because too small triangular dots were considered and this transition regions close to the edge spanned across the whole dot.
Y state: If the magnetic field is applied perpendicular to one of the edges, an exchange "channel" will appear along this side, with a node separating it in two halves.

High frequency response

Figure 4.4 presents the magnetic field dependence of magnetic dynamic permeability measured in the B state, a, and Y state, b, sweeping the static field from positive to negative values. For the B state well resolved spin wave modes show a continuous dependence on the magnetic field nearly down to small (100-200 Oe) field regions, when a domain wall (in the y direction) separating the dots in two domains is formed (figure 4.9, first and second rows, first column). The observed eigenmodes that are roughly evenly spaced from each other correspond to E-SWs along the edges. Given two consecutive eigenmodes, the one with higher frequency corresponds to a wave mode with an extra node of oscillation (compared to the eigenmode with lower frequency) between the two vertices that confine the E-SW (see below). The abrupt magnetization inversion of the triangular dots can be noted in the nonzero negative field (-70 Oe) at which the resonances change from decreasing to increasing in frequency with the decreasing applied field. Apart from this, the modes are nearly symmetric at positive and negative fields. As for the spin waves in the Y state, some of lowest lying modes, however, show a qualitatively different dependence, with discontinuities of the lowest mode frequency with H_{DC}. Dynamic simulations qualitatively reproduce the main observation for the B state and remain practically unaffected by dipolar interactions. As we shall discuss further below, the interdot interaction is mostly relevant for the Y state. Some shift towards higher frequencies (of about 1 GHz) observed in the simulations with respect to the measured eigenfrequencies could be due to the following factors: (i) the saturation magnetization of the Py triangles at room temperature could be smaller than the value used in the simulations done at zero temperature, (ii) the absence of defects in the simulations, and (iii) some difference in the value of damping.

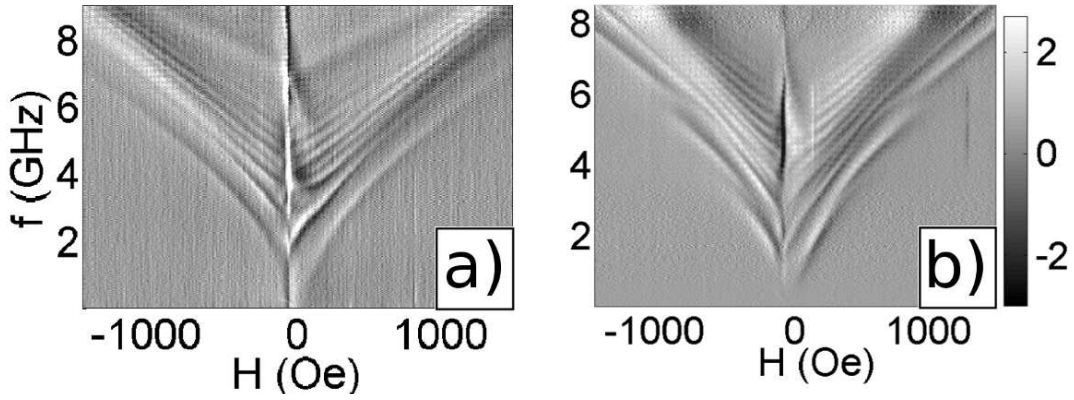

Figure 4.4: *Measured high frequency spectrum of the 30nm thick, 1μm long, magnetic triangles. a) B state. b) Y state. Both plots show the derivative of U with respect to H.*

Following the FFT method described in section 2.3, this first set of simulations used to obtain the frequency spectrum relies on a uniform external excitation of the sample. As we shall explain in more detail in what follows, two main observations will be made:

- A uniform excitation by a short pulse in triangles in the B state produces, after FFT analysis, what looks like standing waves along the two edges inclined with respect to the bias field. These standing waves however, are more standing in the center of the edges, while they propagate at the vertices.
- A local excitation sheds some light on what is really happening in the case of uniform excitation: when exciting a small area in one of the edges (for example, a vertex) with an *ac* field at an eigenfrequency, plane waves propagate uninterruptedly (although experiencing damping as the wavefront advances), until some defect (such as another vertex) is met, which will scatter the wave. Then, this clarifies what happens in the case of uniform excitation, where all cells are excited at once: the pulse generates waves everywhere, and for each eigenfrequency they propagate away from the source while they are damped out. The vertices have the larger amount of exchange energy, and that acts as the stronger source of edge spin waves of the whole dot.

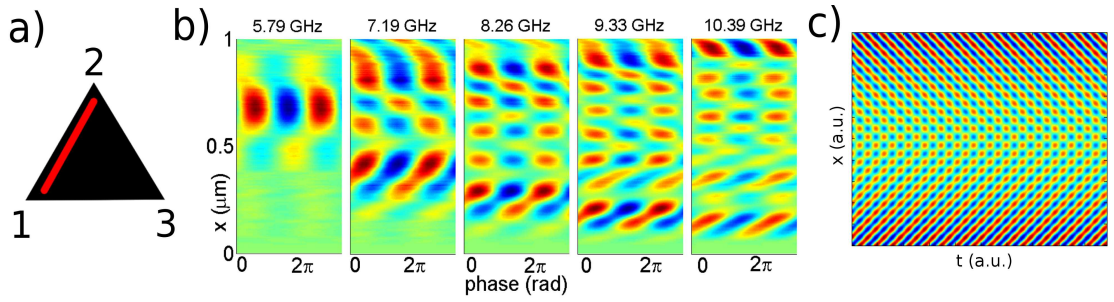

Figure 4.5: *a) The line indicates the cross section where the time evolution shown in b) was considered. b)Time evolution of spin waves excited by a uniform field at the edge of a triangular dot for different frequencies. c) Numeric calculation of the sum of two amplitude decaying waves that propagate in opposite directions.*

Waves excited in vertices will move away from them, and try to reach the neighbor vertex connected by an exchange channel. In the region between two vertices, the waves emitted by each vertex have been damped by approximately the same amount (since both

vertices are at approximately the same distance from this central region. This gives raise to interferences that appear as standing waves. On the other hand, waves appear as propagating near the vertices. This is so because the waves excited in a vertex have not been damped down yet much, while the waves from the neighbor vertex have propagated through the whole edge to get to the first vertex, thus being much lower in amplitude. The interference of these two waves cannot produce standing waves, since one of them is much weaker than the other, and the overall wave looks as propagating.

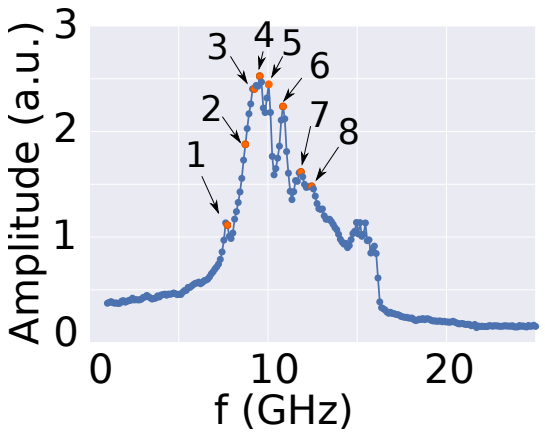

Figure 4.6: *Simulated high frequency spectrum of a 2 µm side, 30 nm thick Py dot in the B state.*

In the B state, we note that these E-SWs gradually transform from propagating (near the vertices) to standing (close to the middle of the triangle side) due to interference of the spin waves with decaying amplitude, emitted by two coherent vertex emitters. Figure 4.5 b presents a typical time evolution of the oscillations along a triangle edge (part a) in the B state, where the interference patterns reconstructed for different SW modes confirm a transformation from the propagating to standing E-SWs. This is seen when uniformly exciting the dot with only one of the eigenfrequencies found with the FFT method. In part c of the figure, the interference of two amplitude decaying waves $(A \cdot \sin(kx \pm \omega t))$ that propagete in opposite directions is shown, which has qualitatively equal properties to the E-SWs in b.

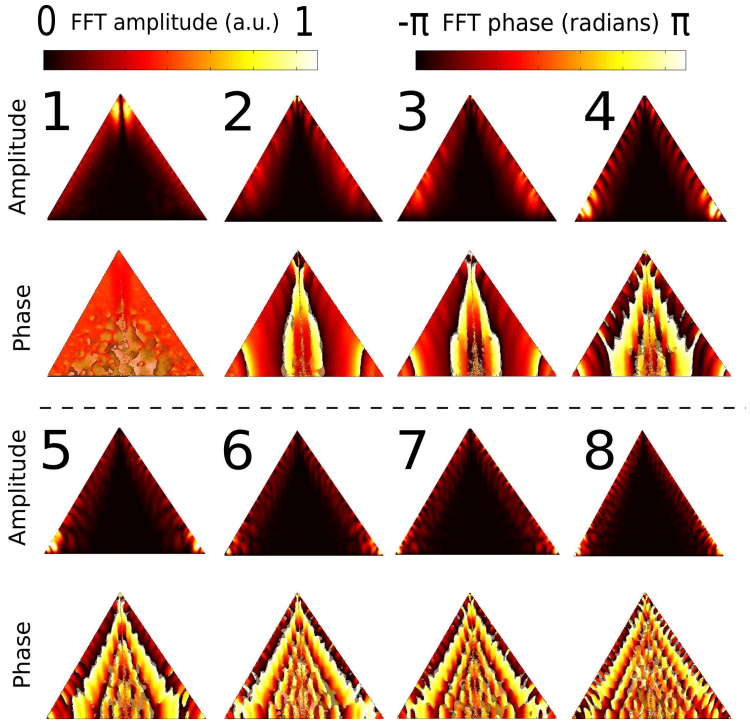

Figure 4.7: *FFT Amplitude and phase profiles of the eigenmodes in the B state, marked with orange circles in figure 4.6.*

An independent way of confirming this is by looking at the spatial distribution of the FFT phase, where close to the vertices the changes in phase (it goes from π to $-\pi$ in the color scale) are more gradual, something that characterizes a propagating wave, while far from them, we see abrupt changes, which indicates that cells close to each other oscillate in oposition of phase, something typical of standing waves (for example, the last modes shown in figure 4.7, last row).

The observed E-SW modes are qualitatively similar to recently reported string-like excitations along topologically pinned domain walls in the metastable double magnetic vortex state (the so called Winter's magnons). The main difference is that in the present case the SW confinement is imposed by the sample boundary and the relative direction of the external magnetic field, while Winter's magnons propagate inside circular dots along topological domain walls pinned in between magnetic vortex cores and half edge antivortices[6].

Also, the magnetic moments at each side of these domain walls are at an angle of 60°, and not 180°, as it was the case in the circular dots in the double vortex state. We have also investigated numerically the possible influence of the variation in the aspect ratio of the triangular dots on the edge spin waves in the B state. Dynamic simulations reveal qualitatively similar E-SWs excited in isosceles triangles with base and height equal to 1000nm (figure 4.10). This demonstrates a sufficient stability of the E-SWs along the edge states to small variation of the lateral dot parameters.

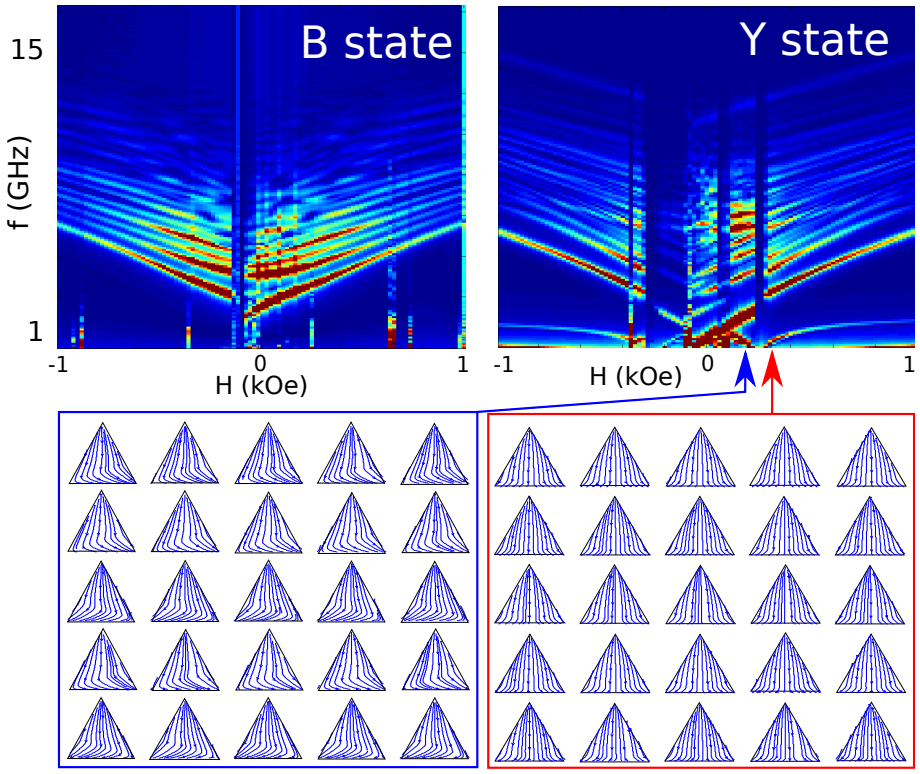

Figure 4.8: *Top row: simulation of the B and Y state as a function of applied magnetic field and frequency. The color scale is the amplitude of $FFT(m_x)$, in arbitrary units. Bottom row: the magnetization state of the dot array, represented by streamlines, at the fields indicated by the red and blue arrows, right before and after a discontinuity in the lowest eigenfrequency.*

Finally, in order to further corroborate the validity of spin wave identification (figure 4.9) we have analyzed in more details the influence of dipolar interdot interactions on the

observed E-SWs by comparing the distribution of exchange energy inside the dots and the stray fields obtained for single dots with those located inside a 4x4 dot array with the same spacing as those studied experimentally. Figure 4.9 summarizes the main observations for the B and Y states by representing the simulation results for a few selected fields. We have found that the topology of the E-DWs in the B state remains qualitatively unchanged when the interdot interaction is switched on (upper half in figure 4.9).

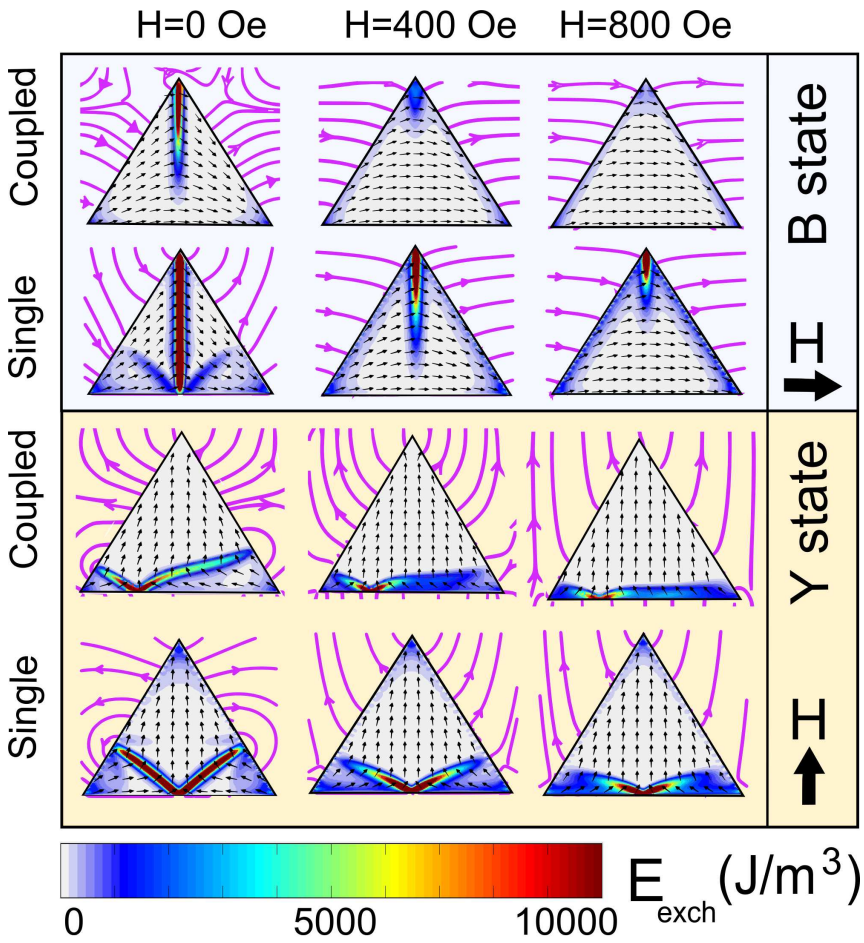

Figure 4.9: *Simulation of laterally coupled (first and third rows) vs uncoupled dots, in the B state (first two rows) and in the Y state (last two rows). Different applied fields correspond to the different columns). The color scale is the exchange energy density, and the streamlines represent the direction of the applied field. Black arrows represent the $\vec{M}$ direction.*

These simulations for couping between neighboring dots are time consuming, and adding new rows and columns of dots rapidly increase the simulation time. Once we had access to faster simulations with MuMax3, we were able to simulate the whole excitation spectrum of a 5x5 array of triangular Py dots as a function of magnetic field (figure 4.8), instead of just the static states, using the pulse excitation method (as a remark, these simulations took a week to complete, each, with 2400x2400 simulation cells). After calculating the spectrum at every individual static field, and arranging them together, we reconstruct with good qualitative agreement the measurement results in figure 4.4. It is particularly interesting how the discontinuities in the lowest frequency modes of the Y state are also present, whereas they do not show up in the B state. Using periodic boundary conditions did not prove to be very useful for getting the discontinuities, it appears to

be an effect that generates at the boundaries of the array, and propagates from there to every dot by interdot interaction. At low fields, in this way, we observe how the direction of magnetization changes from row to row, but due to symmetry, large arrays would have an average value $< m_x >= 0$. Figure 4.8 shows a comparison of the simulation of the m_x amplitude spectra of both states, in arbitrary units. In the bottom row a streamline plot showing the magnetization direction of every dot in the array is provided, both before and after a discontinuity in the lowest frequency mode as a finction of field. One can easily see a different type of magnetic state, since at low enough fields, the discontinuity in the exchange channel typical of the Y state is not present yet. As the field is increased, it will move from one of the vertices in the triangle base towards the center. At low fields, then, the same state as the one measured with MFM in figure 4.2 c. The discontinuity in the modes corresponds to the "depinning" of this defect from a triangle vertex.

These results, added to the variation of the aspect ratio (figure 4.10) in the B state further manifest the robustness of the observed E-SWs. The edge states in the Y state, however, are much more strongly affected by dipolar interaction (lower part in figure 4.9). Seemingly, the main reason of the stronger influence of interactions in the Y state is the capability of a dot upper vertex to displace off the center the bottom E-DW unpinned magnetic charge of the dot above it, thanks to the stray field this vertex generates. This possibility is evidently absent in the interacting B state dots which have only vertex (pinned and dipolar coupled) magnetic charges.

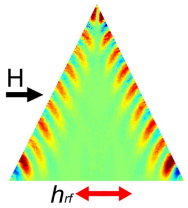

Figure 4.10: *Spin waves in an isosceles triangular dot.*

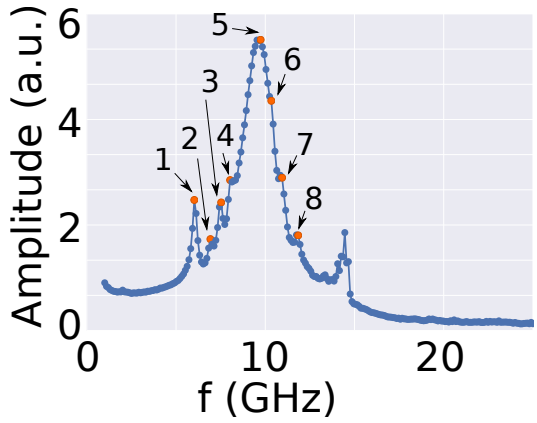

Figure 4.11: *Simulated high frequency spectrum of a 2 μm side, 30 nm thick Py dot in the Y state.*

Spin waves similar to those in the B state can be obtained in the Y state, but only along the side perpendicular to the bias field. As already mentioned, to keep the symmetry in the Y state, the exchange channel at this specific side of the dot has a node where exchange energy is minimum, separating the channel in two halves. SW propagate parallel to the border, as always, but with opposite wavevector in each half under a uniform excitation. Other spin waves can be observed in the highest frequency modes outside the exchange channel, propagating in vertical direction, figure 4.12. Similar to the B state, a shift to higher frequencies at higher fields is present in simulations. In this case, unlike in the B state, higher frequency modes are not always harder to detect. The reason for this is that modes in this case are not confined only to the base of the triangle, but also extend to the rest of the dot, and the coupling of SWs to the rf field is not lower at higher frequencies, as in the B state. This happens because the high frequency excitation is always parallel to the base of the triangles, and this means a maximum torque in the central region of the dot in the Y state, and a minimum torque in the B state.

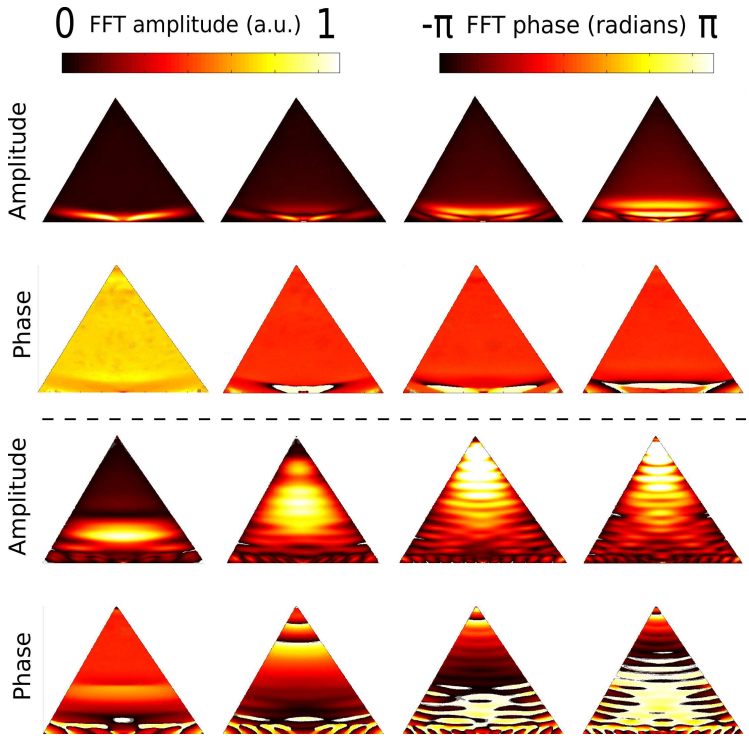

Figure 4.12: *FFT Amplitude and phase profiles of the eigenmodes in the Y state, marked with orange circles in figure 4.12.*

Dispersion relations

Next, a different type of analysis of the simulated spin waves is presented in the form of dispersion of the E-SWs propagating along the left side of the triangle situated between vertices 1 and 3 (figure 4.13). We found that both the space-time and wavenumber-frequency representations point out some spatial E-SW asymmetry which could be linked with contribution of the secondary spin waves reflected from the vertical domain wall separating the dot in two halves at not very high fields, as well as the presence of this wall in vertex 3, while vertex 1 remains unaffected by it. Here the positive $|\vec{k}|$ vector branch corresponds to the SWs emitted by vertex 1 while the negative k branch describes E-SWs emitted by vertex 3 in the direction to vertex 1. The predominantly 1D character of SWs along E-DW in the B state is also corroborated by their approximately parabolic dispersion relation. Indeed, the exact solution for the spin waves in a 1D ferromagnetic chain predicts a parabolic k dispersion[129], valid except in the region of $|\vec{k}| \to 0$ where dipolar contribution dominate. The spin wave dispersion in one-dimensional bi-component magnonic crystal waveguides, as investigated by micromagnetic simulations[130] also shows a parabolic form, but is interrupted by the band gap due to imposed underlying periodicity. The dispersion curve of the spin waves excited along the non uniform E-DW in the Y state (figure 4.14 c) is more complex.

Dispersion relations can be calculated from numerical simulations using 2D Fourier Transform along the desired path. Figure 4.13 shows an example for dispersion relations of SW propagating through an exchange channel in the B state at a bias field of 1000 Oe. The parabolic shape corresponds to spin waves along the path drawn in yellow in the inset sketch. Positive $|\vec{k}|$ represents the waves propagating from the bottom left vertex to the upper vertex, and the opposite applies to negative $|\vec{k}|$. The non symmetric dispersion curve (more intense in positive $|\vec{k}|$) shows that waves propagate more easily towards the upper

vertex than from it. This is due to the difference between the two vertices, the upper one having half of its magnetic moments pointing up and right, half of them pointing down and right, whereas the bottom left vertex has all its moments pointing up and right, and is a more robust emitter of SW.

Also, when the path for calculating the dispersion relation includes the corners, a low frequency mode, independent of k appears. This kind of mode has already been observed in other situations[131] and it represents localized modes at the edges. Not including them in Fourier Transform, as in Fig. 4.13 b, removes the presence of this mode, but not the rest. Why the localized mode is represented as a mode that exists at all wavenumbers, but doesn't change its frequency can be intuitively understood if we think of an analogy of the real and reciprocal representation of a "pulse" function. In real space, a pulse is confined in a narrow region, but to achieve that shape, the corresponding reciprocal representation must include frequencies spread over a large range so that, given enough Fourier components of the correct weight, the pulse shape can be reproduced with an inverse Fourier Transform. The same thing happens here. A localized mode that only exists in the vicinity of a vertex requires a spectrum with components of many different wavenumbers.

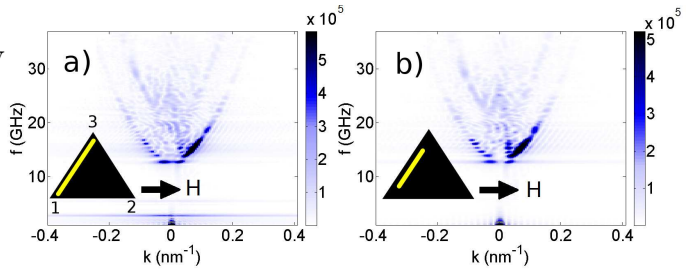

Figure 4.13: *Simulated dispersion relation of SW in the B state at H=1000 Oe. The inset sketch shows the path (yellow line) along which the dispersion relation is calculated. Colors represent the FFT power (a.u.). In a) the vertices are included, whereas in b) they are not. A localized low frequency mode present only in these vertices is observed at around f=2.5 GHz.*

Figure 4.14 considers other cases of interest. Figure 4.14 a considers the case of an isosceles triangle in the B state. Everything remains qualitatively equal to the case of the equilateral shape, and SW propagate likewise through exchange channels. In figure 4.14 c SW propagate in the Y state along the base exchange channels, or in vertical direction, in figure 4.14 b. For both, there is not such a clear distinction between positive and negative values of $\vec{k}$.

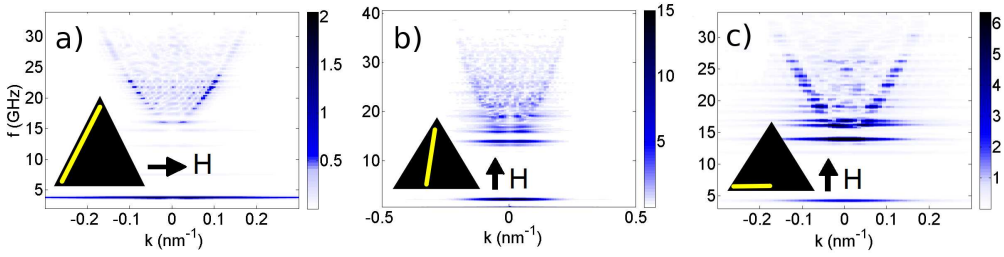

Figure 4.14: *Simulated dispersion relations for a) an isosceles triangle in the B state (H=1000 Oe), along an exchange channel; b) equilateral triangle in the Y state (H=1000 Oe), for vertical SW; c) equilateral triangle in the Y state (H=1000 Oe), along the exchange channel in the base (from the central node to the vertex). Colors represent the FFT amplitude (a.u.)*

Factors which could affect the real device operation

The following factors could influence E-SW based operation of the real devices. Our simulations do not take into account the possible influence of the edge related structural disorder. It could vary locally the magnetic damping. Local changes in the damping (for example due to changes in the conductance close to the film edges) is among other possible factors probably to take into consideration in the propagation of edge spin waves.

Further studies should also verify the influence of the finite temperature, of the additional damping due to coupling to the substrate and other factors on wave propagation. One possible way to improve the applicability and functioning of the E-SW based communication devices would be to fabricate them using YIG films instead of metallic Permalloy, taking advantage of dramatic reduction of damping in these insulating ferromagnets. As to the need for the application of an external magnetic field, its role in the creation of the B state could be played by an exchange bias field, produced by growing the triangles over an underlying antiferromagnetic film. Figure 4.15 shows simulations of hysteresis loops of a triangular dot placed over a layer of fixed spins, which represent an antiferromagnet. Different exchange couplings between the two layers shift the hysteresis cycle to higher or lower fields, so that be B or the Y state could be achieved at zero external field using this method.

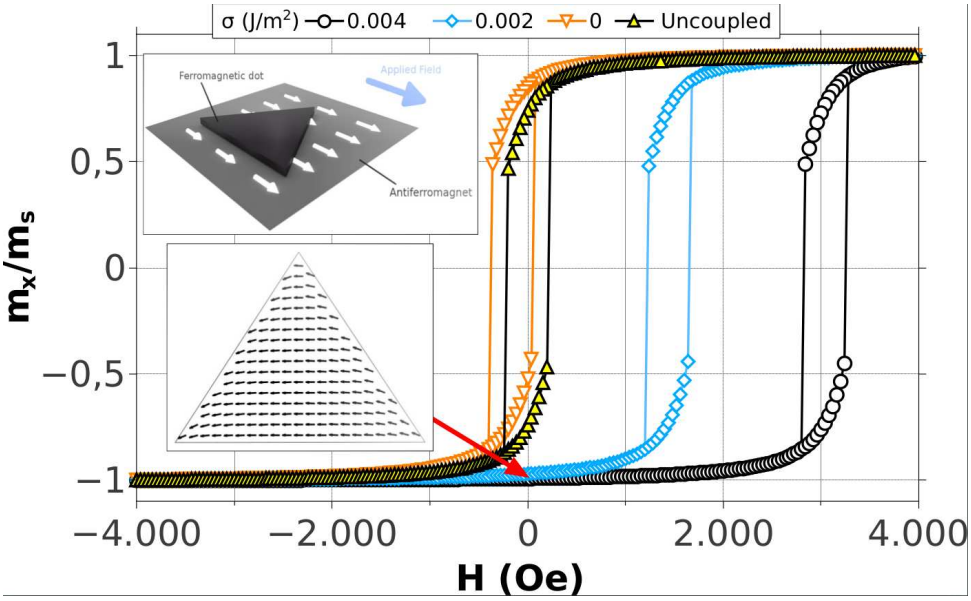

Figure 4.15: *Simulated hysteresis loops for a triangular dot in the B state with different values of exchange bias due to the coupling to an antiferromagnet.*

Spin waves in the vortex state

To study spin waves in the vortex state, a different set of Py triangles has been considered. In this case, the triangles are 2μm in side length, and two different samples have thicknesses 30 and 100 nm. Historically, apart from the vortex state, we decided on studying samples twice as large in lateral size because, for the purpose of transmission of information with edge spin waves, it is interesting to check if they can propagate through distances as long as possible. Therefore, it makes sense to go to larger magnetic elements.

The 30 nm dots are expected to have a weak vortex state, unable to show up during the reversal process. However, the thicker the dot is, the more likely it is to have a vortex state during reversal. The results concerning this will be shown next. Figure 4.16 shows the resulting absorption spectrum of the array of 30 nm dots with the applied field parallel to the triangles base (B state). Picture b is the derivative of a, which allows to observe better the different modes. The spectrum looks similar to that shown previously, in figure 4.4, with several branches evenly spaced and symmetric with respect to $H = 0$ (with a small asymmetry at low fields due to reversal at slightly negative fields.

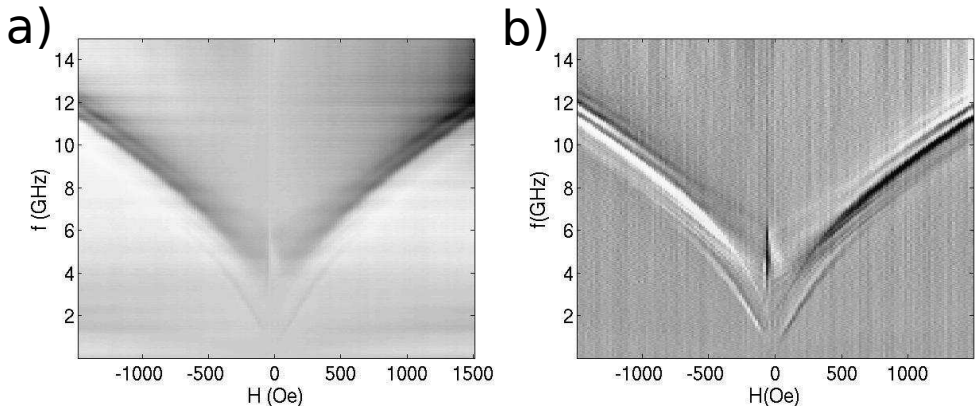

Figure 4.16: *Microwave absorption spectrum of 2 μm, 30 nm thick triangles in the B state. b) is the derivative of a) with respect to field.*

Figure 4.17 shows the same analysis for the 100 nm thick dots. One can clearly see the difference with respect to the case of 30 nm. At low fields the modes corresponding to E-SWs disappear. The field at which different modes disappear coincides with other type of modes, that intersect them.

As in the case of 1 μm dots, the modes of the Y state are slightly different from those of the B state (figure 4.18). Still, at low fields there seems to be a change of magnetic state, since there are again vortex like modes (in the 100 nm thick dots). In general, with our setup the Y state had a weaker signal than the B state, specially for the case of 30 nm (not shown). Interestingly, in the B state, the highest frequency modes become stronger at higher fields, whereas in the Y state they seem to have a constant intensity at all fields. Our interpretation is the following: The microwave magnetic field is always parallel to the triangles base. The DC field is parallel to it in the B state case, whereas it is perpendicular for the Y state. Therefore, in the case of high fields, when the dots are strongly saturated, the Y state has the optimum conditions for a strong torque (DC and *mw* fields perpendicular), and the B state would have zero torque (both fields parallel). For the field region we are studying, this is not the case, since the dot edges bring magnetization parallel to them. Thus, the two sides which are not the base are the only part of the dot which suffer a torque in the B state, while almost the whole dot suffers a torque in the Y

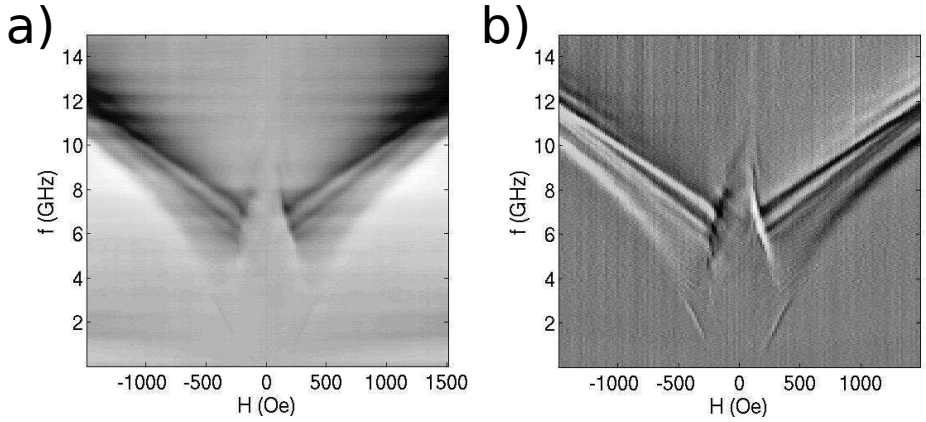

Figure 4.17: *Microwave absorption spectrum of 2 μm, 100 nm thick triangles in the B state. b) is the derivative of a) with respect to field.*

state for all fields. In the B state the region that concentrate spin waves gets narrower at high fields (see also figure 4.24 for the general case). The narrower these zones are, the more able they are to carry spin waves of higher frequencies (until they vanish at too high fields). Then, the modes will have a certain span of fields, and modes at higher frequencies would be at higher fields, unlike in the Y state, when they are always present.

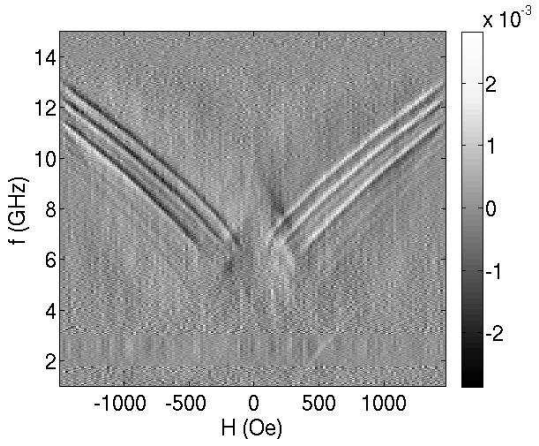

Figure 4.18: *Measured spectrum of 100 nm thick, 2 μm in side, triangular Py dots in the Y state.*

Simulations

The interesting thing of the vortex state in triangular dots (and in general in polygonal dots, but specially in triangular) is that there are very obvious domain walls in predictable locations. They link the vortex core at the center (with zero field) to the vertices. Circular dots could be considered as a limit case of a polygon with infinite sides, therefore infinite domain walls that would merge with others close to them, to end up with no domain walls in practical terms, but a smooth rotation of magnetization. In the metastable double vortex state, there were domain walls, but they were easily lost under external perturbations if pinning is not very high. Triangular dots offer an excellent opportunity to study Winter's magnons in a confined system without the need to apply magnetic fields. Next there are some figures presenting results of MuMax3 simulations of vortex state dynamics in triangles 100 nm thick.

Figure 4.20 shows the amplitude profiles of the first twelve modes found in simulations with zero applied field, along with their corresponding phase profiles. The corresponding

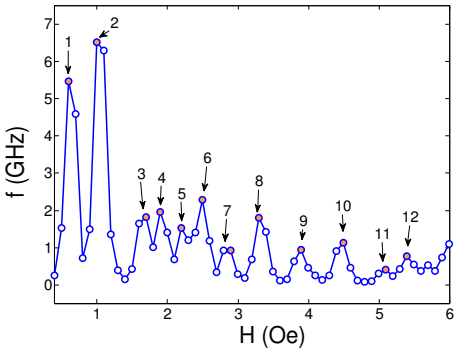

Figure 4.19: *Spectrum of vortex state at* $H = 0$.

eigenfrequencies are those marked in orange dots in the spectrum of the vortex state at zero field shown in figure 4.19. Figure 4.20 is obtained by the Fourier transform of the z component of $\vec{M}$. It is easy to see that at each mode has a node more than the second, in the same manner as standing waves in a string. The first mode is the gyrotropic mode, corresponding to the movement of the vortex core as a whole, around its equilibrium position. The phase gives very important information, allowing us to know what parts of the dot oscillate in phase, or in opposition of phase. For example, a region where the phase smoothly transitions means that waves there will propagate. On the other hand, a region with an abrupt change in phase represents standing wave like behavior, with two areas next to each other oscillating in antiphase. Then, there is no wave propagation, just standing oscillations. All this amplitude and phase analysis is especially useful for structures under uniform high frequency fields, where interferences from different excited regions occur (since we excite the whole dot at the same time). This type of analysis however is not that useful if we only apply an excitation signal in one region, and observe how it propagates throughout the dot, since no excitations from different parts of the dot will interfere to create standing waves. In any case, the pulse method is useful for finding the eigen frequencies quickly.

Local excitation of spin waves

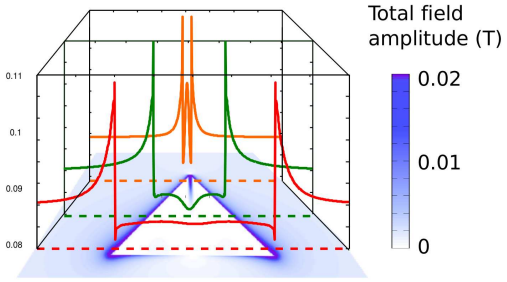

Figure 4.21: *Total field in a triangular dot (L=1*μ*m, t=30nm). The color lines are cross sections of the color plot, as indicated by the dashed lines.* $H_{DC} = 1000$ *Oe*

The presence of E-SWs, and their change in frequency with the applied magnetic field, was demonstrated[132], with a direct excitation of the edge spin wave modes in a broad frequency range. Using a parallel pumping scheme (with homogeneous microwave field being parallel to H_{DC}), in contrast to previous studies of the edge modes[133], ensures that the excitation of the uniform mode inside the device is minimum (due to minimum torque exerted). Another important differentiating factor is that, for triangular dots the edge modes could be excited locally, close to the edge, facilitating their propagation along the edges. Another way to interpret the exchange channels is to look at the local distribution of total magnetic field (figure 4.21). Here we can see how at the edges containing these exchange channels, a strong drop in the total magnetic field occurs. These drops act as potential wells which

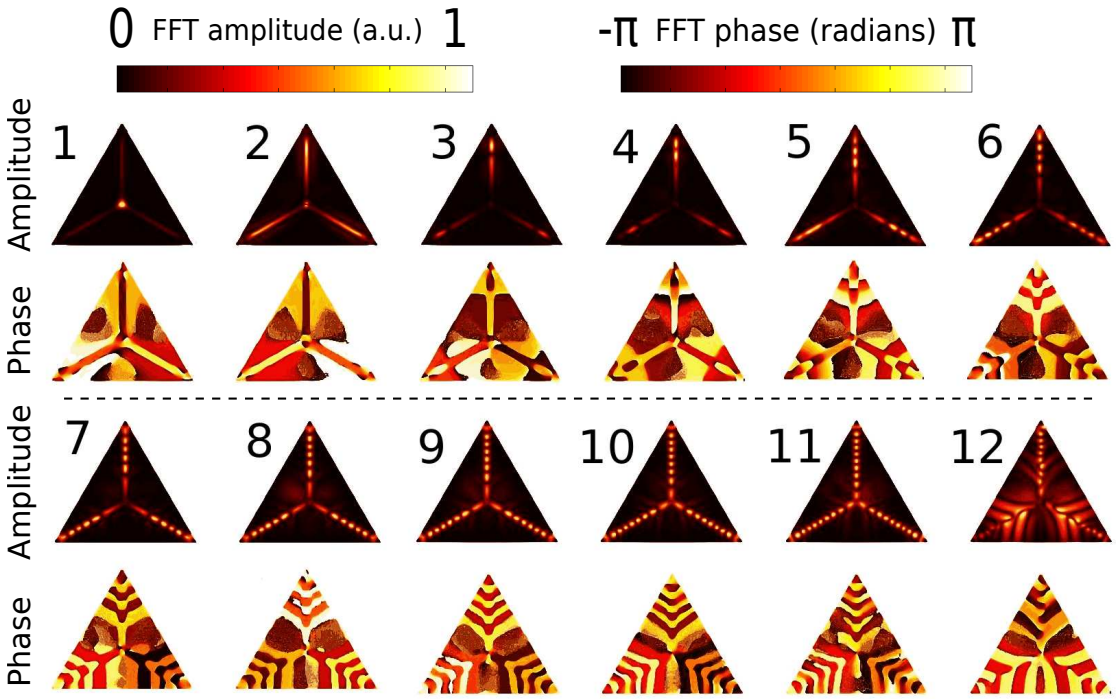

Figure 4.20: *Amplitude profile of m_z for the first 12 modes of vortex state (first and third rows). Below each amplitude profile, the corresponding phase profile (second and fourth rows).*

confine magnons. The color scale is total field, and the lines are cross sections at the locations indicated by dashed lines.

Magnetic charge in the upper vertex

In the B state there is an excess of exchange energy in the upper vertex, typically of wider spatial span than the exchange channels next to the edges of the triangle.

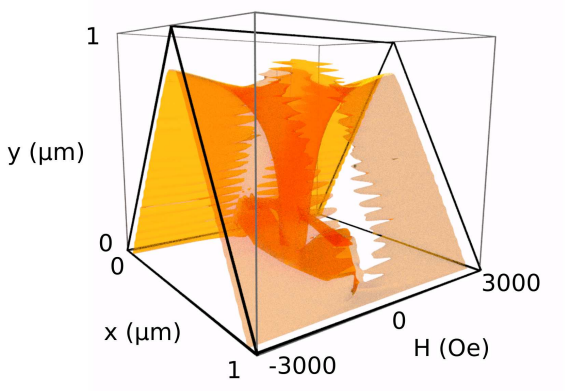

Figure 4.22: *Exchange energy density isosurface at 400 J/m^3, as a function of the in plane spatial coordinates and the applied field.*

The size of this magnetic structure can have an impact in how well spin waves coming from one of the bottom corners transfer to the other side of the upper corner, towards the other bottom corner. Figure 4.22 shows a simulation of an isosurface at a density of exchange energy of 400 J/m^3, as a function of the applied field, and the spatial coordinates in the plane of the dot. Transparency has been added to the isosurface for better appreciating

its field dependence. The central defect reaches the lower side of the triangle at low fields, and also two aditional protuberances appear in diagonal direction. These already appeared in figure 1.11, as a result of the non uniformities that the magnetization distribution adopts at low fields. The central charge (around x=0.5 μm) shrinks at high fields, regardless of the field sign. This explains that the transmission of spin waves through the upper vertex of the triangle gets more unlikely, not only because the whole exchange channels at the edges contract, but also because the exchange energy at the upper vertex also gets reduced. The physical reason for this region to accumulate more exchange energy than the rest of the edges is that it is surrounded by edges on both sides, unlike the exchange channels in the rest of the dot. Therefore, the magnetization there is more pinned by the demagnetization energy, which requires a stronger external field to align parallel to the base. Thus, the stronger gradient in exchange energy.

Generalization to other shapes

Next we demonstrate that edge spin waves are not specific to magnetic triangles, but could be excited along edges of magnetic strips too when a quasi homogeneous DW is created along the device edge.

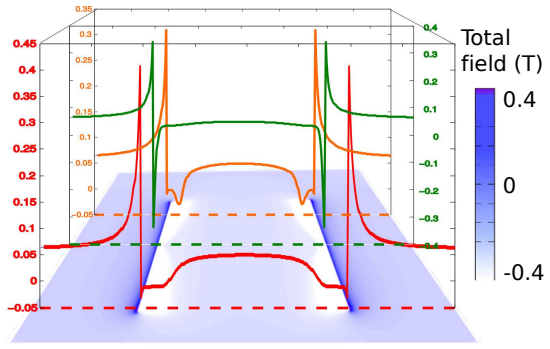

Figure 4.23: *Total field inside a square magnetic dot with field applied parallel to two of its faces. Color lines are cross sections at the positions marked by dashed lines.* $H_{DC} = 1000$ *Oe*

In order to excite spin waves along the edges of a magnetic strip, contrary to the usual practice, the applied magnetic field should not be perpendicular to the strip direction, but tilted at an angle in order to eliminate the possibility of the "butterfly type" interruption in the centre of the exchange energy channels, and which naturally appears in the Y state in triangles, when the external magnetic field is perpendicular to one of the sides. For an arbitrary geometry in magnetic nanostructures (as long as they are not too thin, which would force all the magnetization to lay parallel to the edges), an external field which is inclined with respect to the edges results in uninterrupted exchange channels that can be used for propagating spin waves, with the feature of being able to overcome corners. These corners typically act as receivers of spin waves, that re-emit them, since corners normally entail an increase of exchange energy around them.

Figure 4.24 summarizes our results on the generation of E-SWs in a 30 nm thick Permalloy strip with lateral dimentions of 1 by 0.5 μm. Our simulations show that for the chosen geometry the most homogeneous E-DW show up when in plane magnetic field is inclided to about 27° with respect to the vertical to the **long side of the strip**. Some of these simulations have been made with the help of Javier Robledo, during his undergraduate final project.

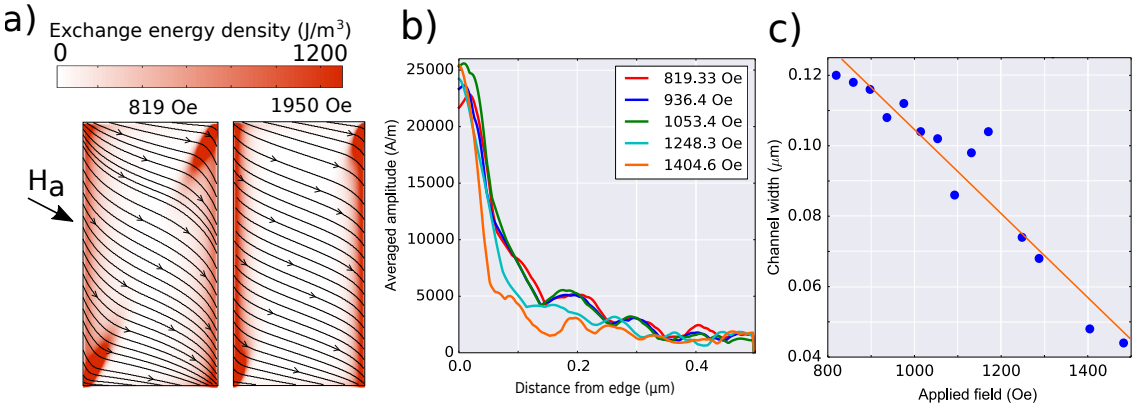

Figure 4.24: *Simulation of rectangular Py dots. a) Exchange energy density at two different applied fields. b) Amplitude of edge spin waves (averaged over the vertical side of the rectangle) vs distance from the edge. c) Width of the exchange channels vs distance from the edge.*

4.6 Scanning Microwave Microscopy

As mentioned in chapter 2, during a three month stay at NIST laboratories in Boulder, USA, the author of this thesis worked in a joint effort to try to visualize spin waves for the first time with the Scanning Microwave Microscopy (SMM) technique for the firts time. This technique, which has been in used for only a few years a the time of writing this thesis, has been mostly used so far to study the response of semiconductor materials and nanostructured systems like nanowires, in the GHz range of frequencies, at the local scale[134,135]. What follows is an attempt to use it to detect and visualize spin waves in confined magnetic systems. These preliminary results have been presented in the MMM Conference 2016[136]. As explained in chapter 2, this technique combines the spatial resolution of an AFM with the capability of performing high frequency measurements of network analyzers, by using a special AFM tip which also acts as an antenna, to locally excite the sample with a high frequency signal.

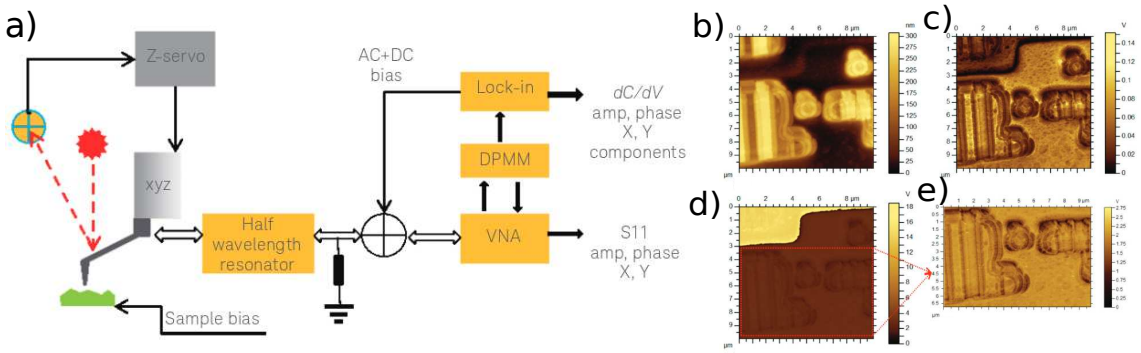

Figure 4.25: *a) Schematics of the DPMM connections to the SMM system. b) Topography of a Si integrated circuit with dopants c) dC/dV amplitude with DPMM d) dC/dV phase e) Zoom of indicated area in d)*[137].

The sample is placed over another antenna, with a coplanar waveguide structure. Then, one has the option of trying to detect the reflection of the signal emitted by the AFM tip, or to transmit it from the tip to the antenna, or vice versa, from the antenna to the tip. These last two options seemed to be the most promising, and we dedicated most of the time of the stay to them. A challenge that is never faced with the traditional

FMR measurements with a sample placed onto a waveguide is that in this case, the high frequency signal emitted by one of the antennas (the tip or the waveguide) must go through the substrate of the sample, so that it can be picked up by the other antenna. This proved to be a challenge the whole time, since the samples tested were not designed with this in mind, and the substrates were too thick for the signal to go throught. With the help of Dr. Joel Weber, at NIST's clean room, part of the substrate of the samples was removed with plasma etching, making it thinner (in some cases, up to about 30% of the original thickness, two or three tenths of a millimiter). This is a somewhat risky process and some sample was completely lost in the process. Therefore, we were able to verify how important for future measurements of this kind is to have a thin substrate. Also, perhaps even more important than the thickness is the material of the substrate is its composition. The samples that we tried (Py triangular dots of 100 nm thickness, 2 μm in diameter) had been grown on a Si substrate. This was not a problem for regular VNA-FMR measurements, but was a huge drawback for SMM, given the semiconducting nature of silicon, which proved to absorb and distort the signal due to its mobile charge carriers. This encourages the use of **thin** and **insulating** substrates, such as glass or sapphire.

Due to time limitations and the lack of availability to grow at that time new samples, we tried to optimize the measurement method to get some useful signal from the dots. Next are described the steps taken until the stay was over:

We tried to amplify the power of the signal sent by the VNA, and also enhance the sensitivity. With the help of Dr. Sam Berweger we set up a DPMM (dopant profile measurement module), which allows to measure differential capacitance dC/dV with a modulation technique (figure 4.25). On one hand, it increases the applied power, and on the other, it gives an adittional quantity from the measurements using a lock-in technique and a modulation - demodulation technique of the VNA signal mixed with a local oscillator signal. This in principle could help to remove some background noise due to the substrate, thanks to this demodulation, which could isolate the singal from the magnet. By itself this also didn't work in getting rid of the background signal.

Also, there was a misleading background signal for certain conditions which looked like the kind of resonances we were looking for, but unresponsive to the applied field. In the end, it turned out to be resonances of the bias electromagnet itself as a response of the microwave variation (in this setup, the magnet yoke is placed very close to the antennas, to reduce the amount of current that generates the magnetic field, by compromising the gap between the magnet poles. Therefore the magnet was in the zone of influence of the microwaves).

To remove this effect, and to further try to reduce the background signal, and to extract from it the triangular dots signal, with the help of Dr. Stephen Russek we added a secondary coil to the electromagnet, to superimpose a small oscillating magnetic field to the bias DC field. This oscillating field was controlled in frequency by a lock-in amplifier, that also fed the reference signal of the DPMM. With the output of the DPMM input in the lock-in, we were able to finally reach a configuration that seemed to be very effective in removing the background noise and signals, due to substrate, cables, DC magnet, etc. The first successful tests were done on a thin Py film, which would in principle have a stronger and easier to identify resonance peak. This can be seen in figure 4.26, where the peaks at symmetric positive and negative fields represent the FMR peak, and move to different fields with the frequency (not shown). There usually is a peak or set of peaks close to zero field, which are not the resonance, and we attribute either to domain wall

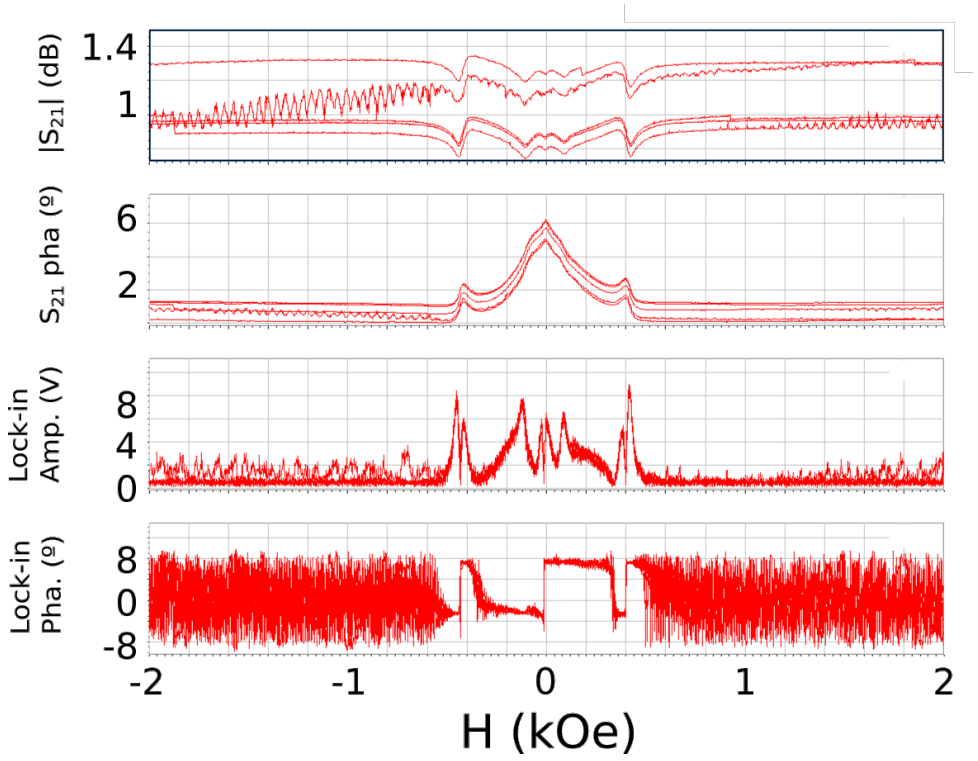

Figure 4.26: *a) VNA amplitude b) VNA phase c) Lock-in amplitude d) Lock-in phase of a uniform permalloy film (50 nm thick).*

oscillations at low fields, when there may be domains present, or to some mode excited in the DC magnet poles, again with possible domains present at zero field.

But when there is not a sharp jump in the phase, we can be sure that it does not correspond to a FMR-like resonance. It is possible to detect a signal even in the VNA directly, but the background drifts much more than in the lock-in signal received via the DPMM. In the lock-in amplitude, one needs to be careful, since this is a differential measurement (in this case, instead of dC/dV, we are controlling the external field, as oposed to the spectroscopy measurements typically done with the DPMM in semiconductors, so we would be getting dC/dH). For this reason, the FMR peaks, while they appear as a single peak in the VNA, in the lock-in measurements they appear as two peaks. This is because the lock-in amplitude is a number always greater than 0, and the negative peak (from the derivative of the part of the FMR peak with negative slope) appears as possitive peak, but the phase contains complementary information.

For some frequencies, the signal may not be so clear in the VNA directly, but the lock-in signal still is able to show the FMR peak very clearly (figure 4.27). The SMM does not allow to perform frequency sweeps, due to limitations in the software controlling the whole device. Instead, a single frequency is selected, and once fixed, the bias DC field is swept. From the transmission as a function of frequency curves, one can guess what frequencies to choose, because only those signals with a large enough value of the transmission parameter manage to make it to the other side of the sample. For example, figure 4.28 shows some frequencies that would in principle work, and that we would choose to use for field sweeps at constant frequency.

Once we found an optimal configuration for the FMR measurements of a uniform film, we replaced it with the array of permalloy triangles. With all these modifications to the initial setup, finally some measurements of the eigenmodes were achieved, showing a

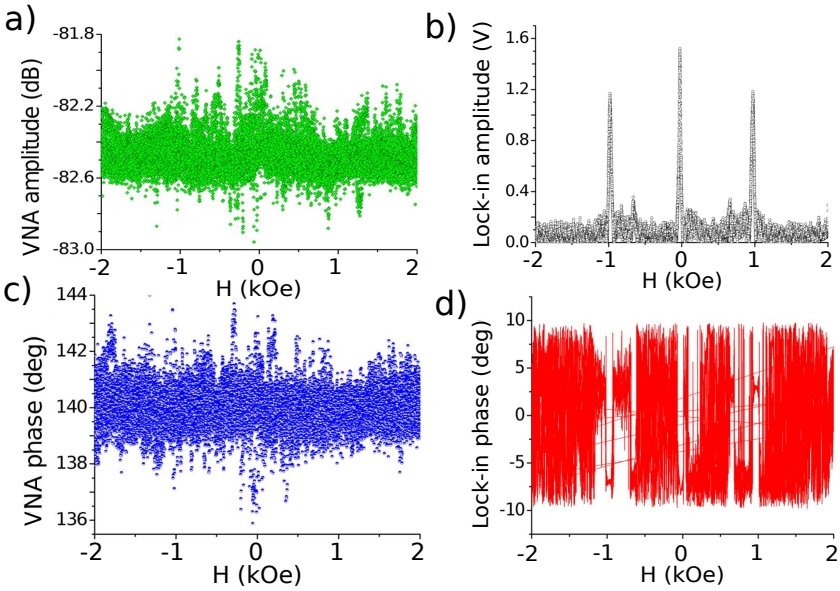

Figure 4.27: *a) VNA amplitude b) VNA phase c) Lock-in amplitude d) Lock-in phase of a uniform permalloy film (50 nm thick) at f=8.68 GHz*

dependence of the frequency with the applied field like the one measured directly with the usual FMR technique. Figure 4.29 shows again amplitude and phase in the VNA, with no FMR signal to be distinguished from the background, and how the lock-in signal shows however reproducible modes (two sweeps in each figure) corresponding to the spin wave modes.

One needs to tune the parameters of the lock-in amplifier, specially the reference frequency and the time constant, as it improves the detection of spin wave modes.

Surprisingly strong is the dependence on the lock-in frequency, as shown in figure 4.30. This means that one has to test several of them to make sure that the signal can be improved before taking many measure. Once a good set of parameters for the lock-in has been found, we present in figure 4.31 b several measurements at different frequencies as a function of the applied field, and a comparison with the known spectrum from usual VNA-FMR measurements in a. Also, some measurements comparing the B and the Y state at f=8.13 show how modes are similar but different in both states, and can be detected. This type of spectroscopic measurements have been found to work better using the CPW below the sample as the microwave source, and the AFM tip as the receiver.

However, for getting spatial scans of the samples, in order to map the local distribution of the high frequency response (which would allow us to visualize the spatial distribution of spin waves), we found that the opposite configuration (using the tip as the emitter and the CPW under the sample as the detector) was the only way to get any image, instead of noise. This is shown in the last two columns of the lower part of figure 4.30.

In the first picture of the bottom row, a topography is shown. This is the profile of the physical height of the sample, obtained by the deflection of the AFM tip due to van der Waals interaction with the sample. In the second and third pictures, the shape of the dot is not from physical contact, but from the amplitude and phase variations of the transmission parameter, measured directly in the VNA. Such clean pictures can only be obtained choosing frequencies that yield a large $|S_{21}|$, like those indicated in figure 4.28 with circles.

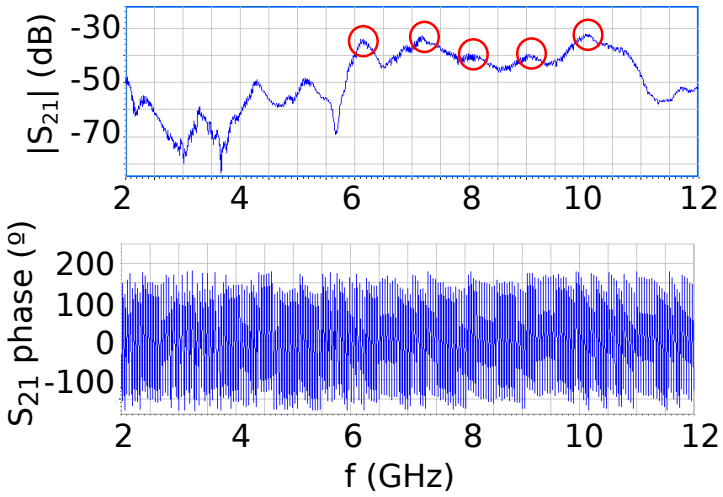

Figure 4.28: *Amplitude (top) and phase (bottom) of the transmission parameter S_{21} as a function of frequency. The circles show candidate frequencies to try.*

Summary and conclusions

In conclusion, we have presented experimental evidence for spin waves propagating along edge states in triangular Py dots. These spin waves are shown to be robust with respect to variation of the dots shape from equilateral to isosceles dots with height equal to the base length. Although the large (few micron and above size) soft magnetic triangles could, in principle, be implemented for information transmission and processing using E-SWs, we hope that our findings will stimulate further experimental efforts in investigation the whole new class of topological spin wave modes propagating along the edges in different types of magnetic devices and creation of alternative ways for spin wave excitation, transmission and manipulation.

Thicker dots, as observed in simulations, present a reversible vortex state that can be recovered after saturation. In this case spin waves could be excited along domain walls in the vortex state. In saturated states (B and Y) the asymmetry in SW dispersion relation suggests the different SW emitting capabilities of the triangle vertices depending on the bias field direction. Interdot interaction has to be carefully considered, since it changes with the magnetic state (mainly in the Y state). Triangular dots are promising magnetic elements opening new possibilities for versatile spin wave excitation and transmission by using vertices and edge states.

Perspectives

Edge spin could potentially become an important tool to transmit information between different parts of a magnetic nanostructure, as well as between different nanostructures. Their unique features allow to direct spin waves through well defined and narrow paths. Likewise, applying an external field in different directions or of different intensities, as well as local fields created with currents or permanent magnets could give raise to different magnetic states which would modify these pathways that spin waves follow, or directly eliminate them. Thus, this concept can be used to design different spin wave logic elements, such as diodes, multiplexors, etc. Also, modulation of signals could be investigated in

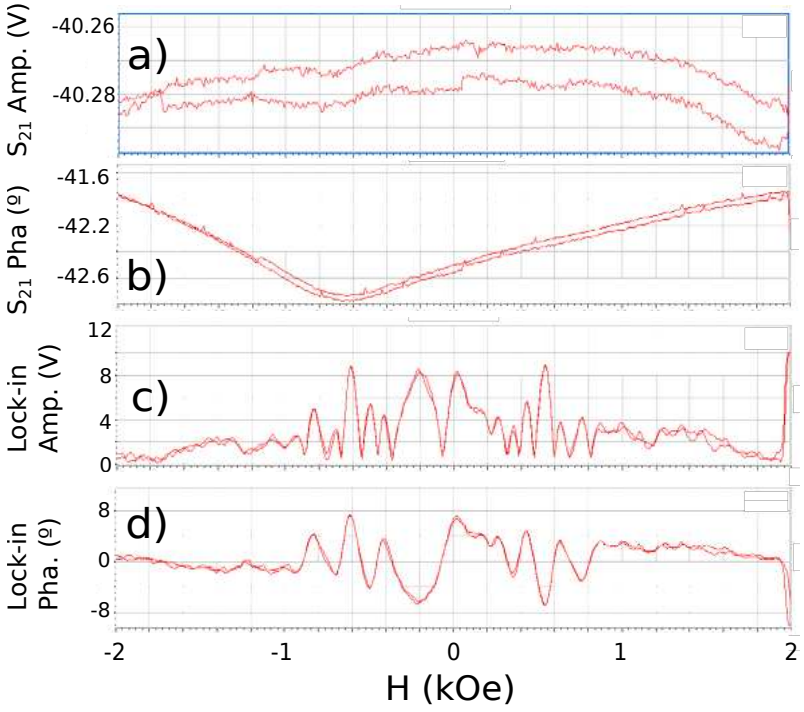

Figure 4.29: *a) VNA amplitude b) VNA phase c) Lock-in amplitude d) Lock-in phase of an array of 100 nm thick 1 μm side length triangular dots in the Y state at f=8.13 GHz.*

more detail in order to produce more complex, non linear devices, logic gates, mixers, etc. Engineering of the shapes of the nanostructures would allow to use edge spin waves to suit different needs, for specific systems of different sizes, configurations, etc. For larger systems, where the waves can be damped before they reach their final destination, it is important to find materials with low magnetic damping. At present, YIG seems to be the ideal candidate, but there are still some difficulties in growing it in lithographic patterns with small features, as compared to metallic materials such as permalloy. Also, simulations of spin waves of different kinds, excited in different manners is a very active field, provided that concepts can be tested much faster and cheaper than relying on fabricating and measuring real samples. Therefore, simulations are probably going to have a big impact on whether edge spin waves end up becoming a reality, and edge spin waves devices become functional building blocks of future spintronic technology.

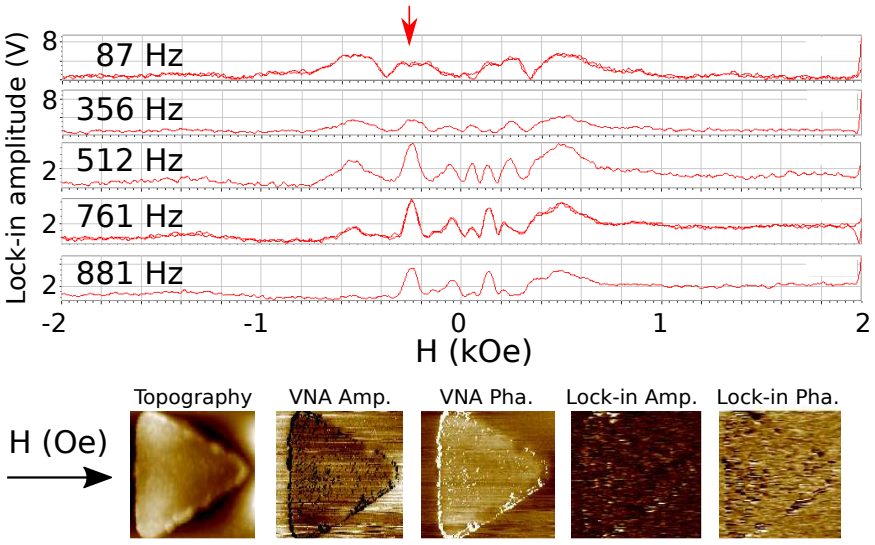

Figure 4.30: *Spin wave modes of the triangle array as a function of the lock-in frequency. Below, from left to right, topography image with the AFM, VNA amplitude, VNA phase, lock-in amplitude and lock-in phase, at the field indicated by the red arrow above, in the Y state.*

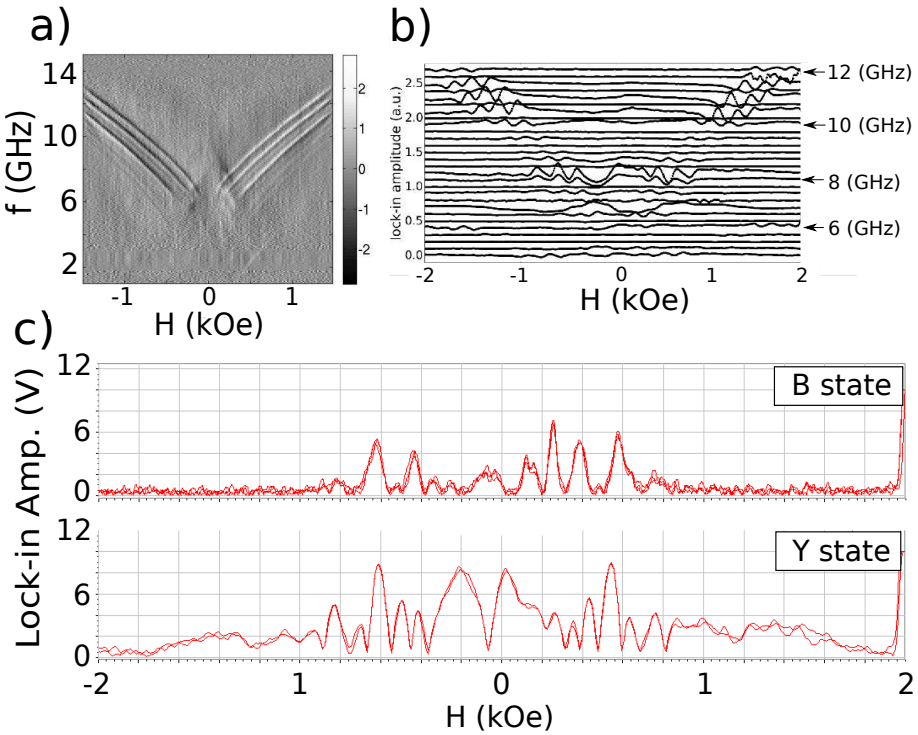

Figure 4.31: *a) VNA FMR and b) SMM measurements of an array of 2 µm, 100 nm thick Py triangles as a function of field. c) Comparison of the FMR spectra in the B and Y states at f=8.13 GHz.*

5. Time-dependent Ginzburg-Landau simulations

This chapter describes the computer program written during this thesis to simulate the Time Dependent Ginzburg-Landau equation (TDGL). The initial motivation to get involved in this task was trying to understand better our measurements of magnetic permeability in superconducting films with vortices at microwave frequencies. The initial attempts to simulate the vortex behavior as a function of time using the TDGL equation date from the early 1990s. The most popular method to tackle this problem is the link variable method[138–143], which uses finite differences (i.e. regular grids and derivatives are approximated by subtractions between neighbors). Some attempts have been made using finite elements[144], but the extra complications that this method has makes it much harder to implement, although it allows to better represent curved shapes.

The work presented below is based on the numerical approach exposed in[145], with important extensions to include arbitrary shapes and calculations in 3D. First, some general concepts about numerical solution of differential equations are explained, followed by a more detailed description of the particular method for solving TDGL.

5.1 Numerical method

Numerical solution of differential equations

There are three types of differential equations to represent physical phenomena:

- Time dependent equations. To solve these equations, one integrates numerically some variable in time. An example of this is the classical three body problem, where one integrates in time the position of a body in the presence of two other bodies, taking into account only their graviational interaction. Time integration uses methods like the simple but effective Euler method, or the more complicated Runge-Kutta.
- Space dependent problems. This type of problems require integrating a differential equation independent of time, such as Laplace's equation for the electrostatic potential. When there is a spatial dependence, one resorts to methods like finite differences or finite elements. Typically an iterative method is used to find a convergent solution.
- Space and time dependent methods. This is the present case of TDGL equation, and it is a combination of the former two. One typically finds by spatial integration the time derivative of the variable of interest (in our case, $\frac{d\Psi(t)}{dt}$, in turn dependent on $\Psi(t)$) and integrates it in time. With the updated value of $\Psi(t)$, $d\Psi(t)/dt$ is calculated again.

Finite difference discretization

Finite difference methods approximage derivatives by differences of a variable between neighboring cells of a mesh. There are three ways of approximating a derivative: forward: $\frac{dy}{dx} \simeq \frac{y(x+h)-h(x)}{h}$, central: $\frac{dy}{dx} \simeq \frac{y(x+h/2)-h(x-h/2)}{h}$ and backward: $\frac{dy}{dx} \simeq \frac{y(x)-h(x-h)}{h}$ The mesh has a constant spacing (not necessarily the same spacing in different directions).

Link variable method

We have used the usual approach to solving the TDGL equations known as link variable method. Normally in finite difference methods the interaction between neighboring cells is expressed (partially or completely) via the spatial derivatives. The interesting feature of the link variable method is that it relates the interaction between neighboring cells with the current flux enclosed by each set of cells forming a closed path, which is also dependent on an external applied field. This is done by introducing the auxiliary "link variables" in all directions, of the form:

$$U^x_{x,y,z} = e^{-i\int_{x_0}^{x} A_x(\lambda,y,z,t)d\lambda}$$
$$U^y_{x,y,z} = e^{-i\int_{y_0}^{y} A_y(x,\omega,z,t)d\omega}$$
$$U^z_{x,y,z} = e^{-i\int_{z_0}^{z} A_z(x,y,\zeta,t)d\zeta}$$

being x,y,z the spatial components, and λ,ω,ζ are auxiliary integration variables in the same directions as x,y,z. They are the integration variables used for calculating $\Psi(x,y,z)$, and x_0,y_0,z_0 are arbitrary positions that in the end cancel out after doing line integrals along closed paths.

Given a plane, XY for example, the rectangle formed by the cells in (i,j), $(i+1,j)$, $(i,j+1)$ and $(i+1,j+1)$ will hold a circulation of the vector potential that can be related to magnetic flux at that position inside the superconductor via link variables:

$$\oint_{\partial\Sigma} \vec{A}\cdot d\vec{l} = \iint_{\Sigma} \vec{B}\cdot d\vec{s} = \Phi_B$$

From such a rectangle the discretized distribution of magnetic field can be found in the $x=i$, $y=j$, $z=k$ coordinates:

$$U^x_{i,j,k}U^y_{i+1,j,k}\overline{U^x}_{i,j+1,k}\overline{U^y}_{i,j,k} = e^{-iB(i,j,k)\Delta x\Delta y}$$

and a similar calculation for the other two planes YZ and ZX. U's are circulated in a sense (for example, clockwise), and $\overline{U}$'s in the opposite, to have a closed circulation loop.

Discretization of the TDGL equations

We start with the TDGL equations in the following dimensionless, for zero scalar potential gauge[138]:

$$\frac{\partial\Psi}{\partial t} = \eta^{-1}[(-i\vec{\nabla}-\vec{A})^2\Psi + (1-T)(|\Psi|^2-1)\Psi]$$
$$\frac{\partial\vec{A}}{\partial t} = (1-T)Re\{\Psi^*(-i\vec{\nabla}-\vec{A})\Psi\} - \kappa^2\vec{\nabla}\times\vec{\nabla}\times\vec{A}$$

Here, lengths are scaled by the the coherence length at zero temperature $\xi_0 = \xi_{T=0}$. Time t is in units of $t_0 = \frac{\pi\hbar}{96k_BT_c}$. The vector potential $\vec{A}$ is expressed in units of $H_{c2}\cdot\xi_0$. The coherence length dependence on temperature is assumed to be well described by $\xi(T) = \xi_0/\sqrt{1-T/T_c}$. κ is the Ginzburg-Landau ratio which decides if a superconductor is type I or II. η is a positive constant with value $\eta = \frac{\xi_0^2}{D\cdot t_0}$, with D the diffusive constant for normal electrons (see deduction in chapter 8, Appendix B). Re means real part.

To reproduce the configuration of our experimental setup, we need to be able to have magnetic fields both parallel and perpendicular to the plane. With the more usual 2D configuration, one can only apply fields perpendicular to the plane, since to consider the

effect of magnetic flux, it has to actually go through some closed path. If one tries to apply a field parallel to the plane (XY, for example) in a 2D simulation, because there is only one cell in the Z direction, no flux can enter. To have nonzero magnetic flux in-plane requires having more than one cell in the perpendicular to the plane direction. However, the more complicated geometry we want to reproduce cannot be achieved in 2D, since magnetic flux (used for boundary conditions) needs at least two layers to be accomodated in the simulated domain (flux enters through a surface, therefore a single layer in 2D is not enough for considering in plane component of the magnetic flux, just perpendicular to the plane). Figure 5.1 shows more graphically the circulation of the link variables in every direction.

The equations integrated in time are four, one for the order parameter (first Ginzburg Landau equation), and the other three for the auxiliar variables known as link variables (see[145] for more details), that can be obtained by rearranging the three components of the second Ginzburg Landau equation for the vector potential. Therefore, the vector potential $\vec{A}$ is not explicitely solved, and it is not needed either.

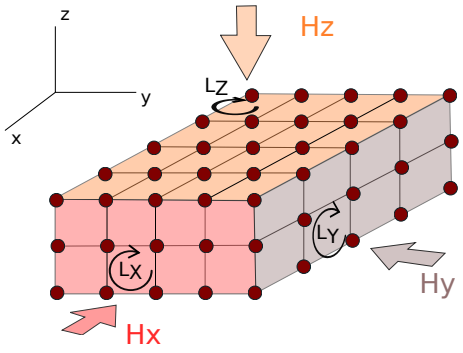

Figure 5.1: *Circulation of the link variables in a 3D simulation.*

Also, we need boundary conditions. The first condition is for Ψ at the boundaries. We will consider the case of samples isolated from their surroundings. This means that no supercurrent flows through the boundary, and is expressed as:

$$\vec{n} \cdot (-i\vec{\nabla} - \vec{A})\Psi = 0$$

A second boundary condition, for the magnetic field, is used. It is through it that magnetic field actually enters inside the sample. It has the form:

$$\vec{n}_i \cdot \vec{\nabla} \times \vec{A} = H_{e,i}$$

Where n_i is the unit vector in the direction of the component of the magnetic field $\vec{H}$ that we are interested in, parallel to a given surface, and $H_{e,i}$ is the value of the same component of the external magnetic field.

An important detail encountered when transitioning from 2D to 3D is described next. To solve the equations for the link variables in the boundary in 2D one uses the circulation (see figure 5.2 for more clarity):

$$L_{i,j} = U^x_{i,j} U^y_{i+1,j} U^{*x}_{i,j+1} U^{*y}_{i,j} = e^{-ia_x a_y H^z_{i,j}}$$

This set of four cells is what we will refer to as "square loop".

By multiplying both sides by de appropriate link variable (conjugated or not) one can isolate the link variable at the edge of the sample for each of the smallest possible square loops to calculate its value from the value of the other three and the applied field.

Passing from 2D to 3D

If one tries now to do the same thing in 3D, there is an inconsistency, because at edges the unknown boundary link variable can take two different values, depending on whether it is calculated from the one or the other loop in which it takes part (figure 5.3). The workaround that we came up with, and works well, is to forget about calculating boundary

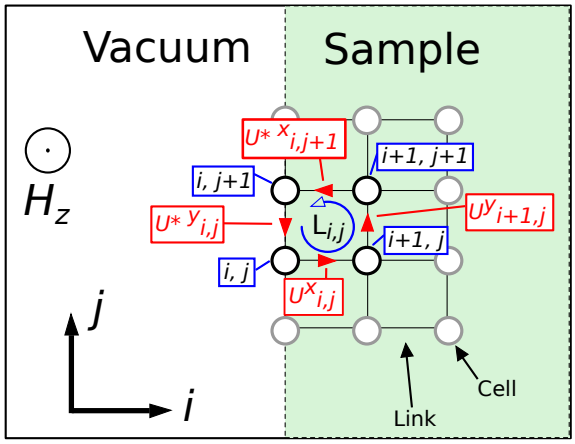

Figure 5.2: *Circulation of link variables at the boundary in 2D.*

link variables, and just force the flux through the boundary square loops. This is, instead of calculating the circulation of the flux in the "squares" of cells at the boundary as the product of each of the four link variables delimiting them, the value of $L_{i,j}$ is set directly to its appropriate value for each field direction, based only on the continuity of the parallel field. The boundary link variables are given arbitrary values. This works because these link variables really aren't used to calculate anything else.

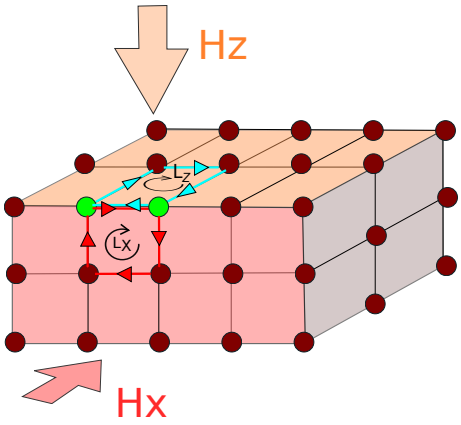

Figure 5.3: *Link variables at the edges (in this figure, between the two green cells) have an uncertain value.*

Having overcome this problem, everything works well. Then, one would expect to see tilted vortices under an inclined field, as indeed happens. Figure 5.4 shows two isosurfaces of early stages of the development of a vortex state under an inclined field in a cube in a simulation with $\kappa = 2$ and 50x50x50 cells. After some simulation time the system stabilizes and tilted vortices are observed (figure 5.5). In these scalar fields $|\Psi(x,y,z)|$ one needs to select Isosurfaces at low values, for example, plot only the points with $|\Psi(x,y,z)| = 0.1$ to clearly see the vortices. In this case, a magnetic field from one corner to the oposite ($(1,1,1)$ direction) is applied. Even without considering demagnetizing effects, vortices start at one border of the sample and end at another one which is not the opposite. The boundary conditions force the direction of magnetic field at the boundaries, and far from them the vortex curves to adapt. Thus, shorter vortices (closer to corners) are also more curved. Calculated isocurrents curl around vortices. Instead of plotting all (or a subset) of the arrows at each cell, as if figure 5.5 a), the supercurrent direction can be easier to understand if we only plot some isolines, as in figure 5.5 b). These isolines clearly show the supercurrent screening taking place in the direction perpendicular to the local field (figure 5.4 a), i.e., the streamlines fall in planes perpendicular to the $(1,1,1)$ direction.

The boundary condition described before for the magnetic field is completely appropriate for the case of 2D simulations where the field is perpendicular to the plane, because this is equivalent to a sample infinitely long in the direction perpendicular to the plane, immersed in a vertical magnetic field. Therefore, this field will only enter through the sample

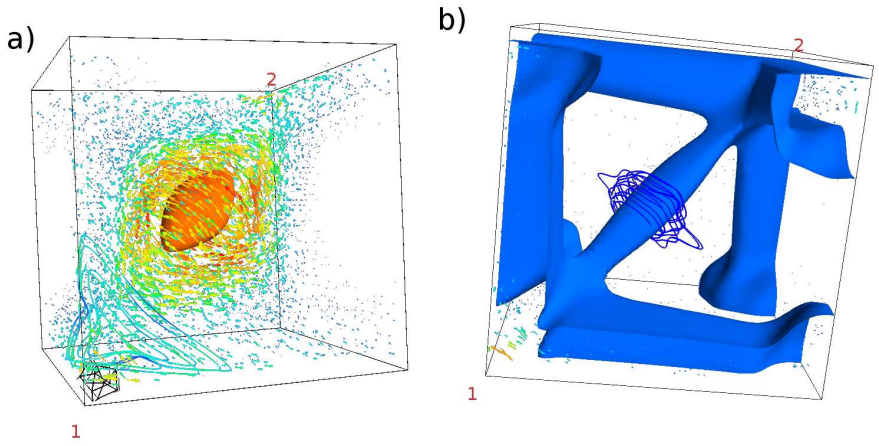

Figure 5.4: *Development of a tilted vortex state. Field is applied in the direction (1,1,1), from corner 1 to corner 2.*

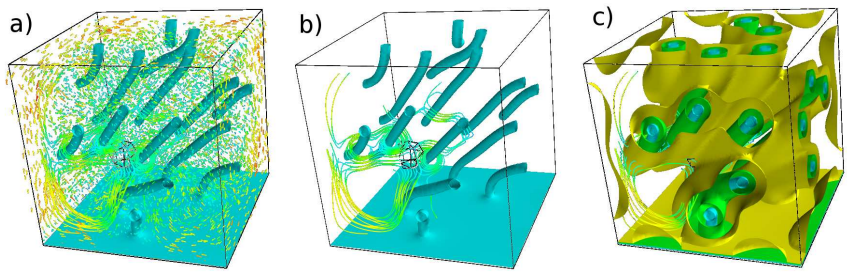

Figure 5.5: *Tilted vortex state. Isosurface at* $|\Psi| = 0.1$*, a) with and b) without arrows representing supercurrents. c) Isosurfaces at* $|\Psi| = 0.1$*,* 0.2 *and* 0.3*.*

boundaries. Passing to 3D geometries, however, breaks the symmetry in the previously infinite direction. Now, the field could enter directly through cells not in the boundary, but, for example, in the central part of the sample. If we were interested in this kind of calculations (for example, the vortices created in the center of a superconducting film, where a magnetic dot is placed, or an MFM tip is scanning), a new approach should be devised to account for this field entering perpendicular to a surface directly, and not through the boundary. Attempts have been made by forcing the magnetic field in central cells with the entrance of vortices, but more work should be done to confirm this. These nonlocal fields in the center of the sample fall out of the scope of this thesis and we will not consider them more. Also, we know that due to Meissner effect, and the critical state model, in most common situations with a sample placed inside a magnetic field, vortices will entrer through the sides of the sample, towards the center, and superconductivity will always be weakened first at the boundaries. This gives us confidence that for our use of the simulations in the case studied in chapter 6, this potential inaccuracy is negligible.

Arbitrary shape boundaries

One of the main interest of this type of simulations is in design superconducting devices prior to actually building them, to avoid trial and error until a device is working as expected. Real devices with a specific application in mind tend to have specific and complex shapes. The program to solve the TDGL equation accepts a bitmap image, which converts and scales to a rectangular array of cells which can be vacuum, superconducting material, or defects. The bitmap image must have vacuum painted as white and superconductor as black. Defects are painted in red or blue, depending on whether they represent holes, or regions of weaker superconductivity. To correctly apply boundary conditions in arbitrary shape boundaries, a function inside the program scans all the cells, identifying those at boundaries. To do that, this function checks if a given cell i) is superconducting and ii) any of its neighboring cells is vacuum. If both conditions hold, that cell is marked as a boundary cell. After that, depending on where the vacuum is located with respect to that cell (above, below, left or right), it is given a different numeric tag. When the time comes to apply the boundary conditions in each iteration, the appropriate condition is applied to each tag (concerning orientation). Doing this, the program can compute curved shapes, not just the easiest case of rectangular samples, as shown in figure 5.6

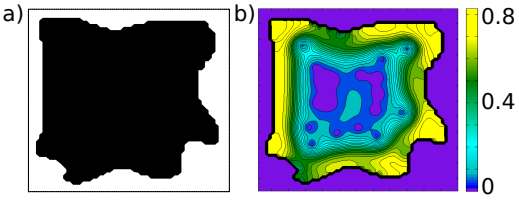

Figure 5.6: *Arbitrary shape simulation. a) Input shape. b) Simulation of* $|\Psi|$.

5.2 Results

Hysteresis loops

Figure 5.7 shows field ramps and the global magnetization response. As expected from a superconductor, magnetization is negative for positive fields, creating a field opposing the external field, so that the internal field is zero in the superconductor. In these time dependent calculations, the speed at which the applied fields change is relevant. In the figure it is easy to see how ramping the field more slowly (more iterations) gives a curve with more jumps. This is so because vortices have more time to enter the sample discretely, overcoming at certain moments, many at once, boundary energy barriers. Faster ramps are less controlled, and vortices enter in a more disorganized manner, leading to a smoother curve, where jumps corresponding to entering vortices are smoothed out. The presence of jumps is also very dependent on the size of the sample. Their relative importance is larger in smaller samples. On the other hand, large samples give the more typical smooth "field penetration regions" found in magnetization measurements.

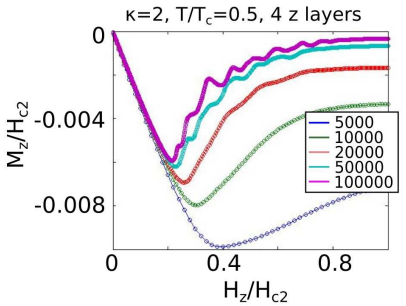

Figure 5.7: *Hysteresis loops from* $H = 0$ *to* $H = H_{c2}$ *in a different number of steps.*

Steady flow of vortices between permanent magnets

In this numerical experiment, we verify the idea of converting magnetostatic energy into a steady flow of vortices in one direction. The setup is simple: a superconducting strip,

with the appropriate width to hold only one row of vortices across its length, and two permanent magnets, each one in an end of the strip, with magnetization pointing in opposite directions, perpendicular to the plane of the strip (figure 5.8).

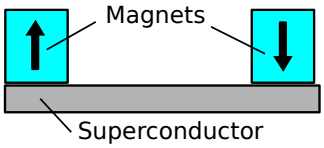

Figure 5.8: *A superconducting strip with two magnets at its ends.*

The magnets are modeled by boundary conditions: a non uniform external field, nonzero at the strip ends (only in a few cells near the center, not the whole lateral side), and zero everywhere else.

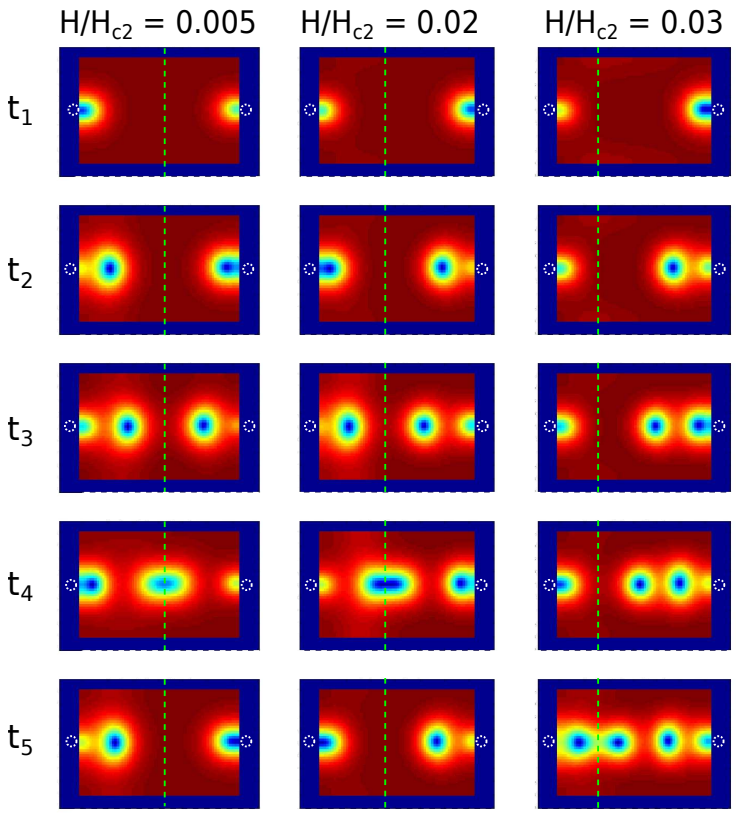

Figure 5.9: *Snapshots of the order parameter of a superconducting strip with magnets at the center of the right and left sides. The left side magnet points opposite to the external field, and the right side magnet points in the same direction as the external field. The external field is indicated at the top of each column. Rows represent snapshots at different times (evenly spaced). The green dashed line indicates the annihilation point of opposite sign vortices created at the sides. The white circles indicate the position of the magnets, which produce a magnetic field of value* $H/H_{c2} = 0.2$ *in that region.*

Of course, this is an approximation, but the fast decay of $\simeq 1/r^3$ typical of dipolar magnetic field suggests that is still valid. If both magnets are equally strong, vortices and antivortices are created in the same amount, and they meet at the center of the strip, as long as they don't need to travel a large distance (if they have, they will exit the superconductor throught the long sides). Since they have different signs, they annihilate. What can be done now is tuning the values of the strength of the magnets, making one higher than the other. In this case, the point where the vortices meet shifts laterally, closer to the weaker magnet. This is so because the stronger magnet manages to get the vortices it creates sooner into the strip than the weaker magnet. We can even get to the poing where there is only a steady flow of vortices from one magnet to the other (when one of them is not strong enough to create vortices, but still stronger than the zero field at the long sides of the strip). Practically, this would mean to tune the values of very

small magnets, which does not seem very feasible or practical. Instead, we can apply a perpendicular to the plane magnetic field, which will oppose the field created by one of the permanent magnets, and reinforce that of the other magnet. One needs to be careful to apply low values to this external field, since if it is too large it can lead to the creation of vortices itself. Instead, by keeping its values low, we are creating a "slope" which will determine where vortices of different signs will annihilate. Figure 5.9 shows how the external field can influence this.

This idea could be implemented for different purposes, such as very precise magnetic field detectors, since moving vortices induce electric fields, which could be tracked by some array of sensors over the strip, to relate the annihilation position of vortices to the external field. Also, electrically charged nanoparticles could be transported by these moving vortices, until they are deposited in the annihilation place, where no longer electric field is induced after annihilation.

Including holes

Another feature that could be added to the program, which fell out of the scope of this thesis due to lack of time to develop it completely, is being able to include holes in the calculations, also of arbitrary cross section but, at least to start with, "drilled" completely perpendicular to the boundary. Again, the idea shown in[145] could be adapted to 3 dimensions. An extra step would be necessary for including multiple holes: since for each hole, the magnetic field in that hole needs to be tracked for imposing boundary conditions, a function could scan the whole sample, to detect which cells belong to what hole. A more or less complicated procedure should be thought of to identify what is a hole, and what cells form it, based on the neighboring cells which have already been scanned and are empty. After that, the cells forming the boundary of each hole should be associated a "type" of cell, depending on where the neighboring empty cell lays with respect to them. With that, and knowing the field already trapped inside each hole, the boundary conditions could be calculated. Whenever a vortex falls inside a hole, the magnetic field in it will experience abrupt jumps.

Including holes in the calculations would allow to simulate effects like periodic pinning, to calculate matching fields, as well as the interaction of vortices with defects of different shapes, for example, as is usually done in the context of ratchet effects with triangular defects[40,146].

Rectification effects

Rectification effects of the vortex lattice have attracted a lot of attention, specially in superconducting films with periodic pinning arrays, typically of triangular elements[40,146,147]. The idea is to create a potential landscape that favors the motion of vortices in one direction with respect to the opposite direction. These systems are of interest both from the applied and fundamental point of view, since they allow to design mechanisms to control the vortex flow artificially. Some other works focus on motion of vortices in structures with ratchet-like shape[148,149]. Also, rectification effects have been found in systems that do not posses obvious ratchet potentials[150]. Most of the work so far considers the motion of vortices already present in the sample, whether it is a uniform film with pinning centers, or patterned superconducting elements. In this case we have applied our program to the case of vortices entering and exiting the sample. Rectification effects in this case occur due to the very geometry of the sample and the energy barriers that vortices need to overcome in order to enter inside. In this set of simulations (figure 5.10 we have

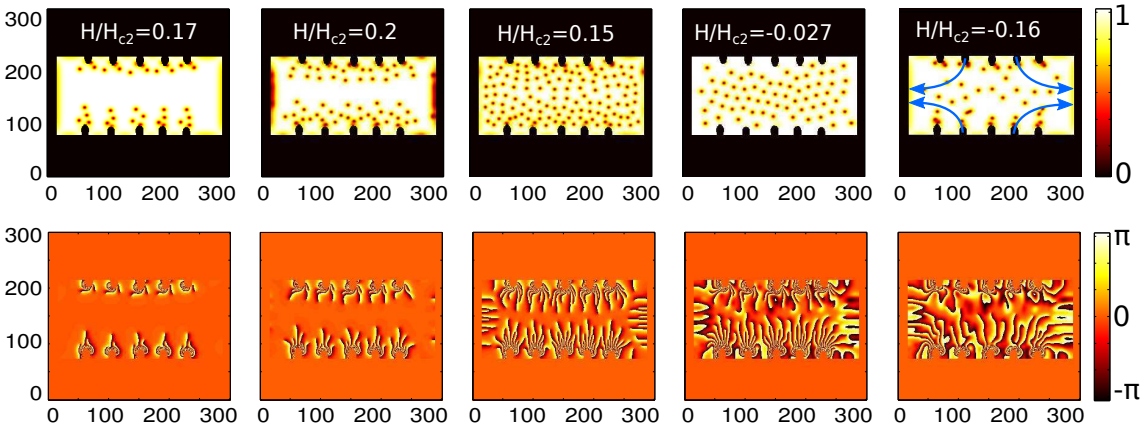

Figure 5.10: *Amplitude (top row) and phase (bottom row) of the order parameter. The perpendicular to the plane field is indicated in each column. The blue arrows indicate the net vortex flux direction.*

put our program to the test to verify two facts: First, adding notches to the boundary facilitates the entrance of vortices through them. This had been already found[151] in circular samples. Second, a rectangular shape with the notches in the long sides, in the presence of a perpendicular to the plane field (which slowly oscillates in value), a larger number of vortices enter through these sides than they exit during an oscillation period. This means that the combination of this geometry with the notches is enough to create a net vortex flux for an external field of zero average value in time. In practice, if such mechanism proved to be true, a voltage could be measured between the sides of the sample.

Motion of vortices under a stationary current

This simulation reproduces the vortex flow under the influece of a current flowing through a superconducting strip. A simple approximation to simulate a current is to, instead of using any current at all, modify the magnetic fields at the boundaries parallel to the flow of current. In one of them, an extra field should be added, and in the other, the same value should be subtracted, since a current flowing uniformly will create a magnetic field around it. This simplification only works for 2D simulations, due to symmetry reasons, since for 3D simulations, the curvature of the magnetic field lines should be taken into account, but in 2D they are perfectly perpendicular to the plane, since this case is equivalent to a sample infinitely long in the z axis. This method has been used before[152]. Figure 5.11 shows snapshots of a simulation of the vortex motion under a current parallel to the long sides of the strip, every 20 timesteps.

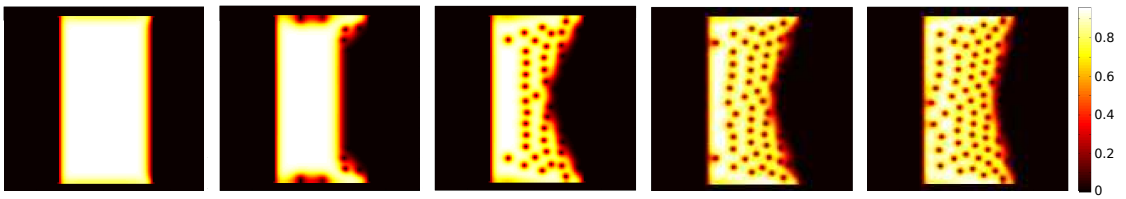

Figure 5.11: *Vortex motion perpendicular to an external current flowing along the long side of the strip (60 ξ in length).*

Spontaneous nucleation of vortices

Usually it is of interest to create vortices in a controlled manner with an applied field, but that is not the only way. Spontaneous formation of vortex antivortex pairs has been observed due to the stray fields of magnetic elements placed on top of superconducting films[153]. A superconductor cooled from above the critical temperature can also develop pairs of vortex antivortex inside[154,155], still having a total zero magnetic flux. This configuration is unstable, and vortices and antivortices will find it favorable to approach and annihilate each other to reduce the magnetic energy. Next we explore the behavior of the program to calculate the spontaneous formation of vortex antivortex pairs in a superconductor in the absence of an external magnetic field, starting from a random distribution of the order parameter centered around $|\Psi| = 0.1$. This is shown in figure 5.12 for a simulation with 1000 x 1000 cells (0.5ξ per cell) in the plane. This replicates the situation of abruptly quenching superconductivity by cooling down a sample in the normal state. After the vortices and antivortices are formed, they start annihilating each other if they happen to be close together. After several annihilations, there will be some vortices and antivortices left, far apart enough to not feel each other's attraction, and the final state will have vortices inside, but still a zero (or close to zero, due to vortices exiting through the boundary) total magnetic field inside.

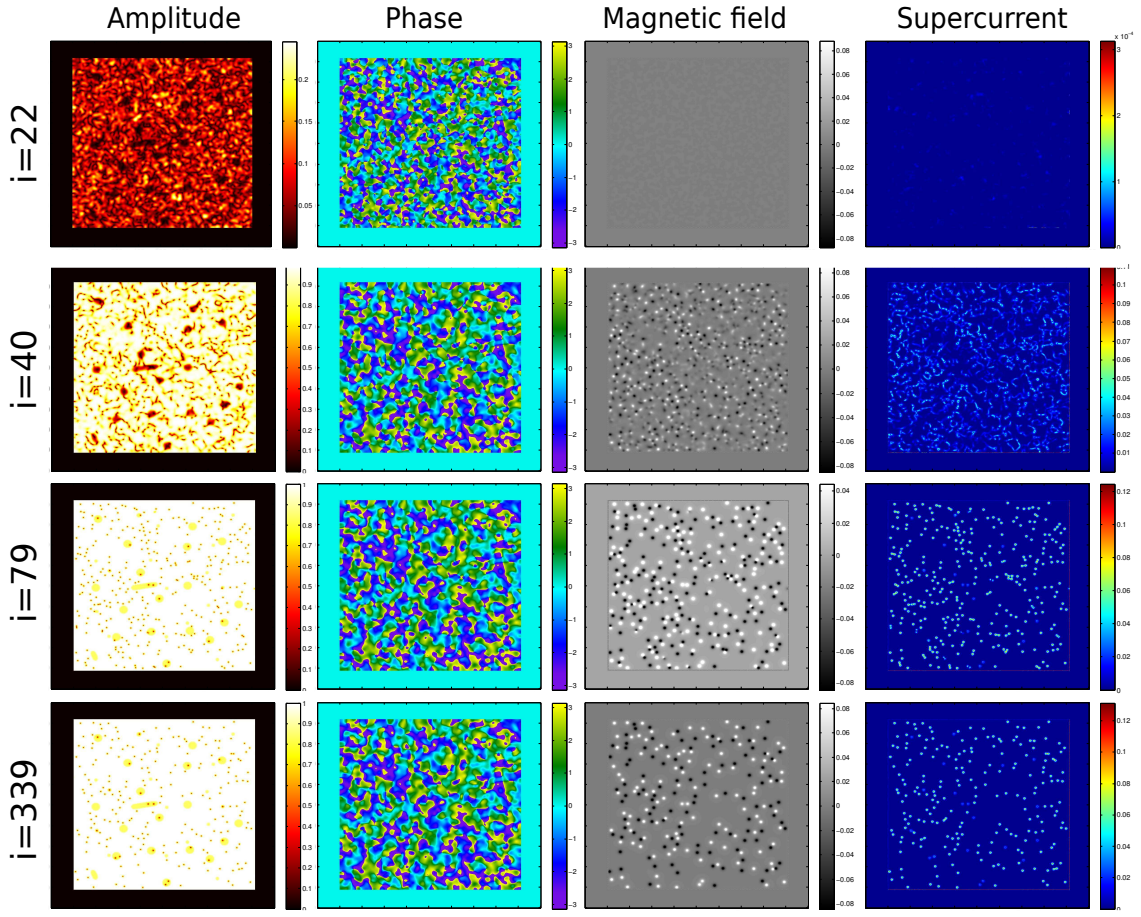

Figure 5.12: *Spontaneous vortex antivortex pairs formation starting from a random order parameter.*

5.3 Perspectives

The numerical solution of the time dependent Ginzburg Landau equation has been an active topic since the early 1990s, until the present moment. Currently there are a number of researchers using these simulations to study theoretically the behavior of increasingly complex superconducting systems. We have focused on a rather simple system, a thin uniform film, under conditions reproducing our measurements (crossed alternating and constant magnetic fields), as well as to predict what would happen under certain conditions, paying attention to the motion of vortices.

The use of these simulations is far from being exhausted. Currently an important effort is being made toward understanding multiband superconductors, such as MgB_2, with several order parameters using numerical methods more complicated that the one presented here, where several order parameters are present and coupled among themselves[156].

Also, as has already happened in the field of electronic circuits design, especially in circuits working at high frequencies, simulations can become a must-have tool to design better performing circuits, without the need to build lots of circuits by trial and error before reaching an optimum configuration. We expect that the same situation will be reached soon with superconducting circuits, which are gaining more and more attention for applications such as superconducting antennas and quantum computers[157].

6. Stimulated superconductivity with vortices

STIMULATION effects in superconductors with vortices under the influence of microwave radiation is the focus of this chapter. The response of superconducting devices to electromagnetic radiation is a core concept implemented in diverse applications, ranging from the currently used voltage standard to single photon detectors in astronomy. Suprisingly, a sufficiently high power subgap radiation may stimulate superconductivity itself. The possibility of stimulating type II superconductors, in which the radiation may interact also with vortex cores, remains however unclear.
This chapter introduces a study of superconductivity enhancement by GHz radiation in type II films with vortices. The magnetic field dependence of the vortex related microwave losses in a film with periodic pinning reveals a reduced dissipation of mobile vortices in the stimulated regime due to a reduction of the core size. To try to understand the effect of microwave stimulated superconductivity on vortices, we will use it in combination with the conditions provided by the matching of the lattices of magnetic and superconducting vortices, to extract information about the vortex motion. Also, the effect of stimulation on superconducting avalanches is studied, which reveals an enhancement of the power needed to trigger them. With the help of time dependent Ginzburg Landau simulations, described in chapter 5, a model to explain the results is presented.

6.1 Introduction

Stimulation of superconductivity

Microwave (*mw*) irradiation has been used to control the quantum properties of different systems, from supercurrents in superconductors to mechanical oscillators[158–161]. Using pumping of energy out of equilibrium for cooling has become a field of interest as well[162,163]. In 1966 microwave stimulated superconductivity (MSSC) was discovered[49] in superconducting bridges (figure 6.1) and later confirmed for different type I superconducting systems such as films[53,55], tunnel junctions[52] or cylinders[54,164]. This counterintuitive effect was explained by Eliashberg[51] as a consequence of an irradiation-induced redistribution of quasiparticles away from the gap edge. Very recently MSSC has been observed in transient regimes (on *ps* time scales) in NbN films[165] and was demonstrated to improve the quality factor of superconducting *mw* resonators[166]. In type II superconductors with magnetic field penetrating in the form of quantized flux (vortices)[167], the reduced inelastic relaxation time could suppress or modify some signatures of MSSC.

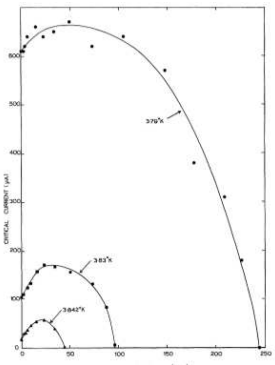

Figure 6.1: *First observation of MSSC[49], critical current vs microwave power.*

A periodic *mw* pump of sufficient amplitude induces the motion of vortices that results in dissipation[34,168–170]. Though dynamics of vortices was extensively addressed[38], the possibility of MSSC in the vortex state is not fully understood. One can speculate that the energy balance in microwave-driven vortices should depend on a competition between friction-induced heating of quasiparticles in the vortex cores[171–173] and energy pumping outside the core at large vortex velocities (Larkin-Ovchinnikov (LO) model)[174]. However, the full picture of nonlinear electromagnetic response of the vortex matter in the proximity to the critical temperature remains unsettled.

Flux avalanches

An avalanche is usually an unpredictable process of abrupt change between metastable states. Scale independent properties of avalanches are surprisingly similar in a wide range of systems ranging from woodquakes and snow and sand avalanches (figure 6.2 a, b) to superconducting flux avalanches[175,176]. Avalanches may be tecnologically useful[177], for example as a tool to investigate dynamic instabilities[178]. In most cases, however, they are considered disturbing, for example in superconducting resonators[46,48]. In type-II superconductors avalanches usually occur in the form of spontaneous penetration of magnetic flux quanta in the Bean-like critical state[176]. The flux rush typically takes place at films edges and forms rather complex dendritic patterns inside the films[179] with morphology being rather similar between different materials. This dendritic branching is common in nature for diffusive systems (figure 6.2).

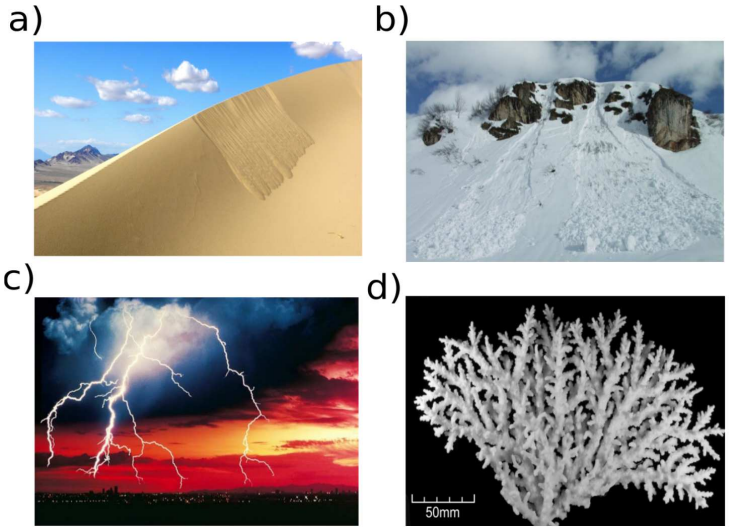

Figure 6.2: *Avalanche phenomenon in a) sand, b) snow. Branching patterns of diffusive systems, in c) lightning, d) coral.*

Thermomagnetic instability models, generally accepted now as a basic mechanism to understand theoretically the avalanche propagation in superconductors[180] suggests that the avalanches are triggered by some (edge located) hot spot created by slowly ramping the transversely applied magnetic field with vortex state being close to Bean critical state. In quasi-equilibrium conditions the avalanche process could be triggered by DC, microwave pulses[181,182] or near resonant frequencies of superconducting cavities[46,48]. The situation is somewhat different with a broadband microwave field sweeps, with avalanches triggered at different depinning frequencies or powers due to complicated local vortex pinning potentials[183].

So far, the most common ways to control and suppress the fast flux instabilities have

made use of nano-morphology[184] or optimization of the heat transfer through coating a superconducting film with a metal layer[185]. The recently observed microwave "cooling" of the vortex matter through stimulated superconductivity[43] provides the possibility of exploring a conceptually different approach to controlling avalanches. Our experimental studies in that direction reveal an entirely unexpected novel effect: the application of *mw* in the frequency range close to specific vortex depinning frequencies makes avalanches substantially more robust to the external radiation power. We relate this effect with the reduction of vortex cores driven by microwave, which consecuently transforms into a reduced local dissipation.

6.2 Sample preparation

We investigated two types of samples: plain 60 nm thick Pb films ($T_c \simeq 7.2$K) and 60 nm thick Pb films deposited over a square array of periodic pinning centers (Pb-PPC), consisting of circular Py dots. The samples were grown by Dr. A. Silhanek, at K. U. Leuven. The Pb films were electron-beam evaporated onto liquid nitrogen-cooled Si/SiO_2 substrates. All samples were covered with a 20 nm thick protective layer of amorphous Ge, to avoid oxidation and keep them from getting scratched, since they are placed face down over the CPW. The Pb film is evaporated in all samples over a surface of 5×5 mm^2. In the Pb-PPC samples, the Pb films were deposited over a 2×2 mm^2 square array of 30 nm thick 1000 nm diameter Py dots, with an interdot distance of 2000 nm.

Hysteresis cycles confirmed that the Pb films are type II SC, in accordance with previous reports[186]. Also, for the second part of the chapter, we have studied 180 nm thick NbN samples grown by Dr. Konstantin Ilin, at IMS Karlsruhe.

6.3 Experiments and simulations

Measurement method

As explained in the methods section (chapter 2) the complex parameter $U \equiv U' + iU''$ is determined as the VNA transmission parameter S_{21}, dependent on microwave power (P), frequency (f), temperature (T) and magnetic field (H), normalized by S_{21} at a reference H or T, in the normal state.

Power values in the experimental figures correspond to the estimated values of power waves travelling through the waveguide, but not absorbed by the vortex system, which would involve too complex and unnecessary considerations, since we only care about relative changes, not absolute values. Absolute values could be of interest, for example, if the size of the structure was critical and the number of vortices inside the sample was of interest. In our case, we are only interested in the overall behavior of the vortex matter, therefore we neglect things such as the VNA calibration, which would only be useful to get the exact values of susceptibility, etc.

The samples studied consist of superconducting thin films of Pb of thicknesses of 60nm and 70nm and and of 180 nm thick NbN films. The lead thicknesses is much lower than that ensuring type II superconductivity[186]. These films have been used in the past in our group (the Pb films), or in other groups (the NbN films), and we knew beforehand that they exhibit avalanch behavior at low enough temperatures and that were reliable. Pb films had already been measured in the past at microwave frequencies in our group. Aside from that, and the features of the cryostat system used, there is no particular reason for not using other materials to check these effects. In fact, MSSC was first discovered in Al.

The measurements have been made in a variable temperature JANIS helium cryostat with a superconducting magnet applying the static fields. The microwave signal is supplied by a gold coplanar waveguide (CPW), over which the sample is placed face down, so that the generated high frequency magnetic field that excites dynamics in the film is directly incident on it (figure 6.3). More details can be found in section 2. To study the behavior of avalanches both the temperature (T) and static magnetic field (H), as well as the microwave power are varied. The presence of avalanches is detected as jumps in the transmission parameter S_{21}, measured by the network analyzer[46,48,183]. In this chapter, unless otherwise specified, we concentrate on the dependence of the microwave power required to trigger avalanches as a function of T and H. The measurements consist of power sweeps at different values of temperature or field, and at fixed microwave frequencies. The temperature and magnetic field sweeps will be extended to up to the values destroying the superconductivity (above T_c or H_{c2}). We shall use the corresponding transmission power sweeps above T_c as a reference when comparing with data obtained in the superconducting state.

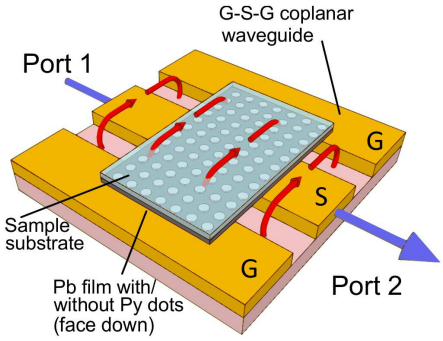

Figure 6.3: *a) Sketch of the sample placed on top of the waveguide, the microwave magnetic field (red arrows) and the microwave current that generates it (blue arrow).*

Simulations

In order to understand better the behavior of vortices under high frequency magnetic fields we have created a computer program to simulate the time dependent Ginzburg-Landau equation. We have used these simulations to try to qualitatively confirm the existence of LO mechanism for microwave driven vortices. Details about the simulation program can be found in chapter 5. Future work could also try to analyze numerically possible coupled magnetic vortex and superconducting vortex dynamics. This task, however, presents a greater challenge because of the need to include dynamics of magnetic pinning centers. The simulated geometry is that of a thin film, with four cells in vertical direction. The in plane dimensions are of $25\xi \times 25\xi \times 3\xi$, being ξ the coherence length (used as unit length, with a non specified value, since it enters the computations through the κ parameter). This is enough to distinguish clearly vortices from each other and from the borders, and at the same time small enough to allow for relatively fast computations. This is necessary because the 3D version of TDGL needs to consider terms that 2D does not, since there are more types of possible border cells, making it unavoidably slower than just N times slower, being N the number of cells in vertical direction. By choosing an appropriate value of $\kappa = 2$, vortices appear when applying a perpendicular to the plane magnetic field above H_{c1}. This field is applied until the vortex lattice is stationary (vortices enter from the borders towards the center). Then, the *ac* magnetic field is applied parallel to the plane (keeping unchanged the perpendicular DC field). Keeping track of macroscopic quantities (such as the total magnetization) we can extract information about the global response of the system (vortices and the rest of the system, including borders), such as difference of phase with respect to external signal (for very high frequencies, vortices start to not being able to follow the field). However, we are more interested in the "microscopic" behavior of vortices, which can be studied by looking directly in the values of $|\Psi|$ at each cell.

6.4 Results

Stimulation of critical temperature and upper critical field. Figure 6.4 a shows the real and imaginary parts of the microwave permeability parameter U measured in Pb-PPC at small *mw* powers. Measurements are done in a temperature (T) sweep for different magnetic fields, at a fixed frequency (f) and are in accordance with the more usual *ac* response at lower frequencies, or models such as that by Coffey and Clem[32], with a decrease in screening (real part) and a maximum near the phase transition in losses (imaginary part). The dependence of the response on the *mw* power (P) for the same Pb-PPC sample is seen in the contour plot for U' in the plane $P-T$ for magnetic field $H=0$ and $f=6$ GHz, (figure 6.4 b).
To characterize the shift of the transition as a function of P, we introduce an effective critical temperature, T_c^*, determined with an error around 1 mK. Figure 6.4 c presents a 3D plot of T_c^* with respect to P and H in the Pb-PPC at $f=6GHz$. One observes a non-monotonic dependence of $T_c^*(P)$, increasing at small P and decreasing at large P. Though the T_c^* does not have the meaning of critical temperature of the superconducting transition, the observed increase of T_c^* can be interpreted as an indication of MSSC.

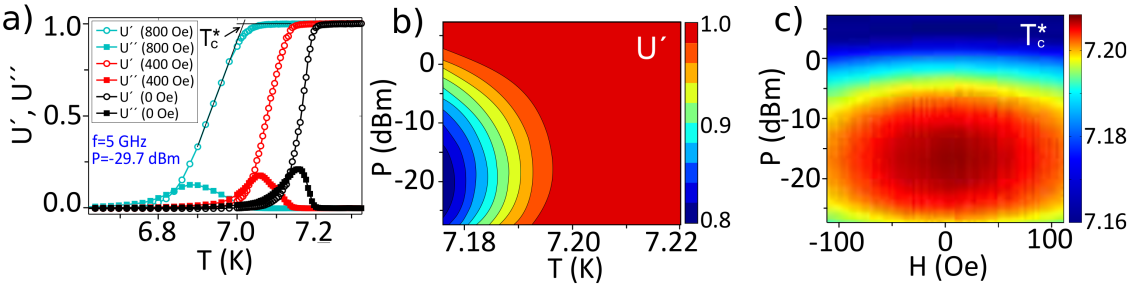

Figure 6.4: *a) High frequency response (real and imaginary) as a function of T, to identify the phase transition. b) Contour plot of the real part as a function of temperature and power. c) Critical temperature as a function of field and microwave power.*

Determination of critical temperature and field

A criterion to determine the critical temperature must be set, since the transition is never perfectly sharp in practice.

The values of T_c^* were found in T sweeps by finding the intersection between a polynomial fit of the response in temperatures for each power in both the superconducting part, and the normal part (figure 6.5 a). The resulting dependence of T_c^* on power clearly shows an increase at intermediate values of power. Analogous results (increase of T_c at intermediate powers) are also achieved when directly plotting the temperature at which the response changes in a (for example) 1% with respect to the normal state. The error in T_c^*, of 1 mK, is obtained statistically as the dispersion in the intersection, found by least squares.

From measurements of $U(f,P,H)$ similar to those shown in figure 6.6 (H sweeps) one can determine H_{c2}^* as the borderline separating the normal region from the superconducting one. As can be seen in figure 6.5 b, showing a typical magnetic field dependence of $U'(f,P,H)$ at $P=-15$ dBm, $T=7.17$ K and $f=6$ GHz while changing the applied field, the transition from normal to superconducting state is not completely abrupt (the same happens when finding T_c^*). We define H_{c2}^* as the intersection of the polynomial fit of $U'(f,P,H)$ at low

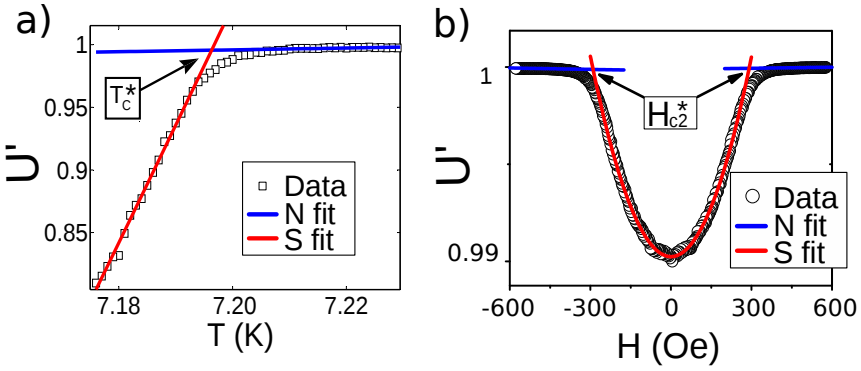

Figure 6.5: *a) Method to determine T_c^*. b) Method to determine H_{c2}^*.*

fields, deep in the superconducting region, shown by a red solid line and the high field level corresponding to the normal state and fitted by blue lines.

The value of critical field for each microwave power is considered as the average of the values obtained for positive and negative fields, to cancel the shift produced by the magnetic field frozen in the superconducting magnet. As with temperature, analogous results (increase of H_{c2}^* at intermediate powers) are also achieved when directly plotting power vs field borderline that causes a certain dropwith respect to the normal state.

Field and temperature dependence

To investigate the nonlinear response in the vortex state as a function of pinning strength, we have made measurements of U' and U'' as functions of H, P, f and T in Pb-PPC. Figure 6.6 a shows a 3D plot of U' for the Pb-PCC sample at $T = 7.19$ K in the variables $H-P$. Dark red tones correspond to the normal state. As H is lowered, the samples become superconducting and the magnetic permeability changes in agreement with expectations[32].

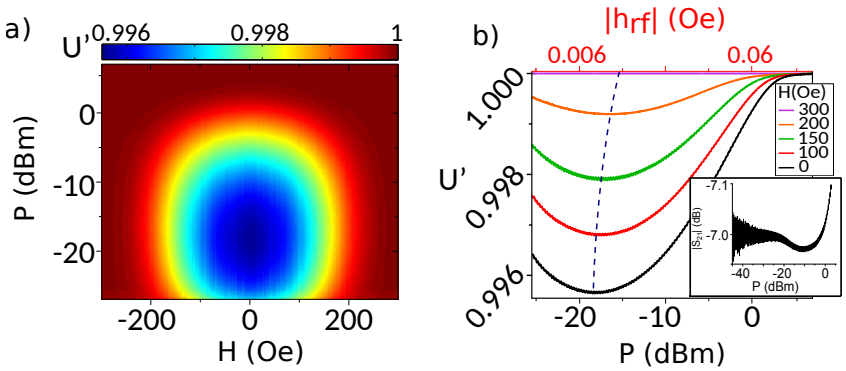

Figure 6.6: *a) Real part (screening) of the superconducting response as a function of power and magnetic field (f=6 GHz). b) Cross sections of figure a) at different fields as a function of power (or high frequency field, in the red scale). The dashed line indicates the minimum of each curve (optimum power). The inset shows a cross section at H=0, for a wider range of power.*

Figure 6.6 b shows a typical set of cross-sections of U' at fixed magnetic fields. While microwave power above 5 dBm destroys superconductivity, for intermediate values the superconducting response is the most intense. We will refer to the applied P that yields the strongest superconducting response as "optimum power" (P_O). The dashed line indicates how P_O changes with H. The response, inset of figure 6.6 b, shows directly a transition

between a linear to a nonlinear vortex response regimes. At lowest powers it flattens and is noisier, since the relative noise is large compared to the weaker signal received in port 2 of the network analyzer.

Figures 6.7 a and b show plots of $H^*_{c2}(P,T)$ in the plain and Pb-PPC samples respectively. For each temperature, H^*_{c2} has been normalized by its value at the lowest P, so relative values of H^*_{c2} can be compared. As $T \to T_c$, the relative increase of H^*_{c2} under *mw* at $P = P_O$ becomes larger. Figure 6.7 c compares the normalized H^*_{c2} as a function of reduced temperature in both types of samples (with and without pinning centers), showing that MSSC effects in H^*_{c2} are stronger in the Pb-PPC sample.

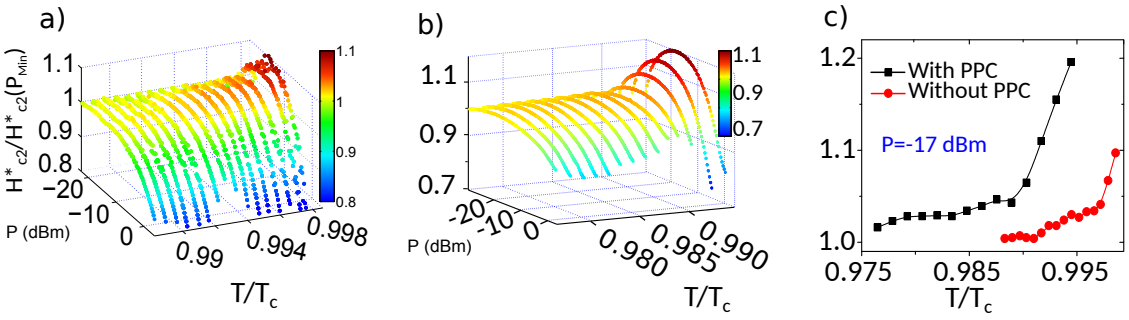

Figure 6.7: *a) and b) Normalized critical field for plain and Pb-PPC samples. c) Comparison between critical fields at P_O.*

Figure 6.8 shows that $P = P_O$ increases with *mw* frequency with a maximum value that saturates around 15 GHz. These frequencies are well below those corresponding to the superconducting gap.

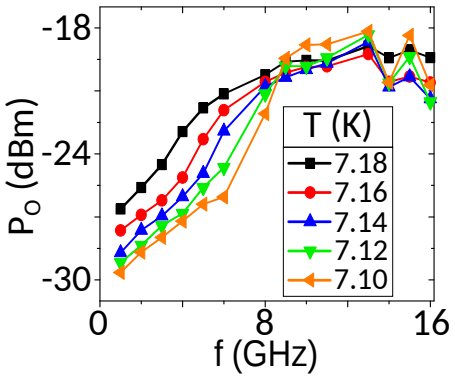

Figure 6.8: *Optimum power vs frequency.*

Reduced dissipation of microwave driven mobile vortex

The changes in P_O indicate that the "*cooling*" effectiveness of *mw* radiation depends on the pinning strength through the applied field which changes the number of vortices and their mobility. In figure 6.9 this fact is exposed for $f = 6$ GHz, at different values of T. Solid lines show P_O vs. magnetic field with matching conditions indicated by vertical dotted lines. Red circles represent a typical measurement of $U'(f,P,H)$ at fixed values of f and P, in which the same matching anomalies appear in the *mw* permeability.

The lowest value of P_O for every temperature is found always at zero field, and decreases locally in matching conditions. This hints the relevance of the vortex mobility for the

value of P_O: **the enhanced vortex mobility out of matching conditions provides relatively larger (respect to matching) P_O values and correspondingly larger "cooling" efficiency**. This counterintuitive result has been corroborated through a set

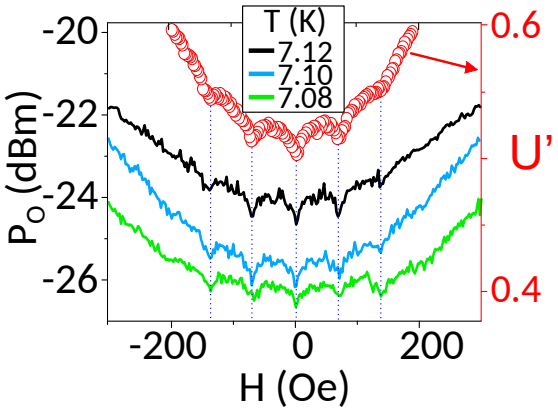

Figure 6.9: *Matching conditions in P_O (lines) and U' (circles).*

of independent experiments investigating the H and P dependences of U''. At low f, when MSSC is not yet pronounced, the dissipation (U'') at matching conditions shows (as expected) dips in a broad range of P (figure 6.10). However, for higher f the dips of losses at matching conditions convert into peaks. The same effect can be observed as a function of power, in figure 6.10. In other words, *vortices moving with higher average velocities out of matching conditions manage to dissipate less than pinned in matching conditions.* These observations indicate a qualitative change in the microwave response of superconducting vortices at high *mw* frequencies.

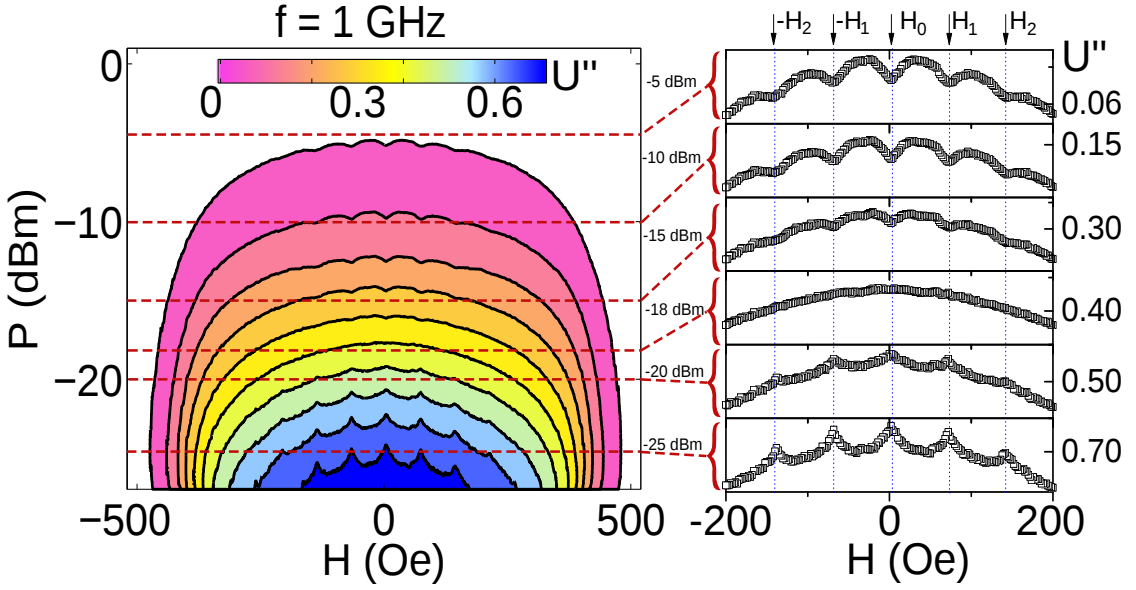

Figure 6.10: *Change from maxima to minima at matching conditions for $f = 1GHz$. To the right, cross sections at the powers indicated by red dashed lines.*

This behavior is found at frequencies below 2 GHz for this system. Figure 6.11 shows some more examples, and how this transition zone, connecting minima with maxima,

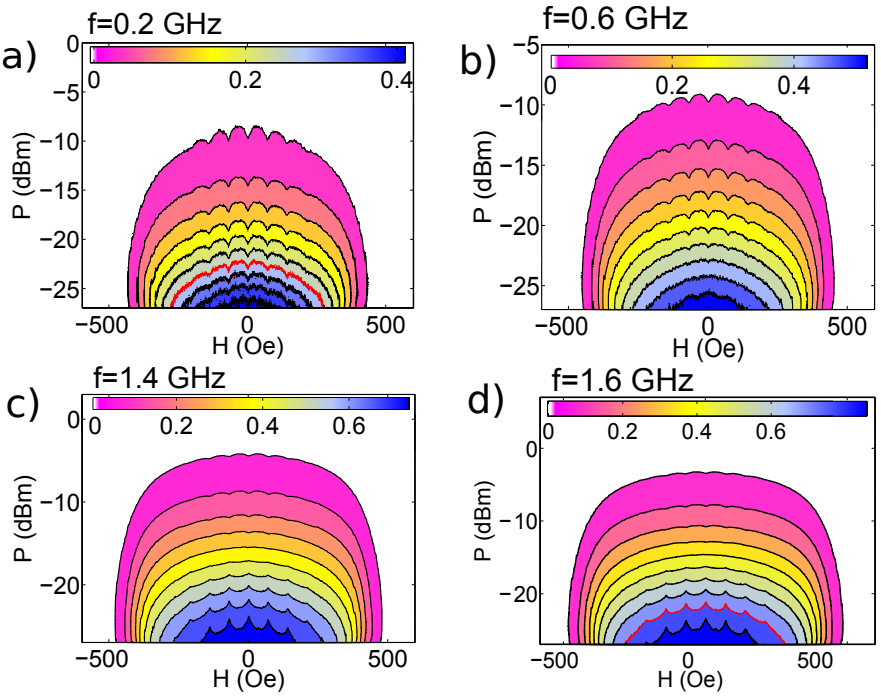

Figure 6.11: *U″ as a function of H and P at different frequencies around 1 GHz. Panels a) and d) highlight a contour in red to stress the change from peaks to dips with frequency.*

moves to different powers. In panel a and d, a red isoline indicates how what are minima for a certain frequency have transformed into maxima for another.

In figure 6.10, matching fields have been indicated (*a posteriori*) with doted lines. From these values we can verificate the interdot separation of the dots comprising the array of PPCs, as follows:

$$H_\perp = \frac{\phi_0}{a^2} \rightarrow a = \sqrt{\frac{\phi_0}{H_\perp}}$$

Our measurements in the case of field perpendicular to the film (figure 6.12) give a value of matching fields of 4.8 Oe. With the standard value of the flux quantum, $\phi_0 = 2.06783 \cdot 10^{-15}$ Wb. Then, the interdot distance is, as expected:

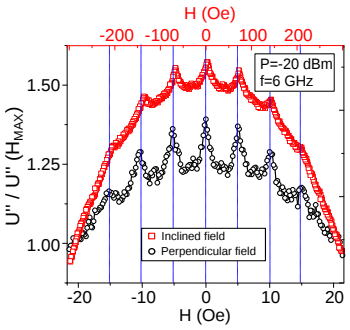

Figure 6.12: *Matching vs field orientation.*

$$a = \sqrt{\frac{\phi_0}{H_\perp}} = 2.075\mu m \simeq 2\mu m$$

Mainly the out of plane component creates the vortices that will give raise to matching conditions. Then, we can estimate the inclination of the field from the matching conditions. We know that matching fields for a perpendicular field occur at 4.8 Oe. Then, if we measure them at 72 Oe in the inclined configuration, as in Fig. 3b and 3c in the main text, we can extract the inclination angle as its sine, which equals the ratio of both quantities: $\sin\alpha = \frac{4.8}{72} = 0.066 \rightarrow \alpha = 3.78°$

Mechanism of nonlinear vortex response and modelling

Mechanisms of nonlinear response of vortices to microwave radiation are far from being fully understood. The Larkin-Ovchinnikov (LO) theory[174] predicts a nonlinear response at sufficiently large electric fields, which induces a high speed DC motion of the vortices. If their speed exceeds some critical value, v_c the current decreases with increasing voltage. This is a consequence of an electronic instability of the non-equilibrium distribution of quasiparticles at high velocities, leading to a reduction of the vortex core size. A further increase of vortex velocity leads to an abrupt switching into a state with higher electric resistivity. On the other hand, the nonequilibrium quasiparticle distribution close to the energy gap where the density of states is maximal can cause stimulation of superconductivity[51]. One can anticipate an interplay between the above mechanisms in a mixed state of *mw* driven type-II superconductors. However, we are not aware of a theory quantitatively interpreting our experimental results.

To understand the nonlinear response of *mw* driven vortices we have simulated the *ac* response of vortices using the time dependent Ginzburg-Landau equations. The time derivative of the order parameter modulus $|\Psi|$ shows that vortices oscillate about their equilibrium positions (figure 6.13), especially at lower frequencies, when they are able to follow the external *ac* field without delay. As the *ac* field amplitude increases (which is equivalent to increasing the *mw* power of our measurements) the order parameter oscillates in magnitude throughout the entire sample, not just near the vortices, being weaker at the maxima of amplitude of *mw* field h_{rf}, as expected. This effect is specially pronounced in the outer part of vortex cores, as can be seen in figure 6.14 b and c. When one compares the radius of a vortex (at a given value of, for example, $|\Psi| = 0.5$, figure 6.14 c) for different moments of an oscillation period, vortices are narrower at zero *ac* field amplitude than at its maximum *ac*.

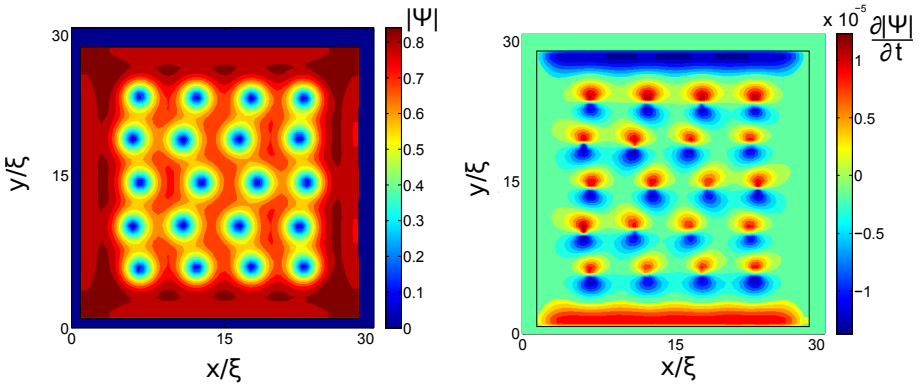

Figure 6.13: *a) Magnitude of the order parameter for $H_{DC} = 0.4H_{c2}$. b) Time derivative of panel a). Vortices move toward the blue area. Half a period later, colors interchange.*

As happens in vortex cores displacement, the higher the frequency of the *ac* field, the more difficult is for a vortex core radius to change size (figure 6.14 d). A transition from linear to nonlinear response regimes is observed, *leading to a substantial reduction of the average vortex size* at high *mw* drives. Time and frequency are in units of $t_0 = \frac{\pi\hbar}{96k_BT_c}$ and $f_0 = \frac{1}{t_0}$.

The oscillations of the vortex core size under *mw* radiation are always present, and are more notorious for higher *ac* field amplitudes, which is in qualitative agreement with the DC model by LO[174]. The above confirmation of LO-type mechanism in *ac* conditions

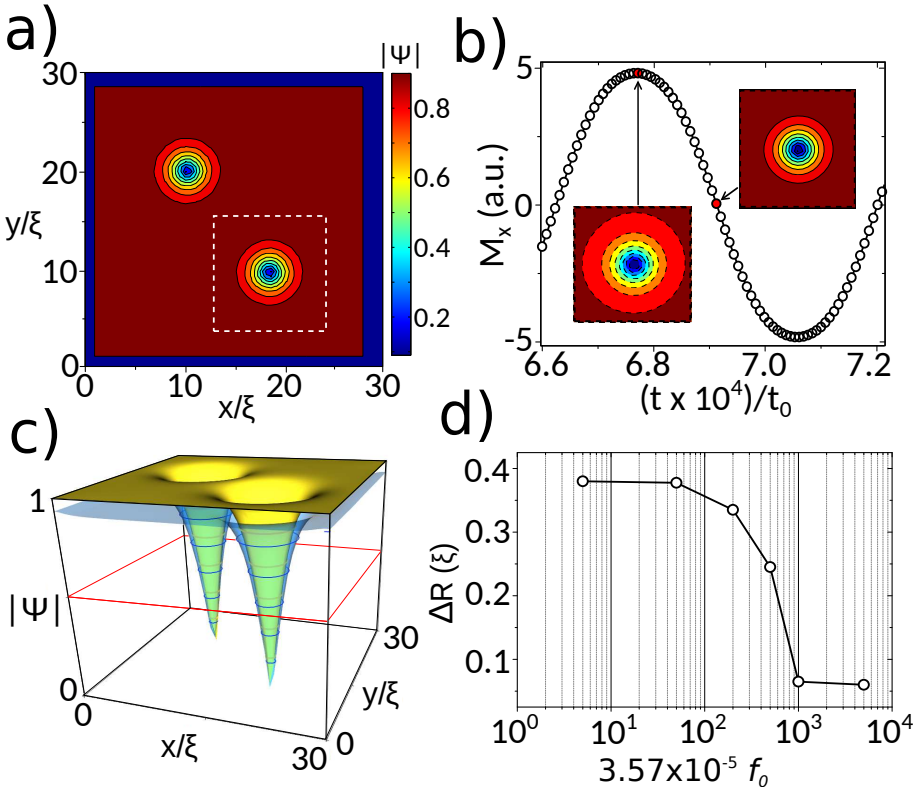

Figure 6.14: *Time dependent Ginzburg-Landau simulations. a) Contour plot of $|\Psi|$ in a square sample, with $H_{DC} = 0.02H_{c2}$ perpendicular to the sample, after applying $H_{DC} = 0.8H_{c2}$ and slowly reducing it. b) Oscillations of M_x following the ac field at 5 GHz. Snapshots of the area marked by dashed white lines in panel a). c) $|\Psi|$ for the two cases considered in b). Yellow surface corresponds to minimum and blue to maximum of $|H_{DC}|$. d) Change of vortex radius (at $|\Psi|$ =0.5, marked by red line in panel c), as a function of frequency.*

agrees with simulations of DC driven vortices[187] and does not exclude electron overheating in the vortex core as an additional factor contributing anomalous velocity dependence of vortex viscosity[173].

The vortex velocity can be limited by the critical value v_c for the LO instability[39,174,188]. Assuming that the maximum *mw*-induced shift of a vortex is limited by the inter-dot distance $a \lesssim (1-1.5)$ μm and that the dependence of P_O on f starts to saturate at $f \gtrsim f_{sat} \sim 10$ GHz we estimate the geometrically restricted maximal vortex velocity as $v_{max} = f_{sat} \cdot a \approx 6-10$ km/s. This is 2-3 times larger than the values of v_c reported for Nb and high-T_c superconducting films[170,189].

It is to be noted that in solving TDGL equations, no energetic considerations for stability of Cooper pairs is made, therefore effects such as Cooper pairs breaking due to absorption of photons of energy above the superconducting gap are not found. An arbitrarily high frequency *ac* field just makes it harder for vortices to follow it, not being frequency a cause of loss of superconductivity. On the other hand, a higher amplitude of the *ac* field does indeed destroy superconductivity. For example, at $|\mathbf{h}_{rf}| = H_{c1}$, $|\Psi| < 1$ far from vortices. Thus, not only vortices are affected by large amplitude ac fields, also the rest of the film (as was already discussed before, concerning the excess of normal quasiparticles (unpaired electrons) when applying an inclined DC field).
It is important to note that in TDGL equations, there is no notion of Cooper pair, neither of

their bonding energy. Typically, photons of energy in the THz range are energetic enough to break a Cooper pair when being absorbed by them, since this energy corresponds to the superconducting gap energy $\Delta \sim$meV. Therefore, even when we apply an *ac* field of frequencies the order of THz, the order parameter is not going to drop to zero because we are reaching the frequency corresponding to the superconducting gap. This concept is not considered in the equations we are solving. TDGL equations are useful for our purpose in that they give information on the redistribution of normal quasiparticles by applying an *ac* field to the vortex lattice, just by the deformation and movement of vortex cores. This redistribution of normal quasiparticles further interacts with the electromagnetic radiation of the waveguide, and create extra losses due to Joule heating.

Influence of defects

In the simulations, no periodic pinning centers array is considered. These simulations are done to better understand the response of vortices to a high frequency magnetic field.

However, the presence of defects can be considered. They are introduced by replacing the term $(|\Psi|^2 - 1)$ by $(|\Psi|^2 - r)$[145]. Here, the term r is a variable that depends on position, and ranges between 1 and 0. By choosing values of r lower than 1, the superconductivity is weaker at those points, and vortices are in a more stable position, so it acts as a pinning center for vortices. In simulations we have used a defect of size ξ, with r=0 to trap a vortex. Several simulations at different frequencies show that regardless a vortex is inside a defect or not, the core size still oscillates under a *mw* signal. However, displacements of the vortex core are different, being more able to follow the external field when trapped. The vortices outside the defects also move but, specially at low frequencies, they tend to move in more circular trajectories, unlike vortices trapped in defects, which move more linearly. Also, radial oscillations of the vortex core size are observed in vortices trapped inside defects with a somewhat larger difference in amplitude at lower frequencies compared to untrapped vortices, as shown in figure 6.15.

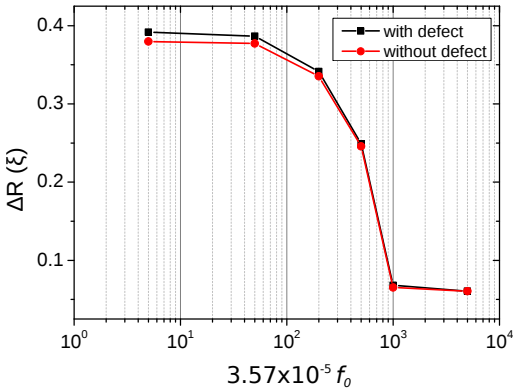

Figure 6.15: *Frequency dependence of radial oscillations magnitude for a vortex trapped in or outside a defect.*

Effect of magnetic pinning centers

Apart from the effects described above, one cannot neglect the fact that magnetic vortices themselves create stray fields which can interact with Cooper pairs and break them, increasing the number of normal quasiparticles. This could explain why the Pb-PPC sample shows a stronger response than the plain film, concerning stimulation effects.

Optimum power close to H_{c2}^* far from T_c

Concerning the dependence of P_O on H, as explained above, it increases when increasing H. Close to T_c this trend is uniform, but at lower temperatures, and higher fields local maxima in optimum power appear (figure 6.16). We explain this behavior as a consequence of a dense vortex structure, when vortices are not able to move as freely as in cases with less

density of them, diminishing the LO effect.

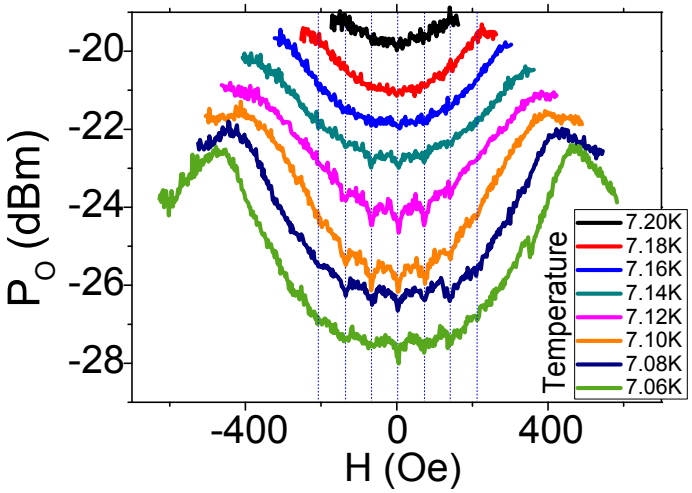

Figure 6.16: *Optimum power as a function of magnetic field in the Pb-PCC film.*

Dependence of the superconductivity stimulation on the magnetic field direction

It has been observed that MSSC is more easily detected with an inclined field than with a field perpendicular to the film plane. We explain this observation as follows: As long as the applied microwave frequencies are substantially lower than the one corresponding to the zero temperature gap values ($f_{Pb}(T = 0\text{K}) = 653$ GHz), and microwaves interact only with normal quasiparticles, the effectiveness of MSSC is conditioned by the presence of low energy normal quasiparticle states[51]. An additional (in-plane) external magnetic field effectively suppresses the order parameter, creating a gapless state in a rather extended field interval $\frac{H_{c2}}{2} < H < H_{c2}$[190]. Then, for the suppressed order parameter values (i.e., close to T_c) the quasiparticles density of states varies roughly as $\sqrt{E}$ (here E is measured from the center of the gap) in the presence of impurities, providing effective quasiparticle excitation by subgap (GHz) microwaves[190].

Our experimental observations reveal a clear enhancement of the MSSC strength in the form of an increase of P_O in the field interval ($\frac{H_{c2}}{3} < H < \frac{3}{5}H_{c2}$) followed by some small suppression of the P_O above $\frac{3}{5}H_{c2}$. Within our model, this increase is related in part with an increase of the low energy quasiparticles DOS in the indicated field interval (mainly from in-plane field component) and an enhanced contribution of the LO effects (from perpendicular field component) while vortex-vortex interaction remains unimportant.

It could be argued that the in-plane component of the inclined field can produce changes in the stray field of the dots, that would in turn affect the behavior of vortices. Experimental data of the dots shows that their annihilation field is higher than the values we work with in this case (dots in the vortex state), so the stray field is always kept to a minimum. Direct measurements of U'' comparing the case of perpendicular and inclined field confirm that matching fields occur at regular values (obviously, after correspondingly scaling the fields, to match the perpendicular to the plane components, figure 6.12), which suggests that the magnetic effect of the vortices is small (otherwise, changes in the regularities of the matching fields might be present, in accordance with the hysteresis of the dots).

Avalanches

Now we will consider the case the case of flux avalanches due to the applied microwave field. As explained earlier, avalanches can be detected as abrupt steps in the microwave response curve. For example, in the case of power (or frequency) sweeps, when a certain power is reached, it will be enough to release an avalanch, and the corresponding change in the magnetic field inside the sample will be detected in the network analyzer as a step[46,48]. Avalanches are typically better observed in plain superconducting films, since artificial pinning centers could help stop them as they advance toward the center of the sample. Figure 6.17 shows MOKE pictures (taken by V. Yurchenko) of a NbN film, which will be described later. This material is known to have the capability to form avalanche patterns, and at the same time has become an interesting due to its applicability, for example, for superconducting nanowire single-photon detectors. At lower temperatures, the avalanches tend to be longer and narrower, whereas at higher temperatures they are wider and shorter.

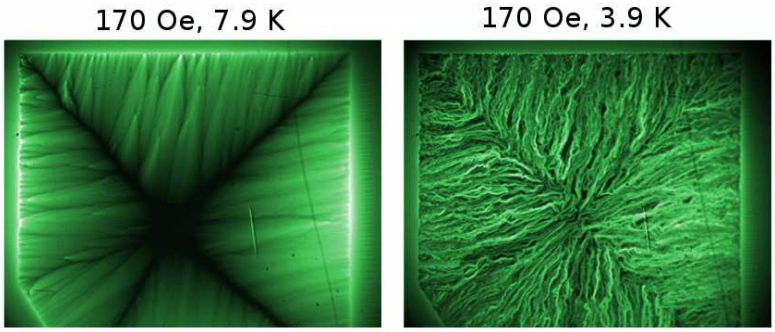

Figure 6.17: *Magnetooptical images of a NbN film at different temperatures for the same applied field. Sample grown by K. Ilin. Image by V. Yurchenko.*

As always, we use the CPW to generate the excitation signal. Most of the microwave field is concentrated close to the central stripline, therefore the high frequency field exciting the sample is local. We expect therefore more eddy currents related heat generated close to the stripline, increasing temperature below the strip. This suggests that the avalanches will most probably be generated near the stripline (sketch in figure 6.18, green branches). Avalanches are thermomagnetic processes. A requirement is that heat is appropriately transported to the substrate, away from the sample. Then, the branch pattern will remain "frozen" inside the film, as long as the applied field is maintained.

In contrast to a previous study carried out by our group, which demonstrated the presence of a set of vortex depinning frequencies in type II superconducting films[183], the present experiments aim to study these avalanche depinning frequencies as a function of the applied microwave power, for a fixed frequency. The applied field is the remanent one after saturating at 1000 Oe and going back to zero field. In figure 6.19 an example of these jumps is presented for a 70 nm thick Pb film. Depending of the direction of the power sweep (from the minimum to the maximum value, blue line, or viceversa, red line) the jumps appear at different powers. This indicates that the release of an avalanche is influenced by the "history" of previously released ones. In the end, at the lowest (or highest) microwave powers, $|S_{21}|$ is at the same value, indicating that the global superconducting state is equivalent after all these avalanche depinnings. Thus, a "histeretic" behavior in microwave power evidences the importance of thermal effects in avalanches. The right panel shows

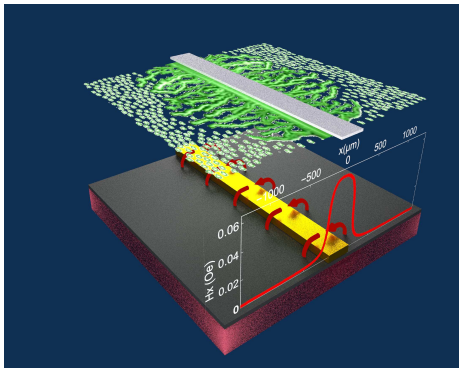

Figure 6.18: *Sketch of the sample. In green a supposed representation of vortices and avalanches, generated mainly by the stripline. The red curve is the amplitude of the x component of the magnetic field generated by the stripline.*

the numeric derivative also for two cycles of power sweeps. These curves are repeatible after many sweeps. In order to test some possible implications of the thermal nature of avalanches, we have done measurements of this type, reaching the final temperature (3K) at different speeds, from the normal state, as shown in figure 6.19 c and d. By looking at the latter, since the derivative more clearly allows to identify the position of the jumps, we conclude that how long it takes to reach the final superconducting state is not a relevant factor, as long as we do it slower than some minutes. Turning the temperature down faster than this from the normal state was not reliable, due to the thermal inertia of our cryogenic system.

Figure 6.20 a shows a power and temperature sweep of the normalized transmission parameter at 5 GHz. One can easily see one of the previously mentioned jumps, and how at temperatures approaching T_c (7.2 K for the Pb films) this jump requires lower power to occur. This is the expected behavior, since higher temperatures favor the entrance of magnetic flux inside the sample. The corresponding differential plot helps to observe other weaker avalanches, all with the same behavior as the main one.

Figure 6.20 c shows the same measurements as a, but close to one of the vortex depinning frequences of 7.5 GHz. One clearly observes an unexpected temperature dependence of *mw* power which is required to trigger avalanches. Approaching critical temperature, at some temperature range (around 6K for the lowest powers, and around 5K for the strongest ones) the expected tendency of decreasing critical power inverts. The closer one apporaches T_c, the more power is required to trigger the avalanches. There is no linear relation between the microwave frequency and the presence or not of this effect. By carefully examining the P-T sweeps (and as will be explained later, the P-H sweeps too) one notices that each time the inversion of the normal tendency to the unexpected one happens, it does in a range of temperatures in which there is a visible maximum in U''. This corresponds to the peak in *mw* losses close to the T_c that has been known to originate from enhanced vortex mobility. The center of this maximum is not always in the same position. At higher applied powers (that increase the sample effective temperature), the peak goes down in the horizontal axis (substrate temperature).

For this reason the inversion of the avalanch deppining power does not occur at the same temperature for every avalanch in figure 6.20, since the peak in U" moves to lower T at higher powers.

In relation to our particular case, the inversion in the avalanch tendency occurs relatively close to T_c, where the gap is already partialy filled by normal electrons providing MSSC

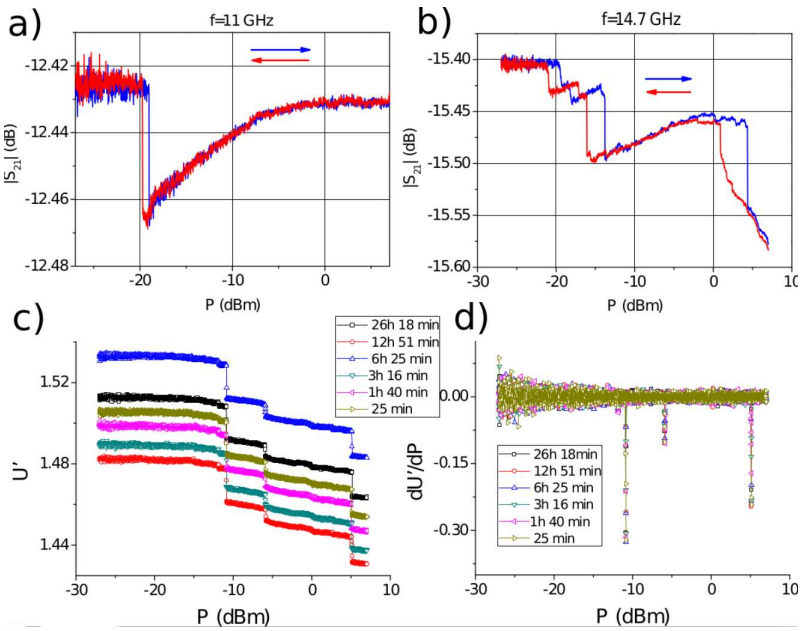

Figure 6.19: *70 nm Pb plain film. Only freezing field, inclined orientation. a) shows a single avalanche process at 11 GHz, and b) several processes, at 14.7 GHz. S_{21} module as a function of microwave power, swept from minimum to maximum power (blue line) or from maximum to minimum (red). c) shows several measurements at 15 GHz in the same conditions, only changing the speed at which 3 K is reached from T_c. d) is the derivative of the curves in c).*

related "cooling". Moreover, the peak in losses U'' implies that a strong increase in vortex mobility is taking place, which may result in both larger presence of normal quasiparticles in the sample and a reduced contribution in vortex dissipation, in contrast to cases with more pinned vortices. The presence of both mechanisms may thus require more microwave power to depin vortices and release the avalanches, since these effects are effectively cooling the sample.

Obviously this effect will occur mostly close to the microwave source (the CPW central conductor). Avalanches triggered at the edges will suffer less the effects of MSSC and therefore their tendency will not change, at the same time that avalanches closer to the stripline will indeed show this change. We attribute to this the fact that sometimes some branches change their curvature, while others nearby do not (figure 6.23).

In figure 6.21 the same effect is observed, now as a function of applied field at a fixed temperature. Again, when the peaks in U'' are observed (this time close to the upper critical field), some (not all, as explained above) of the avalanches show a change in tendency, being necessary more power to trigger them at higher fields, where superconductivity is weaker. As compared to temperature sweeps, field sweeps look more complex, with more avalanch branches present, and some of them experiencing “steps” in field as well. This should not be surprising, as changing the applied field changes the number of vortices present in the sample and enhances non-equilibrium conditions which stimulate avalanch process. Qualitatively similar effects have been observed in NbN films, which are currenly heavily explored in superconducting electronic applications. Figure 6.22 b shows this effect in T sweeps for depinnig power near one of depinnig frequencies. In contrast, with *mw* frequency not being tuned, as shown in figure 6.22 a, the normal behavior is found with critical power monotoniously decreasing with increasing temperature.

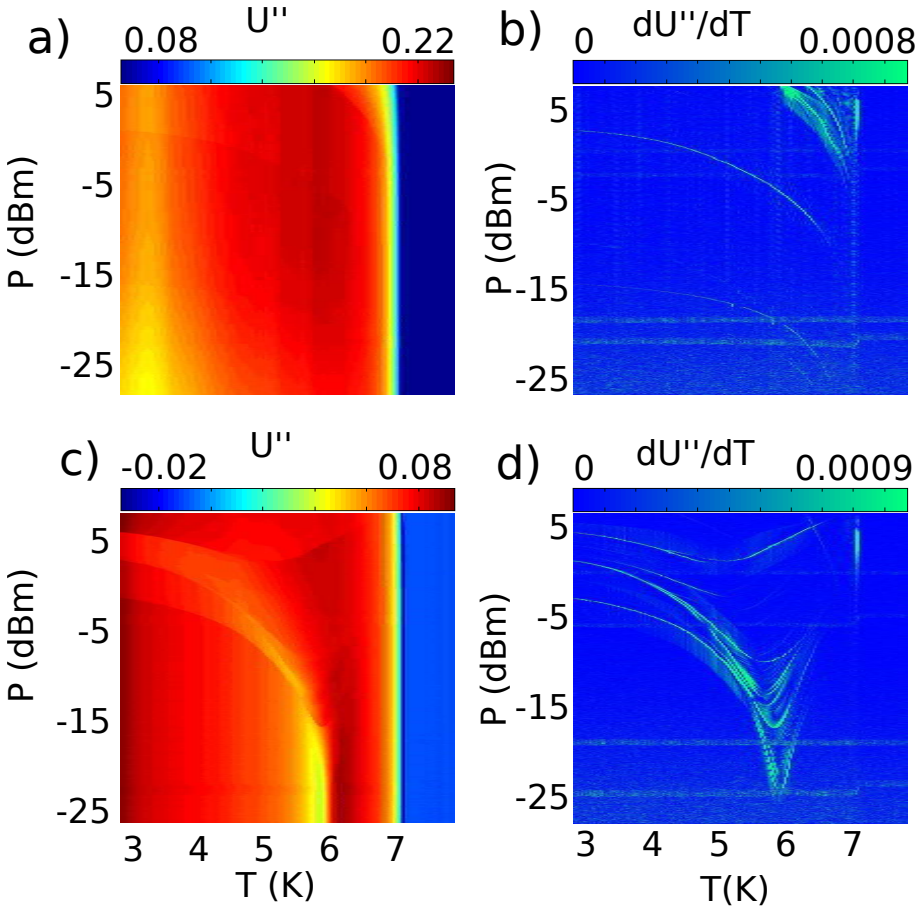

Figure 6.20: *a) Expected avalanch behavior as a function of temperature and power at $f = 9.5GHz$. b) panel is the derivative with respect to temperature of a). c) Same as a), this time at $f = 7.5GHz$, showing unexpected avalanch behavior in the region with the U" peak, dark red colors in c). d) is the derivative of c).*

Close to T_c, at the appropriate deppining frequencies, the vortex core dissipation lowers and more power is therefore needed to trigger the avalanche process. Once outside the peak in U'' the normal behavior is recovered. In the case of figure 6.22 b a second increase in depinning power is observed just before reaching T_c. This fact could explain the splitting of some avalanches as $T \to T_c$, as observed in fig 6.23.

Splitting of avalanches

Sometimes a single step in a power-temperature sweep splits into several of smaller magnitude.

We atribute this to a single avalanche triggered at low temperatures that, at higher temperatures finds it more favorable to appear as several weaker avalanches. Figure 6.23 shows an example of this with several splitting branches, whereas a few of them do not split. We can understand this by the usual behavior of avalanche dendritic patterns with temperature. At lower temperatures, there are fewer, stronger avalanches while at higher temperatures it is favorable to have many of them, of smaller size. The splitting could correspond to the transition from triggering a single large avalanche at lower temperatures, compared to triggering many, smaller ones at higher temperatures.

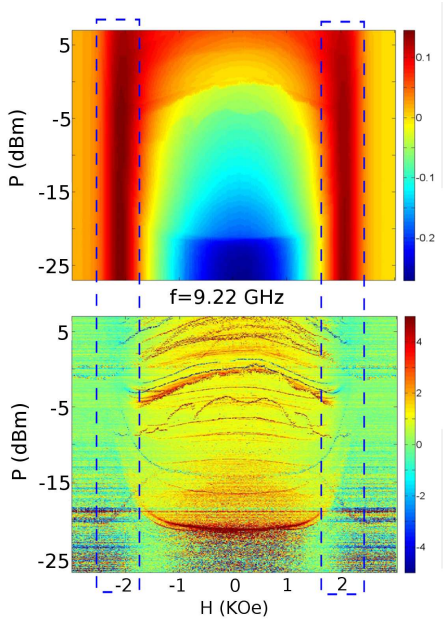

Figure 6.21: *Top: U'' vs H and P. Bottom: Differential plot of top panel. The dashed lines mark the peak in losses.*

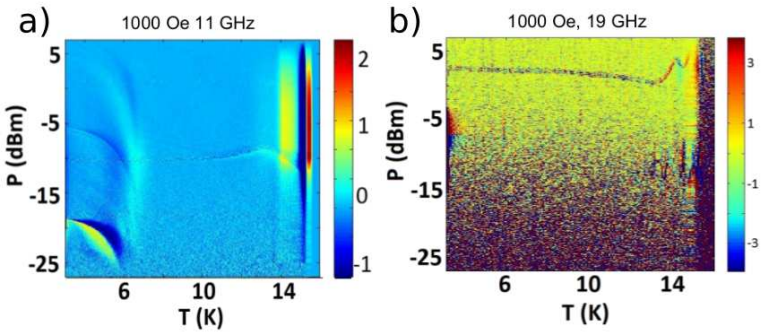

Figure 6.22: *a) Avalanches in a 180 nm NbN film, showing normal behavior at low temperatures, and stimulation near T_c. b) Same measurement for a different frequency. The unexpected behavior related to an excess in losses is present, this time with two increases in depinnin power.*

Change of field dependence of avalanches as a function of frequency

In figure 6.24 we show an analysis similar to the previous section, but as a function of field for a fixed temperature of 5K. In the graph are shown the deppining powers extracted from P-H sweeps at different frequencies.

The different surfaces correspond to different avalanches. At the deppining frequency (in this case 9.2 GHz) all deppining powers go through a minimum. This ensures that the steps correspond to deppining powers that trigger avalanches. If our deppinning frequencies (that we see as a decrease in microwave transmission) corresponded to some kind of reflection of microwaves towards the generator (due to geometrical resonances or some other reason), indeed we would see a maximum in the required power instead of the minimum that is observed. This is so because in that case more power would be needed to compensate for the extra reflection in the cables, connectors, etc.

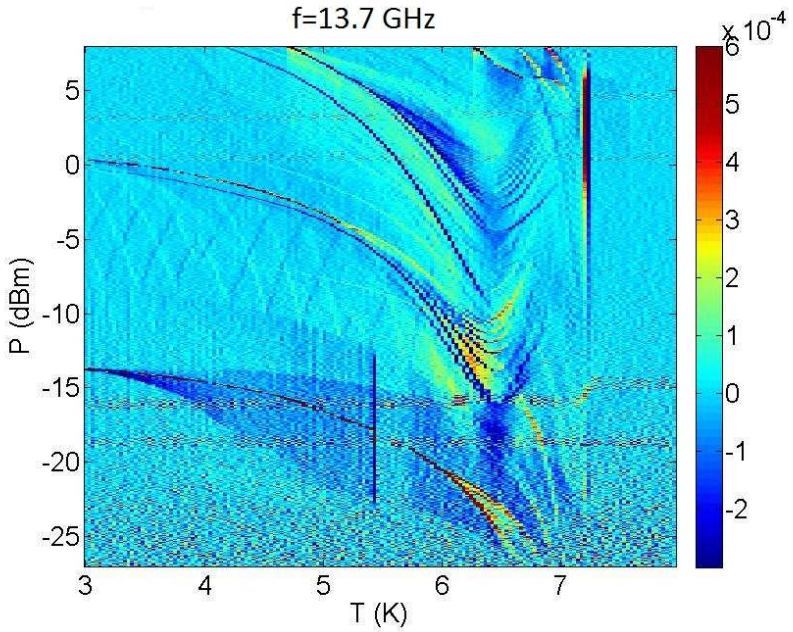

Figure 6.23: *P-T sweep at a deppining frequency (differential plot with respect to T). Multiple avalanches are observed, several of them increasing their deppining power at about 6.5 K. The upper and middle avalanches start to split around 5.5 K into several branches.*

Crossing a deppining frequency

Figure 6.25 shows different sweeps of temperature and power at frequencies approaching and surpassing one of the several deppining frequencies. The avalanches become wider until the stimulation effects are no longer visible as we go even higher in frequency. The maximum in U'' shows also a dependence in frequency, which influences in this way the different shape of the avalanche depinning powers. The dependence of the peak in losses (from the position of this peak is obtained the irreversibility line) is known to depend on the frequency[191], but to the best of our knowledge it has not been tested to frequencies as high as GHz where more complicated behaviors. In particular, in the present case the peak in losses, corresponding to the irreversibility lines, is present or not, for different ranges of frequencies, and its dependence on temperature also depends on the frequency. As far as we can tell from measurements of different quantities, there is a, dependence of the imaginary peak with frequency, which occurs at very specific frequencies, which we have been calling depinning frequencies. Around these frequencies the vortex dissipation undergoes big changes in a narrow frequency window, creating the unexpected avalanche behaviors described in this chapter.

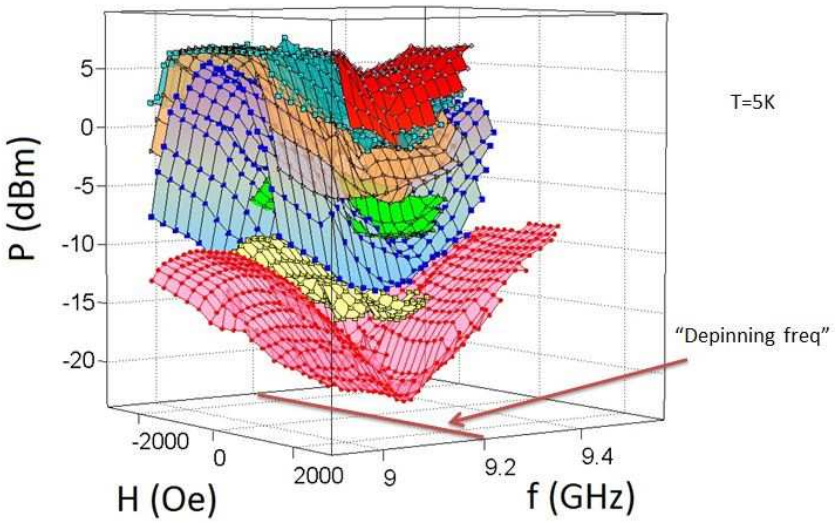

Figure 6.24: *Deppining power for different avalanches as a function of f and H.*

Summary and conclusions

The experimental observation of stimulated superconductivity in type II superconductors has been used to quantify relative changes in vortex dissipation as a function of mobility (pinning). At high enough *mw* power and/or low enough *mw* frequencies when MSSC is not effective, the vortex matching effects are clearly observed as periodic *dips in the mw losses* when $H_\perp = n\Phi_0/a^2$ (n is an integer number and Φ_0 the magnetic flux quantum). In contrast to that, in a broad range of *mw* powers (sufficiently below limiting values which heat the sample) and at high enough frequencies (above about 0.6 GHz) mobile (off-matching) vortices dissipate less than pinned vortices. One clearly observes *peaks in the vortex dissipation* in matching conditions. The higher the frequency, the broader the *mw* power range where matching anomalies are seen as peaks in losses. Microwave stimulation changes from dips at matching fields at the lowest frequencies to peaks at frequencies exceeding a few GHz, in agreement with TDGL simulations, that indicate a transition to a nonlinear regime when mobile (interstitial) vortices dissipate less than pinned ones. The observed effects (transition from peaks to dips) remain qualitatively unchanged for the range up to 3 vortices per pinning center, meaning that intervortex interaction has a weak influence on our resuts. Simulation of the vortex response to a microwave magnetic field shows that the changes of the vortex core radius and (through differential analysis of the modulus of the order parameter) the vortices motion under a high frequency magnetic fiedl field. We find vortex deformation to be minimum because its displacement at microwave frequencies is small in comparison with radius oscillations.

Stray fields of Py dots do not seem to play an essential role for the effects we observe (in the past[192] they have proven to affect the pinning, but not to be the only cause of matching conditions). Also, there is a strong structural pinning profile due to the fact that the SC film covers the array of dots and not vice versa as in[193]. A qualitative similarity in the microwave losses measured with perpendicular or with inclined nearly parallel magnetic fields further confirms that the observed effects are not induced by the presence of an in-plain component of magnetic field.

Also, the stimulation effects on flux avalanches have been studied. When avalanches cross the peak in losses they invert their tendency to weaken as $T \to T_c$ or $H \to H_{c2}$. We attribute the extra losses to an enhanced number of quasiparticles avaliable, that

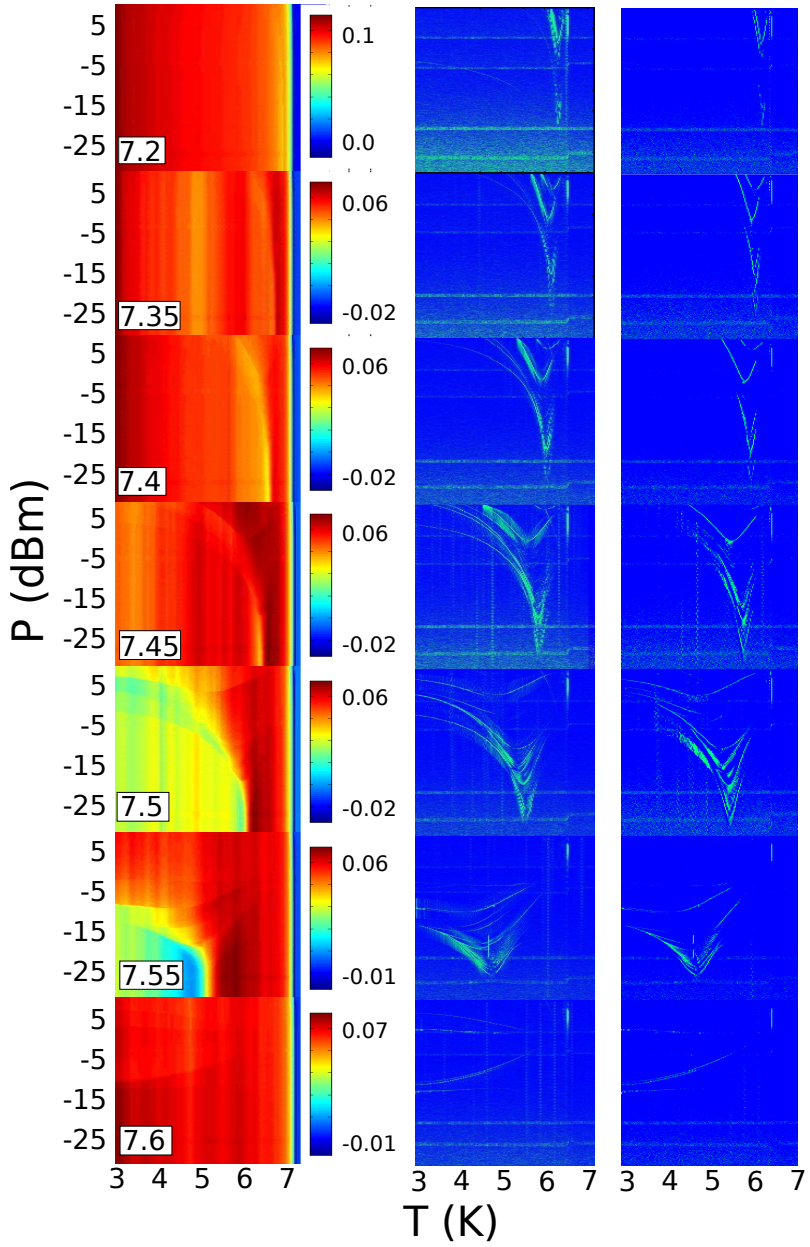

Figure 6.25: *Different sweeps of P and T around a depinning frequency (f=7.5 GHz). The frequency for each row is indicated, in GHz, in the box inside each figure in the first row. The left column is the measurement of U''. The central column is the absolute value of the derivative of the left with respect to temperature. In the right column, every value of the central column has been set to 0 or to 1, below or above a certain threshold, to better identify the avalanches.*

reinforce the stimulation effect on avalanche triggering powers, which make them harder to trigger in this region than would be expected. This effect is specially pronounced at special frequencies which produce a sudden development of the loss peak in the frequencies around it.

We have also observed circumstances in which an avalanche triggering power splis into many. We attribute this to the change of avalanche morphology with temperature, since closer to T_c avalanche patterns typically are more numerous and shorter.

7. Appendix A

Basics of Network Analysis

To describe the behavior of electric circuits when currents and voltages are not constant in time one needs to take into consideration inductance and capacitance, in addition to electrical resistance of the components of the circuit.

The cables that transmit AC signals can be described as transmission lines. Any transmission line has a characteristic impedance per unit length. A typical way to represent the transmission line is breaking it into several portions, connected in series. Each of these portions has some impedance that is modeled as an arrange of lumped elements, as shown in figure 7.1.

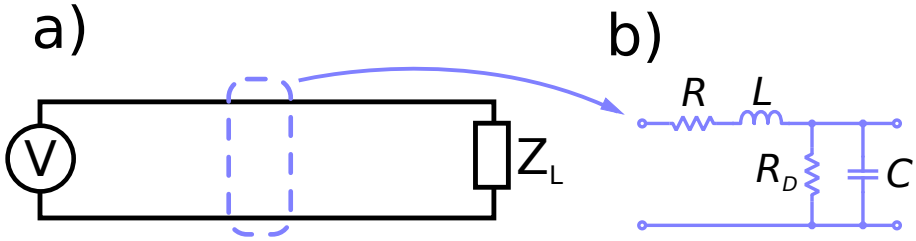

Figure 7.1: *a) A power supply sets a voltage V between the two ends of a load with impedance Z_L. b) Any section of the transmission line can be characterized by a resistance (R), inductance (L), capacitance (C) and resistance due to dielectric loss (R_D).*

Apart from the evident electrical resistance of the conductor, the transmission line will have a certain capacitance, due to the voltage drop between the ground and signal conductors of the line, separated by a dielectric medium.

Also, a parallel resistor represent possible current leakages through the dielectric.

Finally, a lumped inductance models the self inductance of cables, especially important when they bend.

For such a transmission line then, there is a characteristic impedance per unit length which characterizes the transmission line (as long as it keeps the same features along its whole length), given by:

$$Z_0 = \sqrt{\frac{R_0 + j\omega L}{R_D + j\omega C}}$$

As explained below, one needs to make sure that the elements present in a high frequency circuit (as a rule of thumb, we can consider a frequency as "high frequency" when the wavelength of the signal is much shorter than the circuit physical length) are of an impedance as similar as possible to that of the rest of the elements. Otherwise part of the incident waves will be reflected back to the generator and will not reach the elements connected to the circuit.

In DC circuits, a current cannot pass through elements like capacitors, but due to self induction, a voltage variable in time can induce currents even across an air gap. A consecuence of this is that a DC current cannot flow through an open circuit, but an AC current can.

Scattering parameters

Network analyzers measure the so called "scattering parameters". These parameters represent the ratios of voltage (or, sometimes, power) sent from (V_s) and received in (V_r) different ports (or the same port, in the case of reflection measurements). The parameters are numbered with two indices, the first representing the detector port, and the second, the emitter port. Then, for example, S_{11} is the ratio $V_{r,1}/V_{s,1}$, and $S_{1,2}$ is $V_{r,1}/V_{s,2}$ when no other signal is emitted from other ports. When they are, the scattering parameters become more complicated, and are typically grouped in the "transmission matrix". To keep things simple, and since in this thesis only two ports have been used for the measurements, we will only consider the scattering matrix for this case, but it is straightforward to incorporate more ports:

$$\begin{pmatrix} V_{1,r} \\ V_{2,r} \end{pmatrix} = \begin{pmatrix} S_{11} & S_{12} \\ S_{21} & S_{22} \end{pmatrix} \begin{pmatrix} V_{1,s} \\ V_{2,s} \end{pmatrix}$$

Here, $V_{1,r}$ and $V_{2,r}$ are the signals received in ports 1 and 2. They depend on $V_{1,s}$ and $V_{2,s}$, the voltage signals sent from ports 1 and 2. Scattering parameters are normally expressed in decibels. Depending on whether they represent the quotient of voltages or powers, there is a factor of 2 to convert between them. This is so because:

$$S_{xy,P} = \frac{P_x}{P_y} = \frac{V_x^2/R}{V_y^2/R} = \left(\frac{V_x}{V_y}\right)^2 = (S_{xy,V})^2$$

Then, by the definition of decibels,

$$P(dB) = 10 \cdot log\left(\frac{P_x}{P_y}\right) = 20 \cdot log\left(\frac{V_x}{V_y}\right)$$

The previous applies to the module of the voltage and power, but since we are dealing with sinusoidal signals, their phase carries important information. Phase shifts give raise to an imaginary part of the signal, that is not present in the DC response. For example, the imaginary part of the response of an oscillator to a sinusoidal signal contains information about the energy dissipation, given that a dissipating factor will cause the oscillator to not be able to follow in phase the excitation signal. For this reason, the amplitude and phase of the scattering parameters are measured separately.

Impedance matching

To ensure that the maximum possible power is transferred between different elements in a network, one needs to make sure that these elements are all of the same impedance. The impedance has a real (resistive) part, and an imaginary (reactive) part: $Z = R + iX$. Only the resistive part is responsible for Joule dissipation. This is called "impedance matching". This can be explained with the so called "maximum power transfer theorem". Given an electric circuit consisting of a power supply (of value V_S) and two impedances in series (one of them representing the internal impedance, Z_S of the power supply), the power dissipated in the other one (the load), with a resistive value R_L (which would then represent some device connected to the supply) is given by:

$$P_L = I_{rms}^2 R_L = \frac{1}{2}|I|^2 R_L = \frac{1}{2}\left(\frac{|V_S|}{|Z_S + Z_L|}\right)^2 R_L = \frac{1}{2}\frac{|V_S|^2 R_L}{(R_S + R_L)^2 + (X_S + X_L)^2}$$

A way to minimize the power dissipated is to set $X_S = -X_L$ and minimize the resistive part, which remains: $\frac{1}{2}\frac{|V_S|^2 R_L}{(R_S+R_L)^2} = \frac{1}{2}\frac{|V_S|^2}{\frac{R_S^2}{R_L} + R_L + 2R_S}$. We can now find the maxima of the denominator,

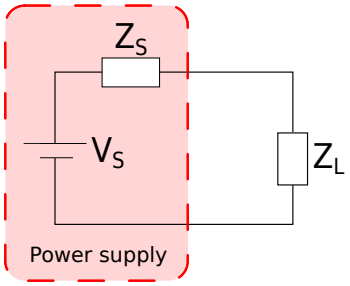

Figure 7.2: *A load connected to a power supply with internal impedance*

which would minimize the power dissipated in R_L: $\frac{d(R_L+2R_S+R_S^2/R_L)}{dR_L} = 1-(R_S/R_L)^2 = 0 \rightarrow R_S = R_L$. Then, the impedance that minimizes the dissipated power when connecting it to a source is $Z_L = R_X + X_S = Z_S^*$, and for this reason all the cables and connectors used in microwave measurements should have the same characteristic impedance. A typical value is 50Ω, which gives a good tradeoff between power handling and low losses.

Internals of a network analyzer

Some of the most important elements in network analyzers are briefly described next:

- **Generator:** Network analyzers use a built-in phase-locked voltage controlled oscillator to generate high frequencies signals.
- **Couplers:** Since the S parameters are ratios between detected and emitted voltages, an important part of the network analyzers hardware is dedicated to precisely know how much power the output signal has, in order to compare it to the inputs. This is done with directional couplers. These devices are able to divert part of the output signal to a detector (like those which received the inputs). How much power is diverted in this way is given by coupling factor. Ideally, One can think of directional couplers as bifurcations for the rf signal, with the particularity that only a certain percentage of the signal follows one way, and the rest follows the other (obviously, there will also be reflections and losses involved). The bifurcation of power, in theory, only occurs for waves travelling in one direction, whereas waves travelling in the opposite one will not be split. In practice, there are leakages, described by a directivity parameter, which have the signal splitted, but in a much smaller amount.
- **Bridges:** To measure impedances, directional bridges are useful. These four terminal devices show a zero voltage drop between two of its arms if the impedance connected to each arm is the same. Thus, when one connects a device with an impedance mismatch, a voltage can be measured to find changes in impedance, both in amplitude and phase.
- **Detectors:** To measure the power of rf signals, a common device is a diode detector, which converts an ac signal to a DC value of power. These detectors cannot provide information about the phase. Modern analyzers use tuned receivers, for their many advantages over diode detectors. In them, the high frequency signal to be detected is mixed with another frequency, from an internal oscillator, to provide an intermediate frequency (IF). By controlling the bandwidth of the IF (a parameter which can be input in the network analyzer), one can control how much noise falls outside of the detection range. This allows for much cleaner signals (at the expense of a longer sweep time). This feature cannot be achieved with diode detectors, which deal with signals (noise or not) in the whole range.

8. Appendix B

Deduction of Ginzburg-Landau equations

In the case of non-zero external magnetic fields, it is useful to work with the Gibbs free energy. The terms including Ψ are to be minimized. Second order derivative terms will be considered zero. We start with general variations of the order parameter for each term:

- $|\Psi|^2 \to |\Psi+\delta\Psi|^2 - |\Psi|^2 =$
  $(\Psi+\delta\Psi)(\Psi^*+\delta\Psi^*) - \Psi\Psi^* =$
  $\Psi\Psi^* + \Psi\delta\Psi^* + \Psi^*\delta\Psi + \delta\Psi\delta\Psi^{*\,0} - \Psi\Psi^* \simeq$
  $\Psi\delta\Psi^* + \Psi^*\delta\Psi$
- $|\Psi|^4 \to |\Psi+\delta\Psi|^4 - |\Psi|^4 =$
  $(|\Psi+\delta\Psi|^2)^2 - |\Psi|^4 =$
  $(\Psi\Psi^* + \Psi\delta\Psi^* + \Psi^*\delta\Psi + \delta\Psi\delta\Psi^*)^2 - |\Psi|^4 =$
  $|\Psi|^4 + |\Psi|^2\Psi^*\delta\Psi + |\Psi|^2\Psi\delta\Psi^* + |\Psi|^2|\delta\Psi|^2 + |\Psi|^2\Psi^*\delta\Psi + (\Psi^*\delta\Psi)^2 +$
  $(\Psi^*\delta\Psi)(\Psi\delta\Psi^*) + \Psi^*\delta\Psi|\delta\Psi|^2 + |\Psi|^2\Psi\delta\Psi^* + (\Psi^*\delta\Psi)(\Psi\delta\Psi^*) + (\Psi\delta\Psi^*)^2 +$
  $\Psi\delta\Psi^*|\delta\Psi|^2 + |\Psi|^2|\delta\Psi|^2 + \Psi^*\delta\Psi|\delta\Psi|^2 + \Psi\delta\Psi^*|\delta\Psi|^2 + |\delta\Psi|^4 - |\Psi|^4 =$
  $2|\Psi|^2\Psi^*\delta\Psi + 2|\Psi|^2\Psi\delta\Psi^* + 2|\Psi|^2|\delta\Psi|^{2\,0} + (\Psi^*\delta\Psi)^{2\,0} + 2|\Psi\delta\Psi|^{2\,0} + 2\Psi^*\delta\Psi|\delta\Psi|^{2\,0} + (\Psi\delta\Psi^*)^{2\,0} +$
  $2\Psi\delta\Psi^*|\delta\Psi|^{2\,0} + |\delta\Psi|^{4\,0} \simeq$
  $2|\Psi|^2\Psi^*\delta\Psi + 2|\Psi|^2\Psi\delta\Psi^*$
- Defining the momentum operator as $\vec{P} = \hbar\left(-i\vec{\nabla} - \frac{e}{c\hbar}\vec{A}\right)$, the variation of the momentum operator is:
  $|\vec{P}\Psi|^2 \to |\vec{P}(\Psi+\delta\Psi)|^2 - |(\vec{P}(\Psi)|^2 =$
  $(\vec{P}(\Psi+\delta\Psi))(\vec{P}(\Psi+\delta\Psi))^* - (\vec{P}\Psi)(\vec{P}\Psi)^* =$
  $(\vec{P}\Psi + \vec{P}\delta\Psi)(\vec{P}^*\Psi^* + \vec{P}^*\delta\Psi^*) - (\vec{P}\Psi)(\vec{P}^*\Psi^*) =$
  $(\vec{P}\Psi)(\vec{P}^*\Psi^*) + (\vec{P}\Psi)(\vec{P}^*\delta\Psi^*) + (\vec{P}\delta\Psi)(\vec{P}^*\Psi^*) + (\vec{P}\delta\Psi)(\vec{P}^*\delta\Psi^*) - (\vec{P}\Psi)(\vec{P}^*\Psi^*) =$
  $(\vec{P}\Psi)(\vec{P}^*\delta\Psi^*) + (\vec{P}\delta\Psi)(\vec{P}^*\Psi^*) + |\vec{P}\delta\Psi|^{2\,0} \simeq$
  $(\vec{P}\Psi)(\vec{P}^*\delta\Psi^*) + (\vec{P}\delta\Psi)(\vec{P}^*\Psi^*)$

Rearranging all the terms, then, the variation of the Gibbs free energy is as follows:

$$\delta G = \int_V \left\{ \alpha(\Psi^*\delta\Psi + \Psi\delta\Psi^*) + \frac{\beta}{2}(2|\Psi|^2\Psi^*\delta\Psi + 2|\Psi|^2\Psi\delta\Psi^*) + \frac{1}{2m}\left[(\vec{P}\Psi)(\vec{P}^*\delta\Psi^*) + (\vec{P}\delta\Psi)(\vec{P}^*\Psi^*)\right] \right\} dV$$

The first Ginzburg Landau equation is obtained by minimizing the free energy with respect to Ψ^*. Therefore, $\delta\Psi = 0$ and $\delta\Psi^* \neq 0$, and the minimized energy is:

$$\delta G|_{\delta\Psi=0} = \int_V \left\{ \alpha\Psi\delta\Psi^* + \beta|\Psi|^2\Psi\delta\Psi^* + \frac{1}{2m}(\vec{P}\Psi)(\vec{P}^*\delta\Psi^*) \right\} dV =$$

The last term can be rewritten as:

$$\frac{1}{2m}(\vec{P}\Psi)(\vec{P}^*\delta\Psi^*) = \frac{\hbar}{2m}\vec{P}\Psi(i\vec{\nabla}\delta\Psi^*) - \frac{e}{2mc}(\vec{P}\Psi)(\vec{A}\delta\Psi^*)$$

The relation $\vec{\nabla}(\vec{P}\Psi\delta\Psi^*) = \vec{P}\Psi\vec{\nabla}(\delta\Psi^*) + \vec{\nabla}(\vec{P}\Psi)\delta\Psi^*$ can be used to get at:

$$\frac{i\hbar}{2m}(\vec{\nabla}(\vec{P}\Psi\delta\Psi^*) - \vec{\nabla}(\vec{P}\Psi)\delta\Psi^*) - \frac{e}{2mc}(\vec{P}\Psi)(\vec{A}\delta\Psi^*)$$

Therefore, inserting the last term of the minimization of energy in the latter form we get:

$$\int_V \left\{ \alpha\Psi\delta\Psi^* + \beta|\Psi|^2\Psi\delta\Psi^* + \frac{i\hbar}{2m}(\vec{\nabla}(\vec{P}\Psi\delta\Psi^*) - \vec{\nabla}(\vec{P}\Psi)\delta\Psi^*) - \frac{e}{2mc}(\vec{P}\Psi\vec{A}\delta\Psi^*) \right\} dV = 0$$

With Gauss Theorem $\int_V (\vec{\nabla}\cdot\vec{u})dV = \oint_{\partial V}(\vec{u}\cdot\vec{n})dS$, with $\vec{n}$ a vector normal to the integration surface, the first term corresponding to the moment operator can be expressed as a surface integral:

$$\int_V \left\{ \alpha\Psi\delta\Psi^* + \beta|\Psi|^2\Psi\delta\Psi^* + \frac{i\hbar}{2m}(-\vec{\nabla}(\vec{P}\Psi)\delta\Psi^*) - \frac{e}{2mc}(\vec{P}\Psi\vec{A}\delta\Psi^*) \right\} dV + \frac{i\hbar}{2m}\oint_{\partial V}((\vec{P}\Psi\delta\Psi^*)\cdot\vec{n})dS = 0$$

For this relation to hold, both integrals must be zero, since there are constants such as α, β and e in the first integral that are absent in the second, therefore in principle they cannot cancel each other out. Equating the argument of the first integral to zero yields the first Ginzburg-Landau equation, noting that the term $\delta\Psi^*$ can be dropped:

$$\alpha\Psi + \beta|\Psi|^2\Psi + \frac{1}{2m}\left(-i\hbar\vec{\nabla}(\vec{P}\Psi) - \frac{e}{c}(\vec{P}\Psi)\vec{A}\right) =$$

$$\boxed{\alpha\Psi + \beta|\Psi|^2\Psi + \frac{\hbar^2}{2m}\left(-i\vec{\nabla} - \frac{e}{\hbar c}\vec{A}\right)^2\Psi = 0}$$

The surface integral that was obtained with the Gauss Theorem provides a boundary condition, since it describes the behavior of Ψ at the surface of the superconductor:

$$\boxed{(\vec{P}\Psi)\cdot\vec{n} = \left(-i\vec{\nabla} - \frac{e}{\hbar c}\vec{A}\right)\Psi\cdot\vec{n} = 0}$$

For the second Ginzburg-Landau equation we need to calculate the following variations with respect to $\vec{A}$:

- $|\vec{P}\Psi|^2 \to |\vec{P}(\vec{A}+\delta\vec{A})\Psi|^2 - |\vec{P}(\vec{A})\Psi|^2 =$
  $\left(-i\vec{\nabla} - \frac{e}{c\hbar}(\vec{A}+\delta\vec{A})\right)^*\Psi^*\cdot\left(-i\vec{\nabla} - \frac{e}{c\hbar}(\vec{A}+\delta\vec{A})\right)\Psi - |\vec{P}(\vec{A})\Psi|^2 =$
  $\left(\vec{P}^*\Psi^* - \frac{e}{c\hbar}\delta\vec{A}^*\Psi^*\right)\left(\vec{P}\Psi - \frac{e}{c\hbar}\delta\vec{A}\Psi\right) - |\vec{P}(\vec{A})\Psi|^2 =$
  $\cancel{|\vec{P}(\vec{A})|^2} - \vec{P}^*\Psi^*\frac{e}{c\hbar}\delta\vec{A}\Psi - \left(\frac{e}{c\hbar}\delta\vec{A}\right)^*\Psi^*\vec{P}\Psi + \cancel{\frac{e}{c\hbar}\delta\vec{A}^*\Psi^*\delta\vec{A}\Psi}^{\to 0} - \cancel{|\vec{P}(\vec{A})|^2} \simeq$
  $\boxed{-\vec{P}^*\Psi^*\left(\frac{e}{c\hbar}\delta\vec{A}\right)\Psi - \left(\frac{e}{c\hbar}\delta\vec{A}\right)^*\Psi^*\vec{P}\Psi}$
- $(\vec{\nabla}\times\vec{A} - \vec{H})^2 \to (\vec{\nabla}\times(\vec{A}+\delta\vec{A}) - \vec{H})^2 - (\vec{\nabla}\times\vec{A} - \vec{H})^2 =$
  $((\vec{\nabla}\times\vec{A} - \vec{H}) + \vec{\nabla}\times\delta\vec{A})^2 - (\vec{\nabla}\times\vec{A} - \vec{H})^2 =$
  $\cancel{(\vec{\nabla}\times\vec{A} - \vec{H})^2} + (\vec{\nabla}\times\delta\vec{A})^2 + 2(\vec{\nabla}\times\vec{A} - \vec{H})(\vec{\nabla}\times\delta\vec{A}) - \cancel{(\vec{\nabla}\times\vec{A} - \vec{H})^2} \simeq$
  $\cancel{(\vec{\nabla}\times\delta\vec{A})^2}^{\to 0} + 2(\nabla\times\vec{A} - \vec{H})(\vec{\nabla}\times\delta\vec{A})$

Replacing these terms in the minimization of the Gibbs free energy with respect to $\vec{A}$ gives:

$$\int \frac{\hbar^2}{2m}\left(-\vec{P}^*\Psi^*\left(\frac{e}{c\hbar}\delta\vec{A}\right)\Psi - \left(\frac{e}{c\hbar}\delta\vec{A}\right)^*\Psi^*\vec{P}\Psi\right) + \frac{2}{8\pi}(\vec{\nabla}\times\vec{A} - \vec{H})(\vec{\nabla}\times\delta\vec{A})dV = 0$$

We can now use the relation: $\vec{\nabla}\cdot(\vec{f}\times\vec{g}) = (\vec{\nabla}\times\vec{f})\cdot\vec{g} - \vec{f}\cdot(\vec{\nabla}\times\vec{g})$ in the following way: $\vec{\nabla}\cdot(\delta\vec{A}\times(\vec{\nabla}\times\vec{A}-\vec{H})) = (\vec{\nabla}\times\delta\vec{A})(\vec{\nabla}\times\vec{A}-\vec{H}) - \delta\vec{A}\cdot\vec{\nabla}\times(\vec{\nabla}\times\vec{A}-\vec{H})$ so that the minimization of energy results:

$$\int\left[\frac{\hbar^2}{2m}\left(-\vec{P}^*\Psi^*\left(\frac{e}{c\hbar}\delta\vec{A}\right)\Psi - \left(\frac{e}{c\hbar}\delta\vec{A}\right)^*\Psi^*\vec{P}\Psi\right) + \right.$$
$$\left. \frac{1}{4\pi}\vec{\nabla}(\delta\vec{A}\times(\vec{\nabla}\times\vec{A})-\vec{H}) + \delta\vec{A}\cdot\vec{\nabla}\times(\vec{\nabla}\times\vec{A}-\vec{H})\right] dV = 0$$

The first part of the second term vanishes, which can be proved with Gauss' theorem, converting the volume integral to a surface one: $\int_V \vec{\nabla}[\delta\vec{A}\times(\vec{\nabla}\times\vec{A})-\vec{H}]dV = \oint_{\partial V}[\delta\vec{A}\times(\vec{\nabla}\times\vec{A})-\vec{H}]d\vec{S}$ Since the volume integral is done over all space, the surface integral would be performed on a surface infinitely far from the sample. Then, no magnetization is present and $\vec{B}=\vec{H}$ (in Gaussian units, $\mu_0=1$). Then, only in this term, $\vec{\nabla}\times\vec{A}=\vec{H}$ and the surface integral is zero. The minimization of the free energy is simplified, multipling everything by c and rearranging terms:

$$\int\delta\vec{A}\left[\frac{\hbar e}{2m}(-\vec{P}^*\Psi^*\Psi - \Psi^*\vec{P}\Psi) + \frac{c}{4\pi}\vec{\nabla}\times(\vec{\nabla}\times\vec{A}-\vec{H})\right]dV = 0$$

As $\delta\vec{A}$ is arbitrary, the factor between square brackets must be zero:

$$\frac{\hbar e}{2m}(\vec{P}^*\Psi^*\Psi + \Psi^*\vec{P}\Psi) = \frac{c}{4\pi}\vec{\nabla}\times(\vec{\nabla}\times\vec{A}-\vec{H})$$

With the definitions: $\vec{P} = \left(-i\vec{\nabla} - \frac{e}{c\hbar}\vec{A}\right)$ and $\vec{B} = \vec{\nabla}\times\vec{A}$, after some more rearrangments we arrive at:

$$\frac{i\hbar e}{2m}(\Psi\vec{\nabla}\Psi^* - \Psi^*\vec{\nabla}\Psi) - \frac{e^2}{cm}\vec{A}|\Psi|^2 = \frac{c}{4\pi}(\vec{\nabla}\times\vec{B} - \vec{\nabla}\times\vec{H})$$

Deduction of the η constant from the first TDGL equation

We start with the equation for Ψ' described in[138]. With respect to the stationary GL equation, we use the symbol $\Psi' = \Psi\cdot\sqrt{\frac{-\alpha}{\beta}}$. This is done for further simplifying the form of the free energy functional, specifically, to get rid of the coefficients α and β that muliply the condensation energy terms Ψ and $|\Psi|^2\Psi$ respectively :

$$\frac{1}{D}\left(\frac{\partial}{\partial t} + i\frac{2e\phi}{\hbar}\right)\Psi' + \frac{1}{\xi^2}(|\Psi'|^2-1)\Psi' + \left(\frac{\vec{\nabla}}{i} - \frac{e_s}{\hbar c}\vec{A}\right)^2\Psi' = 0$$

Here, D is the diffusion constant for the normal phase, χ is the coherence length, e_s is the Cooper pair electric charge ($e_s = 2e$), $\vec{A}$ is the vector potential and ϕ is the electric potential, that thanks to the zero potential gauge can be eliminated. To simplify the equation, a rescaling of the different variables can be made, in order to reabsorb the physical constants in only one coefficient, simplifying calculations later. For this, we scale distances, time, magnetic field, temperature and vector potential as follows:

$$r \to r'\cdot\xi_0$$
$$t \to t'\cdot t_0$$

$$H \to H' \cdot H_{c2}^{T=0}$$

$$T \to T' \cdot T_c$$

$$\vec{A} \to \vec{A}' \cdot \xi_0 H_{c2}^{T=0}$$

Here $H_{c2}^{T=0}$ refers to the upper critical field at zero temperature. t_0 is given by $t_0 = \frac{\pi\hbar}{96 k_B T_c}$, being T_c the critical temperature at zero field. It is connected to the first critical field by the relation $H_{c2}^{T=0} = \sqrt{2}\kappa H_c^{T=0}$(Tinkham, p 135). The primed variables (r', t' and $\vec{A}'$) are dimensionless coefficients, and we will eventually solve the TDGL equations for them. To get the absolute values after the calculations are finished, one must multiply again by the corresponding scaling factor (ξ_0, t_0 or $\xi_0 H_{c2}^{T=0}$).
The rescaling of lengths and time must be taken into account in the gradient and in the time derivative with respect to the dimensionless variables ($\vec{\nabla}'$ and $\partial/\partial t'$):

$$\vec{\nabla} = \left(\frac{\partial}{\partial x} + \frac{\partial}{\partial y} + \frac{\partial}{\partial z}\right) \to \left(\frac{\partial}{\partial (x'\xi_0)} + \frac{\partial}{\partial (y'\xi_0)} + \frac{\partial}{\partial (z'\xi_0)}\right) = \frac{1}{\xi_0}\vec{\nabla}'$$

$$\frac{\partial}{\partial t} \to \frac{\partial}{\partial (t' t_0)} = \frac{1}{t_0}\frac{\partial}{\partial t'}$$

The TDGL equation for Ψ becomes, using also that $\xi = \xi_0/\sqrt{1 - T/T_c}$

$$\frac{1}{Dt_0}\frac{\partial \Psi'}{\partial t'} + \frac{1-T'}{\xi_0^2}(|\Psi'|^2 - 1)\Psi' + \left(\frac{\vec{\nabla}'}{i\xi_0} - \frac{e_s}{\cancel{\hbar} c}\sqrt{2}\kappa\sqrt{\frac{\cancel{\hbar^2}}{2m_s\cancel{|\alpha|}}\frac{4\pi|\alpha|^2}{\beta}}\vec{A}'\right)^2 \Psi' = 0$$

Using the relation

$$\frac{1}{\lambda} = \sqrt{\frac{4\pi|\alpha|e_s^2}{\beta m_s c^2}}$$

and the definition $\kappa = \lambda/\xi$ the TDGL equation for Ψ' simplifies to:

$$\frac{1}{Dt_0}\frac{\partial \Psi'}{\partial t'} + \frac{1-T'}{\xi_0^2}(|\Psi'|^2 - 1)\Psi' + \frac{1}{\xi_0^2}(-i\vec{\nabla}' - \vec{A}')^2\Psi' = 0$$

Dropping the prime symbols, for simplicity, we arrive at the first dimensionless equation:

$$\eta\frac{\partial \Psi}{\partial t} + (1-T)(|\Psi|^2 - 1)\Psi + (-i\vec{\nabla} - \vec{A})^2\Psi = 0$$

With η a dimensionless number:

$$\eta = \frac{\xi_0^2}{Dt_0}$$

Since D and t_0 are in the η parameter, the latter gives an idea of the ratio of the normal and superconducting characteristic times.

Electric and magnetic potentials in CGS units:

$$\vec{E} = -\vec{\nabla}\phi - \frac{1}{c}\frac{\partial \vec{A}}{\partial t}$$

$$\vec{B} = \vec{\nabla} \times \vec{A}$$

The fields (measurable quantities with relevant phisical meaning, fields and currents) remain unchanged under the following gauge transformations:

$$\phi \to \phi + \frac{1}{c}\frac{\partial \chi}{\partial t};\ \vec{A} \to \vec{A} - \vec{\nabla}\chi;\ \vec{j} = \frac{c}{4\pi}\vec{\nabla} \times (\vec{\nabla} \times \vec{A})$$

Since general properties of the vector operators guarantee the invariance of the $\vec{E}$ and $\vec{B}$ fields under these transformations, we can choose any scalar function χ. With the choice:

$$\frac{\partial \chi}{\partial t} = -c\phi$$

The electric potential vanishes:

$$\phi = 0$$

Then, the normal current contribution, that is due to the electric potential ϕ is reabsorbed in the vector potential after this gauge transformation. Also TDGL remain unchanged after the gauge transformation. We can use this fact for simplifying the TDGL equations, taking $\phi = 0$. We only need to solve the equation for $\vec{A}$ and Ψ to get all the information needed about magnetic field and normal and superconducting currents.

Part III

Conclusion

General conclusions

In this thesis the high frequency response of magnetic and superconducting systems in out of equilibrium conditions has been studied both experimentally, and with simulations. As for magnetic systems we have focused on the propagation of spin waves through domain walls in different configurations in the case of triangular permalloy dots, as well as the exploration of methods using artificial pinning to help stabilize metastable states, whose interesting properties can be taken advantage of, as long as the state does not decay into the more stable ground state.
In superconducting systems we have studied the behavior of superconducting vortices in the presence of a microwave field, close to the superconducting transition, both by approaching the critical temperature and the critical field. Also, we have studied these effects in the behavior of flux avalanches. Simulations have been done to understand better the results obtained.

In **chapter 3** we have used artificial pinning centers to modify the magnetization reversal process of cricular magnetic dots, by trapping and stabilizing in them domain walls and vortices. Anisotropic magnetorresistance measurements confirm that vortices releasing from the pinning sites produce steps in the otherwise smooth curves. Simulations confirm this process, and help design new arrangements of pinning centers in order to achieve different reversals and trapping of magnetic structures.

In **chapter 4** we have studied the conditions for the propagation of spin waves in triangular dots in the saturated B and Y magnetic states. In these cases, the magnetic field is applied parallel or perpendicular to a side of the triangle and we observe spin waves modes localized (at least for the first eigenfrequencies) at the triangle borders. These results are extensible to any structure with straigth sides, inclined an angle with respect to the applied field. Higher fields and frequencies yield narrower wavefronts. Further simulations when such spin waves are excited at one localized zone show how the shape of the magnetic system can be designed to fit different purposes, such as overcoming corners or dodge obstacles. Also, the vortex state has proven to be stable for thick enought dots, giving well defined, standing wave oscillaitons along domain walls at different eigenfrequencies, evenly spaced. A clear transition from the saturated state eigenmodes is observed in the excitation spectra.

In **chapter 5** we have described the numerical method to solve the time dependent Ginzburg Landau equation, as well as applied it to some cases to study the motion of superconducting vortices under different types of boundary conditions. We have confirmed the presence of tilted vortices under inclined fields, confirming the correct implementation of the algorithm in three dimensions. We have explored the case of a steady flow of vortices as a consequence of placing two permanent magnets of opposite orientations at both ends of a superconducting strip. We have also put our program to the test for well known phenomena such as vortex motion due to a current flow, or rectification effects. Some further steps to extend the program have been discussed.

In **chapter 6** we have explored the effect of stimulation of superconductivity by microwaves on the vortex motion near the superconducting transition. For this we have used the optimum power (the balance point between stimulation and dissipation in the superconducting system) as a tool to study the vortex dissipation in matching and off-matching conditions, which appear as a consequence of an array of periodic pinning centers on the sample. We have found that less mobile (pinned) vortices can dissipate more energy than the more mobile ones (non pinned), in a similar manner to the well known Larkin Ovchinnikov effect, in our case of alternating motion. A computer model helped us interpret the results. Similarly we have studied the stimulation effect on superconducting flux avalanches, to find that the power required to release an avalanch can be increased thanks to stimulation effects as we approach the superconducting transition, when there is an excess of dissipation.

Conclusiones generales

En esta tesis se ha estudiado, experimentalmente y mediante simulaciones, el comportamiento a altas frecuencias de sistemas magnéticos y superconductores fuera del equilibrio. En lo referente a sistemas magnéticos nos hemos concentrado en la propagación de ondas de espín a través de paredes de dominio en diferentes configuraciones en elementos triangulares de permalloy. También hemos explorado métodos para la estabilización de estados metaestables usando centros de anclaje artificiales. Esto permitiría aprovechar las interesantes propiedades de estos sistemas, mientras no decan a su estado fundamental. En sistemas superconductores hemos estudiado el comportamiento de vórtices superconductores en presencia de una excitación de microondas cerca de la transición superconductora, acercándonos tanto a la temperatura crítica como al campo crítico. También hemos estudiado estos efectos en la el comportamiento de avalanchas de flujo. Se ha realizado simulaciones para entender los resultados experimentales.

En el **capítulo 3** hemos usado centros de anclaje artificial para modificar el proceso de inversión de imanación en elementos magnéticos circulares, atrapando y estabilizando paredes de dominio y vórtices en ellos. Nuestras medidas de magnetorresistencia anisótropa confirmn que los vórtices que se liberan de su fijación en los centros de anclaje producen discontinuidades en curvas de imanación que por lo demás son suaves. Las simulaciones confirman este proceso y además pueden ser utilizadas para diseñar nuevas disposiciones de los centros de anclaje para lograr diferentes inversiones y formas de capturar estructuras magnéticas.

En el **capítulo 4** hemos estudiado las condiciones para la propagación de ondas de espín en elementos triangulares micrométricos en los estados saturados B e Y. En estos casos el campo magnético es aplicado paralelo o perpendicular a uno de los lados del triángulo y observamos modos de ondas de espín localizados (al menos en las primeras frecuencias características) cerca de los bordes del triángulo. Estos resultados son generalizables a cualquier estructura que tenga lados rectos, inclinados cierto ángulo con respecto al campo magnético aplicado. Mayores campos y frecuencias de la excitación de microondas dan lugar a frentes de onda más estrechos. Otras simulaciones muestran cómo, al excitar estas ondas de espín en zonas localizadas, la forma de la estructura magnética puede adaptarse para cumplir diferentes propósitos, como sobrepasar esquinas o sortear obstáculos. También se ha comprobado cómo el estado de vórtice, que es estable para elementos triangulares suficientemente gruesos, puede dar lugar a ondas de espín estacionarias a lo largo de paredes de dominio a diferentes frecuencias características equiespaciadas. Se observa una clara transición de los modos de oscilación en estado saturado al pasar a estado vórtice en el espectro de excitaciones.

En el **capítulo 5** se ha descrito el método numérico para resolver la ecuación de Ginzburg Landau dependiente del tiempo, así como se ha aplicado a algunos casos para estudiar el movimiento de vórtices superconductores con distintos tipos de condiciones de contorno. Hemos comprobado la presencia de vórtices inclinados al aplicar campos magnéticos inclinados, confirmando la implementación del algoritmo en tres dimensiones. Hemos considerado el caso de un flujo continuo de vórtices al colocar dos imanes permanentes con orientaciones opuestas en ambos extremos de una lámina superconductora. También

hemos comprobado algunos otros fenómenos conocidos como el movimiento de vórtices bajo una corriente continua o efectos de rectificación. Por último se ha discutido algunas posibles propuestas para extender las capacidades de este programa.

En el **capítulo 6** hemos estudiado el efecto de estimulación de superconductividad por microondas en el movimiento de vórtices cerca de la transición superconductora. Para esto hemos usado la potencia óptima (el equilibrio entre la estimulación y la disipación en sistemas superconductores) en condiciones de "matching" y fuera de ellas, que aparecen como consecuencia de una disposición de centros de anclaje periódicos colocados sobre la muestra. Hemos detectado que los vórtices menos móviles (anclados) pueden disipar más energía que los más móviles (no anclados), de forma similar al efecto Larkin Ovchinnikov, en nuestro caso en un movimiento oscilatorio. Un modelo numérico nos ha ayudado a interpretar los resultados. Similarmente hemos estudiado el efecto de estimulación en avalanchas de flujo superconductoras, para comprobar cómo la potencia requeridad para desencadenarlas puede ser incrementada gracias a la estimulación al encontrarse la muestra más cerca de la transición superconductora, cuando existe un exceso en la disipación.

List of publications

Publications relevant to the thesis

- A. Lara, V. Metlushko and F. G. Aliev, "Observation of propagating edge spin waves modes", Journal of Applied Physics **114**, 21395 (2013)
- A. Lara, V. Metlushko, M. García-Hernández, F.G. Aliev, "Spin waves along the edge states", SPIN **4**, 1440003 (2014)
- A. Lara, O. V. Dobrovolskiy, J. L. Prieto, M. Huth, and F. G. Aliev, "Magnetization reversal assisted by half antivortex states in nanostructured circular cobalt disks", Applied Physics Letters **105**, 182402 (2014)
- A. Lara, F. G. Aliev, A. V. Silhanek and V. V. Moshchalkov, "Microwave stimulated superconductivity due to presence of vortices", Scientific Reports **5** 9187 (2015)

Participation in other publications

- I. Martínez, J. P. Cascales, A. Lara, P. Andrés and F. G. Aliev, "Transient lateral photovoltaic effect in patterned ferromagnetic metal oxide semiconductor films", Proc. SPIE **9358** 93580O-1 (2015)
- I. Martínez, J. P. Cascales, A. Lara, P. Andrés and F. G. Aliev, "Magnetic state dependent transient lateral photovoltaic effect in patterned ferromagnetic metal oxide semiconductor films", AIP Advances **5**, 117207 (2015)
- A. A. Awad, A. Lara, M. García-Hernández, V. Metlushko, K.Y. Guslienko, F.G. Aliev, "Spin Wave Excitations and Winter's Magnons in Vertically Coupled Vortex State Permalloy Dot". J Supercond Nov Magn. **26**, 2057-2061 (2013).
- A. A. Awad, A. Lara, V. Metlushko, K. Y. Guslienko, and F. G. Aliev. "Broadband probing magnetization dynamics of the coupled vortex state permalloy layers in nanopillars", Appl. Phys. Lett. **100**, 262406 (2012)
- F. G. Aliev, A. A. Awad, D. Dieleman, A. Lara, V. Metlushko, and K. Y. Guslienko, "Localized domain-wall excitations in patterned magnetic dots probed by broadband ferromagnetic resonance". Physical Review B **84**, 144406 (2011)
- D. Herranz, A. Gómez-Ibarlucea, M. Schafers, A. Lara, G. Reiss, and F. G. Aliev, "Low frequency noise due to magnetic inhomogeneities in submicron FeCoB/MgO/FeCoB magnetic tunnel junctions", Applied Physics Letters **99**, 062511 (2011)

Bibliography

[1] A. J. Newell, W. Williams, and D. J. Dunlop. "A generalization of the demagnetizing tensor for nonuniform magnetization". *J. of Geophys. Research, Solid Earth* **98**.B6 (1993), pp. 9551–9555 (cit. on p. 18).

[2] J. R. Hall and H. E. Hook. "Sold State Physics". Wiley, 1994, pp. 227–228 (cit. on p. 19).

[3] K. L. Metlov and K. Y. Guslienko. "Stability of magnetic vortex in soft magnetic nano-sized circular cylinder". *Journal of Magnetism and Magnetic Materials* **242-245** (2002), pp. 1015–1017 (cit. on p. 20).

[4] T. Shinjo et al. "Magnetic vortex core observation in circular dots of permalloy". *Science* **289** (2000), pp. 930–932 (cit. on p. 21).

[5] C. A. F. Vaz et al. "Multiplicity of magnetic domain states in circular elements probed by photoemission electron microscopy". *Phys. Rev. B* **72** (22 Dec. 2005), p. 224426 (cit. on p. 22).

[6] F. G. Aliev et al. "Localized domain-wall excitations in patterned magnetic dots probed by broadband ferromagnetic resonance". *Phys. Rev. B* **84** (14 Oct. 2011), p. 144406 (cit. on pp. 22, 30, 31, 64, 69, 82).

[7] M. Jaafar et al. "Field induced vortex dynamics in magnetic Ni nanotriangles". *Nanotechnology* **19**.28 (2008), p. 285717 (cit. on p. 23).

[8] M. Jaafar et al. "Control of the chirality and polarity of magnetic vortices in triangular nanodots". *Phys. Rev. B* **81** (5 Feb. 2010), p. 054439 (cit. on p. 23).

[9] M. Bailleul et al. "Microwave spectrum of square permalloy dots: Multidomain state". *Phys. Rev. B* **76** (22 Dec. 2007), p. 224401 (cit. on p. 23).

[10] M. Coïsson et al. "Magnetic vortex chirality determination via local hysteresis loops measurements with magnetic force microscopy". *Scientific Reports* **6** (2016) (cit. on p. 23).

[11] F. Montoncello and F. Nizzoli. "Spin modes of triangular magnetic nanodots in the vortex, Y and buckle states". *Journal of Applied Physics* **107**.2, 023906 (2010) (cit. on pp. 24, 74, 75, 79).

[12] *Wikipedia page for Anisotropic Magnetoresistance* (Dec. 2016) (cit. on p. 26).

[13] D. Polder. "On the Quantum Theory of Ferromagnetic Resonance". *Phys. Rev.* **73** (9 May 1948), pp. 1116–1116 (cit. on p. 26).

[14] J. Miltat, G. Albuquerque, and A. Thiaville. "An introduction to micromagnetics in the dynamic regime". *Spin dynamics in confined magnetic structures I* (2002), p. 4 (cit. on p. 26).

[15] T. Moriyama et al. "Anti-damping spin transfer torque through epitaxial nickel oxide". *Applied Physics Letters* **106**.16 (2015), p. 162406 (cit. on p. 27).

[16] M. J. Donahue and D. G. Porter. "OOMMF". *Interagency Report NISTIR 6376* (1999) (cit. on pp. 27, 54, 65, 76).

[17] A. Vansteenkiste et al. “The design and verification of MuMax3”. *AIP Advances* **4** (10), p. 107133 (cit. on pp. 27, 54, 76).

[18] S. O. Demokritov, B. Hillebrands, and A. N. Slavin. “Brillouin light scattering studies of confined spin waves: linear and nonlinear confinement”. *Physics Reports* **348** (2001), pp. 441–489 (cit. on p. 28).

[19] M. Buess et al. “Fourier Transform Imaging of Spin Vortex Eigenmodes”. *Phys. Rev. Lett.* **93** (7 Aug. 2004), p. 077207 (cit. on p. 29).

[20] F. G. Aliev et al. “Spin waves in circular soft magnetic dots at the crossover between vortex and single domain state”. *Phys. Rev. B* **79** (2009), p. 174433 (cit. on p. 30).

[21] J. M. Winter. “Bloch Wall Excitation. Application to Nuclear Resonance in a Bloch Wall”. *Phys. Rev.* **124** (2 Oct. 1961), pp. 452–459 (cit. on p. 30).

[22] F. G. Aliev et al. “Localized domain-wall excitations in patterned magnetic dots probed by broadband ferromagnetic resonance”. *Phys. Rev. B* **84** (14 Oct. 2011), p. 144406 (cit. on p. 31).

[23] C. P. Bean. “Magnetization of High Field Superconductors”. *Reviews of Modern Physics* **36** (1964), pp. 31–39 (cit. on p. 33).

[24] D. Saint-James and P. Gennes. “Onset of superconductivity in decreasing fields”. *Physics Letters* **7**.5 (1963), pp. 306–308 (cit. on p. 34).

[25] J. Bardeen, L. N. Cooper, and J. R. Schrieffer. “Theory of Superconductivity”. *Phys. Rev.* **108** (5 Dec. 1957), pp. 1175–1204 (cit. on p. 34).

[26] R. Feynman. “The Feynman Lectures on Physics”. Vol. 3. *www.feynmanlectures.caltech.edu*. Chap. 21-6 (cit. on p. 34).

[27] L. Landau. “On the theory of phase transitions”. *L. D. Landau Collected Papers* **1** (1969), pp. 234–252 (cit. on p. 35).

[28] W. C. Gonçalves et al. “Numerical solution of the time dependent Ginzburg-Landau equations for mixed (d + s)-wave superconductors”. *Journal of Mathematical Physics* **55**.4 (2014), p. 041501 (cit. on p. 35).

[29] M. Tinkham. “Introduction to Superconductivity”. Dover Publications. Chap. Introduction to electrodynamics of superconductors (cit. on pp. 35, 37).

[30] U. Essmann and H. Trauble. “The direct observation of individual flux lines in type II superconductors”. *Physics Letters* **24A** (1967), pp. 526, 527 (cit. on p. 36).

[31] E. H. Brandt. “Tilted and curved vortices in anisotropic superconducting films”. *Phys. Rev. B* **48** (9 Sept. 1993), pp. 6699–6702 (cit. on p. 36).

[32] M. W. Coffey and J. R. Clem. “Theory of rf magnetic permeability of isotropic type-II superconductors in a parallel field”. *Phys. Rev. B* **45** (1992), p. 9872 (cit. on pp. 36, 38, 117, 118).

[33] P. W. Anderson and Y. B. Kim. “Hard Superconductivity: Theory of the Motion of Abrikosov Flux Lines”. *Rev. Mod. Phys.* **36** (1964), p. 39 (cit. on p. 38).

[34] J. I. Gittleman and B. Rosenblum. “Radio-frequency resistance in the mixed state for subcritical currents”. *Phys. Rev. Lett* **16** (1966), p. 734 (cit. on pp. 38, 114).

[35] E. H. Brandt. “Penetration of magnetic ac fields into type-II superconductors”. *Phys. Rev. Lett.* **67** (16 Oct. 1991), pp. 2219–2222 (cit. on p. 38).

[36] J. D. Johnson, D. N. Zheng, and A. M. Campbell. “IRC in Superconductivity Research Review”. *University of Cambridge* (1994), p. 165 (cit. on p. 39).

[37] D. J. Priour and H. A. Fertig. "Vortex States of a Superconducting Film from a Magnetic Dot Array". *Phys. Rev. Lett.* **93** (5 July 2004), p. 057003 (cit. on p. 39).

[38] G. Blatter et al. "Vortices in high-temperature superconductors". *Rev. Mod. Phys* **66** (1994), p. 1125 (cit. on pp. 39, 114).

[39] A. V. Silhanek et al. "Influence of artificial pinning on vortex lattice instability in superconducting films". *New Journal of Physics* **14** (2012), p. 053006 (cit. on pp. 39, 123).

[40] A. V. Silhanek et al. "Manipulation of the vortex motion in nanostructured ferromagnetic / superconductor hybrids". *Applied Physics Letters* **90** (18 2007), p. 182501 (cit. on pp. 39, 108).

[41] M. Menghini et al. "Direct visualization of magnetic vortex pinning in superconductors". *Phys. Rev. B* **79** (14 Apr. 2009), p. 144501 (cit. on pp. 39, 40).

[42] J. V. de Vondel et al. "Self-organized mode-locking effect in superconductor/ferromagnet hybrids". *Phys. Rev. B* **79** (5 Feb. 2009), p. 054527 (cit. on pp. 39, 74).

[43] A. Lara et al. "Microwave-stimulated superconductivity due to presence of vortices". *Nat. Sci. Reports* **5** (2015), p. 9187 (cit. on pp. 39, 115).

[44] J. I. Martín et al. "Flux Pinning in a Superconductor by an Array of Submicrometer Magnetic Dots". *Phys. Rev. Lett.* **79** (10 Sept. 1997), pp. 1929–1932 (cit. on p. 40).

[45] T. H. Johansen et al. "Dendritic magnetic instability in superconducting MgB_2 films". *Europhys. Lett.* **59**.4 (2002), pp. 599–605 (cit. on p. 40).

[46] G. Ghigo et al. "Switching response of MgB_2 thin-film microwave resonators due to local nonlinear Joule heating". *Phys. Rev. B* **82** (5 Aug. 2010), p. 054520 (cit. on pp. 41, 114, 116, 126).

[47] M. Motta et al. "Controllable morphology of flux avalanches in microstructured superconductors". *Phys. Rev. B* **89** (13 Apr. 2014), p. 134508 (cit. on p. 41).

[48] G. Ghigo et al. "Evidence of rf-driven dendritic vortex avalanches in MgB2 microwave resonators". *Journal Applied Physics* **102** (11), p. 113901 (cit. on pp. 41, 114, 116, 126).

[49] A. F. G. Wyatt et al. "Microwave enhanced critical supercurrents in superconducting constricted Tin films". *Phys. Rev. Lett.* **16** (1966), p. 1166 (cit. on pp. 41, 113).

[50] P. W. Anderson and A. H. Dayem. "Radio-Frequency Effects in Superconducting Thin Film Bridges". *Phys. Rev. Lett.* **13** (6 Aug. 1964), pp. 195–197 (cit. on p. 41).

[51] G. M. Eliashberg. "Film superconductivity stimulated by a high frequency field". *JETP Lett* **11** (1970), p. 114 (cit. on pp. 41, 113, 122, 125).

[52] D. R. Heslinga and T. M. Klapwijk. "Enhancement of superconductivity far above the critical temperature in double-barrier tunnel junctions". *Phys. Rev. B* **47** (1993), p. 5157 (cit. on pp. 42, 113).

[53] S. K. Tolpygo and V. A. Tulin. "Influence of microwave irradiation on high-frequency absorption by thin superconducting films (superconductivity stimulation)". *Sov. Phys. JETP.* **57** (1983), p. 123 (cit. on pp. 42, 113).

[54] J. A. Pals and J. Dobben. "Observation or Order-Parameter Enhancement by Microwave Irradiation in a Superconducting Aluminum Cylinder". *Phys. Rev. Lett.* **44** (1980), p. 1143 (cit. on pp. 42, 113).

[55] J. A. Pals and J. Dobben. “Measurements of microwave-enhanced superconductivity in aluminum strips”. *Phys. Rev. B* **20** (1979), p. 935 (cit. on pp. 42, 113).

[56] R. Stancliff and J. Dunsmore. “The Evolution of RF/Microwave Network Analyzers”. *Agilent technical note* **5989-6353EN** (2014) (cit. on p. 43).

[57] D. Chumakov et al. “Nanosecond time-scale switching of permalloy thin film elements studied by wide-field time-resolved Kerr microscopy”. *Phys. Rev. B* **71** (1 Jan. 2005), p. 014410 (cit. on pp. 45, 46).

[58] O. Karlqvist. “Calculations of the magnetic field in the ferromagnetic layer of a magnetic drum”. *Trans. R. Soc. Technol.* **86** (1 1945) (cit. on p. 46).

[59] C. A. Harper. “High Performance Printed Circuit Boards”. *McGraw Hill Professional* (2000), p. 3.21 (cit. on p. 47).

[60] B. Kuanr, R. Camley, and Z. Celinski. “Extrinsic contribution to Gilbert damping in sputtered NiFe films by ferromagnetic resonance”. *Journal of Magnetism and Magnetic Materials* **286** (2005), pp. 276–281 (cit. on p. 50).

[61] R. D. McMichael and M. D. Stiles. “Magnetic normal modes of nanoelements”. *Journal of Applied Physics* **97**.10 (2005), 10J901. eprint: http://dx.doi.org/10.1063/1.1852191 (cit. on p. 55).

[62] O. Tchernyshyov and G.-W. Chern. “Fractional Vortices and Composite Domain Walls in Flat Nanomagnets”. *Phys. Rev. Lett.* **95** (19 Nov. 2005), p. 197204 (cit. on p. 63).

[63] A. Pushp et al. “Domain wall trajectory determined by its fractional topological edge defects”. *Nat Phys* **9** (2013), pp. 505–511 (cit. on p. 63).

[64] K.-S. Lee et al. “Edge-Soliton-Mediated Vortex-Core Reversal Dynamics”. *Phys. Rev. Lett.* **106** (14 Apr. 2011), p. 147201 (cit. on pp. 63, 64).

[65] D. J. Clarke et al. “Dynamics of a vortex domain wall in a magnetic nanostrip: Application of the collective-coordinate approach”. *Phys. Rev. B* **78** (13 Oct. 2008), p. 134412 (cit. on pp. 63, 64).

[66] T. Shinjo. “Nanomagnetism and Spintronics (2nd edition)” (2014) (cit. on p. 63).

[67] S. Kaka et al. “Mutual phase-locking of microwave spin torque nano-oscillators”. *Nature* **437** (7057 2005) (cit. on pp. 63, 74).

[68] A. A. Awad et al. “Spin excitation frequencies in magnetostatically coupled arrays of vortex state circular Permalloy dots”. *Appl. Phys. Lett.* **97** (2010), p. 132501 (cit. on p. 63).

[69] K. Y. Guslienko. “Magnetic vortex state stability, reversal and dynamics in restricted geometries.” *Journal of Nanoscience and Nanotechnology* **8** (2008), p. 2745 (cit. on pp. 63, 64).

[70] A. Hamadeh et al. “Perfect and robust phase-locking of a spin transfer vortex nano-oscillator to an external microwave source”. *Appl. Phys. Lett.* **104** (2014), p. 022408 (cit. on p. 63).

[71] G. E. Rowlands and I. N. Krivorotov. “Magnetization dynamics in a dual free-layer spin-torque nano-oscillator”. *Phys. Rev. B* **86** (9 Sept. 2012), p. 094425 (cit. on p. 64).

[72] A. Dussaux et al. “Large amplitude spin torque vortex oscillations at zero external field using a perpendicular spin polarizer”. *Appl. Phys. Lett.* **105** (2014), p. 022404 (cit. on p. 64).

[73] J. Li et al. “Stabilizing a magnetic vortex/antivortex array in single crystalline Fe/Ag(001) microstructures”. *Appl. Phys. Lett.* **104** (2014), p. 262409 (cit. on p. 64).

[74] J. A. J. Burgess et al. “Quantitative Magneto-Mechanical Detection and Control of the Barkhausen Effect”. *Science* **339**.6123 (2013), pp. 1051–1054 (cit. on pp. 64, 67, 70).

[75] T. Uhlig et al. “Shifting and Pinning of a Magnetic Vortex Core in a Permalloy Dot by a Magnetic Field”. *Phys. Rev. Lett.* **95** (23 Nov. 2005), p. 237205 (cit. on pp. 64, 67, 70).

[76] G. M. Wysin. “Vortex-in-nanodot potentials in thin circular magnetic dots”. *Journal of Physics: Condensed Matter* **22**.37 (2010), p. 376002 (cit. on p. 64).

[77] M. Rahma et al. “Vortex pinning at individual defects in magnetic nanodisks”. *Journal of Appl. Phys* **93** (2003), p. 7429 (cit. on p. 64).

[78] V. P. Kravchuk et al. “Off-centred immobile magnetic vortex under influence of spin-transfer torque”. *Journal of Physics D: Applied Physics* **44**.28 (2011), p. 285001 (cit. on p. 64).

[79] M. Rahm et al. “Multistable switching due to magnetic vortices pinned at artificial pinning sites”. *Appl. Phys. Lett.* **85** (2004), p. 1553 (cit. on p. 64).

[80] A. R. Pereira et al. “Analytical and Monte Carlo study of two antidots in magnetic nanodisks with vortex-like magnetization”. *Journal of Appl. Phys.* **101** (2007), p. 034310 (cit. on p. 64).

[81] D. Toscano et al. “Dynamics of the vortex core in magnetic nanodisks with a ring of magnetic impurities”. *Appl. Phys. Lett.* **101** (2012), p. 252402 (cit. on p. 64).

[82] F. Hoffmann et al. “Mode degeneracy due to vortex core removal in magnetic disks”. *Phys. Rev. B* **76** (1 July 2007), p. 014416 (cit. on pp. 64, 67).

[83] P. Vavassori et al. “Vortex rotation control in Permalloy disks with small circular voids”. *Journal. Appl. Phys.* **99** (2005), p. 053902 (cit. on p. 64).

[84] M. Rahm, J. Stahl, and D. Weiss. “Programmable logic elements based on ferromagnetic nanodisks containing two antidots”. *Appl. Phys. Lett.* **87** (2005), p. 182107 (cit. on p. 64).

[85] F. G. Aliev et al. “Probing ground state in circular magnetic dots: Single vs. double magnetic vortex”. *ICEAA conference* (Sept. 2010), pp. 160–163 (cit. on pp. 64, 66, 67).

[86] N. Wang, X. L. Wang, and A. Ruotolo. “A Magnetic Flower State-Based Memory Cell”. *IEEE Transactions on Magnetics* **47**.7 (July 2011), pp. 1970–1973 (cit. on pp. 64, 70).

[87] O. I. Freire. “Advances in Magnetic Force Microscopy (PhD thesis)”. *CSIC* (2014), p. 139 (cit. on p. 64).

[88] D. Grujicic and B. Pesic. “Micromagnetic studies of cobalt microbars fabricated by nanoimprint lithography and electrodeposition”. *J. Magn. Magn. Mat.* **285** (2005), p. 303 (cit. on p. 65).

[89] L. Serrano-Ramón et al. “Ultrasmall Functional Ferromagnetic Nanostructures Grown by Focused Electron-Beam-Induced Deposition”. *ACS Nano* **5** (2011), p. 7781 (cit. on p. 68).

[90] D. Herranz et al. “Low frequency noise due to magnetic inhomogeneities in submicron FeCoB/MgO/FeCoB magnetic tunnel junctions”. *Appl. Phys. Lett.* **99** (2011), p. 062511 (cit. on p. 70).

[91] A. Chanthbouala et al. “Vertical-current-induced domain-wall motion in MgO-based magnetic tunnel junctions with low current densities”. *Nature Physics* **7** (2011), p. 626 (cit. on p. 70).

[92] V. V. Kruglyak, S. O. Demokritov, and D. Grundler. “Magnonics”. *Journal of Physics D: Applied Physics* **43**.26 (2010), p. 264001 (cit. on pp. 73, 74).

[93] A. A. Serga, A. V. Chumak, and B. Hillebrands. “YIG magnonics”. *Journal of Physics D: Applied Physics* **43**.26 (2010), p. 264002 (cit. on p. 73).

[94] S.-K. Kim. “Micromagnetic computer simulations of spin waves in nanometre-scale patterned magnetic elements”. *Journal of Physics D: Applied Physics* **43**.26 (2010), p. 264004 (cit. on p. 73).

[95] A. Fert. “Nobel Lecture: Origin, development and future of spintronics*”. *Rev. Mod. Phys.* **80** (4 Dec. 2008), pp. 1517–1530 (cit. on p. 73).

[96] G. E. W. Bauer, E. Saitoh, and B. J. van Wees. “Spin caloritronics”. *Nat. Mater.* **11** (5 2012), pp. 391–399 (cit. on p. 73).

[97] Y. Kajiwara et al. “Transmission of electrical signals by spin-wave interconversion in a magnetic insulator”. *Nature* **464** (7286 2010), pp. 262–266 (cit. on p. 73).

[98] J. Xiao and G. E. W. Bauer. “Spin-Wave Excitation in Magnetic Insulators by Spin-Transfer Torque”. *Phys. Rev. Lett.* **108** (21 May 2012), p. 217204 (cit. on p. 73).

[99] T. Sebastian et al. “Nonlinear Emission of Spin-Wave Caustics from an Edge Mode of a Microstructured $Co_2Mn_{0.6}Fe_{0.4}Si$ Waveguide”. *Phys. Rev. Lett.* **110** (6 Feb. 2013), p. 067201 (cit. on p. 73).

[100] C. Scheck et al. “Low Relaxation Rate in Epitaxial Vanadium-Doped Ultrathin Iron Films”. *Phys. Rev. Lett.* **98** (11 Mar. 2007), p. 117601 (cit. on p. 73).

[101] C. Bayer et al. “Spin waves in an inhomogeneously magnetized stripe”. *Phys. Rev. B* **69** (13 Apr. 2004), p. 134401 (cit. on p. 73).

[102] J. Jorzick et al. “Spin Wave Wells in Nonellipsoidal Micrometer Size Magnetic Elements”. *Phys. Rev. Lett.* **88** (4 Jan. 2002), p. 047204 (cit. on p. 73).

[103] J. W. Lau and J. M. Shaw. “Magnetic nanostructures for advanced technologies: fabrication, metrology and challenges”. *Journal of Physics D: Applied Physics* **44**.30 (2011), p. 303001 (cit. on p. 73).

[104] A. Khitun, M. Bao, and K. L. Wang. “Spin Wave Magnetic NanoFabric: A New Approach to Spin-Based Logic Circuitry”. *IEEE Transactions on Magnetics* **44**.9 (Sept. 2008), pp. 2141–2152 (cit. on p. 73).

[105] B. Lenk et al. “The building blocks of magnonics”. *Physics Reports* **507**.4–5 (2011), pp. 107–136 (cit. on pp. 73, 74).

[106] X. Xing et al. “Engineering spin-wave channels in submicrometer magnonic waveguides”. *AIP Advances* **3**.3, 032144 (2013) (cit. on p. 74).

[107] H. Feldner et al. “Dynamical Signatures of Edge-State Magnetism on Graphene Nanoribbons”. *Phys. Rev. Lett.* **106** (22 May 2011), p. 226401 (cit. on p. 74).

[108] R. Shindou et al. “Topological chiral magnonic edge mode in a magnonic crystal”. *Phys. Rev. B* **87** (17 May 2013), p. 174427 (cit. on p. 74).

[109] R. Shindou et al. “Chiral spin-wave edge modes in dipolar magnetic thin films”. *Phys. Rev. B* **87** (17 May 2013), p. 174402 (cit. on p. 74).

[110] V. E. Demidov et al. “Nano-optics with spin waves at microwave frequencies”. *Applied Physics Letters* **92** (2008), p. 232503 (cit. on p. 74).

[111] D. K. Koltsov, R. P. Cowburn, and M. E. Welland. “Micromagnetics of ferromagnetic equilateral triangular prisms”. *Journal of Applied Physics* **88**.9 (2000), pp. 5315–5317 (cit. on p. 74).

[112] L. Thevenard et al. “Six-fold configurational anisotropy and magnetic reversal in nanoscale Permalloy triangles”. *Journal of Applied Physics* **106**.6, 063902 (2009) (cit. on p. 74).

[113] M. Jaafar et al. “Control of the chirality and polarity of magnetic vortices in triangular nanodots”. *Phys. Rev. B* **81** (5 Feb. 2010), p. 054439 (cit. on p. 74).

[114] C. S. Lin et al. “Spin wave localization in a triangular nanomagnet”. *Journal of Applied Physics* **108**.11, 114305 (2010) (cit. on pp. 74, 75, 79).

[115] R. Huber et al. “Reciprocal Damon-Eshbach-type spin wave excitation in a magnonic crystal due to tunable magnetic symmetry”. *Applied Physics Letters* **102**.1, 012403 (2013) (cit. on p. 74).

[116] S. Choi, K.-S. Lee, and S.-K. Kim. “Spin-wave interference”. *Applied Physics Letters* **89**.6, 062501 (2006) (cit. on p. 74).

[117] S. Mansfeld et al. “Spin Wave Diffraction and Perfect Imaging of a Grating”. *Phys. Rev. Lett.* **108** (4 Jan. 2012), p. 047204 (cit. on p. 74).

[118] S. Choi et al. “Double-contact spin-torque nano-oscillator with optimized spin-wave coupling: Micromagnetic modeling”. *Applied Physics Letters* **90**.8, 083114 (2007) (cit. on p. 74).

[119] F. Macià, A. D. Kent, and F. C. Hoppensteadt. “Spin-wave interference patterns created by spin-torque nano-oscillators for memory and computation”. *Nanotechnology* **22**.9 (2011), p. 095301 (cit. on p. 74).

[120] P. Hyben, K. D. McKinstry, and P. Kabos. “Coupled edge-guided magnetostatic waves”. *J. Appl. Phys.* **73** (1993), p. 7015 (cit. on p. 74).

[121] K. Vogt et al. “Spin waves turning a corner”. *Applied Physics Letters* **101** (2012), p. 042410 (cit. on p. 74).

[122] V. S. Tkachenko et al. “Propagation and scattering of spin waves in curved magnonic waveguides”. *Applied Physics Letters* **101** (2012), p. 152402 (cit. on p. 74).

[123] X. Xing et al. “How do spin waves pass through a bend?” *Sci. Rep.* **3** (2013), p. 2958 (cit. on p. 74).

[124] K. Vogt et al. “Realization of a spin-wave multiplexer”. *Nat. Commun.* **5** (2014), p. 3727 (cit. on p. 74).

[125] A. V. Chumak, A. A. Serga, and B. Hillebrands. “Magnon transistor for all magnon data processing”. *Nat. Comm.* **5** (2014), p. 4700 (cit. on p. 74).

[126] “A European strategy for micro and nanoelectronic components and systems” () (cit. on p. 74).

[127] M. P. Kostylev et al. “Spin-wave logical gates”. *Applied Physics Letters* **87** (2005), p. 153501 (cit. on p. 74).

[128] A. V. Chumak, A. A. Serga, and B. Hillebrands. “Magnon transistor for all-magnon data processing”. *Nat. Commun.* **5** (2014), p. 4700 (cit. on p. 74).

[129] G. Gruner. “The dynamics of spin-density waves”. *Rev. Mod. Phys.* **66** (1 Jan. 1994), pp. 1–24 (cit. on p. 85).

[130] F. S. Ma et al. “Magnonic band structure investigation of one-dimensional bi-component magnonic crystal waveguides”. *Nanosc. Res. Lett.* **7** (498 2012) (cit. on p. 85).

[131] C. Bayer et al. “Spin-wave excitations in finite rectangular elements of $Ni_{80}Fe_{20}$”. *Phys. Rev. B* **72** (6 Aug. 2005), p. 064427 (cit. on p. 86).

[132] A. Lara, V. Metlushko, and F. G. Aliev. “Observation of propagating edge spin waves modes”. *Journal of Applied Physics* **114**.21, 213905 (2013) (cit. on p. 90).

[133] V. E. Demidov et al. “Self-focusing of spin waves in Permalloy microstripes”. *Applied Physics Letters* **91**.25 (2007), p. 252504 (cit. on p. 90).

[134] S. Berweger et al. “Near-field control and imaging of free charge carrier variations in GaN nanowires”. *Applied Physics Letters* **108**.7 (2016), p. 073101 (cit. on p. 93).

[135] J. C. Weber et al. “Gallium nitride nanowire probe for near-field scanning microwave microscopy”. *Applied Physics Letters* **104**.2 (2014), p. 023113 (cit. on p. 93).

[136] A. Lara et al. “Scanning Microwave Microscopy for the Study of Spin Waves.” *MMM conference 2016, abstract book, page 144* (2016) (cit. on p. 93).

[137] “SMM imaging of dopant structures of semiconductor devices”. *Keysight Technologies Application note* (2014) (cit. on p. 93).

[138] R. Kato, Y. Enomoto, and S. Maekawa. “Computer simulations of dynamics of flux lines in type-II superconductors”. *Phys. Rev. B* **44** (1991), pp. 6916–6920 (cit. on pp. 101, 102, 141).

[139] F. Liu, M. Mondello, and N. Goldenfeld. “Kinetics of the superconducting transition”. *Phys. Rev. Lett* **66** (1991), pp. 3071–3074 (cit. on p. 101).

[140] H. Frahm, S. Ullah, and A. Dorsey. “Flux dynamics and the growth of the superconducting phase”. *Phys. Rev. Lett* **66** (1991), pp. 3067–3070 (cit. on p. 101).

[141] R. Kato, Y. Enomoto, and S. Maekawa. “Effects of the surface boundary on the magnetization process in type-II superconductors”. *Phys. Rev. B* **47** (1993), pp. 8016–8024 (cit. on p. 101).

[142] M. Machida and H. Kaburaki. “Direct simulation of the time-dependent Ginzburg-Landau equation for type-II superconducting thin film: Vortex dynamics and V-I characteristics”. *Phys. Rev. Lett* **71** (1993), pp. 3206–3209 (cit. on p. 101).

[143] C. Bolech, G. C. Buscaglia, and A. López. “Numerical simulation of vortex arrays in thin superconducting films”. *Phys. Rev. B* **52** (1995), pp. 15719–15722 (cit. on p. 101).

[144] Q. Du, M. D. Gunzburger, and J. S. Peterson. “Solving the Ginzburg-Landau equations by finite-element methods”. *Phys. Rev. B* **46** (1992), pp. 9027–9034 (cit. on p. 101).

[145] G. Buscaglia, C. Bolech, and A. López. “Connectivity and Superconductivity”. J. Berger and J. Rubinstein Eds., Springer, 2000. Chap. On the numerical solution of the time-dependent Ginzburg-Landau equations in multiply connected domains (cit. on pp. 101, 103, 108, 124).

[146] D. Perez de Lara et al. “Vortex ratchet reversal: Role of interstitial vortices”. *Phys. Rev. B* **83** (17 May 2011), p. 174507 (cit. on p. 108).

[147] E. Gonzalez et al. “Reversible rectification of vortex motion in magnetic and non-magnetic asymmetric pinning potentials.” *Physica C* **437–438** (2006), pp. 77–81 (cit. on p. 108).

[148] M. Morelle, N. Schildermans, and V. V. Moshchalkov. “Rectification effects in superconducting triangles”. *Applied Physics Letters* **89**.11 (2006), p. 112512 (cit. on p. 108).

[149] N. S. Lin et al. “Rectification of vortex motion in a circular ratchet channel”. *Phys. Rev. B* **84** (14 Oct. 2011), p. 144511 (cit. on p. 108).

[150] V. V. Pryadun et al. “Plain superconducting films as magnetic field tunable two-dimensional rectifiers”. *Applied Physics Letters* **88**.6 (2006), p. 062517 (cit. on p. 108).

[151] T. S. Alstrøm et al. “Magnetic Flux Lines in Complex Geometry Type-II Superconductors Studied by the Time Dependent Ginzburg-Landau Equation”. *Acta Applicandae Mathematicae* **115**.1 (2011), pp. 63–74 (cit. on p. 109).

[152] G. R. Berdiyorov et al. “Finite-size effect on the resistive state in a mesoscopic type-II superconducting stripe”. *Phys. Rev. B* **79** (17 May 2009), p. 174506 (cit. on p. 109).

[153] M. Iavarone et al. “Imaging the spontaneous formation of vortex-antivortex pairs in planar superconductor/ferromagnet hybrid structures”. *Phys. Rev. B* **84** (2 July 2011), p. 024506 (cit. on p. 110).

[154] M. Donaire, T. W. B. Kibble, and A. Rajantie. “Spontaneous vortex formation on a superconducting film”. *New Journal of Physics* **9**.5 (2007), p. 148 (cit. on p. 110).

[155] T. Koyama et al. “Spontaneous vortex formation in a quench process in superconducting films with small holes”. *Physica C: Superconductivity and its Applications* **445–448** (2006). Proceedings of the 18th International Symposium on Superconductivity (ISS 2005)Advances in Superconductivity {XVIIIProceedings} of the 18th International Symposium on Superconductivity (ISS 2005), pp. 257–259 (cit. on p. 110).

[156] M. Milosevic and R. Geurts. “The Ginzburg-Landau theory in application”. *Physica C* **470**.19 (2010). Vortex Matter in Nanostructured Superconductors, pp. 791–795 (cit. on p. 111).

[157] J. Clarke and F. K. Wilhelm. “Superconducting quantum bits”. *Nature* **453** (2008), pp. 1031–1042 (cit. on p. 111).

[158] N. H. Lindner, G. Refael, and V. Galitski. “Floquet topological insulator in semiconductor quantum wells”. *Nature Phys.* **7** (2011), pp. 490–495 (cit. on p. 113).

[159] J. W. McIver et al. “Control over topological insulator photocurrents with light polarization”. *Nature Nanotech* **7** (2012), pp. 96–100 (cit. on p. 113).

[160] F. S. Bergeret et al. “Theory of microwave-assisted supercurrent in quantum point contacts”. *Phys. Rev. Lett.* **105** (11 2010), p. 117001 (cit. on p. 113).

[161] T. A. Palomaki et al. “Coherent state transfer between itinerant microwave fields and a mechanical oscillator”. *Nature* **495** (2013), pp. 210–214 (cit. on p. 113).

[162] P. Bhadrachalam et al. “Energy-filtered cold electron transport at room temperature”. *Nature Comms.* **5** (2014), p. 4745 (cit. on p. 113).

[163] M. J. Martínez-Pérez and F. Giazotto. "A quantum diffractor for thermal flux". *Nature Comms* **5** (2014), p. 3579 (cit. on p. 113).

[164] O. Entin-Wohlman. "Comment on the observation of order-parameter enhancement by a change in the magnetic flux". *Phys. Rev. B* **23** (1981), p. 2428 (cit. on p. 113).

[165] M. Beck et al. "Transient increase of the energy gap of superconducting NbN thin films excited by resonant narrow-band terahertz pulses". *Phys. Rev. Lett* **110** (2013), p. 267003 (cit. on p. 113).

[166] P. J. de Visser et al. "Evidence of a nonequilibrium distribution of quasiparticles in the microwave response of a superconducting aluminum resonator". *Phys. Rev. Lett* **112** (2014), p. 047004 (cit. on p. 113).

[167] A. A. Abrikosov. "The magnetic properties of superconducting alloys". *J. Phys. Chem. Solids* **2** (1957), p. 199 (cit. on p. 113).

[168] R. Marcon et al. "Vortex-motion dissipation in high-T_c superconductors at microwave frequencies." *Phys. Rev. B* **43** (1991), p. 2940 (cit. on p. 114).

[169] M. Golosovskyv, M. Tsindlekht, and D. Davidov. "High-frequency vortex dynamics in $YBa_2Cu_3O_7$". *Supercond. Sci. Technol* **9** (1996), pp. 1–15 (cit. on p. 114).

[170] R. Wördenweber et al. "Regimes of flux transport at microwave frequencies in nanostructured high-T_c films". *Physica C* **479** (2012), p. 69 (cit. on pp. 114, 123).

[171] J. R. Clem. "Local temperature-gradient contribution to flux-flow viscosity in superconductors." *Phys. Rev. Lett* **20** (1968), p. 735 (cit. on p. 114).

[172] A. Shekhter, L. N. Bulaevskii, and C. D. Batista. "Vortex viscosity in magnetic superconductors due to radiation of spin waves". *Phys.Rev. Lett* **106** (2011), p. 037001 (cit. on p. 114).

[173] A. Gurevich and G. Ciovati. "Dynamics of vortex penetration,jumpwise instabilities and nonlinear surface resistance of type-II superconductors in strong rf fields". *Phys. Rev. B* **77** (2008), p. 104501 (cit. on pp. 114, 123).

[174] A. I. Larkin and Y. N. Ovchinnikov. "Nonlinear conductivity of superconductors in the mixed state". *Sov. Phys. JETP* **41** (1976), p. 960 (cit. on pp. 114, 122, 123).

[175] T. Mäkinen et al. "Avalanches in Wood Compression". *Phys. Rev. Lett.* **115** (2015), p. 055501 (cit. on p. 114).

[176] S. Field et al. "Superconducting Vortex Avalanches". *Phys. Rev. Lett.* **74** (1995), p. 1206 (cit. on p. 114).

[177] M. Nada, M. Nakamura, and H. Matsuzaki. "25-Gbit/s burst-mode optical receiver using high-speed avalanche photodiode for 100-Gbit/s optical packet switching". *Optics Express* **22** (2014), p. 443 (cit. on p. 114).

[178] O. Jukimenko et al. "Multidimensional Instability and Dynamics of Spin Avalanches in Crystals of Nanomagnets". *Physical Review Letters* **113** (2014), p. 217206 (cit. on p. 114).

[179] T. H. Johansen et al. "Dendritic magnetic instability in superconducting MgB2 films". *Europhys. Lett.* **59** (2002), p. 599 (cit. on p. 114).

[180] A. L. Rakhmanov et al. "Finger patterns produced by thermomagnetic instability in superconductors". *Phys. Rev. B* **70** (2004), p. 224502 (cit. on p. 114).

[181] A. V. Bobyl et al. "Current-induced dendritic magnetic instability in superconducting MgB_2 films". *Applied Physics Letters* **80** (2002), p. 4588 (cit. on p. 114).

[182] P. Cuadra-Solıs et al. “Avalanche-like vortex penetration driven by pulsed microwave fields in an epitaxial LaSrCuO thin film”. *Journal of Applied Physics* **114** (2013), p. 233902 (cit. on p. 114).

[183] A. A. Awad et al. “Flux avalanches triggered by microwave depinning of magnetic vortices in Pb superconducting films”. *Physical Review B* **84** (2011), p. 224511 (cit. on pp. 114, 116, 126).

[184] V. V. Yurchenko et al. “Thermo-magnetic stability of superconducting films controlled by nano-morphology”. *Applied Physics Letters* **102** (2013), p. 252601 (cit. on p. 115).

[185] E.-M. Choi1 et al. “Suppression of dendritic flux jumps in MgB_2 films coated with a gold rim”. *Supercond. Sci. Technol.* **22** (2009), p. 015011 (cit. on p. 115).

[186] G. J. Dolan and J. Silcox. “Critical Thicknesses in Superconducting Thin Films”. *Phys. Rev. Lett.* **30** (1973), p. 603 (cit. on p. 115).

[187] D. Y. Vodolazov and F. M. Peeters. “Rearrangement of the vortex lattice due to instabilities of vortex flow”. *Phys. Rev. B* **76** (2007), p. 014521 (cit. on p. 123).

[188] S. G. Doettinger et al. “Electronic instability at high flux-flow velocities in high-T_c superconducting films”. *Phys. Rev. Lett* **73** (1994), p. 1691 (cit. on p. 123).

[189] G. Grimaldi et al. “Magnetic field and temperature dependence of the critical vortex velocity in type-II superconducting films”. *J. Phys.: Condens. Matter* **21** (2009), p. 254207 (cit. on p. 123).

[190] S. Dukan and Z. Tesanovic. “Density of states of a type-II superconductor in a high magnetic field: Impurity effects”. *Phys. Rev. B* **56** (2 July 1997), pp. 838–845 (cit. on p. 125).

[191] P. Prozorov et al. “Frequency dependent irreversibility line and undirectional magnetic anistrophy in thin YBa2Cu3O7-x films irradiated with heavy ions”. *Physica C* **235** (1994), pp. 3063–3064 (cit. on p. 131).

[192] A. Gomez et al. “Control of dissipation in superconducting films by magnetic stray fields”. *Applied Physics Letters* **102**.5 (2013), p. 052601 (cit. on p. 132).

[193] M. M. V. and P. F. M. “Commensurate vortex configurations in thin superconducting films nanostructured by square lattice of magnetic dots”. *Physica C* **404** (2004), p. 246 (cit. on p. 132).